

# $\gamma$ -Ray Lines – Signatures of Nucleosynthesis, Cosmic Rays, Positron Annihilation, and Fundamental Physics

Thomas Siegert<sup>1\*</sup>, Francesca Calore<sup>2</sup>, Pierre Jean<sup>3</sup>,  
Mark Leising<sup>4</sup>, Nicolas de Séréville<sup>5</sup>, Gerald H. Share<sup>6,7</sup>,  
Vincent Tatischeff<sup>5</sup>, Wei Wang<sup>8</sup>, Meng-Ru Wu<sup>9,10,11</sup>

<sup>1</sup>Julius-Maximilians-Universität Würzburg, Institut für Theoretische Physik  
und Astrophysik, Lehrstuhl für Astronomie, Emil-Fischer-Str. 31, 97074  
Würzburg, Germany.

<sup>2</sup>LAPTh, CNRS, USMB, 74940 Annecy, France.

<sup>3</sup>IRAP, Université de Toulouse, CNRS, CNES, 9 avenue du colonel Roche, BP  
44346, 31028 Toulouse, France.

<sup>4</sup>Clemson University, Department of Physics and Astronomy, Clemson, SC  
29634-0978, USA.

<sup>5</sup>Université Paris-Saclay, CNRS/IN2P3, IJCLab, 91405 Orsay, France.

<sup>6</sup>Astronomy Department, University of Maryland, College Park, MD 20740,  
USA.

<sup>7</sup>TSC, Resident at the Naval Research Laboratory, Washington, DC  
20375-5352, USA.

<sup>8</sup>School of Physics and Technology, Wuhan University, Wuhan 430072, People's  
Republic of China.

<sup>9</sup>Institute of Physics, Academia Sinica, Taipei, 11529, Taiwan.

<sup>10</sup>Institute of Astronomy and Astrophysics, Academia Sinica, Taipei, 106319,  
Taiwan.

<sup>11</sup>Physics Division, National Center for Theoretical Sciences, Taipei, 106319,  
Taiwan.

\*Corresponding author(s). E-mail(s): [thomas.siegert@uni-wuerzburg.de](mailto:thomas.siegert@uni-wuerzburg.de);

Contributing authors: [calore@lapth.cnrs.fr](mailto:calore@lapth.cnrs.fr); [pjean@irap.omp.eu](mailto:pjean@irap.omp.eu);

[lmark@clemson.edu](mailto:lmark@clemson.edu); [nicolas.de-sereville@ijclab.in2p3.fr](mailto:nicolas.de-sereville@ijclab.in2p3.fr); [gershare@aol.com](mailto:gershare@aol.com);

[vincent.tatischeff@csnsm.in2p3.fr](mailto:vincent.tatischeff@csnsm.in2p3.fr); [wangwei2017@whu.edu.cn](mailto:wangwei2017@whu.edu.cn); [mwu@as.edu.tw](mailto:mwu@as.edu.tw);

## Abstract

The nuclear gamma-ray ( $\gamma$ -ray) lines in the MeV range of the electromagnetic spectrum hold a vast variety of astrophysical, particle-physical, and fundamental physical information that is otherwise extreme difficult to access. MeV  $\gamma$ -ray line observations provide the most direct evidence for ongoing nucleosynthesis in galaxies by measuring freshly produced radioactive isotopes from massive stars, supernovae (SNe), classical novae (CNe), or binary neutron star mergers (BNSMs). Their flux ratios can determine the low-energy cosmic ray (LECR) spectrum in different objects and of the Milky Way as a whole. Different phases of the interstellar medium (ISM) are traced by hot nucleosynthesis ejecta, cooling positrons, or cosmic ray (CR) interactions with molecular clouds. Positron annihilation itself can be considered as an astrophysical messenger as their production and destruction in typical space environments is inevitable. Finally, as-of-yet unknown signatures from beyond Standard Model (BSM) physics might have their elusive imprints in  $\gamma$ -ray lines.

This Chapter gives an overview of historical  $\gamma$ -ray line measurements, newest results, and open questions that may only be solved by a new generation of MeV telescopes.

**Keywords:** nucleosynthesis, supernovae, massive stars, classical novae, neutron star mergers,  $\gamma$ -ray lines, cosmic-rays, nuclear excitation, positron annihilation, dark matter

## Contents

<b>List of Acronyms</b>	<b>4</b>
<b>1 Introduction</b>	<b>5</b>
1.1 Defining a $\gamma$ -Ray Line . . . . .	5
1.1.1 Astrophysical $\gamma$ -Ray Lines . . . . .	6
1.1.2 Taking into Account the Instrument . . . . .	6
1.2 Astrophysical Line Fluxes and Luminosities . . . . .	7
1.2.1 Radioactive Decay . . . . .	8
1.2.2 Nuclear Excitation . . . . .	9
1.2.3 Positron Annihilation . . . . .	10
1.2.4 Dark Matter Decay and Annihilation . . . . .	12
1.2.5 Opacity to $\gamma$ -rays . . . . .	13
<b>2 Observations and Predictions of <math>\gamma</math>-Ray Lines</b>	<b>14</b>
2.1 Diffuse Emission from Radioactive $^{26}\text{Al}$ . . . . .	14
2.1.1 Measurements of the 1809 keV Line . . . . .	15
2.1.2 Production and Destruction of $^{26}\text{Al}$ . . . . .	18
2.1.3 Understanding and Interpreting $^{26}\text{Al}$ Measurements . . . . .	19
2.2 Diffuse Emission from Radioactive $^{60}\text{Fe}$ . . . . .	26
2.2.1 Production of $^{60}\text{Fe}$ . . . . .	26
2.2.2 $\gamma$ -Ray Detections and Predictions of $^{60}\text{Fe}$ in the Galaxy . . . . .	26

2.2.3	Ratio of $^{60}\text{Fe}/^{26}\text{Al}$	29
2.3	$\gamma$ -Ray Lines from Classical Novae	32
2.3.1	Properties of Nuclear $\gamma$ -Rays from Classical Novae	32
2.3.2	Observations of $\gamma$ -Rays from Classical Novae	34
2.3.3	Conclusions	37
2.4	$\gamma$ -Ray Lines from Supernovae	39
2.4.1	$\gamma$ -Ray Lines from the $^{56}\text{Ni}$ Decay Chain in Type Ia Supernovae	42
2.4.2	$\gamma$ -Ray Lines from Core-Collapse Supernovae	49
2.4.3	Future Prospects of Supernova Observations	55
2.5	Nuclear $\gamma$ -Ray Lines from <i>r</i> -Process Sources	57
2.5.1	<i>r</i> -Process Nucleosynthesis	57
2.5.2	$\gamma$ -Rays from Individual <i>r</i> -Process Sources	58
2.5.3	Diffuse Extended <i>r</i> -Process $\gamma$ -Ray Emission	60
2.6	Nuclear De-Excitation $\gamma$ -Ray Lines from Low-Energy Cosmic Rays	63
2.6.1	Utilising Low-Energy Cosmic Rays	63
2.6.2	MeV $\gamma$ -Ray Line Observations and Predictions	64
2.7	Solar Flare $\gamma$ -Rays	67
2.7.1	Particle Acceleration in Flares	67
2.7.2	The Solar $\gamma$ -Ray Spectrum	68
2.7.3	The $\gamma$ -Ray Continuum from Electrons	68
2.7.4	Neutron-Capture and Annihilation Lines	69
2.7.5	Nuclear De-Excitation Lines	70
2.8	Solar System Bodies and their $\gamma$ -Ray Albedos	73
2.8.1	Calculations of $\gamma$ -Ray Albedos	73
2.8.2	$\gamma$ -Ray Measurements of Solar System Objects	76
2.9	The Positron Annihilation Line at 511 keV	78
2.9.1	Overview of 511 keV Observations	78
2.9.2	Possible Positron Sources	82
2.9.3	The Positron Puzzle	86
2.9.4	Positron Annihilation is not Always a 511 keV Line	92
<b>3</b>	<b>Outlook</b>	<b>94</b>
3.1	Laboratory Measurements for the Production of $\gamma$ -Ray Emitters	94
3.1.1	Reaction Rates, Nuclear Cross-Sections and Their Determination	94
3.1.2	Observed $\gamma$ -Ray Emitters	95
3.1.3	Yet to be Observed $\gamma$ -ray Emitters	98
3.1.4	Perspectives	99
3.2	Quo Vadis, $\gamma$ -Ray Line Science?	99
3.2.1	Neutron Capture Line: 2223 keV	99
3.2.2	Dark Matter and other Beyond-Standard-Model Candidates	102
3.3	What is Needed? – A New MeV $\gamma$ -Ray Mission	107
<b>References</b>		<b>109</b>

## List of Acronyms

<b>ACS</b>	anticoincidence system	<b>INTEGRAL</b>	International Gamma-Ray Astrophysics Laboratory
<b>AGB</b>	asymptotic giant branch	<b>ISM</b>	interstellar medium
<b>ALP</b>	axion-like particle	<b>JT</b>	Jovian Trojan
<b>BAT</b>	Burst Alert Telescope	<b>KBO</b>	Kuiper Belt Object
<b>BATSE</b>	Burst and Transient Source Experiment	<b>LMC</b>	Large Magellanic Cloud
<b>BBN</b>	Big Bang Nucleosynthesis	<b>LECR</b>	low-energy cosmic ray
<b>BH</b>	black hole	<b>LoS</b>	line of sight
<b>BNSM</b>	binary neutron star merger	<b>LP</b>	Lunar Prospector
<b>BSM</b>	beyond Standard Model	<b>MBA</b>	Main Belt Asteroid
<b>Cas A</b>	Cassiopeia A	<b>MESA</b>	Modules for Experiments in Stellar Astrophysics
<b>CGB</b>	Cosmic Gamma-Ray Background	<b>MRSN</b>	magneto-rotational supernova
<b>CMB</b>	Cosmic Microwave Background	<b>NEAR</b>	Near Earth Asteroid Rendezvous
<b>CME</b>	coronal mass ejection	<b>NFW</b>	Navarro-Frenk-White
<b>CXB</b>	Cosmic X-Ray Background	<b>NS</b>	neutron star
<b>CN</b>	classical nova	<b>NT</b>	Neptunian Trojan
<b>COBE</b>	Cosmic Background Explorer	<b>NuSTAR</b>	Nuclear Spectroscopic Telescope Array
<b>CEJSN</b>	common envelope jet supernova	<b>OSSE</b>	Oriented Scintillation Spectrometer Experiment
<b>COMPTEL</b>	Imaging Compton Telescope	<b>PTSN</b>	phase-transition supernova
<b>ccSN</b>	core-collapse supernova	<b>Ps</b>	Positronium
<b>CGRO</b>	Compton Gamma Ray Observatory	<b>PSYCO</b>	population synthesis code
<b>COSI</b>	Compton Spectrometer and Imager	<b>RHESSI</b>	Reuven Ramaty High Energy Solar Spectroscopic Imager
<b>CR</b>	cosmic ray	<b>RMS</b>	root mean square
<b>DM</b>	dark matter	<b>SEP</b>	Solar energetic particle
<b>DMR</b>	Differential Microwave Radiometer	<b>SFR</b>	star formation rate
<b>EC</b>	electron capture	<b>SMM</b>	Solar Maximum Mission
<b>FIP</b>	first ionisation potential	<b>SN</b>	supernova
<b>FoV</b>	field of view	<b>SNR</b>	supernova remnant
<b>FWHM</b>	full width at half maximum	<b>SN Ia</b>	type Ia supernova
<b>GRS</b>	Gamma-Ray Spectrometer	<b>SPI</b>	Spectrometer onboard INTEGRAL
<b>GRAND</b>	Gamma Ray and Neutron Detector	<b>TGRS</b>	Transient Gamma-Ray Spectrometer
<b>GRIS</b>	Gamma Ray Imaging Spectrometer	<b>TS</b>	test statistic
<b>GEANT4</b>	GEometry ANd Tracking 4	<b>WD</b>	white dwarf
<b>GF</b>	giant flare	<b>WIMP</b>	weakly interacting massive particle
<b><math>\gamma</math>-ray</b>	gamma-ray	<b>WISP</b>	weakly interacting slim particle
<b>HEAO 3</b>	High Energy Astronomy Observatory 3	<b>WR</b>	Wolf-Rayet
<b>IBIS</b>	Imager on Board the INTEGRAL Satellite		
<b>IC</b>	Inverse Compton		
<b>IMF</b>	initial mass function		

# 1 Introduction

Written by Thomas Siegert

The MeV range is prone to many astrophysical processes that give rise to  $\gamma$ -ray lines (e.g., Ramaty and Lingenfelter, 1979; Schönfelder, 2001; Diehl et al., 2018). Here, we define  $\gamma$ -ray lines as mono-energetic spectral features, whose detailed analyses inform about the microphysical mechanisms that ultimately lead to observable large-scale phenomena. In this chapter, we distinguish between decay  $\gamma$ -rays from nucleosynthesis ejecta and the nuclear excitation of circum- and ISM, as well as matter of major and minor bodies, by low-energy cosmic rays LECRs followed by de-excitation, even though the emission mechanism is identical (Ramaty and Lingenfelter, 1979; Lingenfelter and Ramaty, 1986; Diehl et al., 2018). The possible subsequent annihilation of positrons created in these processes is treated individually as well because several different interaction channels can lead to the production of positrons than just radioactive decay (Lingenfelter and Ramaty, 1986; Prantzos et al., 2011). Finally,  $\gamma$ -ray lines may also be produced through BSM processes directly (Lewin and Smith, 1996; Bergström et al., 1998).

This Chapter will focus on the observational characteristics of  $\gamma$ -ray lines. Details of the individual source types can be found elsewhere in this volume, and we refer the reader to these Chapters. Typically, Chapters that consider nuclear  $\gamma$ -rays start by listing a table of lines with line energies, lifetimes, channels, and if they have been detected. Here, we are attempting to show a much broader overview of  $\gamma$ -ray line observations and their potential for future MeV space missions. Therefore, we postpone the list of lines to the individual subsections because a single table would be too large and incomprehensive.

In what follows, we outline how  $\gamma$ -ray line measurements are to be understood in general. This means, we introduce the concept of  $\gamma$ -ray lines in space and in the measurement, and how they can change due to different (astro-)physical considerations. The applications to prominent  $\gamma$ -ray lines are then found in Sec. 2.

## 1.1 Defining a $\gamma$ -Ray Line

We define the spectral shape of any  $\gamma$ -ray line,  $L(E; \vec{\varphi})$ , as a function of photon energy,  $E$ , and a set of parameters,  $\vec{\varphi}$ , by a convolution of its intrinsic (microphysical) line shape,  $I(E; \vec{\vartheta})$ , with an astrophysical broadening shape,  $A(E; \vec{\varrho})$ , as

$$L(E; \vec{\varphi}) = \int_{-\infty}^{+\infty} dE' I(E'; \vec{\vartheta}) \cdot A(E - E'; \vec{\varrho}). \quad (1)$$

In many cases,  $I(E; \vec{\vartheta})$  has the shape of a Lorentz curve with  $\vec{\vartheta}$  including the centroid of the line,  $E_{\text{lab}}$ , and its natural broadening (e.g., its lifetime; Krane, 1987). Often, the spectral resolution of typical detectors in space applications is much larger than the natural line width, so that in all meaningful studies,  $I(E; \vec{\vartheta})$  can be approximated as a  $\delta$ -function,

$$I(E; \vec{\vartheta}) \approx I_0 \delta(E - E_{\text{lab}}), \quad (2)$$

with  $I_0$  being the amplitude of the line.

### 1.1.1 Astrophysical $\gamma$ -Ray Lines

The astrophysical shape,  $A(E; \vec{\varrho})$ , then describes the entire expectation towards the measurement and can be of any physically allowed form, such as symmetric or asymmetric Gaussians, box-like shapes, multiple components, etc., depending on the actual geometry of the object, its kinematics, and physical effects like absorption. In most astrophysical studies,  $A(E; \vec{\varrho})$  can be approximated by a Gaussian,

$$A(E; \vec{\varrho}) \approx G(E; \Delta E, \sigma) = \frac{A_0}{\sqrt{2\pi} \cdot \sigma} \exp\left(-\frac{1}{2} \frac{(\Delta E)^2}{\sigma^2}\right), \quad (3)$$

where  $\Delta E$  describes the line shift with respect to the laboratory energy,  $\sigma$  describes the astrophysical line broadening, and  $A_0$  the astrophysical line flux.

#### 1.1.1.1 Doppler Shift

The line shift can be directly related to the non-relativistic Doppler shift by

$$\frac{\Delta E}{E_{\text{lab}}} = \frac{v}{c}, \quad (4)$$

where  $v$  is the relative velocity of the object to the observer, and  $c$  is the speed of light. A ‘blue-shift’ of the line indicates that  $v$  is positive and that object and observer are approaching each other.

#### 1.1.1.2 Doppler Broadening

The astrophysical line broadening  $\sigma$  can also be linked to a Doppler-broadening velocity of an object, but which depends on the actual situation, and should take into account opacities and density distributions (Ferrière, 2001). On the one hand, in cases in which an observer sees a spatially unresolved expanding sphere, assumed to be homogeneously filled and expanding at the same velocity isotropically with  $v_{\text{exp}}$ , the astrophysical shape is *not* Gaussian, but a boxcar that ranges from  $E_{\text{lab}}(1 - v_{\text{exp}}/c)$  to  $E_{\text{lab}}(1 + v_{\text{exp}}/c)$  (Chan and Lingenfelter, 1987). The same shape applies to a thin shell. If, nevertheless, this shape is to be approximated as a Gaussian, the full width at half maximum (FWHM) of the Gaussian would be

$$\text{FWHM} = 2\sqrt{2 \ln 2} \cdot \sigma = 2 \frac{v_{\text{exp}}}{c} E_{\text{lab}} \Leftrightarrow \sigma \approx 0.85 \frac{v_{\text{exp}}}{c} E_{\text{lab}}. \quad (5)$$

On the other hand, the  $\sigma$  value of the astrophysical Gaussian shape can also be discussed in terms of the turbulent motion or temperature, that is, not bulk motion, or in terms of conditions for annihilation. We will return to these interpretations in the respective subsections.

### 1.1.2 Taking into Account the Instrument

Beyond the astrophysical line shape, the measured line shape is subject to the spectral response of the detectors used (Knoll, 2000). This means the energy resolution of the

instrument has to be taken into account to interpret the measurement correctly. While also here, the line shape can be very asymmetric, for example from incomplete charge collection (Knoll, 2000; Diehl et al., 2018), due to degradation of the detectors due to cosmic-ray bombardment, or simply from the electronics, a symmetric Gaussian is typically sufficient to describe the instrumental resolution. As a result, Eq. (1) has to be convolved with the spectral response (e.g., Pendleton et al., 1995; Siegert et al., 2022). In a simple measurement of turbulent motion, for example, the measured line width,  $\sigma_{\text{meas}}$ , is then approximately the quadratic sum of the instrumental line width ('resolution'),  $\sigma_{\text{inst}}$ , and the astrophysical line width,  $\sigma_{\text{astro}}$ ,

$$\sigma_{\text{meas}}^2(E) = \sigma_{\text{inst}}^2(E) + \sigma_{\text{astro}}^2(E) \quad (6)$$

Taking into account that instrumental resolutions,  $\text{FWHM}_{\text{inst}}(E)/E$ , are typically on the order of 0.1% (Ge) to 10% (NaI), and further depend on the photon energy with an approximate square-root dependence,  $\text{FWHM}_{\text{inst}}(E) \propto \sqrt{E}$ , it becomes evident that the spectral resolution in the MeV range is generally improving as a function of energy. However, due to other constraints, such as detector efficiency and photon count statistics, the 'best' measurements are typically achieved between 0.5–2.5 MeV. Continuing the example of turbulent motion along the line of sight (LoS), the width of the astronomical component is directly related to the 1D LoS root mean square (RMS),

$$\sigma_{\text{astro}} = \frac{\langle v_{\text{los}}^2 \rangle^{1/2}}{c} E_{\text{lab}}. \quad (7)$$

For turbulent motion in the ISM,  $\sigma_{\text{astro}}$  is about 100 km s<sup>-1</sup> (Ferrière, 2001), which results in a Doppler broadening of 0.6 keV at 1809 keV (radioactive <sup>26</sup>Al, see Sec. 2.1). Even with Ge detectors and their excellent energy resolution of  $\approx 3.1$  keV (FWHM at 1809 keV), the measured line width would only be 3.4 keV (FWHM), that is, slightly above instrumental resolution.

## 1.2 Astrophysical Line Fluxes and Luminosities

The astrophysical line flux,  $A_0$ , together with the amplitude of the intrinsic line,  $I_0$ , can be combined into a measurable flux,  $F$ . Typically,  $F$  is in units of ph cm<sup>-2</sup> s<sup>-1</sup> if integrated over the region of interest, or if the source is point-like, or in units of ph cm<sup>-2</sup> s<sup>-1</sup> sr<sup>-1</sup> to take into account possible spatial variations. In general,  $F$  depends on the astrophysics studied. Again, we distinguish between radioactive decay, nuclear excitation, positron annihilation, and BSM processes, such as dark matter (DM) annihilation and decay. We can separate the microphysical components from the astrophysical (geometrical) ones by considering

$$F(\ell, b) = \rho_0 \cdot \frac{1}{4\pi \text{ sr}} \int_0^\infty ds \rho(\tilde{x}(s, \ell, b), \tilde{y}(s, \ell, b), \tilde{z}(s, \ell, b)), \quad (8)$$

where  $(\tilde{x}, \tilde{y}, \tilde{z})^T$  is the LoS vector from the observer ( $s = 0$ ) to infinity,  $(\ell, b)$  are (Galactic) coordinates,  $\rho(x, y, z)$  is a normalised, unitless emissivity distribution in three

dimensions, and  $\rho_0$  is the (central) emissivity in units of  $\text{ph cm}^{-3} \text{s}^{-1}$ . The microphysical input is completely covered in  $\rho_0$ . The factor  $(4\pi \text{sr})^{-1}$  is explicitly written out for the full differential flux as a function of the chosen coordinates,  $F(\ell, b)$ . Integrating over the sphere of the sky results in the total flux,

$$F = \int_{-\pi}^{+\pi} d\ell \int_{-\pi/2}^{+\pi/2} \sin(b) db F(\ell, b), \quad (9)$$

in units of  $\text{ph cm}^{-2} \text{s}^{-1}$ . The volume integral over the emissivity,

$$L = \rho_0 \cdot \int_{-\pi}^{+\pi} d\ell \int_{-\pi/2}^{+\pi/2} \sin(b) db \int_0^{\infty} ds s^2 \rho(\tilde{x}(s, \ell, b), \tilde{y}(s, \ell, b), \tilde{z}(s, \ell, b)), \quad (10)$$

describes the luminosity,  $L$ , of the source in units of  $\text{ph s}^{-1}$ . Since the central emissivity is independent of the coordinates, we can describe the luminosity as  $L = \rho_0 \cdot V_{\text{eff}}$ , with  $V_{\text{eff}}$  being an ‘effective volume’ of the astrophysical source. In this regard, the volume integral can also be carried out in more suitable coordinates and does not necessarily need to start from the observer. This is important to note because it directly relates the microphysics to the shape of the object studied. Keeping this general description of flux and luminosity, we can also define an ‘effective distance’ to any source type (extended or point-like) by

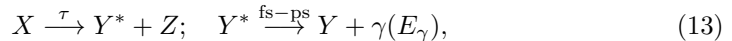
$$d_{\text{eff}} := \left[ \frac{L}{4\pi F} \right]^{1/2}, \quad (11)$$

which is simply the weighted emissivity distribution, and does not depend on the microphysics. For the classical case of point sources (ps) with  $\rho(x, y, z) = \delta(x - x_0)\delta(y - y_0)\delta(z - z_0)$ , and an absolute distance to the observer of  $d = (x_0^2 + y_0^2 + z_0^2)^{1/2}$ , the effective distance reduces to the absolute distance, and the general ‘inverse square law’ is recovered,

$$F_{\text{ps}} = \frac{L_{\text{ps}}}{4\pi d_{\text{ps}}^2}. \quad (12)$$

### 1.2.1 Radioactive Decay

The generic equation of photons from radioactive decays is



where the parent nucleus,  $X$ , is decaying into a nuclearly excited state of a daughter nucleus,  $Y^*$ , within a lifetime  $\tau$ , and some other particle(s), named  $Z$ . This process can happen through all possible decay channels, such as  $\alpha$ - or  $\beta^{\pm}$ -decay, electron capture (EC), or similar. The excited daughter nucleus has a typical lifetime of fs to ps and, on astronomical time scales, immediately de-excites by emitting a photon,  $\gamma$ , with energy  $E_{\gamma}$ . In an even more general case, there can be cascades or these de-excitations so that one decay can result in several decay  $\gamma$ -rays with specific branching ratios. The fundamental statement for these decay  $\gamma$ -rays is that they can only be

produced once – when the parent nucleus decayed, it cannot produce these photons any more. However, the daughter nucleus might also be radioactive and could itself decay and therefore lead to additional  $\gamma$ -rays. This fact will become important in the case of type Ia supernovae (SNe Ia).

In the case of decaying isotopes (e.g., [Clayton, 1968](#); [Woosley and Weaver, 1995](#)), we consider the total radioactive mass of an object,  $M_0$ , made of an isotope  $i$  with atomic mass  $m_i$ , that is decaying with a lifetime  $\tau_i$ . Then, the activity is

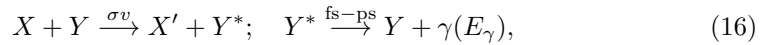
$$A_i(t) := \frac{N_i(t)}{\tau_i} = \frac{M(t)}{m_i \tau_i} = \frac{M_0}{m_i \tau_i} \exp\left(-\frac{t - t_0}{\tau_i}\right), \quad (14)$$

with  $M(t) = M_0 \exp\left(-\frac{t - t_0}{\tau_i}\right)$  describing the decay of the total mass as a function of time,  $t$ , so that  $M(t_0) = M_0$ . The activity is directly related to the luminosity of this astrophysical source by considering that each decay has a probability of  $p_i$  to emit a photon from the excited daughter nucleus. It follows that

$$L_i(t) = A_i(t)p_i = \frac{M_0 p_i}{m_i \tau_i} \exp\left(-\frac{t - t_0}{\tau_i}\right). \quad (15)$$

### 1.2.2 Nuclear Excitation

The generic equation of photons from nuclear excitation followed by de-excitation is



where an energetic particle,  $X$ , typically a CR proton or alpha, interacts with an almost stationary particle,  $Y$  ([Ramaty and Lingenfelter, 1979](#); [Kozlovsky et al., 2002](#)). Then, there is a chance, given by the cross-section,  $\sigma$ , and the relative velocity,  $v$ , that the particle  $Y$  becomes nuclearly excited to  $Y^*$ . Similar to the radioactive decay, the excited state immediately de-excites by emitting a  $\gamma$ -ray at a specific energy. However, opposed to the case of radioactive decay, this typically happens for stable nuclei in the ISM so that the excitation and de-excitation process is in balance and reflects the spectrum of LECRs and the ambient densities. Also, most of the excitations will lead to the first excited state and only rarely will higher levels be occupied. This is changed, however, for the case of nuclear excitation of nuclei in planetary atmospheres and solid bodies where the densities are much larger than in the ISM and the chances to populate higher levels are sizeable.

In the case of exciting isotopes, we consider the particle number density of a (stable) species  $i$  in the ISM,  $n_i$ , in units of  $\text{cm}^{-3}$ , that interacts with a spectrum of CRs of the form  $dn_{\text{CR}}(E)/dE$  in units of  $\text{cm}^{-3} \text{eV}^{-1}$ , given the interaction cross-section for nuclear excitation,  $\sigma_{\text{ex}}(E)$ , and the relative velocity,  $v_{\text{rel}}(E)$ . The emissivity is then calculated as

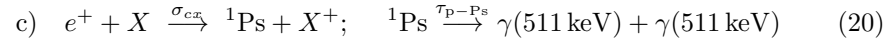
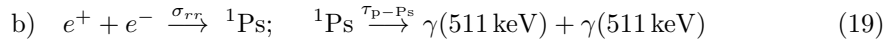
$$\rho_0 = \int_{E_{\text{th}}}^{\infty} dE \frac{dn_{\text{CR}}(E)}{dE} n_{\text{ISM}} \sigma_{\text{ex}}(E) v_{\text{rel}}(E), \quad (17)$$

where  $E_{\text{th}}$  is the threshold energy for the nuclear excitation to a certain level. Note that in the more general case, the photons created in the process could also be absorbed

again, so that additional factors have to be included. Likewise, there are also competing processes to the excitation, such as spallation, elastic scattering, transmutation, etc., which may also lead to (different)  $\gamma$ -ray photons or to none. An important process in this context is the neutron capture by protons, forming deuterium, and a  $\gamma$ -ray line at 2224 keV (see Secs. 2.7 & 3.2.1; see also Share and Murphy, 1995; Hua and Lingefelter, 1987). In the case of two-plasma interactions, also the shape of the resulting  $\gamma$ -ray lines will be influenced by the plasma temperature and asymmetric two-peak structures may emerge due to the relativistic Doppler effect (Aharonian and Sunyaev, 1984; Yoneda et al., 2023).

### 1.2.3 Positron Annihilation

A generic equation of photons from positron annihilation does not exist, because there are several channels that can lead to the  $\gamma$ -ray line at 511 keV photon energies. We will give three production channels in the following:



where the cases a), b), and c), are direct annihilation (da), radiative recombination (rr), and charge exchange (cx), respectively (Guessoum et al., 2005). As will be discussed further in Secs. 2.9 & 2.9.4, all these positron annihilation channels do *not* necessarily result in a 511 keV line (Ore and Powell, 1949; Aharonian and Atoyan, 1981, 2000). Case a) only results in a 511 keV line, if the kinetic energies of the participating particles are small, for example on the order of a few 100 eV at most. At higher energies, the relative velocities of the electron and the positron leads to a conversion of also their kinetic energies into photons, resulting in a continuous spectrum from  $m_e/2$  to  $T + m_e/2$ , with  $m_e$  being the rest mass energy of the electron and  $T$  its kinetic energy (Aharonian and Atoyan, 2000). The direct annihilation spectrum can be single- or double-peaked, and the internal shape depends on the kinetic energies of both particles (Svensson, 1982, 1983). Case a) competes with case b) in the absence of atoms. Radiative recombination of free positrons with free electrons is the dominant process below  $\sim 30$  eV (Prantzos et al., 2011). Then, an intermediate bound state, called Positronium (Ps), is formed (Ore and Powell, 1949; Deutsch, 1951a). The exotic atom of Ps behaves similarly to a hydrogen atom, but with a limited lifetime of  $\tau_{\text{p-Ps}} = 0.124$  ns in the case of para-Ps, i.e. the  ${}^1\text{Ps}$  state. Para-Ps is *decaying* via the electromagnetic force to two photons that carry 511 keV each. Due to its finite lifetime, the para-Ps  $\gamma$ -ray line has a natural width of  $5.3 \mu\text{eV}$ , and is as such always taken as a delta-function. In three out of four recombinations, however, the  ${}^3\text{Ps}$  state is formed, called ortho-Ps, which has a longer lifetime of  $\tau_{\text{o-Ps}} = 13.9 \mu\text{s}$  (Deutsch, 1951b). In this case, due to parity conservation, ortho-Ps is decaying into three photons with a characteristic spectrum that peaks at 511 keV (Ore and Powell, 1949), but shows no  $\gamma$ -ray line. In the presence of atoms ( $X$ ), case c) is the dominant channel by far (four to six orders of magnitude in cross-section) above the species-specific threshold

(Guessoum et al., 1991). The cross-section of charge exchange typically peaks slightly above threshold, for example around 12 eV with a threshold of 6.8 eV in the case of natural hydrogen, and competes with the process of atomic or molecular excitation (see Guessoum et al., 2005, 2010; Prantzos et al., 2011; Siegert, 2023, for a more detailed description).

In any of the three cases, the annihilation rate / **Ps**-formation rate per unit volume can be calculated as

$$\Gamma_{\pm} = n_+(E_+)n_x(E_x)\sigma_x(E_+, E_x)v_{\text{rel}}(E_+, E_x), \quad (21)$$

where  $n_+(E_+)$  is the particle number density of positrons in units of  $\text{cm}^{-3}$  with kinetic energy  $E_+ \lesssim 1 \text{ keV}$ ,  $n_x(E_x)$  is the particle number density of species  $x$ , with either being free electrons or at least one-electron atoms or molecules, having a kinetic energy  $E_x \lesssim 1 \text{ keV}$ ,  $\sigma_x(E_+, E_x)$  being the corresponding cross-section in units of  $\text{cm}^{-2}$ , and  $v_{\text{rel}}(E_+, E_x)$  is the relative velocity (Svensson, 1982). In this calculation, we only consider non-relativistic particles ( $E_+ \lesssim 1 \text{ keV}$ ) to obtain an order of magnitude estimate for the annihilation rate. **Ps** only forms efficiently for small relative velocities of the participating particles. In the general case of arbitrary kinetic energies, the distribution functions for the positrons and species  $x$  has to be taken into account, in addition to using the differential cross-section  $d\sigma_x(E_+, E_x, \mu)/dE$ . In the case of slow participating partners, it is often enough to use non-differential values. Now, in order to calculate the emissivity of *only* the 511 keV line, we need to take into account the formation of **Ps** with a fraction  $f_{\text{Ps}}$ , typically called the **Ps**-fraction: The **Ps**-fraction can be calculated from the statistical weight of **Ps** decaying into two or three photons, and the number of direct annihilations without **Ps** formation. The multiplicity of a particular spin state is  $(2S + 1)$ , so that para-**Ps** will be formed 1/4 of the time, and ortho-**Ps** 3/4 of the time. While para-**Ps** emits two photons, ortho-**Ps** will emit three photons, so that the emissivity  $\rho_{3\gamma}$  is proportional to  $3\frac{3}{4}f_{\text{Ps}} = \frac{9}{4}f_{\text{Ps}}$ . The two-photon emissivity (the 511 keV line) is then given by the sum over para-**Ps** decays and the direct annihilation emissivity, weighted with the respective **Ps**-fraction,  $\rho_{2\gamma} \propto 2\frac{1}{4}f_{\text{Ps}} + 2(1 - f_{\text{Ps}}) = 2 - \frac{3}{2}f_{\text{Ps}}$  (Leventhal et al., 1978). Linking the annihilation rate to the 511 keV emissivity, we find

$$\rho_{2\gamma} = \Gamma_{\pm} \left( 2 - \frac{3}{2}f_{\text{Ps}} \right), \quad (22)$$

with  $f_{\text{Ps}}$  being related to the ratio of the two-photon to three-photon fluxes,  $R_{32} = F_{3\gamma}/F_{2\gamma}$ , by

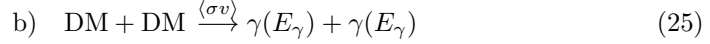
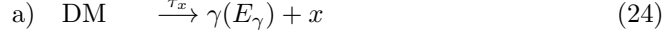
$$f_{\text{Ps}} = \frac{8R_{32}}{6R_{32} + 9}. \quad (23)$$

The **Ps**-fraction is a function of the **ISM** / surrounding conditions, such as ionisation state and temperature (Guessoum et al., 1991, 2005; Churazov et al., 2005; Jean et al., 2006). Likewise, the line width, and in general the line shape of the 511 keV from these processes, also depend on the ionisation state and temperature. This can be used to formulate ‘annihilation conditions in the **ISM**’ if the **Ps**-fraction and the 511 keV line width can be measured in detail.

As a final remark for positron annihilation physics, there would be also annihilation with bound electrons which is subdominant in the **ISM** case, but can play a major role in the case of annihilation on dust grains and solid bodies (see Secs. 2.8 & 2.9; see also [Guessoum et al., 2005](#); [Sieger, 2017](#)).

#### 1.2.4 Dark Matter Decay and Annihilation

There are at least two generic equations that may generate **γ-ray** lines from **BSM**-processes, such as **DM** decay or annihilation ([Bergström et al., 1998](#)):



We refer to case a) as **DM** decay, where the second particle,  $x$ , could either be another photon of same energy  $E_\gamma$ , or a neutrino,  $\nu_a$ , which may mix with a fourth generation of (sterile) neutrinos,  $\nu_s$  (e.g., [Abazajian et al., 2001](#)). In the case of a two-photon decay, the **γ-ray** line would be found at  $E_\gamma = m_{\text{DM}}/2$  with an amplitude of 2. In the mixed final state, the **γ-ray** line would be found at  $E_\gamma = m_{\nu_s}/2$  with an amplitude of 1. The emissivity of **DM** decay is – formally – calculated as

$$\rho_{\text{decay}} = \frac{\Gamma}{m_{\text{DM}}} \rho_s, \quad (26)$$

where  $\Gamma = \tau^{-1}$  is the decay rate, in units of  $\text{s}^{-1}$ , of the **DM** particle with mass  $m_{\text{DM}}$  in units of g, and  $\rho_s$  is the central mass density of a **DM** density halo profile in units of  $\text{g cm}^{-3}$ . The decay rate,  $\Gamma$ , is then model dependent (see Sec. 3.2.2), and  $\rho_s$  has to be inferred from other measurements, such as the rotation curve of a galaxy, to obtain the gravitational potential. In order to comply with the notation in the literature ([Jungman et al., 1996](#)), the **DM** flux is typically written in the form

$$\left( \frac{dN}{dE dA dt d\Omega} \right)_{\text{decay}} = \frac{\Gamma}{4\pi \text{sr}} \frac{1}{m_{\text{DM}}} \left( \frac{dN}{dE} \right)_\gamma \int_0^\infty ds \rho_s \cdot \rho(r(s, \ell, b)), \quad (27)$$

where the integral term is typically referred to as the ‘D-factor’, and the term  $(dN/dE)_\gamma$  is the photon spectrum. Comparing Eq. (27) to Eqs. (26) and (8), the individual terms can be identified.

In a similar way, case b), the **DM** annihilation can be described. Here, the general description of **LoS** integrals and emissivities also works, but is less commonly used,

$$\rho_{\text{annihilation}} = \frac{\langle\sigma v\rangle}{m_{\text{DM}}^2} \rho_s^2. \quad (28)$$

Instead, we will use the typical notation in the literature ([Jungman et al., 1996](#)) which calculates the differential flux as

$$\left( \frac{dN}{dE dA dt} \right)_{\text{ann}} = \frac{\langle\sigma v\rangle}{4\pi \text{sr}} \frac{1}{m_{\text{DM}}^2} \left( \frac{dN}{dE} \right)_\gamma \times \int_{\Delta\Omega} d\Omega \int_0^\infty ds [\rho_s \cdot \rho(r(s, \ell, b))]^2, \quad (29)$$

where the double-integral, sometimes normalised by the region of interest,  $\Delta\Omega$ , is typically referred to as the ‘J-factor’ (e.g., [Evans et al., 2012](#)), often shown in units of  $\text{GeV}^2 \text{cm}^{-5}$  or  $\text{M}_\odot^2 \text{pc}^{-5}$ . The differential flux in units of  $\text{phcm}^{-2} \text{s}^{-1} \text{sr}^{-1}$  simply uses the [LoS](#) integral without the solid-angle integration. Because [DM](#) annihilation is a two-body process, the density and [DM](#) mass have to be squared. Instead of the decay rate, now the velocity-averaged annihilation cross-section,  $\langle\sigma v\rangle$  ([Steigman et al., 2012](#)), in units of  $\text{cm}^3 \text{s}^{-1}$  dictates the amplitude of the flux. Similar to case a),  $\langle\sigma v\rangle$  is model dependent. The spectrum – only considering [γ-ray](#) lines again,  $(dN/dE)_\gamma$ , is now peaking at  $E_\gamma = m_{\text{DM}}$ .

### 1.2.5 Opacity to [γ](#)-rays

Gamma-ray photons propagating through matter are generally attenuated by photo-electric absorption, Compton scattering, and pair production, which combine into an energy-dependent opacity,  $\kappa(E)$ , in units of  $\text{cm}^2 \text{g}^{-1}$ . The radiative-transfer equation,

$$\frac{dI(E, r(s, \ell, b))}{ds} = -\kappa(E, r(s, \ell, b)) I(E, r(s, \ell, b)), \quad (30)$$

connects the specific intensity,  $I(E)$ , to the local opacity and the current intensity along the [LoS](#)  $s$ . The negative sign indicates that absorption and scattering ‘remove’ photons from the beam as they propagate. The cumulative effect is expressed through the optical depth,  $\tau(E)$ , which determines whether photons escape or are absorbed,

$$\tau(E) = \int \kappa(E, r(s, \ell, b)) \varrho(r(s, \ell, b)) ds. \quad (31)$$

Here, the optical depth is the [LoS](#) integral of the opacity weighted with the mass density,  $\varrho$ , in units of  $\text{g cm}^{-3}$ . We note that  $\tau$  may either be considered as an intrinsic property of an emission region or a value along a [LoS](#), representing the number of mean-free-paths encountered by a photon. A photon escapes or propagates freely when  $\tau \lesssim 1$  and is strongly attenuated when  $\tau \gg 1$  ([Rybicki and Lightman, 1979](#)).

In the diffuse [ISM](#), with  $n \sim 1 \text{ cm}^{-3}$  and column densities  $N \sim 10^{21} \text{ cm}^{-2}$  ([Morrison and McCammon, 1983](#)), [γ-ray](#) photons above a few keV experience  $\tau \ll 1$  and propagate effectively in an optically thin regime. In contrast, stellar envelopes, [CNe](#), and young [SNe](#) with densities  $\varrho \sim 10^{-12}-10^{-7} \text{ g cm}^{-3}$  and column densities  $N \sim 10^{25}-10^{29} \text{ cm}^{-2}$  yield large optical depths at early times ([Chan and Lingenfelter, 1987](#); [Pinto and Woosley, 1988](#)). Typical mass attenuation coefficients for neutral gas are  $\kappa = \mu/\varrho \approx \{10^{-1}, 10^{-2}, 10^{-3}, 10^{-4}\} \text{ cm}^2 \text{g}^{-1}$  at photon energies  $\{10, 100, 1000, 10000\} \text{ keV}$ , respectively. These give optical depths in [ISM](#) of approximately  $\tau \sim \{10^{-3}, 10^{-4}, 10^{-5}, 10^{-6}\}$ , that is, negligible attenuation. For an [SN Ia](#) a few days after explosion with  $\varrho \sim 10^{-11} \text{ g cm}^{-3}$  and size  $R \sim 10^{14} \text{ cm}$ , the corresponding optical depths are  $\tau \sim \{10^2, 10^1, 1, 10^{-1}\}$  at the same energies ([Milne et al., 2004](#)). This means that only  $\gtrsim \text{MeV}$  photons begin to escape at early times. The resulting [γ-ray](#) line shapes in [SNe Ia](#) are therefore altered by Comptonisation and Doppler-broadening within the ejecta (see also Sec. [2.4.2](#)). After escape, the photons propagate freely through the optically thin Galactic environment.

## 2 Observations and Predictions of $\gamma$ -Ray Lines

*Written by Thomas Siegert, with contributions from multiple authors (see below)*

In this Section, we will summarise different observations and predictions of  $\gamma$ -ray lines in the MeV band, ranging from diffuse emission of radioactivities in the Milky Way (e.g.,  $^{26}\text{Al}$ ,  $^{60}\text{Fe}$ , and  $^{22}\text{Na}$ ; Secs. 2.1, 2.2 & 2.3), to point-like sources such as **SNe Ia** (e.g.,  $^{56}\text{Ni}$  decay chain; Sec. 2.4.1), core-collapse supernova (**ccSNe**) (e.g.,  $^{56}\text{Ni}$  and  $^{44}\text{Ti}$  decay chain; Sec. 2.4.2), **CNe** (e.g.,  $^7\text{Be}$ ; Sec. 2.3), or **BNSMs** (*r*-process elements; Sec. 2.5). Afterwards, **CR** excitation in the **ISM** and supernova remnants (**SNRs**) (e.g.,  $^{12}\text{C}$  and  $^{16}\text{O}$ ; Sec. 2.6) will be outlined, and similar processes are discussed in the context of solar flares (e.g.,  $^2\text{H}$ ; Sec. 2.7) and in planetary atmospheric and solid bodies (e.g.,  $^{56}\text{Fe}$ ,  $^{16}\text{O}$ ; Sec. 2.8). The positron annihilation line at 511 keV, though mentioned indirectly in every subsection as secondary process, will be discussed in more detail in a separate section (Sec. 2.9). The importance of understanding lifetimes of radioactive isotopes and cross-sections of nuclear excitation, particle capture, and spallation will be discussed further in the context of an outlook and where  $\gamma$ -ray line science should proceed to (Sec. 3.1). Finally, due to the rising interest in  $\gamma$ -ray signatures from **DM** decay and annihilation, we devote a small section to **BSM** processes (Sec. 3.2).

### 2.1 Diffuse Emission from Radioactive $^{26}\text{Al}$

*Written by Thomas Siegert*

Besides the 511 keV line (Sec. 2.9), the 1808.65 keV line from the radioactive decay of  $^{26}\text{Al}$  ( $\tau_{26} = 1.04$  Myr,  $p_\gamma = 0.997$ ,  $p_{\beta^+} = 0.82$ , see also Fig. 1, left) is the best-studied  $\gamma$ -ray line in terms of sensitivity (flux), spectral resolution (Doppler shifts and broadening), and angular resolution (imaging). It was only the second  $\gamma$ -ray line detected from outside the Solar System by High Energy Astronomy Observatory 3 (**HEAO 3**) observations (Mahoney et al., 1984). The line was found at  $1808.49 \pm 0.41$  keV, revealing that active nucleosynthesis is ongoing in the Milky Way. The detection of this line firmly established the presence of freshly synthesised material in the **ISM**. Subsequent balloon experiments, such as the Gamma Ray Imaging Spectrometer (**GRIS**), reinforced these findings and refined intensity estimates of the line (Teegarden et al., 1991). Although limited by lower sensitivities and shorter observation times, these early missions paved the way for the more precise studies later conducted by the Imaging Compton Telescope (**COMPTEL**) onboard the Compton Gamma Ray Observatory (**CGRO**) satellite.

One of the most widely accepted sources of  $^{26}\text{Al}$  are massive stars, in particular during their Wolf-Rayet (**WR**) phases when intense stellar winds expel freshly synthesised isotopes (Meynet et al., 1997). Subsequent **ccSN** explosions from these same progenitors also contribute to the overall  $^{26}\text{Al}$  budget through explosive nucleosynthesis (Woosley and Weaver, 1995). In addition, **CNe** on oxygen-neon (ONe) white dwarfs (**WDs**) have long been suggested as potential contributors, although their overall yield remains subject to significant modelling uncertainties (e.g., José and Hernanz, 1998; Vasini et al., 2025, see also Sec. 2.1.3.3). Another minor channel is found in asymptotic giant branch (**AGB**) stars, where dredge-up processes can bring  $^{26}\text{Al}$  to the surface and release it via pulsation-driven mass loss (Mowlavi and Meynet, 2000).

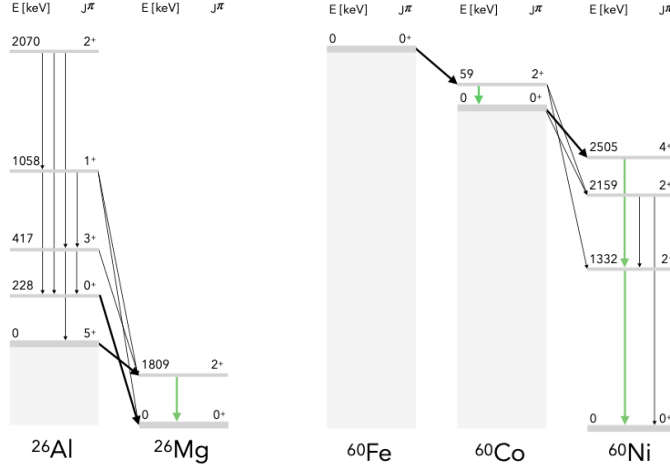


**Fig. 1** Nuclear energy level schemes. Transitions associated with observationally relevant  $\gamma$ -ray emission are marked in green. Left:  $^{26}\text{Al}$  (from [Endt, 1990](#); [Iliadis et al., 2011](#); [Pleintinger, 2020](#)). Right:  $^{60}\text{Fe}$  (from [Rugel et al., 2009](#); [Pleintinger, 2020](#)).

CR spallation has been examined as a non-negligible mechanism in certain environments, in addition to nuclear excitation of stable  $^{26}\text{Mg}$  (see Sec. 2.6). However, its importance relative to stellar production is generally viewed as small ([Clayton, 1984](#)). All these processes, to varying degrees, ensure a continuous enrichment of the ISM, allowing  $^{26}\text{Al}$  to serve as a unique tracer of recent Galactic nucleosynthesis.

[Knöldlseder et al. \(1999\)](#) showed that the Galactic distribution of the 1.8 MeV emission measured with [COMPTEL](#) strongly correlates with sites of intense star formation, in particular the 53 GHz free-free emission map obtained by the Differential Microwave Radiometer ([DMR](#)) onboard the Cosmic Background Explorer ([COBE](#)), highlighting massive stars as key producers. [Diehl et al. \(2006\)](#) then refined these findings using data from the International Gamma-Ray Astrophysics Laboratory ([INTEGRAL](#)), demonstrating that the large-scale 1.8 MeV emission pattern traces Galactic spiral arms rich in young, high-mass stellar populations. These observations underscore the dominance of [WR](#) phases and subsequent [ccSNe](#) in synthesising  $^{26}\text{Al}$ .

### 2.1.1 Measurements of the 1809 keV Line

#### 2.1.1.1 Overview of Historic Measurements – the COMPTEL Era

With the launch of [CGRO](#) in 1991, the [COMPTEL](#) instrument conducted the first detailed all-sky surveys of the  $^{26}\text{Al}$  decay line. Early analyses (e.g., [Diehl et al., 1995](#)) revealed a prominent band of emission along the Galactic plane, confirming massive star regions as principal  $^{26}\text{Al}$  sources. Quantitatively, [COMPTEL](#) found a total Inner Galactic flux of  $(2.8 \pm 0.6) \times 10^{-4} \text{ ph cm}^{-2} \text{ s}^{-1}$  in the longitude range  $-60^\circ \leq \ell \leq +60^\circ$  ([Oberlack et al., 1996](#)). These observations achieved detections at high significance (often  $\gtrsim 10\sigma$ ) and demonstrated that bright emission features correlate with known star-forming complexes, for example in Cygnus ([del Rio et al., 1996](#)), Carina ([Knöldlseder et al., 1996](#)), and Vela ([Diehl et al., 1995](#)). This reinforced the link

to WR stars and ccSNe. Subsequent work refined these flux estimates while improving imaging techniques, ultimately showing that  $^{26}\text{Al}$  is distributed throughout the Galactic disk in association with regions of recent, high-mass star formation (Oberlack et al., 1996; Plüsck et al., 2001, see also Fig. 2, top). Overall, COMPTEL’s systematic surveys and sensitivity enhancements brought a solid foundation to the 1.8 MeV  $\gamma$ -ray line as a key tracer of ongoing nucleosynthesis in the Milky Way.

### 2.1.1.2 Recent Measurements: Imaging Spectroscopy with SPI

Since the launch of the INTEGRAL satellite in 2002, the SPI has provided unprecedented sensitivity and spectral resolution (3.1 keV FWHM at 1.8 MeV) for observations of the  $^{26}\text{Al}$   $\gamma$ -ray line. One of the first major highlights came from Diehl et al. (2006), who measured a total Inner Galactic flux of  $(3.0 \pm 0.3) \times 10^{-4} \text{ ph cm}^{-2} \text{ s}^{-1}$ , confirming COMPTEL’s result, and found a line centroid of  $1808.72 \pm 0.19 \text{ keV}$ , with an astrophysical line width of 0.4–1.9 keV (FWHM). These results suggested that  $^{26}\text{Al}$ -enriched material travels at velocities of a few  $100 \text{ km s}^{-1}$  inside the Milky Way.

Subsequent targeted studies refined these findings in specific star-forming regions: Martin et al. (2009) focused on the Cygnus OB associations, deriving a local flux of  $(3.9 \pm 1.1) \times 10^{-5} \text{ ph cm}^{-2} \text{ s}^{-1}$ , underscoring the role of massive stellar clusters in that region. In Diehl et al. (2010), the nearby Scorpius-Centaurus association was measured in detail, tying its 1.8 MeV emission directly to young OB stars at close proximity (see also Krause et al., 2018, for a refined measurement including multiwavelength studies). A breakthrough came in the work by Kretschmer et al. (2013), who constructed a longitude-velocity diagram by the Doppler shifts in the 1.8 MeV line. This showed both, the kinematic imprint of the large-scale Galactic rotation, and a preferential direction of  $^{26}\text{Al}$  ejecta along the spiral arms towards smaller densities (Krause et al., 2015).

The first image reconstruction of the 1.8 MeV line with SPI was performed by Bouchet et al. (2015). Their map (Fig. 2, middle) showed hotspots in prominent star-forming complexes along the Galactic plane, but could not recover all the suggested sources from COMPTEL measurements. The reason for this is the rather inhomogeneous exposure of SPI compared to COMPTEL: INTEGRAL performed targeted observations of mainly the Galactic bulge and disk, and other prominent regions, such as the Orion-Eridanus superbubble (Siegert and Diehl, 2017), have only been visited irregularly during the 22 yr mission. More recently, Siegert et al. (2023) compared SPI data with advanced, three dimensional, population synthesis models to link the observed  $^{26}\text{Al}$  distribution to the star formation rate (SFR), nucleosynthesis calculations from massive star models, and feedback processes throughout the Galaxy. Their major finding was an exceptionally high star formation rate of  $\gtrsim 5 \text{ M}_\odot \text{ yr}^{-1}$ , which will be discussed below in Secs. 2.1.3 & 2.1.3.3. Finally, Pleintinger et al. (2023) leveraged the capabilities of SPI by including “double event data”, that is, events that trigger two SPI detectors simultaneously, to achieve the best constraints yet on the line flux  $((1.84 \pm 0.03) \times 10^{-3} \text{ ph cm}^{-2} \text{ s}^{-1})$ , centroid,  $(1808.74 \pm 0.04 \text{ keV})$ , and width  $(1.6 \pm 0.3 \text{ keV FWHM})$ . Over two decades of SPI observations have thus firmly established  $^{26}\text{Al}$  as a powerful tracer of massive-star nucleosynthesis and Galactic structure.

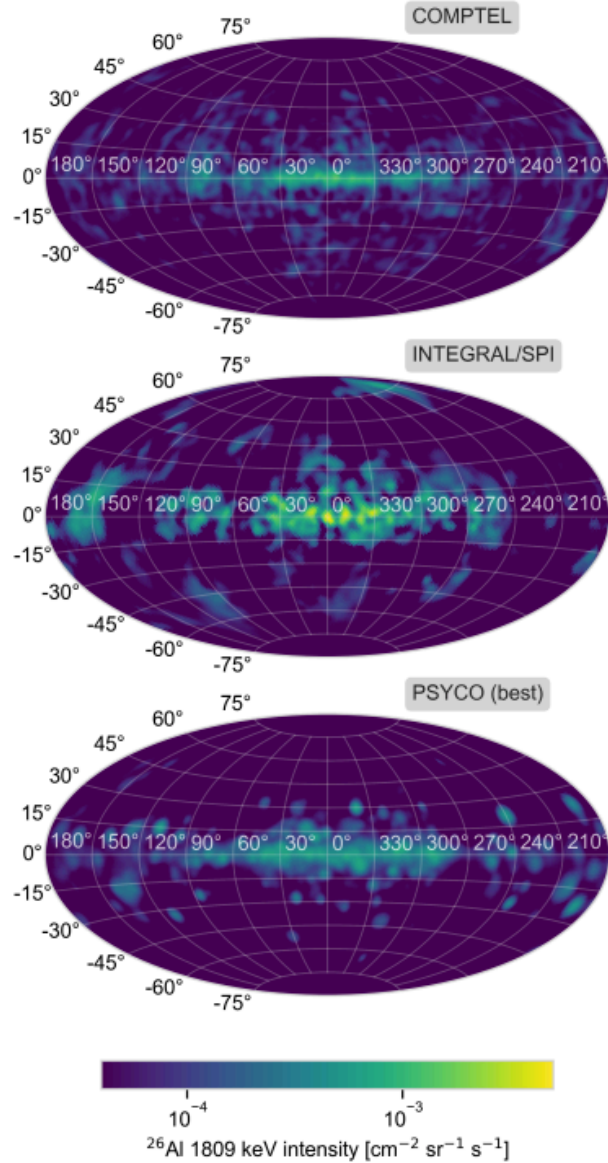


**Fig. 2** Compilation of observational maps (top: COMPTEL (Oberlack et al., 1996); middle: Spectrometer onboard INTEGRAL (SPI) (Bouchet et al., 2015), compared to a best-fitting 3D population synthesis model, PSYCO, (Pleintinger, 2020)), adopted to match the instrument resolution of  $3^\circ$ . The minimum intensity is set to  $5 \times 10^{-5} \text{ ph cm}^{-2} \text{ s}^{-1} \text{ sr}^{-1}$  to mimic potentially observable structures (from Siegert et al., 2023).

However, with more sensitivity comes more questions, which will only be addressed by improved measurements.

### 2.1.2 Production and Destruction of $^{26}\text{Al}$

Detailed overviews of the nuclear structure and reaction rates of  $^{26}\text{Al}$  can be found in [Iliadis et al. \(2011\)](#). The primary production path for  $^{26}\text{Al}$  is the proton-capture reaction  $^{25}\text{Mg}(p, \gamma)^{26}\text{Al}$  in hydrogen-burning environments (NeNaMgAl-cycle). Since the seed isotope  $^{25}\text{Mg}$  largely reflects a star's initial metallicity, the synthesis of  $^{26}\text{Al}$  can be sensitive to the star's chemical composition.

Despite its robust creation,  $^{26}\text{Al}$  also undergoes destruction, mainly via neutron-capture channels  $^{26}\text{Al}(n, p)^{26}\text{Mg}$  and  $^{26}\text{Al}(n, \alpha)^{23}\text{Na}$ . A lesser contribution to the destruction comes from the proton-capture route  $^{26}\text{Al}(p, \gamma)^{27}\text{Si}$ , which is suppressed by the Coulomb barrier ([Parikh et al., 2014](#)). In hot stellar interiors,  $^{26}\text{Al}$  can bypass its otherwise forbidden ground-state decay (from  $5^+$  to  $0^+$ ) by populating excited levels such as 228 keV ( $0^+$ ), 417 keV ( $3^+$ ), or 1058 keV ( $1^+$ ). The equilibrium abundance of the isotope in these environments is strongly temperature-dependent: For example, the ratio  $Y_{26}/Y_{27}$  can vary from 0.03 to 0.8 as central stellar temperatures rise from  $6 \times 10^7$  K to  $10^8$  K in intermediate-mass **AGB** stars. During hot-bottom burning in **AGB** envelopes,  $^{26}\text{Al}$  can be produced in significant quantities, with the final yield depending on thermal pulses and convective mixing processes (see, e.g., [Mowlavi and Meynet, 2000](#), for **AGB** nucleosynthesis details).

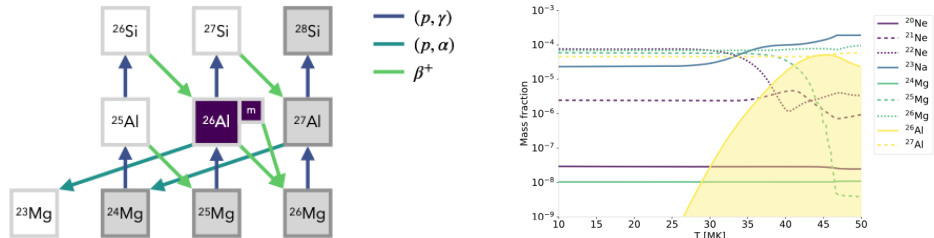


**Fig. 3** Left: Nuclear production and destruction channels of  $^{26}\text{Al}$ . Stable isotopes are marked in dark grey (from [Prantzos and Diehl, 1996](#); [Pleintinger, 2020](#)). Right: Temperature dependence of element abundances in the NeNaMgAl-cycle in an intermediate-mass **AGB** star.  $^{26}\text{Al}$  is shown as yellow shaded region. The x-axis can also be read as radial information with hotter regions being closer to the stellar centre (from [Lugardo et al., 2018](#); [Pleintinger, 2020](#)).

Another path arises with the meta-stable isomeric state  $^{26}\text{Al}^m$ , which has a half-life of 6.34 s and becomes significant once temperatures exceed  $10^8$  K. Above about  $4.5 \times 10^8$  K, ground and isomeric states reach thermal equilibrium, so that rapid convective transport away from high-temperature zones can effectively preserve  $^{26}\text{Al}$ . In advanced burning stages or **SN** shocks, increased neutron fluxes and high temperatures further influence the  $^{26}\text{Al}$  yields. Additional explosive contributions arise during **ccSNe** and **CNe**, where proton captures and neutrino interactions can boost production by 20–30% (e.g., [Sieverding et al., 2017](#), see also Sec. 2.3). Moreover, explosive Ne/C-burning

via the chain  $^{24}\text{Mg}(n, \gamma) ^{25}\text{Mg}(p, \gamma) ^{26}\text{Al}$  can produce typical  $^{26}\text{Al}$  mass fractions of about  $3 \times 10^{-5}$  in stellar ejecta.

Finally, the typical yield of  $^{26}\text{Al}$  per massive star consequently depends on many factors, of which stellar mass is the dominant one. The wind yields range from  $10^{-10}$ – $10^{-7} \text{ M}_\odot$  for the least-massive stars around  $10$ – $15 \text{ M}_\odot$ , up to  $10^{-4}$ – $10^{-3} \text{ M}_\odot$  at the high mass end around  $60$ – $120 \text{ M}_\odot$ . The **SN** yields are typically on the order of  $10^{-5}$ – $10^{-4} \text{ M}_\odot$ . Weighted with an initial mass function (**IMF**), it becomes evident that most  $^{26}\text{Al}$  should be produced by massive stars in the range  $10$ – $30 \text{ M}_\odot$  (Pleintinger, 2020). The latest model calculations estimate the  $^{26}\text{Al}$  yield in **AGB** stars to be around  $10^{-8}$ – $10^{-6} \text{ M}_\odot$  per star (Karakas and Lattanzio, 2014). The **CN** yields range from  $10^{-9}$ – $10^{-7} \text{ M}_\odot$  per **ONe** nova event (e.g., José and Hernanz, 1998; Starrfield et al., 2020).

### 2.1.3 Understanding and Interpreting $^{26}\text{Al}$ Measurements

From the above numbers, it can be easily estimated, how much  $^{26}\text{Al}$  would be present in the Milky Way, given some information on the **SN** rate, for example. Turning this around, measuring the  $^{26}\text{Al}$  flux and distribution in the Galaxy can provide an estimate of the **SN** rate and the **SFR**.

Assuming one dominant source for the moment (see Sec. 2.1.3.3), massive star and their **SNe**, we can convert the measured flux value of  $1.8 \times 10^{-3} \text{ ph cm}^{-2} \text{ s}^{-1}$  into a quasi-persistent mass of  $^{26}\text{Al}$  given Eqs. (9,10,15). For this, one needs to assume a 3D distribution of the emission. It was found that a doubly-exponential disk with a scale radius of  $5.8 \pm 0.6 \text{ kpc}$  and a scale height of  $0.8 \pm 0.2 \text{ kpc}$  fits the **SPI**  $\gamma$ -ray data well (Pleintinger et al., 2019). From these values, a conversion from flux to luminosity and therefore mass is straightforward as  $1 \text{ M}_\odot$  of  $^{26}\text{Al}$  corresponds to a luminosity of  $1.4 \times 10^{42} \text{ s}^{-1}$ , and a flux of  $3 \times 10^{-4} \text{ ph cm}^{-2} \text{ s}^{-1}$ , assuming a distance to the Galactic centre of  $8.2 \text{ kpc}$ . Given the total flux measurement, we would have a total mass of around  $6 \text{ M}_\odot$  of  $^{26}\text{Al}$  in the Milky Way. Now, given the average yield per massive star of  $(1\text{--}2) \times 10^{-4} \text{ M}_\odot$ , we see that on the order of  $(3\text{--}6) \times 10^4$  massive stars contribute to the Galactic  $1.8 \text{ MeV}$  line. The **SN** rate is then the number of contributing stars over the lifetime of  $^{26}\text{Al}$ , that is, 3–6 per century. Clearly, these values are only rough estimates but give an excellent overview of the concept. A more complex consideration of the flux values as well as the spatial distribution of the  $1.8 \text{ MeV}$  line gives a total  $^{26}\text{Al}$  mass of  $1.2$ – $2.4 \text{ M}_\odot$  in the Galaxy, which leads to a **SN** rate of  $1.8$ – $2.8$  per century (Pleintinger, 2020; Siegert, 2023).

The **SN** rate is directly linked to the **SFR** in the Galaxy, roughly by

$$\text{SFR} = R_{\text{SN}} \langle M^* \rangle f_{\text{SN}}^{-1}, \quad (32)$$

where  $R_{\text{SN}}$  is the **SN** rate,  $\langle M^* \rangle$  is the average stellar mass in a star formation event, and  $f_{\text{SN}}$  is the fraction of all stars that actually undergo a **SN** explosion (Diehl et al., 2006). The average stellar mass is given by the assumed **IMF** and may range around  $0.3$ – $0.7 \text{ M}_\odot$ . The fraction of stars that undergo a **ccSN** explosion depends on both, a minimum stellar mass, typically chosen as  $8 \text{ M}_\odot$ , and the assumed “explodability”, that is, up to which mass stars explode or directly collapse into a black hole (**BH**).

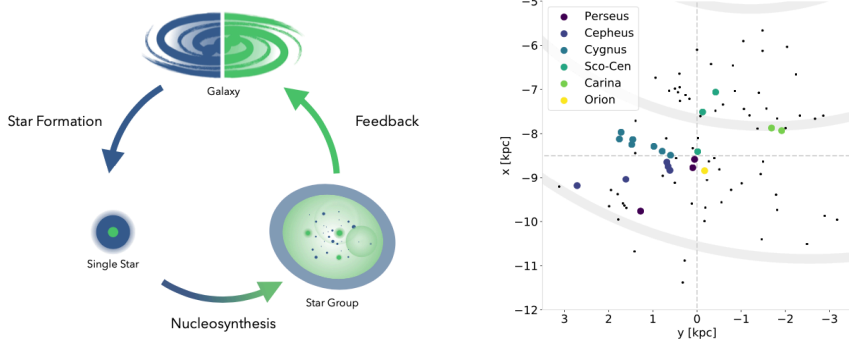


**Fig. 4** Left: Schematic representation of the cosmic cycle of matter with metallicity symbolically increasing from blue to green. The cycle progresses in three fundamental steps over three major scales (from Pleintinger, 2020). Right: Spatial distribution of nearby OB associations within 3.5 kpc in the Galactic plane. Dots denote the positions of OB associations from the Gaia catalogue (Mel'nik and Dambis, 2017). Spiral arm tangents are shown in thick grey lines (from Pleintinger, 2020).

The question of the explodability is an important one as it scales the total mass, flux, SFR and SN rate. Several different models consider explosions up to  $25 M_{\odot}$  (e.g., Limongi and Chieffi, 2018), or up to  $100 M_{\odot}$  (e.g., Janka, 2012), or even ‘islands’ of stars that can explode and those that cannot (e.g., Sukhbold et al., 2016). The fraction of stars that might explode is then on the order of  $(1\text{--}4) \times 10^{-3}$ . Taking these values into account, a SFR between 1 and  $17 M_{\odot} \text{ yr}^{-1}$  is found, with an average around  $3.5 M_{\odot} \text{ yr}^{-1}$ . This value, compared to literature values, appears reasonable, although on the high side of estimates (e.g., Licquia and Newman, 2015, see also Secs. 2.1.3.2 & 2.1.3.3).

All these estimates, however, strongly depend on the massive star evolution models, their nucleosynthesis calculations, that is, wind and SN yields, the binarity of massive stars, and – probably most important – ignore the fact that there are other contributors to  $^{26}\text{Al}$  in the Milky Way. In addition, an enhanced local production inside the Local Bubble may play a significant role in estimating the actual total flux. For this reason, these estimates are often based on the central radian of the Milky Way, and not necessarily on the entire sky. In the following, we will discuss several effects that might impact these measurements, and how they can be addressed in the future.

#### 2.1.3.1 Cosmic Cycle of Matter – Nucleosynthesis Feedback

“[...] feedback is the mechanism by which a process loop alters itself. While the main system stays the same procedurally with every iteration, feedback describes an inherent sub-loop of self-driven change in process parameters. In other words, feedback is the mechanism underlying any kind of evolution. [...] Such a kind of evolution must have taken place on cosmic scale” (Pleintinger, 2020, p. 5), as well as happens also locally, and then disturbs the view and interpretation of Galactic measurements. The cosmic cycle of matter (Fig. 4, left) happens on all scales so that a local production, for example in one or several recent ccSN events inside the Local Bubble (e.g., Schulreich et al., 2023), would lead to an enhanced flux compared to the Galactic average. This would explain the large scale height distribution that has been found by Pleintinger

et al. (2019), sometimes reaching 2 kpc or above, whereas the average was found to be below 300 pc.

In technical terms, coded aperture mask telescopes, such as **SPI**, have problems in identifying emission regions with small gradients or isotropic emission (e.g., Siegert et al., 2022). However, the contrast between different longitudes in the Galaxy, as well as the large scale height from individual doubly-exponential disk fits, could point to a local contribution. The Local Bubble would therefore lead to an all-sky 1.8 MeV flux on the order of a few  $10^{-6}$  ph cm $^{-2}$  s $^{-1}$  (Siegert et al., 2024) – too little to explain the large **SFR**, but large enough to increase the scale height to extreme values. The nearby star-forming regions (Fig. 4, right) may also show an enhanced nucleosynthesis contribution and lead to a skewed perspective on the entire Galaxy (Pleintinger, 2020). In Pleintinger (2020), it was found that the nearby ( $\lesssim 3.5$  kpc) groups may reduce the Galactic-wide 1.8 MeV flux by 20–30%. This reduces the **SFR** by the same percentage and alleviates some of the tension.

### 2.1.3.2 From Single Stars to the Galaxy

In order to model the entire Galaxy, Siegert et al. (2023), based on the work by Pleintinger (2020), used a bottom-up, 3D population synthesis code (**PSYCO**) to place constraints on the **SFR**, the **SN** rate, and the structure of the Galaxy in  $^{26}\text{Al}$  as well as  $^{60}\text{Fe}$ . The variety of massive star models should be gauged, starting from a single massive star. However, the 1.8 MeV  $\gamma$ -ray line fluxes from all nearby massive stars are below the sensitivity threshold for **COMPTEL** (Oberlack et al., 2000) and **SPI** (Pleintinger, 2020). In the most promising case of the binary star system  $\gamma^2$  Velorum, the most recent spectrum (Fig. 5, top) gives an upper limit of  $1.7 \times 10^{-5}$  ph cm $^{-2}$  s $^{-1}$ , which is only weakly constraining the initial stellar mass of the star to  $\lesssim 50 M_\odot$ , depending on the nucleosynthesis model, and the distance to the star (see Oberlack et al., 2000, see also Fig. 6). Flux estimates from individual stars would fall into the range of a few  $10^{-6}$  ph cm $^{-2}$  s $^{-1}$  or below, so that with next generation telescopes, it would be possible to calibrate massive star evolution models.

While for now, a single star (binary) is too weak to be detectable, several massive star groups (see above) have been identified as striking  $^{26}\text{Al}$  sources. In the case of Perseus OB2, for example (Pleintinger, 2020), with an age of 6 Myr and an initial  $2 \times 10^4$  stars at a distance of 200–400 pc, a sizeable amount of  $^{26}\text{Al}$  could be expected. With more than 15 Ms of observation time with **SPI**, Perseus OB2 was found at a flux level of  $(6.3 \pm 2.8) \times 10^{-5}$  ph cm $^{-2}$  s $^{-1}$ , in agreement with 1.8 MeV fluxes from the same regions in the  $^{26}\text{Al}$  all-sky maps (Fig. 2). Applying a superbubble expansion model, homogeneously filled with  $^{26}\text{Al}$ , this flux converts to an  $^{26}\text{Al}$  mass of  $(5.1 \pm 2.2) \times 10^{-4} M_\odot$  for the entire OB association. This number can be compared to stellar evolution models in the context of **PSYCO** by calculating the expectation of a population of  $2 \times 10^4$  stars as a function of time. In Fig. 6, right, we show the  $^{26}\text{Al}$  and  $^{60}\text{Fe}$  profiles, as well as their ratio, of a coeval population attempting to mimic Perseus OB2. It is clear that the stochasticity of the **PSYCO** calculations determine the accuracy of the derived parameters. In principle it would be possible to determine the age of the population, however only if more details about the remaining stars are

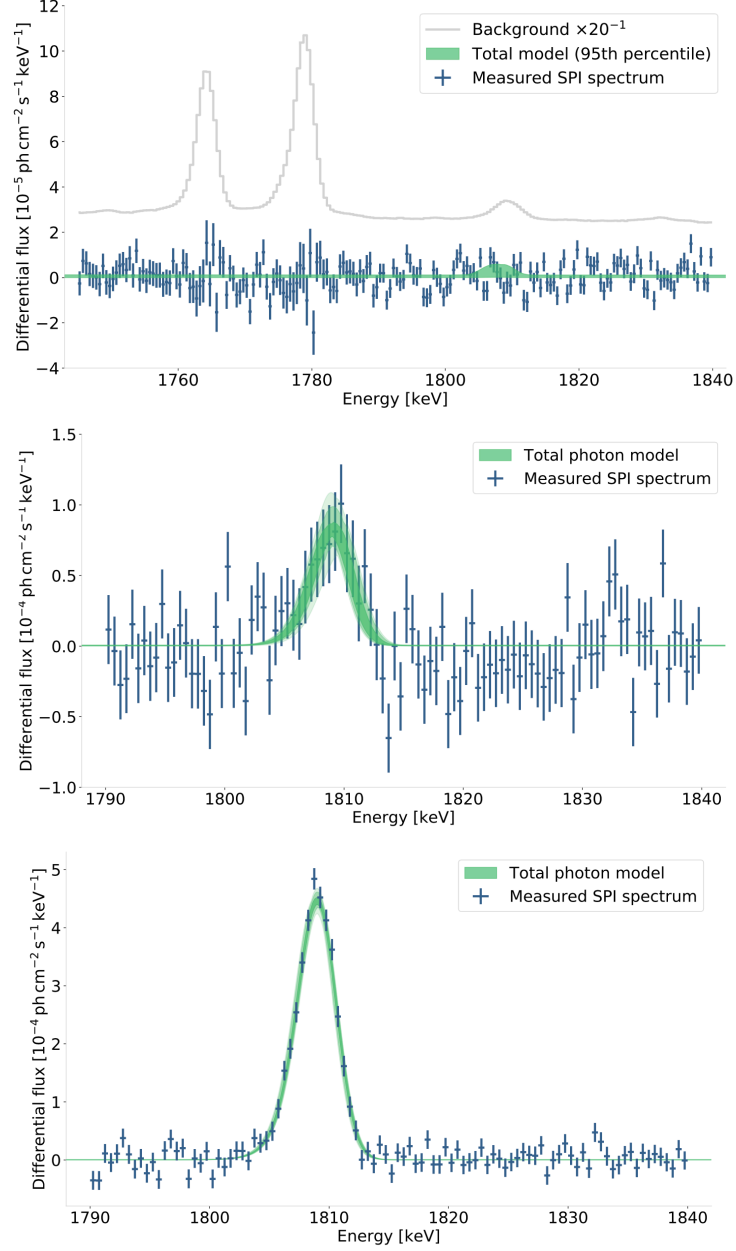


**Fig. 5** SPI spectra (blue data points) around the 1809 keV line for three different cases. Top:  $\gamma^2$  Velorum from 1745–1840 keV. The line is not detected but a  $2\sigma$  upper limit of  $1.7 \times 10^{-5} \text{ ph cm}^{-2} \text{ s}^{-1}$  is indicated by the green band. The instrumental background in the same energy range is shown as grey histogram, scaled by a factor of 20 for better comparison. Clearly, the higher the background flux, the larger the error bars per 0.5 keV bin. Middle: Region around the Perseus OB associations. The line flux is  $(3.6 \pm 0.4) \times 10^{-4} \text{ ph cm}^{-2} \text{ s}^{-1}$ , broadened by  $(1.13 \pm 0.55) \text{ keV}$  and shifted by  $(0.34 \pm 0.22) \text{ keV}$ . Bottom: Galactic-wide spectrum. The line flux is  $(1.87 \pm 0.03) \times 10^{-3} \text{ ph cm}^{-2} \text{ s}^{-1}$  with a Doppler shift of  $(0.37 \pm 0.04) \text{ keV}$  and an astrophysical line width of  $(0.62 \pm 0.32) \text{ keV}$  which corresponds to a thermal broadening around  $80 \text{ km s}^{-1}$  (from [Pleintinger, 2020](#)).

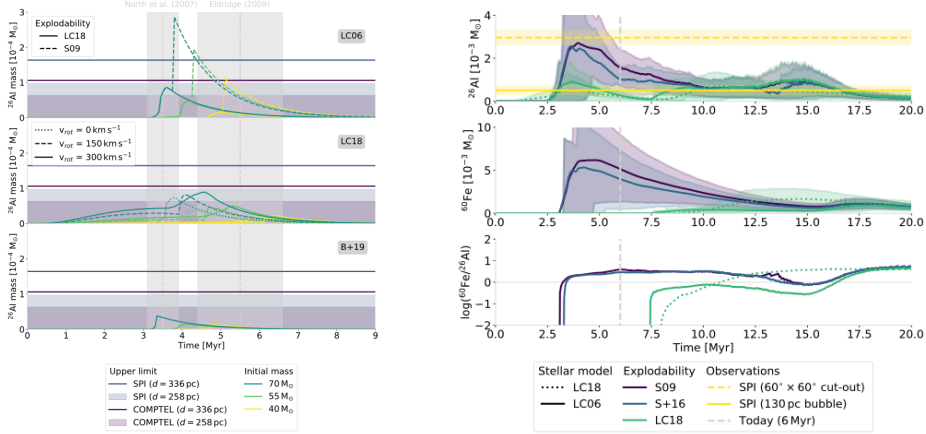


**Fig. 6** Left: Comparison of single star model predictions with observational limits of  $\gamma^2$  Velorum measured with SPI and COMPTEL. Three different stellar initial masses are show. The panels correspond to single star models (LC06; Limongi and Chieffi, 2006) (top), (LC18; Limongi and Chieffi, 2018) LC18 (middle), and binary models (B+19; Brinkman et al., 2019) (bottom). The predicted values lie mostly just below the upper limits (from Pleintinger, 2020). Right: Population synthesis profiles of  $^{26}\text{Al}$  and  $^{60}\text{Fe}$  from a stellar group representing the Perseus OB2 association. The calculations are based on the evolution stellar models LC06 (solid lines) and LC18 (dotted lines). Different explodability models are applied to the LC06 tracks. Shaded 68% uncertainty regions are obtained from 1000 Monte Carlo runs each. The two measured values are based on the SPI 1.8 MeV map (dashed line, see also Fig. 5, middle) or a superbubble model with size  $R = 130$  pc at the position of Perseus OB2 (solid line). The group's age is marked at 6 Myr (from Pleintinger, 2020).

known. If we compare the values at the age of Perseus OB2 at 6 Myr, we find a generally good agreement with the models from Limongi and Chieffi (2018), explaining the measurements best. However, also other models match the measurements, although on the low-side of their expectations, probably because of the enhanced explodability (e.g., Smartt, 2009; Sukhbold et al., 2016).

Building the entire Galaxy is also possible with PSYCO, based on the embedded cluster mass function and an assumption on the birthplaces of OB associations. Similar to a Galactic chemical evolution model, an “empty” galaxy is filled with superbubbles, which themselves are filled with  $^{26}\text{Al}$  and  $^{60}\text{Fe}$ , that evolve according to Weaver et al. (1977). The initial parameters here are the SFR, a specific stellar evolution model that determines the yields per star group, an explodability model, a geometric representation of the Galaxy (spiral arms, scale height), and the metallicity gradient of the Galaxy. At some point during this evolution, the decay and the production of radioactive nuclei are balanced and a snapshot of the simulated galaxy can be taken (see Fig. 2, bottom). Since this is aimed at mimicking the Milky Way, some foreground sources can be introduced. Repeating this analysis for several thousand Monte Carlo runs leads to estimates of the initial parameters, and parameters linked to them, such as the SN rate. Siegert et al. (2023) find a SN rate of 1.8–2.8 per century, similar to other studies, however only at the expense of a SFR of  $4\text{--}8 M_{\odot} \text{ yr}^{-1}$ , several factors higher than typically found (e.g., Licquia and Newman, 2015, with  $1\text{--}2 M_{\odot} \text{ yr}^{-1}$ ). The uncertainty range here already includes all possible assumptions as

detailed above that actually fit the **SPI** data. One advantage of this method compared to hydrodynamics simulations (e.g., Fujimoto et al., 2018; Rodgers-Lee et al., 2019) is that many realisations of the same assumptions can quickly be calculated, so that a large parameter space can be explored. Another advantage is that **PSYCO** predictions can be directly fitted to the raw  $\gamma$ -ray data and checked for consistency: if one realisation of a parameter set does not fit well, several others might, so that a distribution around the parameters can be found, leading to uncertainty estimates.

#### 2.1.3.3 *Is it Only Massive Stars?*

The high **SFR** measured in the Milky Way from  $^{26}\text{Al}$   $\gamma$ -ray line observations, independent of the method, leads to the question how to significantly scale it down, not by a few per cent, but by several factors. In most studies, the assumption is that the 1.8 MeV line is purely from massive star winds and **ccSNe**. With this assumption, it is clear that, depending on the massive star evolution models and nucleosynthesis yields, a high **SFR** is inevitable because these evolution models also need to match many other observations. Therefore,  $^{26}\text{Al}$  could either be special and all models are wrong, or, more reasonable, the assumptions on the Galactic-wide modelling are lacking input. Certainly, the **PSYCO** approach handles the unknown unknowns, that is, how many stars and stellar groups are formed where and at what frequency, to the extent that it matches other observations, but always with the free parameter of **SFR**. The **LoS** integration in **PSYCO** assumes homogeneously filled spheres, which, to a very good approximation, fits several nearby massive star groups. However, there is the effect of bubble merging (e.g., Krause et al., 2014) which alters the average structure of the bubbles, there is the fact that  $^{26}\text{Al}$  is long-lived enough to also mix with the bubble shells (Schulreich et al., 2023), and there is the density gradient in the Milky Way which can make bubbles appear stretched, such as Orion-Eridanus (e.g., Burrows et al., 1993). While on the Galactic scale, these effect may have little to no impact on the total flux because they average out over the contributions of several tens of thousand groups, the nearby associations may lead to an enhanced flux. While this may make on the order of 20–30% as described above, one would need to decrease the **SFR** even further by about 50–75%.

The explodability of massive stars is an open question: While only  $25\text{ M}_\odot$  stars or below have been observed to actually explode (e.g., Smartt, 2015), a higher contribution of so-called supermassive stars with masses of up to  $300\text{ M}_\odot$  (Martinet et al., 2022) might also alleviate some of this tension. A measurement of this effect might only be possible in extragalactic objects, such as the Large Magellanic Cloud (**LMC**), to prove the enhanced  $^{26}\text{Al}$  production without creating more stars.

The binary evolution of massive stars may also play a bigger role than expected: About 50–70% of massive stars are found in binary systems (e.g., Sana et al., 2012). Brinkman et al. (2019, 2021, 2023) estimated the yield of  $^{26}\text{Al}$  from binary systems using the 1D Modules for Experiments in Stellar Astrophysics (**MESA**) code (Paxton et al., 2011). The nucleosynthesis is treated ‘on the fly’ so that the stars actually exchange information (e.g., Roche-Lobe overflow, orbital evolution, tidal interactions) but still in a 1D setting. It has been shown that the yields of binary stars from this approach can be larger, but a full 3D calculation is missing. Next-generation telescopes

could measure the 1.8 MeV line from individual and binary stars to better gauge the models.

The most interesting factor, however, may be another, long-neglected, source type: **CNe**. Based on a 2D Galactic chemical evolution model, [Vasini et al. \(2025\)](#) found that the fraction of  $^{26}\text{Al}$  from massive stars may be only 25%, whereas **CNe** could make up to 75%. Interestingly, these would be the exact numbers required to completely relieve the tension between the 1.8 MeV  $\gamma$ -ray line measurements and other studies. The **CN** effect will also come back in the measurements of  $^{60}\text{Fe}$ , in that the flux ratio of  $^{60}\text{Fe}/^{26}\text{Al}$  can hardly be explained by the consensus model of massive star evolution. Clearly, the  $^{26}\text{Al}$  yields from **CNe** can hardly be calibrated because the expected ejecta masses are around  $10^{-9}\text{--}10^{-7}\text{ M}_\odot$  (e.g., [José and Hernanz, 1998](#); [Starrfield et al., 2020](#)), so that at a distance of 1 kpc, the 1.8 MeV flux would be only  $10^{-9}\text{ ph cm}^{-2}\text{ s}^{-1}$  at best – impossible for any  $\gamma$ -ray telescope to measure in the near future. Nevertheless, radioactive  $^{26}\text{AlF}$  molecules have been detected in the old remnant CK Vul (previously believed to be a **CN**, but shown to be probably a stellar merger remnant), proving that, indeed, other objects produce  $^{26}\text{Al}$ , but at a difficult to determine yield ([Kamiński et al., 2018](#)). A reasonable measurement that could be done already today, and which has been attempted with **COMPTEL** ([Knöldlseder, 1999](#)) as well as **SPI** ([Martin et al., 2009](#)), is to disentangle the distribution of  $^{26}\text{Al}$  as a function of Galactocentric radius: The **CN** distribution would peak around the Galactic centre, whereas there, the massive star contribution is nearly zero, but rises towards a maximum around a few kpc (see also [Vasini et al., 2025](#)). With good angular resolution and deep exposures, a mass profile of  $^{26}\text{Al}$  could be constructed and then again compared to the expected spatial distributions from Galactic chemical evolution models.

## 2.2 Diffuse Emission from Radioactive $^{60}\text{Fe}$

*Written by Wei Wang*

Similar to the case of  $^{26}\text{Al}$ ,  $\gamma$ -ray line emission from the radioactive decay of  $^{60}\text{Fe}$  reflects the ongoing nucleosynthesis in our Galaxy. As opposed to  $^{26}\text{Al}$ ,  $^{60}\text{Fe}$  is believed to be only produced in [ccSNe](#) and not in stellar winds.

### 2.2.1 Production of $^{60}\text{Fe}$

The radioactive isotope  $^{60}\text{Fe}$  can be produced in suitable astrophysical environments through successive neutron captures on pre-existing Fe isotopes such as stable  $^{54,56,57,58}\text{Fe}$  in a neutron-rich environment. Candidate regions for  $^{60}\text{Fe}$  production are the He and C burning shells inside massive stars, where neutrons are likely to be released from the  $^{22}\text{Ne}(\alpha, n)$  reaction.  $^{60}\text{Fe}$  production may occur any time during late evolution of massive stars towards [ccSNe](#) (e.g., Woosley and Weaver, 1995; Limongi and Chieffi, 2003, 2006, 2018; Pignatari et al., 2016; Sukhbold et al., 2016; Jones et al., 2019). The EC variant of such SNe may be a most-significant producer of  $^{60}\text{Fe}$  in the Galaxy (Wanajo et al., 2013, 2018; Jones et al., 2016, 2019).

There are, however, other possible astrophysical sources of  $^{60}\text{Fe}$ : From similar considerations,  $^{60}\text{Fe}$  could also be made and released in super-AGB stars (Lugardo et al., 2012). Furthermore, high-density [SNe Ia](#) explosions, which would include a deflagration phase (Woosley, 1997), could produce even larger amounts per event, and which could form a point-like  $\gamma$ -ray emission source. Much of such newly-produced  $^{60}\text{Fe}$  should be ejected with the [SN](#) explosion, in particular if produced outside the inner cores of these objects (see Jones et al., 2019, for a discussion of [ccSNe](#) ejecta).

### 2.2.2 $\gamma$ -Ray Detections and Predictions of $^{60}\text{Fe}$ in the Galaxy

$^{60}\text{Fe}$  has a long lifetime with a radioactive half-life  $T_{1/2} \simeq 2.6$  Myr (Rugel et al., 2009; Wallner et al., 2015; Ostdiek, 2016), it can survive after ejection into the [ISM](#). Several detections of  $^{60}\text{Fe}$ -enriched material in various terrestrial as well as lunar samples (Knie et al., 2004; Wallner et al., 2016, 2021; Fimiani et al., 2016) confirm the evidence for one or more very nearby sources of  $^{60}\text{Fe}$  within several Myr. The detection of  $^{60}\text{Fe}$  in [CRs](#) also implies that the time required for acceleration and transport to Earth is around several Myr (Binns et al., 2016; Schulreich et al., 2023), so that the  $^{60}\text{Fe}$  source distance does not greatly exceed the distance [CRs](#) can diffuse over this time ( $\lesssim 1$  kpc).

The  $\gamma$ -ray line emission from  $^{60}\text{Fe}$  can directly diagnose the production sites in the Galaxy.  $^{60}\text{Fe}$   $\beta$ -decays to  $^{60}\text{Co}$ , which decays within 5.3 yr to stable  $^{60}\text{Ni}$  in an excited state that cascades into its ground state by  $\gamma$ -ray emission at 1173.23 and 1332.49 keV, respectively. The  $^{60}\text{Co}$  ground state transition is accompanied by a  $\gamma$ -ray line at 59 keV, however only in 2% of all decays. Thus, observations typically focus on the two high energy  $\gamma$ -ray lines.

Before [INTEGRAL](#), different  $\gamma$ -ray missions have searched for the  $\gamma$ -ray lines from the diffuse  $^{60}\text{Fe}$  emission in the Galaxy, however only reported marginal detections or upper limit constraint with a significance level below  $3\sigma$  (Leising and Share, 1994; Harris et al., 1997; Diehl et al., 1997; Smith, 2004). This suggested that the  $^{60}\text{Fe}$  emission signal in the Galaxy is very weak. With nearly 3 yr of [SPI](#) observations,

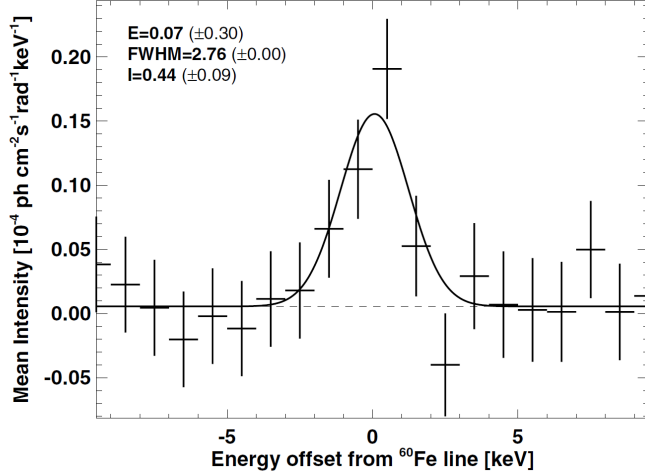


**Fig. 7** The combined spectrum of the two  $^{60}\text{Fe}$   $\gamma$ -ray lines in the inner Galaxy observed by INTEGRAL/SPI (from Wang et al., 2007). In the laboratory, the  $^{60}\text{Fe}$  line energies are 1173.23 and 1332.49 keV, respectively. Shown here are the two lines superimposed with the centroids at 1173 and 1333 keV set to a zero shift. The detection significance of the lines combined was  $\sim 4.9\sigma$ . The solid line represents a fitted Gaussian profile of fixed instrumental width (2.76 keV FWHM), and a flat continuum. The average line flux is estimated as  $(4.4 \pm 0.9) \times 10^{-5} \text{ ph cm}^{-2} \text{ s}^{-1} \text{ rad}^{-1}$ .

both  $\gamma$ -ray lines at 1773 and 1332 keV have been detected for the first time (Wang et al., 2007). Combining  $^{60}\text{Fe}$  spectra from independent model fits, an  $^{60}\text{Fe}$  signal from the Galaxy with a significance of  $4.9\sigma$  is reported with the average flux of  $(4.4 \pm 0.9) \times 10^{-5} \text{ ph cm}^{-2} \text{ s}^{-1} \text{ rad}^{-1}$  from the inner Galactic region (see Fig. 7). Wang et al. (2020) further determined an  $^{60}\text{Fe}$  line flux of  $\sim (3.1 \pm 0.5) \times 10^{-4} \text{ ph cm}^{-2} \text{ s}^{-1}$  for the whole sky, and a line flux of  $\sim (4.5 \pm 0.8) \times 10^{-5} \text{ ph cm}^{-2} \text{ s}^{-1}$  for the inner Galactic region based on 15 yr of SPI data. The uncertainties after three and after 15 years of observations with SPI are similar due to the radioactive build-up of the instrumental  $^{60}\text{Ni}$  lines at the exact same photon energies (Diehl et al., 2018). This means that only the first few years of a space mission are potentially useable to firmly detect and study the  $^{60}\text{Fe}$   $\gamma$ -ray lines. However, other orbit considerations and material choices might alleviate this problem. Since at least two, but probably more than ten, ccSNe happened in the vicinity of the moving Solar System, there is also the expectation of  $\gamma$ -ray line emission from the Local Bubble in which the Sun is currently located. Siegert et al. (2024) predict a quasi-isotropic flux of  $^{60}\text{Fe}$  and  $^{26}\text{Al}$   $\gamma$ -ray lines, as well as the associated 511 keV line, based on a geometric model (Pelgrims et al., 2020; Zucker et al., 2022) and hydrodynamics simulations (Schulreich et al., 2023). The total  $^{60}\text{Fe}$   $\gamma$ -ray line flux inside the Local Bubble may range from  $(0.5\text{--}4.2) \times 10^{-5} \text{ ph cm}^{-2} \text{ s}^{-1}$  with an isotropic fraction of 20–50%. Likewise, the  $^{26}\text{Al}$  line form the Local Bubble may be  $(0.3\text{--}2.0) \times 10^{-5} \text{ ph cm}^{-2} \text{ s}^{-1}$  across the entire sky, in which the 511 keV has a typical contribution of 41%. Coded mask telescopes, such as SPI, cannot measure these isotropic fluxes, but future Compton telescopes could.

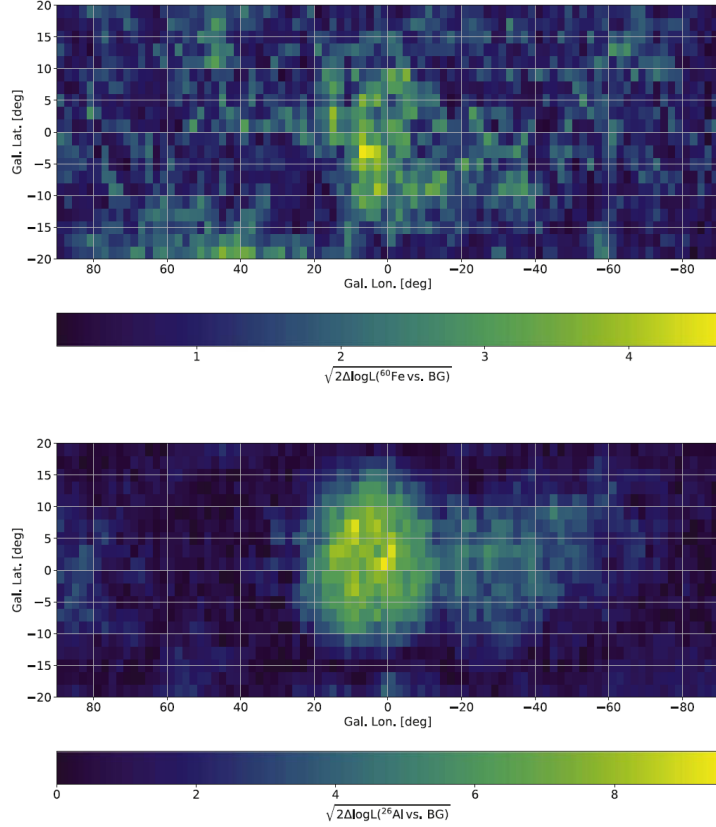


**Fig. 8** The distributions of two  $\gamma$ -ray line emissions for both  $^{60}\text{Fe}$  (top) and  $^{26}\text{Al}$  (bottom) obtained by SPI scanning the inner part of the Galactic plane ( $-90^\circ < \ell < 90^\circ$ ;  $-20^\circ < b < 20^\circ$  (from Wang et al., 2020). Each pixel represents an individual point source test to identify excess emission above instrumental background, separated by  $2^\circ$  (test statistic (TS) map).  $^{60}\text{Fe}$  emission is very weak, and its morphology is still unknown, but it is not a point-like source (such as only the Galactic centre), and probably of diffuse nature. It could be similar to  $^{26}\text{Al}$ , however the uncertainties of also diffuse emission model fits are too large.

The robust detections of  $^{60}\text{Fe}$  by SPI can also be used to constrain the morphology of the weak  $^{60}\text{Fe}$  emission in the Galaxy. By using a so-called TS map, testing for excess emission above the instrumental background at different positions in the sky between  $-90^\circ < \ell < 90^\circ$  and  $20^\circ < b < 20^\circ$ , the sky distribution of  $^{60}\text{Fe}$  can be investigated. With a  $\sim 5\sigma$  detection of  $^{60}\text{Fe}$  in the whole sky, it is possible to test whether  $^{60}\text{Fe}$  is point-like or truly diffuse, and whether  $^{60}\text{Fe}$  and  $^{26}\text{Al}$  share a similar morphology (Fig. 8). It was suggested that the  $^{60}\text{Fe}$  and  $^{26}\text{Al}$  emission distributions cannot be attributed to one or several point sources in the Galactic plane region.

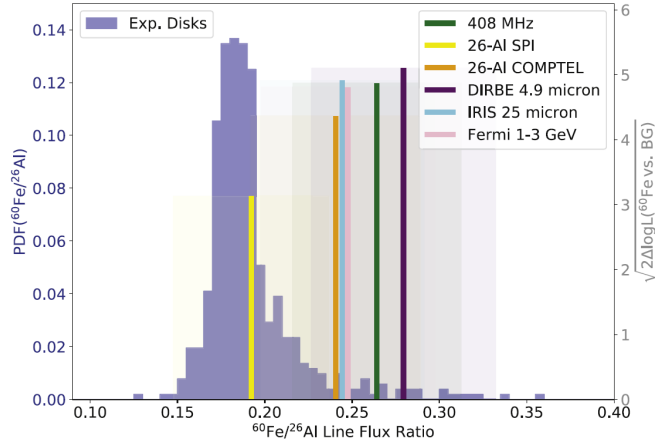


**Fig. 9** The flux ratio of  $^{60}\text{Fe}/^{26}\text{Al}$  determined by 15 yr of SPI observations (from Wang et al., 2020) based on model fitting of all-sky distributions, including a series of doubly-exponential disk models (blue) and a set of Galactic emission maps as tracers (vertical lines). The uncertainties are noted as shaded bands. Including the uncertainties of the fluxes from each spectral fit, the estimated  $^{60}\text{Fe}/^{26}\text{Al}$  flux ratio from the set of exponential disks is  $0.18 \pm 0.04$ .

### 2.2.3 Ratio of $^{60}\text{Fe}/^{26}\text{Al}$

The long-lived  $^{60}\text{Fe}$  and  $^{26}\text{Al}$  isotopes are expected to accumulate in the ISM from many sources if those ejection events occur more often during their radioactive lifetime, leading to diffuse emission of radioactivity  $\gamma$ -rays. Since  $^{60}\text{Fe}$  and  $^{26}\text{Al}$  are expected to have a similar origin, the yield ratio  $^{60}\text{Fe}/^{26}\text{Al}$  in the Galaxy is expected to not be dependent on the distance uncertainties. Therefore, an accurate measurements of the  $^{60}\text{Fe}/^{26}\text{Al}$   $\gamma$ -ray line flux ratio provides an excellent test of the different models for massive star nucleosynthesis. The steady-state mass of these radioactive isotopes maintained in the Galaxy through such production counterbalanced by radioactive decay, and thus converts into a ratio for the  $\gamma$ -ray line flux in each of the two lines through

$$\frac{F(^{60}\text{Fe})}{F(^{26}\text{Al})} = 0.43 \cdot \frac{\dot{M}(^{60}\text{Fe})}{\dot{M}(^{26}\text{Al})}. \quad (33)$$

At present, various models have predicted the values of the  $^{60}\text{Fe}/^{26}\text{Al}$  ratio. Timmes et al. (1995) carry the massive-star yields into an estimate of chemical evolution for  $^{60}\text{Fe}$  and  $^{26}\text{Al}$  in the Galaxy, predicting a  $\gamma$ -ray flux ratio of 0.16. Further revisions of the model give the different prediction of the  $^{60}\text{Fe}/^{26}\text{Al}$  ratio from  $\sim 0.1$ –1.0 (Limongi and Chieffi, 2003, 2006, 2018; Rauscher et al., 2002; Prantzos, 2004; Woosley and Heger, 2007). The large uncertainties of the theoretical values come from both astrophysics and nuclear physics.

The yields of these two isotopes depend sensitively on both the stellar evolution details, such as shell burnings and convection, the final stages of the massive star

evolution, and also the nuclear reaction rates. [Tur et al. \(2010\)](#) found that the production of  $^{60}\text{Fe}$  and  $^{26}\text{Al}$  is sensitive to the  $3\alpha$  reaction rates during He burning, that is, the variation of the reaction rate by a factor of two would make a factor of nearly ten change in the  $^{60}\text{Fe}/^{26}\text{Al}$  ratio.  $^{60}\text{Fe}$  may be destroyed within its source by further neutron captures:  $^{60}\text{Fe}(n, \gamma)$ . Since its closest parent,  $^{59}\text{Fe}$  is unstable, the  $^{59}\text{Fe}(n, \gamma)$  production process competes with the  $^{59}\text{Fe}$   $\beta$ -decay to produce an appreciable amount of  $^{60}\text{Fe}$ : This reaction pair dominates the nuclear-reaction uncertainties in  $^{60}\text{Fe}$  production, with  $^{59}\text{Fe}(n, \gamma)$  being difficult to measure in nuclear laboratories due to its long lifetime and multitude of reaction channels ([Jones et al., 2019](#)). Using an effective He-burning reaction rates can account for correlated behaviour of nuclear reactions and mitigate the overall nuclear uncertainties in these shell burning environments ([Austin et al., 2017](#)).

Thus, astronomical observations of the  $^{60}\text{Fe}/^{26}\text{Al}$  ratio will also help to constrain the nuclear-reaction aspects of massive stars, given the experimental difficulties to measure all reaction channels involved at the astrophysically-relevant energies. Assuming that the sky distribution of  $^{60}\text{Fe}$  follows the [CGRO/COMPTEL](#) all-sky 1809 keV emission map of  $^{26}\text{Al}$  (e.g., [Oberlack et al., 1996](#); [Plüschke et al., 2001](#)), the early [SPI](#) observations yield a flux ratio of  $^{60}\text{Fe}/^{26}\text{Al}$  in the range of  $\sim 0.09\text{--}0.21$  ([Wang et al., 2007](#)) and  $\sim 0.08\text{--}0.22$  ([Bouchet et al., 2011, 2015](#)). To cater for the uncertainty of the spatial extent of  $^{60}\text{Fe}$  emission, [Wang et al. \(2020\)](#) performed different tests to avoid possible biases in determining the ratio. In order to fit the  $^{60}\text{Fe}$  and  $^{26}\text{Al}$  (all-)sky distributions, they first created a grid of doubly-exponential disk models with different characteristic scale radii from 0.5 to 8.0 kpc and scale heights from 0.01 to 2.0 kpc in a grid of 512 possibilities. The  $^{60}\text{Fe}/^{26}\text{Al}$  ratio distribution from all 512 exponential-disk configurations is presented in Fig. 9, including characteristic uncertainties. The average  $^{60}\text{Fe}/^{26}\text{Al}$  ratio based on this analysis gives a value of  $0.18 \pm 0.04$ . [Wang et al. \(2020\)](#) also fitted the  $^{60}\text{Fe}$  diffuse emissions with a set of maps representing different source tracers (e.g., the 408 MHz radio map, infrared emission, high-energy  $\gamma$ -ray and X-ray sky maps). These sky maps with significant detections of and adequately describing both  $^{26}\text{Al}$  and  $^{60}\text{Fe}$  emission lines can also constrain the  $^{60}\text{Fe}/^{26}\text{Al}$  values (Fig. 9). The average ratio values distribute around 0.25, generally with an upper limit range near 0.3.

The  $^{60}\text{Fe}/^{26}\text{Al}$  ratio has been promoted as a useful test of stellar evolution and nucleosynthesis models, because the actual source numbers and their distances may cancel out largely in such a ratio. The present  $\gamma$ -ray line studies give an observational ratio of  $\sim 0.15\text{--}0.3$  in the Galaxy, while theoretical predictions seem to produce relatively large values. Massive star models with a solar composition and a standard stellar mass distribution from 13 to  $120\text{ M}_\odot$  predict  $^{60}\text{Fe}$  and  $^{26}\text{Al}$  yields with and without rotation effects ([Limongi and Chieffi, 2018](#)): With rotation, the flux ratio is  $0.8 \pm 0.4$ , but the ratio reduces to  $\sim 0.2\text{--}0.6$  in the case of non-rotating models. In addition, if only the mass range from  $13\text{--}40\text{ M}_\odot$  is considered, the  $^{60}\text{Fe}/^{26}\text{Al}$  ratio is estimated to be  $\sim 0.07\text{--}0.15$ . The stellar evolution for the stars more massive than  $40\text{ M}_\odot$  has considerable uncertainties, for example from the stellar winds and the effect on the stellar structure and evolution. Some stars may not explode as [ccSNe](#), but rather collapse

directly to black holes. Thus, massive stars above  $40 M_{\odot}$  may not have the effective contribution to  $^{60}\text{Fe}$  production and could be ignored in a stellar mass-weighted Galactic average. Compared to the most recent  $\gamma$ -ray observations, the present models would either over-estimate  $^{60}\text{Fe}$  yields or under-estimate the  $^{26}\text{Al}$  production (Wang et al., 2020).

This problem, however, may be alleviated if other  $^{26}\text{Al}$  production channels than only massive stars, their winds, and their [ccSNe](#) are taken into account. Vasini et al. (2025) suggests that up to 75% of the Galactic  $^{26}\text{Al}$  mass – and therefore flux if distributed similarly – may be due to [CNe](#), based on a Galactic chemical evolution model. If this scenario is true, as has also been suggested early on in the study of the  $^{26}\text{Al}$   $\gamma$ -ray line (e.g., Leising and Clayton, 1985; José et al., 1997; Bennett et al., 2013), the  $^{60}\text{Fe}/^{26}\text{Al}$  flux ratio from only massive stars in the Galaxy may be increased by a factor of four, more in line with massive star model predictions.

## 2.3 $\gamma$ -Ray Lines from Classical Novae

Written by Pierre Jean

It is commonly accepted that a **CN** arises from the thermonuclear explosion of an accreted layer on a **WD** in a binary system. The thermonuclear runaway converts hydrogen into helium via the CNO process while synthesizing medium atomic number elements. [Clayton and Hoyle \(1974\)](#) first proposed **CNe** as sources of nuclear  $\gamma$ -rays, yet such emission has not been observed with past or current  $\gamma$ -ray spectrometers (see also [Clayton, 1981](#)). **CNe** are promising for observing nucleosynthesis in  $\gamma$ -rays because freshly produced elements are rapidly transported from the production zone by convection during the outburst or via ejected material; under these conditions, unstable nuclei decay in less dense matter, allowing de-excitation  $\gamma$ -rays to escape and be detected. Typical ejected masses of  $\sim 10^{-6}\text{--}10^{-4} M_\odot$  are low compared to those from **SNe Ia** and **ccSNe**, and these small amounts of unstable nuclei render the expected  $\gamma$ -ray lines faint and difficult to detect without improvements on the sensitivity of  $\gamma$ -ray instruments.

### 2.3.1 Properties of Nuclear $\gamma$ -Rays from Classical Novae

The synthesized material during the thermonuclear runaway depends on the underlying **WD** composition – carbon-oxygen (CO) or oxygen-neon (ONe), with ONe being more massive. The pre-outburst abundance is set by mixing core and accreted material. During the outburst, CO novae mainly synthesise light and intermediate-mass elements of the CNOF group, while ONe novae, thanks to higher temperatures and densities, also produce heavier elements (e.g., from the NeNa and MgAl groups). Tab. 1 lists the main unstable nuclei that yield nuclear  $\gamma$ -ray emission. Both **CNe** types produce  $^7\text{Li}$ , with CO novae ejecting about ten times more than ONe novae ([José and Hernanz, 1998](#)), and the isotopes  $^{22}\text{Na}$  and  $^{26}\text{Al}$  are more abundant in ONe novae.

Radionuclei(decay mode)	Main $\gamma$ -ray emission	Half-life	Nova type
$^7\text{Be}(\text{EC})$	478 keV	53 days	CO
$^{13}\text{N}(\beta^+)$	$\leq 511$ keV	10 min	CO & ONe
$^{18}\text{F}(\beta^+ & \text{EC})$	$\leq 511$ keV	1.8 h	CO & ONe
$^{22}\text{Na}(\beta^+ & \text{EC})$	1275 keV	2.6 yr	ONe
$^{26}\text{Al}(\beta^+ & \text{EC})$	1809 keV	0.7 Myr	ONe

**Table 1** List of the main radioactive nuclei with their characteristics, their main  $\gamma$ -ray emission (lines) and the type of **CNe** in which they are produced (adapted from [Hernanz, 2014](#)).

The produced nuclei are proton-rich and unstable, as expected from fast hydrogen burning in the CNO cycle, and decay by  $\beta^+$  or **EC**. Positrons from the short-lived  $\beta^+$ -decay of  $^{13}\text{N}$  and  $^{18}\text{F}$  rapidly lose kinetic energy and annihilate in the expanding envelope. The steep temperature gradient in the envelope ensures convection transports unstable nuclei to the surface faster than their lifetime. Thus,  $\beta^+$ -unstable nuclei decay in a less opaque medium, enabling  $\gamma$ -rays from positron annihilations to escape.

This yields a 511 keV line and a continuum  $\leq$  511 keV from ortho-Ps annihilation and Compton scattering. Similarly, positrons from  $^{22}\text{Na}$  decay contribute about three orders of magnitude less at early times than those from  $^{13}\text{N}$  and  $^{18}\text{F}$ . Furthermore, shortly after the explosion, positrons from  $^{22}\text{Na}$  decay are expected to escape the ejecta (e.g., at  $\sim 25$  d for a CN with  $1.25 M_{\odot}$  (Hernanz and José, 2006)). Due to its lifetime, most positrons from  $^{26}\text{Al}$  decay escape into the ISM and likely travel far from the CN before annihilation. Leising and Clayton (1987) first studied the positron fate in CNe envelopes and estimated  $\gamma$ -ray light curves. Gomez-Gomar et al. (1998) later analysed the temporal and spectral properties of  $\gamma$ -ray line emissions from ONe and CO novae. They employed a hydrodynamical code with a nuclear reaction network to compute the envelope properties and radioactive synthesis. Radiative transfer was computed via Monte Carlo simulations. Fig. 10 shows the spectra obtained with this method for CN models available in 2014. The 511 keV line and continuum are clearly visible. The low-energy cutoff ( $\sim 20$ –30 keV) arises from photoelectric absorption, and the 170 keV feature from 511 keV photon backscattering in the ejecta.

The light curves of the 478 keV ( $^{7}\text{Be}$ ) and 1275 keV ( $^{22}\text{Na}$ ) lines peak at 5–10 d post-peak temperature, depending on the CN type and ejecta mass. This maximum occurs when the ejecta become transparent to  $\gamma$ -rays, as the lifetimes of  $^{7}\text{Be}$  and  $^{22}\text{Na}$  exceed the ejecta dynamical timescale. The 511 keV line and ortho-Ps peak is more complex, given the short lifetimes of  $^{13}\text{N}$  and  $^{18}\text{F}$  and the dependence on photon energy and ejecta dynamics. Leising and Clayton (1987) modelled 511 keV emissions peaking at 40 min and 6 h from  $^{13}\text{N}$  and  $^{18}\text{F}$ , respectively, with fluxes of  $5 \times 10^{-3}$  to  $10^{-1} \text{ ph cm}^{-2} \text{ s}^{-1}$  for fast CNe at 1 kpc. Gomez-Gomar et al. (1998) obtained similar 511 keV flux maxima at about 1 h and 5–8 h post-peak temperature (see also Hernanz et al., 1999). With revised nuclear rates, Hernanz (2014) reported maximum fluxes of  $10^{-2}$  and  $8 \times 10^{-4} \text{ ph cm}^{-2} \text{ s}^{-1}$  for CO and ONe novae (both  $1.15 M_{\odot}$  at 1 kpc), respectively. Recently, Leung and Siegert (2022) performed similar studies; they found  $\gamma$ -ray fluxes over three orders of magnitude lower than those reported by Hernanz (2014) for similar CO and ONe novae. This is mainly due to their use of lower expansion velocities and peak temperatures than previous studies. Thus, the ejecta become transparent later (5–10 d), by which time most short-lived nuclei have decayed.

Since the radioactive nuclei decay in an expanding envelope, the  $\gamma$ -ray lines are broadened by the Doppler effect. The early 511 keV line is expected to have a width of 5–8 keV (FWHM), model-dependent, and is slightly blue-shifted since only photons from the external envelope escape opacity (Hernanz et al., 1999; Leising and Clayton, 1987). For CO novae models ( $0.8 M_{\odot}$  and  $1.15 M_{\odot}$ ) with ejecta velocities of 1300–2500  $\text{km s}^{-1}$ , the 478 keV line has a width of 3–7 keV (FWHM). For ONe novae with ejecta velocities around 2500  $\text{km s}^{-1}$ , the 1275 keV line is broadened by about 20 keV (Gomez-Gomar et al., 1998).

Positrons from CNe also contribute to the diffuse 511 keV emission in the Galaxy. However,  $\beta^+$ -decays from CNe alone cannot account for the full annihilation rate (see Sec. 2.9). Positrons from  $^{13}\text{N}$  and  $^{18}\text{F}$  decay within the envelope, causing transient emission, and the  $^{26}\text{Al}$  and  $^{22}\text{Na}$  yields from CNe are likely insufficient. Assuming an ONe nova produces up to  $10^{-8} M_{\odot}$  of  $^{22}\text{Na}$  and that ONe novae represent about one-third of  $35 \text{ yr}^{-1}$ , Prantzos et al. (2011) estimated a positron production rate of  $\lesssim$

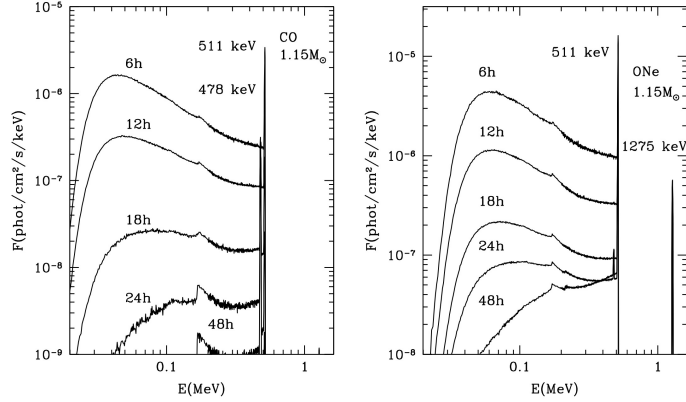


**Fig. 10** Model of early  $\gamma$ -ray spectra emitted by a CN at a distance of 1 kpc as a function of time after the peak in temperature of the thermonuclear runaway (from Hernanz, 2014).

$1.5 \times 10^{41} \text{ e}^+ \text{ s}^{-1}$ , only a few percent of the measured rate. This is further supported by the non-detection of diffuse and point-like  $^{22}\text{Na}$   $\gamma$ -rays from the Galaxy (Sec. 2.3.2.1).

### 2.3.2 Observations of $\gamma$ -Rays from Classical Novae

#### 2.3.2.1 $\gamma$ -Ray Emission from $^{22}\text{Na}$ Decays

The 1275 keV line flux expected from an individual ONe nova is

$$F_{22} = 3.8 \times 10^{-4} \times \left( \frac{d}{1 \text{ kpc}} \right)^{-2} \times \left( \frac{M_{22}}{10^{-8} M_\odot} \right) \times \exp \left( -\frac{\Delta t}{\tau_{22}} \right) \text{ ph cm}^{-2} \text{ s}^{-1}, \quad (34)$$

where  $M_{22}$  is the ejecta mass of  $^{22}\text{Na}$ ,  $\Delta t$  is the time since outburst,  $\tau_{22}$  the lifetime of  $^{22}\text{Na}$ , and  $d$  is the distance to the CN. Leising et al. (1988) undertook the first attempt to search for the 1275 keV line from individual CNe. They analysed data of the Gamma-Ray Spectrometer (GRS) onboard the Solar Maximum Mission (SMM) from 1980 to 1987. They did not detect the line and thus derived upper limit fluxes of four nearby CNe, which resulted in a most constraining upper limit of  $^{22}\text{Na}$  ejecta mass of  $7 \times 10^{-7} M_\odot$  from N Vul 1984b. Later, Iyudin et al. (1995) obtained an upper limit of  $3.7 \times 10^{-8} M_\odot$  from the observation of eleven Galactic CNe exploding between 1991 and 1993, with COMPTEL. The more recent results come from the observations with SPI: Siegert et al. (2021) derive an upper limit of  $1.3 \times 10^{-7} M_\odot$  from V5115 Sgr, a probable ONe nova that exploded on March 2005, assuming a distance of 3 kpc.

Given that the lifetime of  $^{22}\text{Na}$  exceeds the typical interval between ONe novae in the Galaxy ( $R_{\text{CNe}} \approx 11\text{--}17 \text{ yr}^{-1} \Leftrightarrow \tau_{\text{ONe}} \approx 0.06\text{--}0.09 \text{ yr}$ ), the accumulated  $^{22}\text{Na}$  should yield a diffuse 1275 keV  $\gamma$ -line in the Milky Way. However, the cumulative flux is dominated by just a few tens of CNe (e.g.,  $\tau_{22} \times R_{\text{ONe}} \approx 50$  on average), so the diffuse emission fluctuates. Fig. 11 illustrates the total 1275 keV flux variations over a  $12.5^\circ$  region around the Galactic centre, computed via Monte Carlo simulation by Jean et al. (2000). The flux is normalized to the mass of  $^{22}\text{Na}$  ejected per outburst. In this case, a single CN at year 8.6 contributes 91% of the total flux. After year 20, the flux fluctuates

with a maximum amplitude of  $\pm 40\%$  around a mean of about  $10^3 \text{ ph cm}^{-2} \text{ s}^{-1} \text{ M}_\odot^{-1}$ . Subsequent studies with updated **CN** rates have also been performed and showed similar features (Siegert et al., 2021; Shafter, 2017).

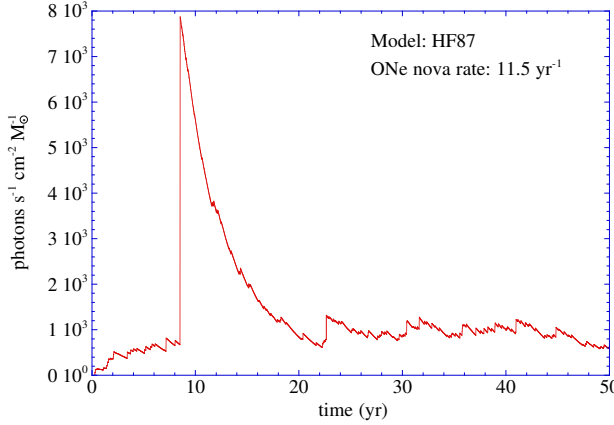


**Fig. 11** Example of the normalised 1275 keV flux in a  $12.5^\circ$  region around the Galactic centre as a function of time with a ONe nova rate of  $11.5 \text{ yr}^{-1}$ . The flux from the Galactic centre direction can be dominated by a single nearby **CN**, such as around year 8.6.

Higdon and Fowler (1987) were the first to search for the Galactic diffuse emission of the  $\gamma$ -ray line from the cumulative decay of  $^{22}\text{Na}$  ejected by active ONe novae. They compared their Monte Carlo emission model with the upper flux limits from HEAO 3 observations by Mahoney et al. (1982). Their model, based on M31's stellar distributions scaled to the Milky Way's disk, spheroid, and local **CN** rate, yields an upper mass limit of  $5.6 \times 10^{-7} \text{ M}_\odot$  per **CN**. However, this result is uncertain due to the unknown spatial distribution and rate of **CNe**, as interstellar extinction obscures many Galactic **CNe** at optical wavelengths. Analyses of SMM data yielded an upper flux limit of  $1.2 \times 10^{-4} \text{ ph cm}^{-2} \text{ s}^{-1}$  from the Galactic centre region; assuming a **CN** rate of  $40 \text{ yr}^{-1}$ , this implies an upper limit of  $2 \times 10^{-8} \text{ M}_\odot$  of  $^{22}\text{Na}$  ejected per **CN** (Leising et al., 1988). With a more realistic ONe nova rate of  $\sim 10 \text{ yr}^{-1}$  (Jean et al., 2000), the upper limit becomes  $8 \times 10^{-8} \text{ M}_\odot$ . Using six years of COMPTEL data of the Galactic bulge, Jean et al. (2001) derived an upper limit of  $6 \times 10^{-7} \text{ M}_\odot$  per **CN**, accounting for uncertainties in the ONe nova rate and spatial distribution. Fifteen years of SPI observations yielded an upper limit of  $2.7 \times 10^{-7} \text{ M}_\odot$  from the 1275 keV diffuse emission (Siegert et al., 2021).

The latest study of the  $^{22}\text{Na}$  amount ejected per ONe nova was conducted by Fougères et al. (2023) that accounted for updated nuclear rates. They showed that the  $^{22}\text{Na}$  ejecta depend on the accretion rate and the initial **WD** luminosity. They calculated  $^{22}\text{Na}$  ejecta masses of  $(4\text{--}8) \times 10^{-9} \text{ M}_\odot$ , depending on the **WD** mass for an initial luminosity of  $10^{-2} \text{ L}_\odot$  and an accretion rate of  $2 \times 10^{-10} \text{ M}_\odot \text{ yr}^{-1}$ . For a  $1.2 \text{ M}_\odot$  **WD**, they obtained  $^{22}\text{Na}$  ejecta masses of  $(0.3\text{--}8) \times 10^{-9} \text{ M}_\odot$ . This is about one to two orders of magnitude lower than the upper limits obtained with  $\gamma$ -ray observations.

### 2.3.2.2 $\gamma$ -Ray Emission from $^{26}\text{Al}$ Decays

The spatial distribution of the 1809 keV line from  $^{26}\text{Al}$  measured by **COMPTEL** fits with the distribution of the young stellar population rather than with the old star (**CN**) population (Knöldlseder et al., 1999). Its origin is mainly explained by massive stars that eject freshly produced  $^{26}\text{Al}$  via winds during their Wolf-Rayet phase or when they explode at the end of their life. Crude estimation of the amount of  $^{26}\text{Al}$  produced by **CN** in the Milky Way was found to be of  $\sim 0.4 \text{ M}_\odot$  (José et al., 1997). With updated nuclear reaction rates and a new chemical evolution model, Canete et al. (2023) reached a similar result with an estimation of the maximum contribution of **CN** of  $\sim 0.2 \text{ M}_\odot$ . With such a value, the contribution of all **CN** would yield to a total 1809 keV flux of  $\lesssim 4 \times 10^{-5} \text{ ph cm}^{-2} \text{ s}^{-1}$  which is about a factor of nine times less than the flux in the inner Galaxy measured by **SPI** (Diehl et al., 2006; Pleintinger et al., 2023). This is in stark contrast to recent Galactic Chemical Evolution estimates by Vasini et al. (2025) who predict a contribution of up to 75% of the  $^{26}\text{Al}$  mass in the Galaxy (see also Sec. 2.2.3).

### 2.3.2.3 $\gamma$ -Ray Emission from $^7\text{Be}$ Decays

The 478 keV line emission from a **CN** has not been detected yet. Neglecting absorption at the early stage of the outburst, the instantaneous line flux from the decay of a certain mass of  $M_7$  of  $^7\text{Be}$  ejected at a distance  $d$  by a **CN** (José and Hernanz, 1998) is

$$F_7 = 2.2 \times 10^{-6} \times \left( \frac{d}{1 \text{ kpc}} \right)^{-2} \times \left( \frac{M_7}{10^{-10} \text{ M}_\odot} \right) \times \exp \left( -\frac{\Delta t}{\tau_7} \right) \text{ ph cm}^{-2} \text{ s}^{-1}. \quad (35)$$

Using SMM observations, Harris et al. (1991) reported upper limits on the line flux around  $10^{-3} \text{ ph cm}^{-2} \text{ s}^{-1}$  from three Galactic **CNe** at distances  $\leq 3.5 \text{ kpc}$ , between 1982 and 1986. They derived a most constraining upper limit of the  $^7\text{Be}$  mass ejected of  $5.2 \times 10^{-8} \text{ M}_\odot$  from N Cen 1986, which was assumed to be at a distance of 1.1 kpc. More recently, Siegert et al. (2018) obtained an upper limit of  $1.2 \times 10^{-8} \text{ M}_\odot$  from the observation with **SPI** of V5668 Sgr in 2015 assuming a distance of 1.6 kpc. Combining this result with the  $^7\text{Be}$  mass estimated from UV observations, Siegert et al. (2018) concluded that the **CN** should be at a distance larger than 1.2 kpc. The observations of the cumulative 478 keV line emission from the Galactic centre region provide less constraining upper mass limits than the ones obtained from observation of individual **CN** (Harris et al., 1991; Siegert et al., 2021). With a better distance estimation of V5668 Sgr and a revised analysis of **SPI** data, Siegert et al. (2021) obtained an upper limit of  $3 \times 10^{-8} \text{ M}_\odot$ . This value is similar to the one obtained by Izzo et al. (2025) with the observation of V1369 Cen in 2013, with **SPI**. Here again, the upper limit masses derived from  $\gamma$ -ray observations are about two orders of magnitude larger than the masses estimated by theoretical studies. However, some UV observations of **CN** suggest higher  $^7\text{Be}$  ejecta masses, such as around  $10^{-9} \text{ M}_\odot$  (e.g., Tajitsu et al., 2016; Molaro et al., 2020), based on relative abundance measurements.

#### 2.3.2.4 Prompt $\gamma$ -Ray Emissions

Several attempts have been made to detect the prompt  $\leq 511$  keV emissions from **CN** using space-borne  $\gamma$ -ray detectors with wide fields of view. The delay between the prompt  $\gamma$ -ray emission and the optical maximum being uncertain, the analyses should be performed on long observation periods around the outburst date. Moreover, the theoretical duration of the brightest  $\leq 511$  keV emission ( $\lesssim 1$  h) is similar to the typical orbital period ( $\sim 1.5$  h) of instrument in low Earth orbit, such as the Burst and Transient Source Experiment (**BATSE**) onboard **CGRO** and the Burst Alert Telescope (**BAT**) onboard **Swift**. In these conditions, it is not possible to continuously monitor the sources and, therefore, it is difficult to extract upper limits on fluxes, since the source may have been occulted by Earth during its maximum emission. Gamma-ray detectors in high eccentric orbits, such as the anticoincidence system (**ACS**) of **SPI** (Jean et al., 1999) or in interplanetary space such as Transient Gamma-Ray Spectrometer (**TGRS**) onboard the **Wind** probe, do not have such a limitation but they cannot perform images of sources and they experience a higher instrumental background.

Hernanz et al. (2000) did not detect the prompt emission in the 250–511 keV band of **BATSE** from two nearby **CN** (Nova Cyg 1992 and Nova Vel 1999). By analysing **TGRS** data within 6 h intervals, Harris et al. (2000) obtained upper limits on the 511 keV line of  $(2\text{--}3) \times 10^{-3}$  ph cm $^{-2}$  s $^{-1}$  from five **CN**, between 1995 and 1997. Senziani et al. (2008) searched for the emission in the 14–200 keV data from **Swift/BAT** from 24 **CN** by analysing periods from 20 d before to 20 d after their optical discoveries, during the first three years of the **Swift** mission. Using models of the prompt emission from Hernanz et al. (1999) and the Monte Carlo simulation method described in Jean et al. (2000), these authors estimated a rate of detection of two to five **CN** in ten years of the **Swift** mission. The lack of claimed detection up to now with **Swift/BAT** suggests that the model would overestimate the flux in that energy band. Siegert et al. (2018) did not find significant excess at 511 keV from V5668 Sgr in 2015 with **SPI** data. They found six excesses in the **SPI/ACS** data during the weeks before the discovery of the **CN** but their temporal signatures do not correspond to the expected prompt emission. Other retrospective searches with **INTEGRAL** did also not yield any significant detections up to the year 2018 (Urruty, priv. comm.).

### 2.3.3 Conclusions

Observations of  $\gamma$ -ray lines from **CNe** can reveal the underlying **WD** type (CO or **ONe**) and constrain nucleosynthesis during the thermonuclear runaway, enhancing our understanding of Galactic element origins. The spectral and temporal features of the early 511 keV line and  $\gamma$ -ray continuum ( $\leq 511$  keV) provide insights into the expanding envelope, its early convection, and opacity through the distribution of  $\beta^+$ -emitters. A key expected result is the yet-unknown delay between the thermonuclear runaway's peak temperature and the optical maximum. No  $\gamma$ -ray emission has been detected from **CNe**, partly due to the lack of a nearby outburst during the 22-year **INTEGRAL** mission. Current upper limits remain uncertain because of poorly known distances, rates, and spatial distributions of Galactic **CNe**. Most limits exceed theoretical masses by over an order of magnitude. A new generation of  $\gamma$ -ray instruments with at least

an order of magnitude improved sensitivity is needed. The upcoming Compton Spectrometer and Imager ([COSI](#)) mission, set to monitor the 0.2–5.0 MeV band from 2027 ([Tomsick et al., 2024](#)) with a  $\sim 25\%$  wide field of view and imaging capability, will efficiently observe prompt emissions from nearby [CNe](#). [COSI](#) could detect the 1275 keV line from a  $1.25 M_{\odot}$  ONe nova within  $\lesssim 2.5$  kpc.

## 2.4 $\gamma$ -Ray Lines from Supernovae

Written by Mark Leising & Thomas Siegert

The light of SNe (both ccSNe and SNe Ia) is powered by radioactive decays (Burbidge et al., 1957; Colgate and White, 1966). Differences in  $\gamma$ -ray line observations arise from the yield per event and the progenitor system's density structure and dynamics. In general, both SNe produce large amounts of  $^{56}\text{Ni}$  – up to  $0.1 \text{ M}_\odot$  for ccSNe (e.g., Andrews et al., 2020) and  $0.1\text{--}1.0 \text{ M}_\odot$  for SNe Ia (e.g., Stritzinger et al., 2006). The  $^{56}\text{Ni}$  decay chain produces  $\gamma$ -ray lines via the EC decay of  $^{56}\text{Ni}$  (6.1 d half-life) to  $^{56}\text{Co}$  at 158 and 812 keV, and the EC+ $\beta^+$  decay of  $^{56}\text{Co}$  (77.2 d half-life) to  $^{56}\text{Fe}$  at 847 and 1238 keV. Other isotopes are produced in yields an order of magnitude lower than  $^{56}\text{Ni}$ , yet they still provide key insights into explosion energy and ejecta distribution. The long-lived  $^{44}\text{Ti}$  is expected in both SNe types but has been observed only in ccSNe (e.g., Weinberger et al., 2020).  $^{44}\text{Ti}$  (59 yr half-life) decays by EC to  $^{44}\text{Sc}$ , emitting  $\gamma$ -ray lines at 67.9 and 78.3 keV.  $^{44}\text{Sc}$  decays in 4 h to stable  $^{44}\text{Ca}$  (mainly via  $\beta^+$ -decay), emitting a  $\gamma$ -ray photon at 1157 keV. Measuring these  $\gamma$ -ray line fluxes determines the absolute ejecta masses of these isotopes in SNe. The  $^{56}\text{Ni}$  to  $^{44}\text{Ti}$  yield ratio links early nucleosynthesis to late-time observations, constraining progenitor systems even centuries after the event (e.g. Magkotsios et al., 2010). Another Chapter of this volume details theoretical explosion mechanisms, progenitors, yields, and open questions for ccSNe and SNe Ia. This section discusses  $\gamma$ -ray line observations from SNe and their leverage to understanding SN explosions, nucleosynthesis, Galactic chemical evolution, massive star evolution, and cosmology. Sec. 2.4.1 focuses on thermonuclear SNe, while Sec. 2.4.2 highlights two ccSNe: SN 1987A in the LMC and the 350 yr-old SNR Cassiopeia A (Cas A) in the Milky Way.

In addition to the  $^{56}\text{Ni}$  and  $^{44}\text{Ti}$  decay chains, other radioactive isotopes can produce  $\gamma$ -ray line emission in both ccSNe and SNe Ia. Tab. 2 summarises the measured and expected  $\gamma$ -ray lines from both SN types. Although only a few  $\gamma$ -ray lines have been unambiguously detected, their measurements are invaluable for deciphering SN physics (Prantzos, 2011). They enhance our understanding of individual SN events and Galactic chemical evolution by tracking long-lived isotopes such as  $^{26}\text{Al}$  and  $^{60}\text{Fe}$  (e.g., Timmes et al., 1995; Prantzos, 2008; Kobayashi et al., 2020; Vasini et al., 2022, see Secs. 2.1 & 2.2). Since  $\gamma$ -rays from the  $^{56}\text{Ni}$  and  $^{44}\text{Ti}$  decay chains have been extensively studied over the past 50 years, we first detail out their expected fluxes before discussing individual SN types.

According to Eq. (15), the photon flux,  $F_{56}$ , of a mass,  $M_{56}$ , of  $^{56}\text{Ni}$  (for the major 847 keV line) at a distance,  $d$ , is given by

$$F_{56} = 9.3 \times 10^{-3} \times \left( \frac{d}{1 \text{ Mpc}} \right)^{-2} \times \left( \frac{M_{56}}{0.5 \text{ M}_\odot} \right) \times \exp \left( -\frac{\Delta t}{\tau_{56}} \right) \text{ ph cm}^{-2} \text{ s}^{-1}, \quad (36)$$

which applies around 40–100 d post-explosion for SNe Ia (when the envelope is mostly optically thin) and around 1–2 yr for ccSNe. This results in considerably lower fluxes after the  $\gamma$ -ray line light curve peak, of  $5 \times 10^{-3} \times [d/(1 \text{ Mpc})]^{-2} \text{ ph cm}^{-2} \text{ s}^{-1}$  around day 70 for typical SNe Ia and  $4 \times 10^{-3} \times [d/(50 \text{ kpc})]^{-2} \text{ ph cm}^{-2} \text{ s}^{-1}$  for unobscured ccSNe. While this approximation holds for SNe Ia at later times, the 847 keV fluxes for

**Table 2** List of the radioactive nuclei, their half life times, decay modes, prominent  $\gamma$ -ray lines and branching ratios in ccSNe and SNeIa (adapted from Andrews et al., 2020). Detected  $\gamma$ -ray lines in SNe are shown in bold-face. The SN type indicates where the isotopes are *most commonly* found (all isotopes are produced in both types to some extent). The contribution to a possible 511 keV line and annihilation continuum from  $\beta^+$ -decays is discussed in Sec. 2.9.

Isotope	Half-life	Decay Mode(s)	$E_\gamma$ [keV]	Percentage	SN type
$^{56}\text{Ni} \rightarrow ^{56}\text{Co}$	6.075 d	EC ( $\sim 100\%$ )	<b>158.4</b> 269.5 480.4 750.0 <b>811.9</b> 1561.8	98.8% 36.5% 36.5% 49.5% 86.0% 14.0%	both
$^{56}\text{Co} \rightarrow ^{56}\text{Fe}$	77.24 d	EC (81.6%), $\beta^+$ (18.4%)	<b>846.8</b> 1037.8 <b>1238.3</b> 1771.4 2598.5	99.9% 14.1% 66.5% 15.4% 17.0%	both
$^{47}\text{Ca} \rightarrow ^{47}\text{Sc}$	4.536 d	$\beta^-$ ( $\sim 100\%$ )	1297.1	67.0%	ccSNe
$^{47}\text{Sc} \rightarrow ^{47}\text{Ti}$	3.3492 d	$\beta^-$ ( $\sim 100\%$ )	158.4	68.3%	ccSNe
$^{43}\text{K} \rightarrow ^{43}\text{Ca}$	22.3 h	$\beta^-$ ( $\sim 100\%$ )	372.8 396.9 593.4 617.5	86.8% 11.9% 11.3% 79.2%	ccSNe
$^{44}\text{Ti} \rightarrow ^{44}\text{Sc}$	60.0 yr	EC ( $\sim 100\%$ )	<b>67.9</b> <b>78.3</b>	93.0% 96.4%	both
$^{44}\text{Sc} \rightarrow ^{44}\text{Ca}$	4.0 h	EC (5.7%), $\beta^+$ (94.3%)	<b>1157.0</b>	99.9%	both
$^{48}\text{Cr} \rightarrow ^{48}\text{V}$	21.56 d	EC (98.5%), $\beta^+$ (1.5%)	112.3 308.2	96.0% 100.0%	both
$^{48}\text{V} \rightarrow ^{48}\text{Ti}$	15.97 d	EC (49.6%), $\beta^+$ (50.4%)	983.5 1312.1	100.0% 96.0%	both
$^{52}\text{Mn} \rightarrow ^{52}\text{Cr}$	21.1 min	EC (70.6%), $\beta^+$ (29.4%)	744.2 935.5 1434.1	90.0% 94.5% 1.0%	both
$^{59}\text{Fe} \rightarrow ^{59}\text{Co}$	44.49 d	$\beta^-$ ( $\sim 100\%$ )	1099.2 1291.6	56.5% 43.2%	both
$^{57}\text{Ni} \rightarrow ^{57}\text{Co}$	35.6 h	EC (64.7%), $\beta^+$ (35.3%)	1377.6 1919.5	81.7% 12.3%	both
$^{57}\text{Co} \rightarrow ^{57}\text{Fe}$	271.74 d	EC ( $\sim 100\%$ )	<b>122.1</b> <b>136.5</b>	85.6% 10.7%	both
$^{26}\text{Al} \rightarrow ^{26}\text{Mg}$	$7.17 \times 10^5$ yr	EC (18.3%), $\beta^+$ (81.7%)	<b>1808.7</b> 1129.7	99.8% 2.5%	ccSNe
$^{60}\text{Fe} \rightarrow ^{60}\text{Co}$	$2.60 \times 10^6$ yr	$\beta^-$ ( $\sim 100\%$ )	58.6	99.8%	ccSNe
$^{60}\text{Co} \rightarrow ^{60}\text{Ni}$	5.27 yr	$\beta^-$ ( $\sim 100\%$ )	<b>1332.5</b> <b>1173.2</b>	99.9% 99.9%	ccSNe

ccSNe must be corrected for the envelope opacity (e.g. Fu and Arnett, 1989; Grebenev and Syunyaev, 1987; Palmer et al., 1993).

In both cases, however, the simplest approximation includes a time-, that is, radius-dependent optical depth,  $\tau_\gamma(t)$ , that takes into account the overlaying total ejecta mass,  $M_{\text{ej}}$ , the expansion velocity of the SN envelope,  $v_{\text{ej}}$ , and a SN-specific and in general energy-dependent opacity,  $\kappa_\gamma$ , in units of  $\text{cm}^2 \text{g}^{-1}$  (Grebenev and Syunyaev,

1987). Then, the optical depth can be approximated as

$$\tau_\gamma(t) = \frac{\kappa_\gamma M_{\text{ej}}}{4\pi v_{\text{ej}}^2 t^2}, \quad (37)$$

where the general trend,  $\tau \propto t^{-2}$ , exists in all **SN** models. By applying the optical depth to the general flux function, Eq. (36), we find

$$F_{56}(t) = F_{56}^{\text{unabs}}(t) \times \exp \left[ -636 \left( \frac{\kappa_\gamma}{0.03 \text{ cm}^2 \text{ g}^{-1}} \right) \left( \frac{M_{\text{ej}}}{1 \text{ M}_\odot} \right) \left( \frac{v_{\text{ej}}}{10000 \text{ km s}^{-1}} \right)^{-2} \left( \frac{\Delta t}{1 \text{ d}} \right)^{-2} \right], \quad (38)$$

where typical values are given in the equation for **SNe Ia**. In the case of **ccSNe**, the opacity may range within  $0.02\text{--}0.05 \text{ cm}^2 \text{ g}^{-1}$ , the ejecta mass is much larger with  $5\text{--}20 \text{ M}_\odot$ , and the ejecta velocity somewhat smaller  $5000\text{--}10000 \text{ km s}^{-1}$ . From these simple considerations, it can be seen that the **ccSNe  $\gamma$ -ray** line flux can be suppressed by one or two orders of magnitude even within the first year after the explosion, whereas **SNe Ia** become transparent to  $\gamma$ -rays after a few weeks. The absorbed photons will be re-processed in the envelope and will power the UVOIR lightcurve (see Sec. 2.4.2). It should be noted that this model can fall short in explaining actual observations of, for example, SN 1987A (e.g., Leising and Share, 1990).

Considering  $^{44}\text{Ti}$ , the unabsorbed flux is calculated as before,

$$F_{44} = 7.6 \times 10^{-4} \times \left( \frac{d}{3.3 \text{ kpc}} \right)^{-2} \times \left( \frac{M_{44}}{10^{-4} \text{ M}_\odot} \right) \times \exp \left( -\frac{\Delta t}{\tau_{44}} \right) \text{ ph cm}^{-2} \text{ s}^{-1}, \quad (39)$$

with typical values given for the **SNR Cas A**. For **Cas A**'s age of about 350 yr, the expected flux is on the order of  $10^{-5} \text{ ph cm}^{-2} \text{ s}^{-1}$ , consistent with previous measurements (e.g., Iyudin et al., 1994; The et al., 1996; Vink et al., 2001; Renaud et al., 2006; Grefenstette et al., 2014; Siegert et al., 2015; Weinberger et al., 2020, see also Sec. 2.4.2). Within the first two years post-explosion, not all three  $\gamma$ -ray lines from the  $^{44}\text{Ti}$  decay chain are visible: The 1157 keV line from  $^{44}\text{Sc}$  appears around the same time as the 847 and 1238 keV  $^{56}\text{Co}$  lines, but the 68 and 78 keV “hard X-ray lines” emerge only about ten years later due to the high opacity ( $\kappa_\gamma \approx 1 \text{ cm}^2 \text{ g}^{-1}$ ). However, the expected rise in the low-energy lines has not yet been observed in any **SN** explosion. Since the late 1960s, the **Cas A**  $^{44}\text{Ti}$   $\gamma$ -ray line flux has decreased by a factor of two. Different instruments, epochs, and sensitivities to various lines (68 & 78 keV vs. 1157 keV) make this decay difficult to probe (see, e.g., Siegert et al., 2015). At late times, although line ratios should approach unity, the stable nucleus  $^{44}\text{Ca}$  may be re-excited by **LECRs**, enhancing its flux (Siegert et al., 2015, see also Sec. 2.6).

Because radioactive nuclei may decay through several competing channels, the total decay rate is therefore the sum of the individual processes:

$$\lambda_{\text{tot}} = \lambda_{\text{EC}} + \lambda_{\beta^+} + \lambda_{\beta^-} + \lambda_\gamma + \dots \quad (40)$$

Thus, the mean lifetime is given by  $\tau_{\text{tot}} = 1/\lambda_{\text{tot}}$ , so that if one channel is suppressed, the total lifetime increases correspondingly. In astrophysical plasmas the **EC** component is particularly sensitive to the ionisation state as it requires the presence of bound K-shell<sup>1</sup> electrons,

$$\lambda_{\text{EC}} = \lambda_{\text{EC}}^0 f_e. \quad (41)$$

Here  $\lambda_{\text{EC}}^0$  is the laboratory **EC** decay rate and  $f_e$  is the fraction of occupied inner shells, which can be strongly reduced in highly ionised environments (Motizuki and Kumagai, 2004).

For  $^{44}\text{Ti}$  with decays almost entirely through **EC**, even modest stripping of inner electrons can decrease  $\lambda_{\text{EC}}$  significantly and thus extend the effective lifetime in young **SNRs**. This effect is relevant for SN 1987A and **Cas A** (see Secs. 2.4.2.1 & 2.4.2.2), where shock heating and incomplete recombination can maintain ions in highly ionised states, thereby reducing the  **$\gamma$ -ray** and hard X-ray flux expected from the  $^{44}\text{Ti}$  decay chain. Such environmental dependence introduces uncertainties when comparing theoretical yields to observed line intensities, especially at early times when ionisation is highest.

The same mechanism could influence other isotopes that have an **EC** decay branch, such as  $^{26}\text{Al}$  with its  $\sim 18\%$  **EC** component. In hot regions of the **ISM** or in shocked ejecta, partial ionisation may reduce the **EC** contribution to the total decay rate of  $^{26}\text{Al}$ , increasing its effective lifetime relative to laboratory conditions by at most 22%.

## 2.4.1 **$\gamma$ -Ray Lines from the $^{56}\text{Ni}$ Decay Chain in Type Ia Supernovae**

### 2.4.1.1 *Measurements of $^{56}\text{Ni}$ Decay $\gamma$ -Rays*

Clayton et al. (1969) recognised decades ago the potential of  **$\gamma$ -ray** line observations for understanding **SN** explosions. This included especially the lines of the decay of abundant  $^{56}\text{Ni}$  and  $^{56}\text{Co}$ ,  $^{57}\text{Co}$ , longer-lived  $^{44}\text{Ti}$  and  $^{44}\text{Sc}$ , as well as  $^{48}\text{V}$  and  $^{48}\text{Cr}$  (see Tab. 2). At the time, they were considering “Type I” **SNe**, before the various cases and progenitors were recognised. The  $A = 56$  isotopes are clearly produced in large amounts in thermonuclear – or Type Ia – supernovae (**SNe Ia**), as they power much of the luminous display, especially after a few weeks of the initial explosion. Although the  $^{56}\text{Co}$ ,  $^{44}\text{Sc}$ , and  $^{44}\text{Ti}$   **$\gamma$ -ray** line predictions were eventually realised (the latter two only in **ccSNe** as of yet; see Sec. 2.4.2), decades of attempts to measure these  **$\gamma$ -ray** lines yielded only upper limits. One of the more surprising upper limits was obtained for  $^{56}\text{Co}$  emission from SN 1986G in the nearby galaxy Centaurus A (Matz and Share, 1990).

More distant **SNe Ia** were observed with instruments with somewhat better sensitivity, but without clear  **$\gamma$ -ray** line detections (Lichti et al., 1994; Leising et al., 1995; Georgii et al., 2002; Isern et al., 2013). SN 2014J, at a distance of 3.3 Mpc in the galaxy M82, was detected in the  $^{56}\text{Co}$  lines at 847 and 1238 keV at a few  $\sigma$  significance in each of four, month-long intervals (Churazov et al., 2015; Diehl et al., 2015, see also Figs. 12 & 13). Weak features corresponding to the  $^{56}\text{Ni}$  line energies at 158 and 812 keV were also measured from the direction to SN 2014J, and interpreted as  $^{56}\text{Ni}$  propelled ahead of the main ejecta, perpendicular to the **LoS** (Diehl et al., 2014). The  $^{56}\text{Co}$   **$\gamma$ -rays** from that same material are not evident. An alternative study by

---

<sup>1</sup>Also L-shell or free electrons can lead to **EC** on nuclei but at a much smaller probability.

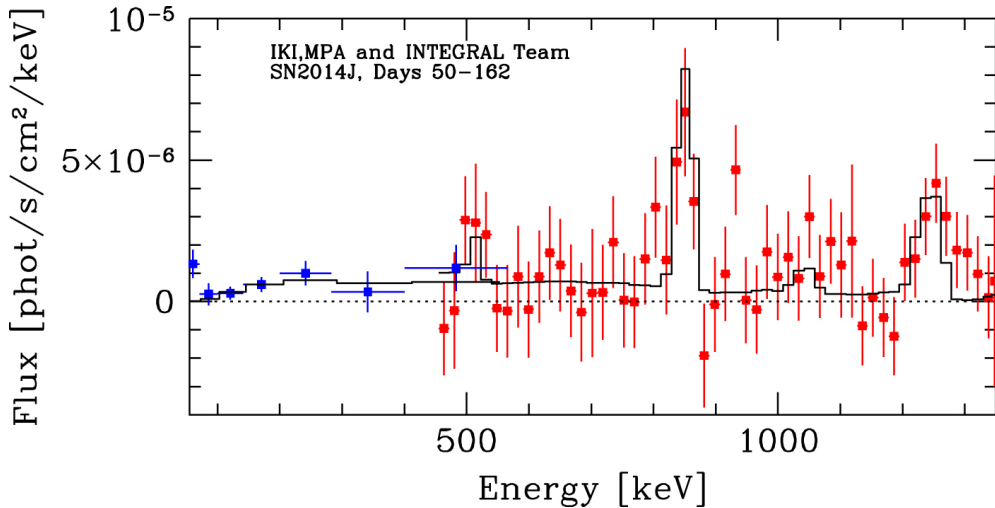


**Fig. 12** Integrated spectrum of SN 2014J measured by **INTEGRAL/SPI** and Imager on Board the INTEGRAL Satellite (**IBIS**) (from Churazov et al., 2014). Two  $^{56}\text{Co}$  lines and the scattered continuum are apparent. This is the first **SN Ia** firmly detected in  $\gamma$ -rays.

Isern et al. (2016) also found an early  $^{56}\text{Ni}$  signal at a similar flux level, but with lines broadened and redshifted. It was concluded that the measured signals of the  $^{56}\text{Ni}$  decay lines were probably originating from SN 2014J because the ejecta masses were estimated to be within each others uncertainties, but the geometrical scenarios have to be left indecisive.

#### 2.4.1.2 Utilising $\gamma$ -Ray Lines to Study Supernova Interiors

Many calculations of the  $^{56}\text{Ni}$ – $^{56}\text{Co}$   $\gamma$ -ray line light curves and spectra have been made for many hydrodynamic models of SNe Ia of all types (e.g., Nomoto et al., 1984; Burrows and The, 1990; Müller et al., 1991; Höflich et al., 1998; Gómez-Gomar et al., 1998; Milne et al., 2004; Sim and Mazzali, 2008; Maeda et al., 2012; Summa et al., 2013; The and Burrows, 2014). Monte Carlo  $\gamma$ -ray transport calculations have been the method of choice and are quite accurate. In the past, limited Monte Carlo samples yielded limited precision calculations, but that is rarely an issue nowadays. The resulting light curves for a suite of different models cover the flux-time plane quite thoroughly, making interpretation of observed light curves of limited precision quite challenging, given the great variety of models (see, e.g., Churazov et al., 2015; The and Burrows, 2014; Diehl et al., 2015). Only exquisitely precisely measured line profiles might allow one to favour one model, or one progenitor type or total ejecta mass, based on simple comparisons to spectra or light curves. However, global comparisons of many observations tied together by the physics of  $\gamma$ -ray escape offer better prospects:

The  $\gamma$ -ray line transport through the SN ejecta is comparably simple, even though that of the scattered continuum and the energy deposition are not. These photons interact overwhelmingly through Compton scattering on all electrons, bound and free,

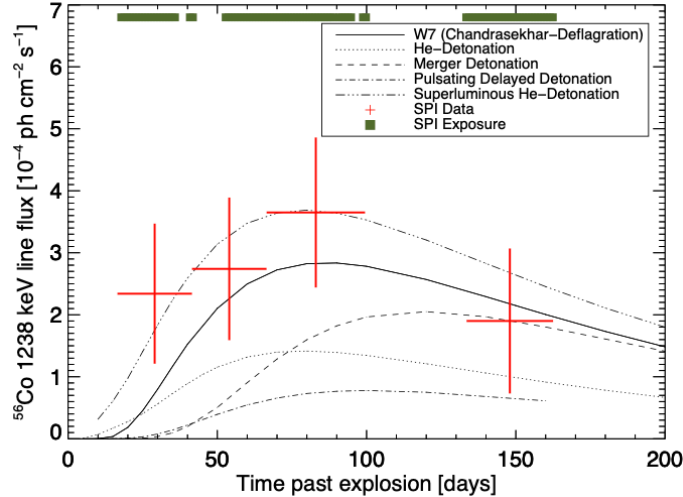


**Fig. 13** SN 2014J signal intensity variations for the 847 keV line (red data points; note that the y-axis label should be 847 keV, not 1238 keV) as observed with SPI (from Diehl et al., 2015). The fluxes were derived by Gaussians fitted to the spectra of the  $^{56}\text{Co}$  line at four independent epochs. For reference, several candidate model light curves are shown from The and Burrows (2014).

equally. Once a photon scatters, it is removed from the line, as in an absorption process. Most SNe Ia are expected to be quite spherically symmetric, with net polarization of continuum photons usually significantly less than 1%, indicating geometric asymmetry of the electron scattering photosphere of  $\lesssim 10\%$  (Wang and Wheeler, 2008; Porter et al., 2016; Cikota et al., 2019; Höflich et al., 2023). Homologous expansion of the ejecta is obtained just seconds after the explosion (Nomoto et al., 1984; Röpke, 2005), so deeper layers are progressively uncovered over months. While there might be aspherical effects of the nuclear burning that set in in the first seconds, calculating the mean escape of  $\gamma$ -ray lines versus time and energy at later times is rather straightforward.

Taking advantage of the assumptions of spherical symmetry and homologous expansion, Leising (2022) showed that the synthesised  $^{56}\text{Ni}$  mass, and the otherwise difficult to obtain total ejecta mass and kinetic energy, could be extracted with good precision from measured  $\gamma$ -ray line light curves and/or line profiles. Further, for sufficiently precise  $\gamma$ -ray measurements, the distribution of  $^{56}\text{Ni}$  as a function of the velocity in the ejecta, and density profile parameters can be derived. Total ejecta mass determinations to  $0.1 M_{\odot}$  could exclude Chandrasekhar-mass explosions, or merger models, or instead identify them as the progenitor systems. Total kinetic energy and  $^{56}\text{Ni}$  mass measurements would clarify intermediate mass element nucleosynthesis and gravitational binding energy.  $^{56}\text{Ni}$  distribution measurements would elucidate nuclear burning sites and flame propagation.

The  $\gamma$ -ray line escape calculations are based on the well known fact that a thin expanding spherical shell emits a flat topped line profile (see Sec. 1.1.1.2). Then an overlying spherical shell absorbs at all energies according to its optical depth along the observer's line of sight to a source element, and an interior shell absorbs only part

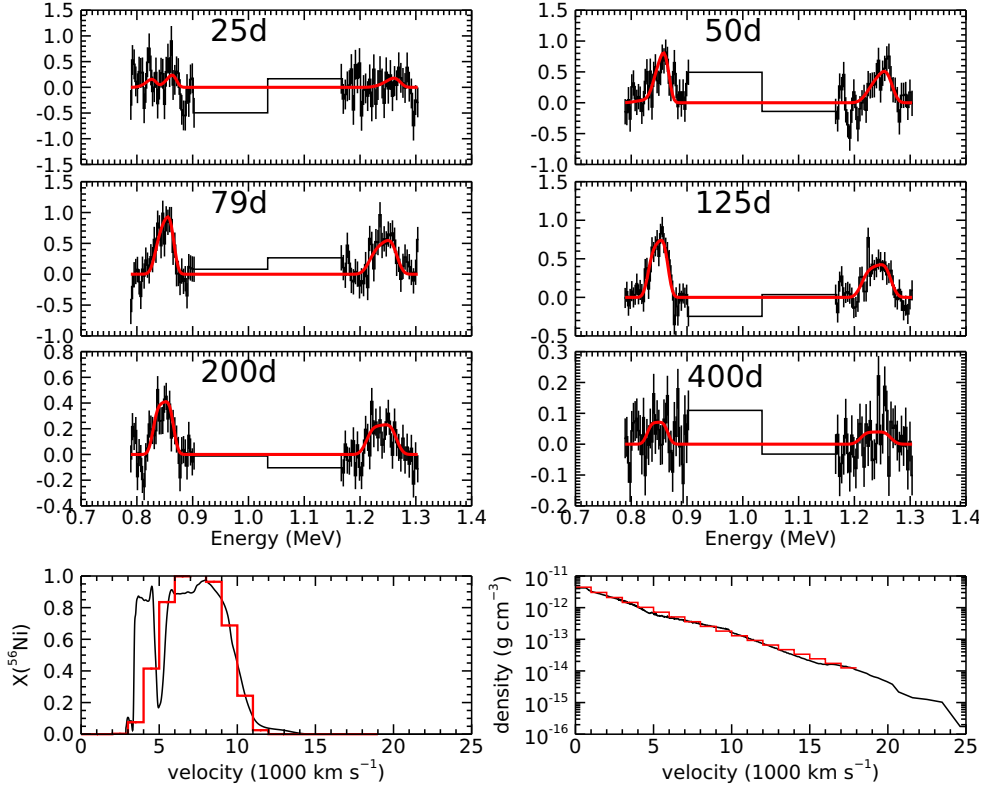


**Fig. 14** Example fit of the density and  $^{56}\text{Ni}$  mass fraction distributions to line profiles simulated from the model 7p0z22d20\_27 (Diamond et al., 2015) at a distance of 20 Mpc. This is for an instrument with energy resolution  $\Delta E/E = 1\%$  and  $3\sigma$  sensitivity to narrow lines of  $10^{-6} \text{ ph cm}^{-2} \text{ s}^{-1}$  within 1 Ms. Twenty observation periods over 400 d are fitted – shown are six snapshots. The fitted SNeIa parameters and resulting line intensity profiles are shown in red. In the bottom panels, the black curves show the model 7p0z22d20\_27 distributions from which the simulated data were derived (from Leising, 2022).

of the redshifted side of the line. For multiple shells, one adds the optical depths at each line of sight velocity. This is the same for lines of different energies, except for the different Compton optical depths. As time progresses, the source functions decay – or, for  $^{56}\text{Co}$ , is fed by the parent decay and decays itself. The optical depths of all shells fall with time, as  $t^{-2}$ . Given the  $^{56}\text{Ni}$  abundance and total electron density versus radial velocity, all  $\gamma$ -ray line profiles are easily obtained for all times to first order. These can be compared directly to a series of measured spectra, or integrated over each line to be compared to line flux data. While it is not possible to invert the transfer process to get the  $^{56}\text{Ni}$  abundance and density profiles, it is possible to iteratively vary them to fit the observational data quite well.

The precision with which the SN properties can be determined is limited entirely by the measurement uncertainties, at least for most events for the foreseeable future. For these photon-limited measurements, the nearest SNeIa will be best understood:

For example, for a future wide-field instrument with narrow-line,  $3\sigma$  flux sensitivity of  $10^{-6}$  ph cm $^{-2}$  s $^{-1}$  within 1 Ms of observation time, and energy resolution  $\Delta E/E = 1\%$ , we can expect to measure the  $^{56}\text{Ni}$  mass to  $0.02 M_{\odot}$  accuracy, ejecta masses to  $0.1 M_{\odot}$ , and kinetic energies to  $0.3 \times 10^{51}$  erg, for a normally bright **SN Ia** similar to typical delayed detonation models, for a distance of 20 Mpc (Leising, 2022). The distribution of  $^{56}\text{Ni}$  with radial velocity can also be well recovered in such a measurement. An example of such a measurement is shown in Fig. 14 for a simulated event.

Even for instruments with similar line sensitivity, but several percent energy resolution, such as scintillators, which cannot determine the line profiles to high accuracy, the integrated line flux measurements can still provide nearly the same determination of **SNe Ia** parameters. In this case, good coverage of the light curve over at least several months is essential, and suggests that wide-field and/or scanning instruments are necessary. On the other hand, if  $\gamma$ -ray optics can be deployed to provide large collecting area for relatively small detectors, as in other wavelength bands, excellent sensitivity could be achieved. If combined with good energy resolution, just a few pointings before and after the  $\gamma$ -ray peak could reveal the underlying **SN Ia** characteristics.

#### 2.4.1.3 Other $\gamma$ -Ray Lines from Type Ia Radioactivity

Other potentially detectable isotopes from **SNe Ia** include  $^{57}\text{Co}$  and  $^{44}\text{Ti}$ , which offer key insights into nuclear burning conditions.  $^{57}\text{Co}$  (half-life 272 d) is produced as  $^{57}\text{Ni}$  (half-life 36 h) alongside  $^{56}\text{Ni}$ . It significantly powers late light curves, and the  $^{57}\text{Ni}/^{56}\text{Ni}$  ratio is at or above the solar value (0.023) in many models (e.g., Tiwari et al., 2022). Measuring  $^{57}\text{Ni}$  from late light curves is challenging and model-dependent. The  $^{57}\text{Co}$  122 keV  $\gamma$ -ray line can directly diagnose **SN Ia** burning in nearby events. For example, a **SN Ia** at 1 Mpc ejecting  $0.5 M_{\odot}$  of  $^{56}\text{Ni}$  with a solar  $^{57}\text{Ni}/^{56}\text{Ni}$  ratio would yield a flux of  $2.4 \times 10^{-5}$  ph cm $^{-2}$  s $^{-1}$  at one year post-explosion.

Although  $^{44}\text{Ti}$  and  $^{44}\text{Sc}$   $\gamma$ -ray lines are detected in **ccSNe**, they remain unconfirmed in thermonuclear remnants. An excess at 60–85 keV, possibly from the  $^{44}\text{Ti}$  decay (68 & 78 keV) in Tycho’s **SNR** (Troja et al., 2014), is unverified by other studies (e.g., Lopez et al., 2015; Weinberger et al., 2020). The broad range of  $^{44}\text{Ti}$  yields in **SN Ia** models makes it a strong diagnostic. Typically, yields are below  $10^{-4} M_{\odot}$  in Chandrasekhar models but can reach up to  $10^{-3} M_{\odot}$  in surface helium detonation or **WD** merger models (Woosley et al., 1986; Leung and Nomoto, 2020; Roy et al., 2022). Besides a few young **SN Ia** remnants, other undetected **SNe Ia** might show measurable  $^{44}\text{Ti}$ . For instance,  $10^{-3} M_{\odot}$  of  $^{44}\text{Ti}$  at 10 kpc could yield  $3 \times 10^{-6}$  ph cm $^{-2}$  s $^{-1}$  per line even after 500 yr.

For  $^{48}\text{V}$  ( $\gamma$ -ray lines at 983 and 1312 keV), only a few studies have searched its emission in nearby remnants. Panther et al. (2021), following Sim et al. (2012), set an upper limit on the  $^{48}\text{Cr}$  production in SN 2014J of  $\lesssim 0.1 M_{\odot}$ , roughly an order of magnitude above expectations. The  $^{48}\text{V}$  lines might reach  $10^{-4}$  ph cm $^{-2}$  s $^{-1}$  in **SNe Ia** at approximately 1 Mpc. These lines could be detected by next-generation telescopes with proper pointing strategies or a large fields of view (see Sec. 2.4.3).

#### 2.4.1.4 $\gamma$ -Ray Line Contributions to the Cosmic $\gamma$ -Ray Background

We refer to the Cosmic Gamma-Ray Background (CGB) as the diffuse, all-sky, and nearly isotropic emission observed between photon energies of  $\sim 100$  keV and several tens of MeV. Measurements by instruments such as HEAO1 (Kinzer et al., 1997; Gruber et al., 1999), SMM (Watanabe et al., 2000), COMPTEL (Weidenspointner et al., 2000), and INTEGRAL (Churazov et al., 2007; Türler et al., 2010) have shown that the spectrum in this range consists of a smoothly varying continuum that cannot be fully explained by resolved sources alone, implying a substantial contribution from faint or distant populations (The et al., 1993). The origin of the MeV CGB remains one of the central questions in high-energy astrophysics because the putative source types trace nucleosynthesis, compact-object formation, cosmic star formation, and the cosmological evolution. In general, several astrophysical source types may contribute to the CGB in this band: Potential candidates include active galactic nuclei (especially Seyfert galaxies), star-forming galaxies (e.g., Ueda et al., 2003; Inoue, 2014), SNe Ia (e.g., The et al., 1993), ccSNe (e.g., Chugai, 2023), compact object mergers such as BNSMs (Ruiz-Lapuente and Korobkin, 2020), radioactive isotopes ejected by stellar populations (Lacki et al., 2014), and more exotic origins such as DM annihilation or decay (e.g., Iguaz et al., 2021). Many of these source types produce  $\gamma$ -ray lines or Comptonised continuum emission that are redshifted and blended into a diffuse background when integrated over cosmic time.

SNe Ia are of particular interest because they produce large quantities of radioactive  $^{56}\text{Ni}$  and  $^{56}\text{Co}$ , whose  $\gamma$ -ray lines dominate the spectrum of young SNe Ia. Since SNe Ia serve as standardisable candles for cosmology (Arnett, 1982; Phillips, 1993), their rate evolution is well-studied and their contribution to the CGB directly encodes the cosmic history of stellar evolution and chemical enrichment (The et al., 1993). The emitted  $\gamma$ -rays undergo Compton scattering and absorption in the ejecta and intergalactic medium, and when redshifted across the Hubble flow they contribute to the MeV-band CGB. In general, the spectrum of the CGB from a cosmological source population is

$$I(E) = \frac{c}{4\pi} \int_0^{z_{\max}} \frac{R(z) L[E(1+z)]}{H(z)(1+z)} dz, \quad (42)$$

where  $R(z)$  is the comoving volumetric rate density of the source population,  $L(E)$  is the rest-frame photon luminosity spectrum per event, and  $H(z)$  is the Hubble expansion function (Timmes and Woosley, 1993). Eq. (42) applies to any transient population and makes explicit how the redshift distribution and intrinsic spectral models govern the CGB.

Historically, the first quantitative estimate of the SNe Ia contribution to the CGB was carried out by The et al. (1993), who modelled the  $\gamma$ -ray line emission from  $^{56}\text{Co}$  decay and folded these spectra through cosmic SNe Ia rate histories available at the time. Their result indicated that SNe Ia could provide a non-negligible fraction of the MeV background, although uncertainties in star formation and SNe Ia delay times left a large allowed range. Subsequent improvements in SNe Ia modelling led to updated CGB predictions (Watanabe et al., 1999). With improved radioactive-transfer simulations and updated cosmic rate measurements, the authors show that SNe Ia

alone likely fall short of explaining the entire MeV background. Later refinements (Ahn et al., 2005) incorporated better constraints on **SN Ia** delay-time distributions and emphasised that contributions peak around a few MeV but still remain below the observed intensity. Follow-up analyses (Lien and Fields, 2012) further strengthened this conclusion by combining new **SN Ia** rate measurements with modern cosmological parameters. Recent reviews of **SN Ia** progenitors and their environmental signatures (Ruiz-Lapuente et al., 2016) further emphasise that the diversity of explosion channels and circumstellar conditions directly impacts the  $\gamma$ -ray signal and thus the integrated CGB contribution. We show the example from Ruiz-Lapuente et al. (2016); Ruiz-Lapuente and Korobkin (2020) of **SN Ia** and other  $\gamma$ -ray lines contributions to the CGB in Fig. 15

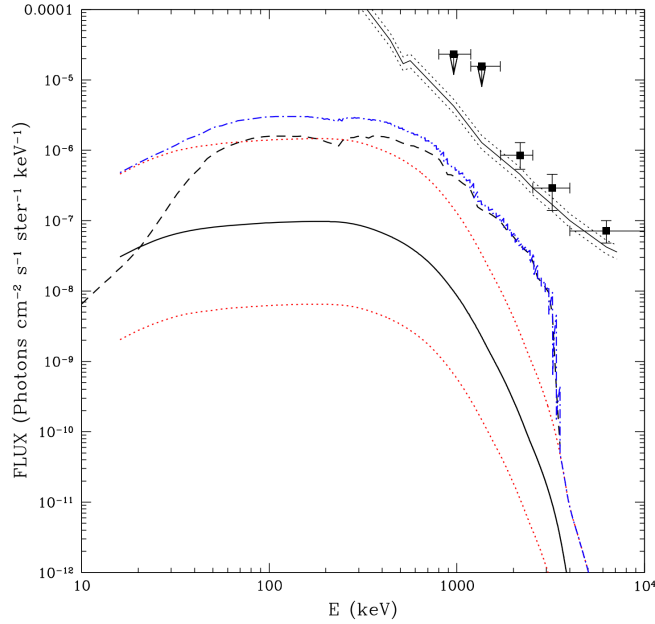


**Fig. 15** Comparison of the **SNe Ia** contribution (black dashed lines Ruiz-Lapuente et al., 2016) to the CGB (black data points) to the total emission expected from **BNSMs** (red dash-dotted), including both the kilonova and late-time remnant phases. The red dotted curves mark the corresponding upper and lower bounds arising from uncertainties in the **BNSM** ejecta masses (from Ruiz-Lapuente and Korobkin, 2020).

In addition to **SNe Ia**, **ccSNe** also produce  $\gamma$ -rays through radioactive isotopes such as  $^{56}\text{Ni}$ ,  $^{56}\text{Co}$ ,  $^{44}\text{Ti}$ , and longer-lived  $^{26}\text{Al}$  and  $^{60}\text{Fe}$ , plus potential *r*-process elements. However, the **ccSN** contribution to the MeV CGB is expected to be smaller than that of **SNe Ia** due to the heavier obscuration by massive stellar envelopes, which significantly delays and reduces  $\gamma$ -ray escape. Nevertheless, their high rate means **ccSNe** still form a baseline contribution to the MeV background across cosmic time (Chugai, 2023).

Compact-object mergers (e.g., **BNSMs**) generate radioactive ejecta responsible for kilonova emission, and these ejecta produce  $\gamma$ -ray lines from *r*-process nuclei (see Sec. 2.5). The bulk of this emission peaks in the X-ray and soft  $\gamma$ -ray domain and might be highly absorbed. Recent work by Ruiz-Lapuente and Korobkin (2020) suggests that **BNSMs** may still contribute a small (few percent) amount to the MeV **CGB**. These contributions remain highly uncertain because *r*-process heating, opacity, and ejecta composition vary significantly between merger models.

Possible contributions from local environments must also be considered in this context. The Local Bubble (Breitschwerdt et al., 1996) contains unresolved radioactive-emission sites such as from  $^{26}\text{Al}$  (1809 & 511 keV) or  $^{60}\text{Fe}$  (1173 & 1332 keV) whose contributions may be measurable already with next generation telescopes (Schulreich et al., 2023; Siegert et al., 2024). Similarly, a putative **DM** halo could contribute a large amount of positrons from its decay or annihilation, leading to a local 511 keV line (Iguaz et al., 2021). This line would contribute to the isotropic emission and imprint on top of the cosmological **CGB**, similar to the nuclear lines. Finally, the neutron capture line onto protons at 2224 keV throughout cosmic time may serve as a ‘hydrogen calorimeter’ if the thermalisation time of spallation neutrons is short enough (Ramaty and Lingenfelter, 1980, see also Sec. 3.2.1). Together, these components highlight that while **SNe Ia** remain the dominant and best-understood candidate among stellar explosions, a combination of multiple astrophysical and possibly exotic processes is required to explain the full MeV-band **CGB**.

#### 2.4.2 $\gamma$ -Ray Lines from Core-Collapse Supernovae

While there are at least 300 **SNRs** inside the Milky Way (Green, 2019), only one has been identified as being a  $\gamma$ -ray line source so far: the 350 yr old **SNR Cas A**. Several other candidates would match reasonable ages and distances to observe longer-lived isotopes, such as  $^{44}\text{Ti}$ , but which, so far, only resulted in upper limits. Prompt emission from the  $^{56}\text{Ni}$  decay chain has never been observed in a **SN** inside the Milky Way, but in one of its satellite galaxies: SN 1987A in the **LMC**. In SN 1987A, also the  $^{44}\text{Ti}$  lines have been detected (Boggs et al., 2015), making it a unique object to study over decades.

In this Section, we will discuss the two cases of SN 1987A (Sec. 2.4.2.1) and **Cas A** (Sec. 2.4.2.2), and list the most recent upper limits of other interesting **SNRs** according to Weinberger et al. (2020) in Tab. 3. In the light of these limits, it is clear that more sensitive instruments are required to solve the mystery of why there is only one  $^{44}\text{Ti}$  in the Milky Way so far (e.g., The et al., 2006, see also Sec. 2.4.3).

##### 2.4.2.1 SN 1987 A in the Large Magellanic Cloud

There are several studies that tried – and managed – to identify  $\gamma$ -ray lines (or hard X-ray emission associated with Compton-scattered  $\gamma$ -ray lines) from SN 1987A at early times after the initial explosion (e.g., Englhauser et al., 1989; Sunyaev et al., 1990; Matz et al., 1988; Sunyaev et al., 1987), together with theoretical expectations for this particular source (e.g., Grebenev and Syunyaev, 1987; Pinto and Woosley, 1988; Shigeyama and Nomoto, 1990; Arnett et al., 1989; Bussard et al., 1989, including multi-wavelength considerations). While it is important to acknowledge the vast ambitions

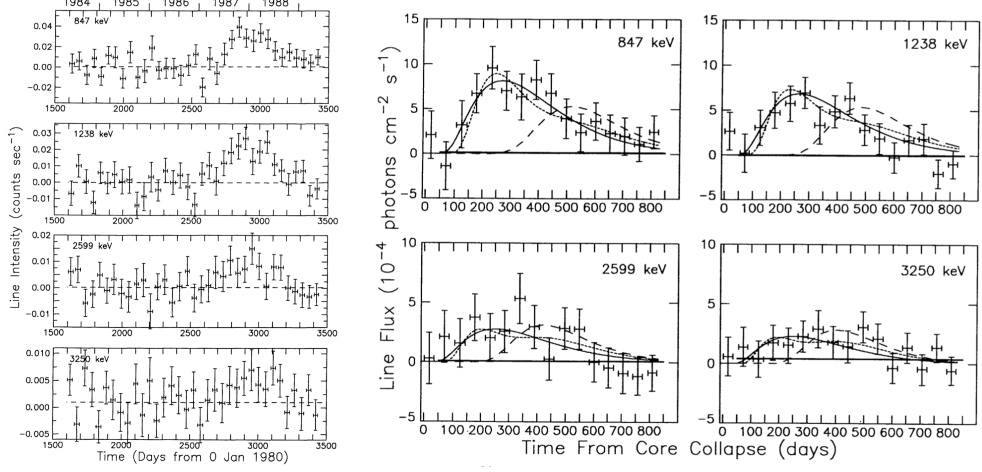


**Fig. 16** Left: Detection of SN 1987A in four  $\gamma$ -ray lines with **SMM/GRS** in counts per second. Right:  $\gamma$ -ray line fluxes of the  $^{56}\text{Co}$  decay in SN 1987A as a function of time, together with three model light curves (from [Leising and Share, 1990](#), see also main text).

and huge efforts to obtain reasonable measurements, a most comprehensive study of the  $^{56}\text{Ni}$  decay chain, and the associated  $\gamma$ -ray line light curves is given in [Leising and Share \(1990\)](#) about three years after the explosion (see also [Palmer et al., 1993](#)).

Besides the two prominent lines from the  $^{56}\text{Co}$  decay at 847 (99.9%) and 1238 keV (66.5%), the authors also extracted the light curves of the weaker 2599 (17.0%) and 3250 keV (7.9%) lines<sup>2</sup> using **SMM/GRS**. The **SMM** observations that include SN 1987A lasted 1984 until 1989 May, and used a background method based on occultation of the **LMC**, that is, an on-off method ([Li and Ma, 1983; Vianello, 2018](#)). From August 1987 to May 1988, the  $\gamma$ -ray line fluxes of the four lines were  $(8.0 \pm 0.9)$ ,  $(5.4 \pm 0.7)$ ,  $(2.6 \pm 0.7)$ , and  $(2.5 \pm 0.5) \times 10^{-4} \text{ ph cm}^{-2} \text{ s}^{-1}$ , respectively. All lines have been found at the instrumental resolution of **GRS**, and the line centroids are consistent with the expected laboratory energies. In Fig. 16, the light curves of the four lines are shown, first as identification in detector count units (left), and then comparing to models (right).

[Leising and Share \(1990\)](#) discuss three theoretical models for the four  $\gamma$ -ray line light curves, assuming an initial  $^{56}\text{Ni}$  mass of  $0.07 \text{ M}_\odot$  and a distance of 50 kpc. *Model 1* follows Eq. (38), where the opacity (or optical depth) decreases as  $t^{-2}$ . This model peaks too late and fails to match early measurements. This discrepancy suggests a range of optical depths rather than a single value. *Model 2* improves upon Eq. (38) by allowing two distinct  $^{56}\text{Co}$  abundances at different depths. It fits the light curves well by describing 95% of  $^{56}\text{Co}$  under an optical depth  $\tau_I = 200(100 \text{ d}/t)^2$  and 5% under  $\tau_{II} = 16(100 \text{ d}/t)^2$ , leading to an earlier rise and a longer decay. The lower  $\tau$  corresponds to a hydrogen mass of  $1 \text{ M}_\odot$  expanding at  $3000 \text{ km s}^{-1}$  (cf. Eq. (37)). Conceptually, this may represent two distinct  $^{56}\text{Ni}$  clumps displaced by mechanisms

<sup>2</sup>The 3250 keV should actually be at a laboratory energy of 3253 keV but which was not known to this accuracy at the time. Also, this line is not the fourth strongest in the  $^{56}\text{Co}$  decay, see Tab. 2

such as “jets” or “bubbles” in the remnant of SN 1987A. These 3D structures reappear in the measurements of Cas A (Sec. 2.4.2.2). *Model 3* assumes homogeneous mixing of  $^{56}\text{Co}$ , meaning outer layers emit earlier than inner ones. This model also fits the data well, although it may be somewhat unrealistic. The outer region’s column depth is equivalent to a hydrogen mass of  $0.33 M_{\odot}$  expanding at  $3000 \text{ km s}^{-1}$  (cf. Eq. (37)). Based on Fig. 16, this model requires very low early optical depths for  $^{56}\text{Co}$  and a thick inner region (massive or slowly moving) that obscures most of it, keeping the  $\gamma$ -ray line flux low at later times.

Measurements of the ejected  $^{57}\text{Ni}$  (via  $^{57}\text{Co}$   $\gamma$ -ray line observations) help locate the boundary between ejected and accreted matter – the “mass cut” (e.g., Thielemann et al., 1990; Woosley and Hoffman, 1991; Wang and Burrows, 2024). This is because the neutron-to-proton ratio increases toward the star’s centre. During the first three years, the  $^{57}\text{Co}$   $\gamma$ -ray lines at 122 and 136 keV from SN 1987A are undetectable due to high theee opacity, inferred from  $^{56}\text{Co}$  measurements. Fluxes of a few  $10^{-5} \text{ ph cm}^{-2} \text{ s}^{-1}$  are expected around 1000–1200 days post-explosion, corresponding to  $1.7 \times 10^{-3} M_{\odot}$ . Clayton et al. (1992) discuss individual measurements of  $^{57}\text{Co}$  decay  $\gamma$ -rays (Kurfess et al., 1992), showing higher fluxes than expected, typically factors of 2–3. After day 1000,  $^{57}\text{Co}$  becomes the dominant power source for the bolometric light curve until  $^{44}\text{Ti}$  takes over around day 2000. The  $^{57}\text{Ni}/^{56}\text{Ni}$  production ratio was found to be about five times the solar value. This implies roughly  $0.009 M_{\odot}$  of  $^{57}\text{Ni}$  in SN 1987A. Astrophysical models incorporating opacity, nucleosynthesis, ejecta mass, and velocity yield a  $^{57}\text{Ni}/^{56}\text{Ni}$  ratio of 1–3. Although these considerations partly reduce the overproduction, nucleosynthesis and chemical evolution still faced a major problem.

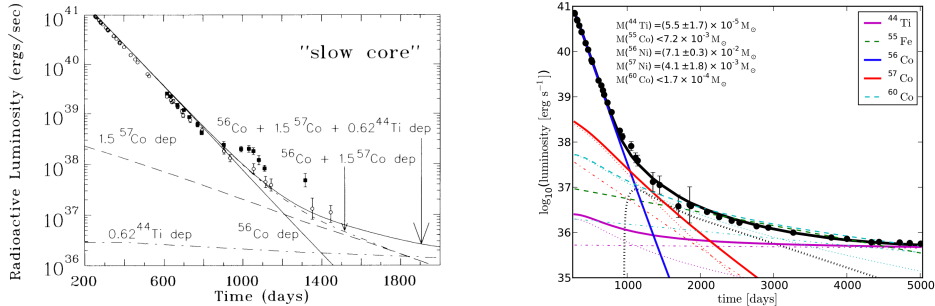


**Fig. 17** Bolometric light curves of SN 1987A up to day 1500 (left; from Clayton et al., 1992) and up to day 5000 (right; from Seitenzahl et al., 2014) after the explosion. Given the updated observations and information, the derived masses of the radioactivities change by factors of 2–3, except for  $^{56}\text{Ni}$ , being consistent with  $0.07 M_{\odot}$ .

In Fig. 17, the bolometric light curves with considerations at early times (Fu and Arnett, 1989; Clayton et al., 1992) as well as 14 years after the explosion (Seitenzahl et al., 2014) are shown<sup>3</sup>. It becomes evident that longer observations resulted in updates on the  $^{57}\text{Ni}$  mass, but not on the  $^{56}\text{Ni}$  mass. Seitenzahl et al. (2014) found a  $^{57}\text{Ni}$  mass of  $(4.1 \pm 1.8) \times 10^{-3} M_{\odot}$ , about 2–3 times smaller than the initial estimates.

<sup>3</sup>SN 1987A shows a re-brightening after that time due to shock heating.

In addition, they could estimate the mass of  $^{44}\text{Ti}$  to be around  $(5.5 \pm 1.7) \times 10^{-5} \text{ M}_\odot$ . This, however, is about six times smaller than obtained from **INTEGRAL/IBIS**  $\gamma$ -ray line measurements by [Grebenev et al. \(2012\)](#), finding  $(3.1 \pm 0.8) \times 10^{-4} \text{ M}_\odot$ . Finally, [Boggs et al. \(2015\)](#), utilising the Nuclear Spectroscopic Telescope Array (**NuSTAR**), found a  $^{44}\text{Ti}$  mass of  $(1.5 \pm 0.3) \times 10^{-4} \text{ M}_\odot$ . All these values do not agree, making it difficult to judge the actual nucleosynthesis happening inside SN 1987A without improved  $\gamma$ -ray line measurements.

The hard X-ray lines from SN 1987A reported by [Boggs et al. \(2015\)](#) show Doppler-shifts and -broadening corresponding to ejecta velocities of several thousand  $\text{km s}^{-1}$ , revealing high-speed radioactive material. These features are interpreted as signatures of an asymmetric explosion geometry with clumpy or plume-like structures transporting freshly synthesized  $^{44}\text{Ti}$  outward. This is similar to the highly solved **NuSTAR** picture from [Cas A](#) (Sec. 2.4.2.2), where spatially resolved  $^{44}\text{Ti}$  maps show strong velocity asymmetries that support such explosion dynamics. Because the 1157 keV  $\gamma$ -ray line of  $^{44}\text{Sc}$  would provide much higher spectral resolving power and therefore more precise constraints on ejecta kinematics, improved measurements of this line remain essential for advancing structural and dynamical studies in combination with nucleosynthesis yields.

#### 2.4.2.2 Cassiopeia A

The [Cas A SNR](#) is about 350 yr old (e.g., [Alarie et al., 2014](#)), so that certainly, no  $^{56}\text{Ni}$ ,  $^{56}\text{Co}$ ,  $^{57}\text{Ni}$ , or  $^{57}\text{Co}$  can be present in the still expanding remnant. Given the bolometric light curve, kinematic studies, and light echoes, the [Cas A](#)  $^{56}\text{Ni}$  mass was estimated to be around  $0.058\text{--}0.16 \text{ M}_\odot$  (e.g., [Eriksen et al., 2009](#)). At this age, however, a sizeable amount of  $^{44}\text{Ti}$  is still left to decay, about 2% of the initial ejecta mass, so that the flux today should be on the order of  $10^{-5} \text{ ph cm}^{-2} \text{ s}^{-1}$  (see Eq. (39)). Indeed, fluxes measured from [Cas A](#) within the last 20 years range from  $(1.0\text{--}12.5) \times 10^{-5} \text{ ph cm}^{-2} \text{ s}^{-1}$  (e.g., [Siegert et al., 2015](#); [Tsygankov et al., 2016](#); [Wang and Li, 2016](#); [Grefenstette et al., 2017](#); [Weinberger et al., 2020](#), see also Tab. 3). Within this period, the  $^{44}\text{Ti}$   $\gamma$ -ray line flux should have decreased by 20%, which is not enough to explain the variations of the line measurements. It appears that the high-energy  $\gamma$ -ray line at 1157 keV from the  $^{44}\text{Sc}$  decay to stable  $^{44}\text{Ca}$  appears systematically stronger than the  $^{44}\text{Ti}$  decay lines at 68 and 78 keV to  $^{44}\text{Sc}$  ([Siegert et al., 2015](#)). This can be interpreted in several ways, of which we outline three in the following.

[Siegert et al. \(2015\)](#) found an enhanced flux of the 1157 keV line relative to the 78 keV line in **SPI** data. [Weinberger et al. \(2020\)](#) reanalysed over five additional years of data and indicated that the high-energy line was previously misinterpreted, implying an even higher flux. The 78 keV line maintained a similar flux, consistent with **NuSTAR** and **IBIS** measurements of  $(1.0\text{--}3.2) \times 10^{-5} \text{ ph cm}^{-2} \text{ s}^{-1}$ . Although **COMPTEL** and **SPI** were the only instruments to measure the high-energy line until 2025, this flux difference hints at possible astrophysical effects: Stable  $^{44}\text{Ca}$  could be excited by **LECRs** and de-excite, emitting only the 1157 keV line (see also Sec. 2.6). Since  $^{44}\text{Sc}$  is very short-lived (4 h), no de-excitation  $\gamma$ -rays lines at 68 or 78 keV are expected ([Siegert et al., 2015](#)). Although plausible, this scenario would require a  $^{44}\text{Ca}$  density in [Cas A](#) that is orders of magnitude higher than typically observed. Furthermore, other lines

**Table 3** Astrophysical parameters for the most promising SNRs for detections of  $^{44}\text{Ti}$ , together with measured values and upper limits. The age of the remnant is given for 01.01.2011 AD, which was the average observation date in this study. Age uncertainties of the time bin are included in the mass estimates. Distance to Vela Jr. is estimated from  $^{44}\text{Ti}$  yields. Distance to G1.9+0.3 is estimated from absorption towards the Galactic centre. Exposure is dead time corrected, effective SPI exposure. Alternative flux measurements with NuSTAR and IBIS are also shown (adapted from Weinberger et al., 2020, see also references therein).

	Cas A	SN 1987A	Vela Jr.	Tycho	Kepler	G1.9+0.3
Distance [kpc]	$3.3 \pm 0.1$	$49.6 \pm 0.5$	0.2	$4.1 \pm 1$	$5.1^{+0.8}_{-0.7}$	8.5
Explosion Date	1681	1987	$\sim 1320$	1572	1604	1890
Age [yr]	330	24	690	438	406	120
Type	IIb	II-P	II	Ia	Ia	Ia
Exposure [Ms]	11.2	7.0	8.3	10.3	29.3	30.6
Gal. Cor. $l, b$ [deg]	111.7, -2.1	279.7, -31.2	266.3, -1.21	120.1, 1.4	4.5, 6.8	1.9, 0.3
Flux $^{44}\text{Sc}$ [ $10^{-5}$ ph cm $^{-2}$ s $^{-1}$ ]	$9.5 \pm 3.0$	$< 4.1$	$< 4.7$	$< 6.2$	$< 2.6$	$< 3.7$
Flux $^{44}\text{Ti}$ [ $10^{-5}$ ph cm $^{-2}$ s $^{-1}$ ]	$3.3 \pm 0.9$	$< 1.9$	$< 2.8$	$< 1.5$	$< 1.3$	$< 1.1$
Flux Combined [ $10^{-5}$ ph cm $^{-2}$ s $^{-1}$ ]	$4.2 \pm 1.0$	$< 1.8$	$< 2.1$	$< 1.4$	$< 1.1$	$< 1.0$
Mass Combined [ $10^{-4} M_{\odot}$ ]	$2.6 \pm 0.6$	$< 6.9$	$< 0.3$	$< 4.8$	$< 4.0$	$< 0.3$
- - - - -						
NuSTAR [ $10^{-5}$ ph cm $^{-2}$ s $^{-1}$ ]	$1.8 \pm 0.3$	$0.35 \pm 0.07$	—	$< 1.0$	—	$< 1.5$
NTEGRAL/IBIS [ $10^{-5}$ ph cm $^{-2}$ s $^{-1}$ ]	$1.3 \pm 0.3$	$1.7 \pm 0.4$	$< 1.8$	$< 1.5$	$< 0.63$	$< 0.9$

(e.g., from stable  $^{56}\text{Fe}$  in the  $^{56}\text{Ni}$  decay chain) should exhibit a stronger de-excitation flux, but is not observed. The  $3\sigma$  upper limit on the 847 keV line from Cas A is approximately  $5 \times 10^{-5}$  ph cm $^{-2}$  s $^{-1}$  for a 4 keV (FWHM) line (Weinberger, 2021). That study also set a flux limit on the  $^{12}\text{C}$  line at 4.4 MeV (94 keV FWHM) of  $5 \times 10^{-5}$  ph cm $^{-2}$  s $^{-1}$ , compared to an expected  $\sim 10 \times 10^{-5}$  ph cm $^{-2}$  s $^{-1}$  (Summa et al., 2011, see, however, (Liu et al., 2023)). This discrepancy has implications for the LECR spectrum and the density structure of the SNR (see also Sec. 2.6). Consequently, the CR excitation scenario is ruled out.

Another plausible explanation would be an increased absorption of the lower energy lines. Two thirds of dust in the Milky Way are probably produced by ccSNe (McKinnon et al., 2016), so that an enhanced dust production in Cas A could alter the LoS fluxes beyond the expected branching ratios. The attenuation coefficients for the 1157 keV line compared to the 68 and 78 keV lines, considering different dust species, are about a factor of 3–12 smaller (Iyudin et al., 2019). This directly impacts the measured flux values, and could lead to a fraction of 16–80% of the low-energy line fluxes being absorbed by dust (Weinberger et al., 2020). This scenario appears more realistic, but cannot be proven without further measurements of the high-energy line, for example with COSI (Tomsick et al., 2024).

The third, and probably most realistic, scenario is a mixture of systematic uncertainties, wrong assumed line profiles such as the typically used Gaussians vs. the more appropriate tophat function which might overestimate the fluxes (Weinberger et al., 2020), and absorption. Nuclear excitation of the  $^{44}\text{Ca}$  line does happen, but its  $\gamma$ -ray line flux would be orders of magnitude below the measured values.

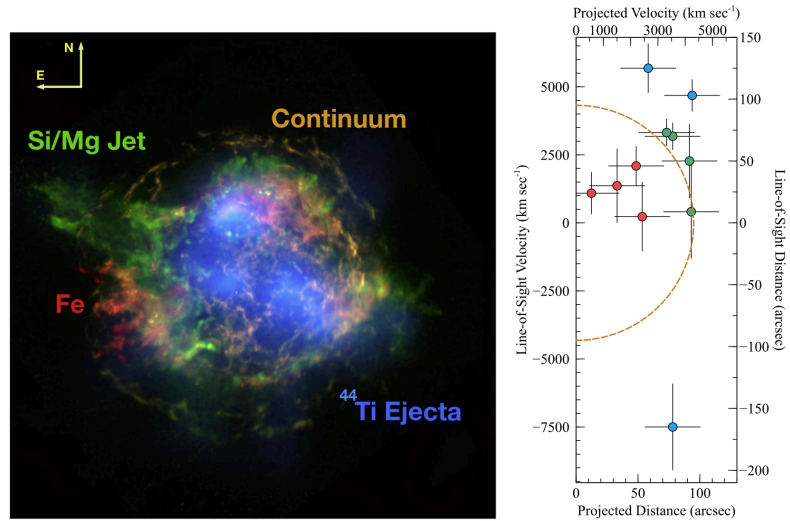


**Fig. 18** Left: Spatial distribution of  $^{44}\text{Ti}$  (blue) in Cas A as measured with NuSTAR, compared to other X-ray features. The ratio in the Si/Mg band highlights the NW/SW ‘jet’ structure in green. Image credit: Robert Hurt, NASA/JPL-Caltech (from Grefenstette et al., 2014, 2017). Right: Doppler velocity measurements of  $^{44}\text{Ti}$  clumps along the LoS in Cas A. The reverse shock radius is marked by the golden dashed curve at 95 arcsec projected distance (from Grefenstette et al., 2017).

Cas A’s age and proximity enable measurements of line fluxes, bulk motion, and broadening. With NuSTAR’s focussing optics,  $^{44}\text{Ti}$  clumps can be mapped (see Fig. 18), revealing a structured line profile that is neither purely Gaussian nor tophat-like. The clumpiness in Cas A extends along the jet axis, as seen in Si and Mg X-ray emissions and fast optical knots. Most  $^{44}\text{Ti}$  clumps are concentrated near the expansion center, with 80% located inside the reverse shock radius (Grefenstette et al., 2014). Theoretical  $^{44}\text{Ti}$  and  $^{56}\text{Ni}$  line profiles can be compared to observations to identify “jetted” or “clumpy” structures, revealing the explosion physics (e.g. Vance et al., 2020; Orlando et al., 2021). 3D SN models, especially for Cas A (2017; Wongwathanarat et al., 2017), can be used to test the previously conjectured “inverted” nucleosynthesis ejecta (see Hwang et al., 2004). See the Chapter on explosions in this volume for further details on SN modelling.

Clearly, Cas A appears as an exceptional SNR because the measured fluxes suggest an otherwise never seen  $^{44}\text{Ti}$  ejecta mass of  $(1.0\text{--}2.0) \times 10^{-4} M_{\odot}$ . Typical ccSNe model calculations suggest an order of magnitude less  $^{44}\text{Ti}$  ejecta, and only models with asymmetries show masses of up to  $10^{-4} M_{\odot}$  (e.g., Wongwathanarat et al., 2017; Maeda and Nomoto, 2003; Seitzenzahl et al., 2013; Fink et al., 2010, 2014, also including SNeIa models). However, the question “Are  $^{44}\text{Ti}$ -producing supernovae exceptional?” (The et al., 1996) can be answered by Hinchliffe’s rule<sup>4</sup> because also SN 1987A appears to have a large  $^{44}\text{Ti}$  mass (Boggs et al., 2015). On the other hand, the Vela Jr. SNR appears to have an at least five- to tenfold smaller  $^{44}\text{Ti}$  yield,

<sup>4</sup>According to a large online encyclopedia, the concept known as *Hinchliffe’s rule*, after physicist Ian Hinchliffe, states that if a research paper title is in the form of a yes-no question, the answer to that question will probably be “no”.

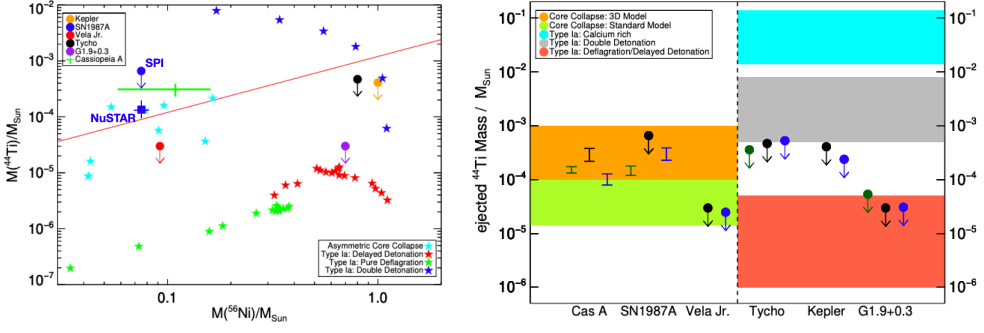


**Fig. 19** Left: Measured  $^{56}\text{Ni}$  vs.  $^{44}\text{Ti}$  yields for different SNRs (also SNe Ia), compared to different model calculations. The red line marks the solar  $^{44}\text{Ca}/^{56}\text{Fe}$  ratio ( $1.2 \times 10^{-3}$ ; Anders and Grevesse, 1989), which is used as a reference criterion to judge supernova model subtypes. Upper limits from SPI are shown as filled circles, measurements (Cas A only) by the green cross, and NuSTAR measurements by a blue square (adapted from Weinberger et al., 2020). Right: Comparison of  $^{44}\text{Ti}$  ejecta masses from different measurements (black: SPI; green: NuSTAR; blue: INTEGRAL/IBIS) in ccSNe (left) and SNe Ia (right) (from Weinberger et al., 2020).

although the source is much closer than Cas A, however at an age of almost 700 yr. The distance information on Vela Jr. is vague and ranges from 0.2 kpc up to more than 0.5 kpc, which would change the expected flux from  $(1\text{--}2) \times 10^{-5} \text{ ph cm}^{-2} \text{ s}^{-1}$  to almost  $10 \times 10^{-5} \text{ ph cm}^{-2} \text{ s}^{-1}$  (Eq. (39)). The latter is excluded by INTEGRAL measurements (Tab. 3), so that either the distance is larger than 0.2 kpc or the  $^{44}\text{Ti}$  ejecta mass is significantly smaller than for Cas A and SN 1987A. Both scenarios could be investigated by a more sensitive instrument, such as COSI (Tomsick et al., 2024). For more information about  $^{44}\text{Ti}$  nucleosynthesis, including  $\alpha$ -rich freeze-out, we refer the reader to the Chapter on Explosions.

Finally, upper limits obtained for the three youngest SNe Ia exclude the double detonation model and faint SN 2005E-like scenarios (Weinberger et al., 2020, see also Sec. 2.4.1).

#### 2.4.3 Future Prospects of Supernova Observations

While numerous  $\gamma$ -ray instruments with line sensitivity goals near  $10^{-6} \text{ ph cm}^{-2} \text{ s}^{-1}$  within 1 Ms have been proposed over the past three decades, none have been, or are currently being, realised. Such an instrument would revolutionise our measurements of the basic quantities defining SNe. However, COSI (Tomsick et al., 2024) is being developed by NASA for launch in 2027. It is a relatively small instrument whose strength is a wide field and nearly continuous coverage of the entire sky, which are particularly well suited to studying broadly distributed Galactic  $\gamma$ -ray lines and continuum, as well as transients. COSI's sensitivity requirements are  $(2\text{--}3) \times 10^{-5} \text{ ph cm}^{-2} \text{ s}^{-1}$ , with energy resolution below 1% for each of the most prominent SN  $\gamma$ -ray lines. With multiple lines and good coverage of the light curve peak, COSI should clearly detect  $^{56}\text{Co}$  in approximately one SNe Ia per year. With some good fortune, SNe Ia at the distances of, e.g., SN 2011fe and SN 2014J could be characterised in unprecedented detail.

In the case of [ccSNe](#), these sensitivities still only reach the Milky Way, plus 100 kpc. For more  $^{44}\text{Ti}$  [γ-ray](#) line measurements, a sensitivity of  $\lesssim 10^{-5} \text{ ph cm}^{-2} \text{ s}^{-1}$  would be required. Taking into account the line broadening, a ‘narrow line sensitivity’ closer to  $10^{-6} \text{ ph cm}^{-2} \text{ s}^{-1}$  is necessary to study more than three [SNRs](#). A Galactic [ccSN](#) would allow us to study not just three isotopes but potentially the whole list in Tab. 2. Such observations would be unique and would revolutionise our understanding of [ccSNe](#).

## 2.5 Nuclear $\gamma$ -Ray Lines from *r*-Process Sources

Written by Meng-Ru Wu

### 2.5.1 *r*-Process Nucleosynthesis

Nearly half of elements heavier than iron in nature are produced by the so-called rapid neutron capture nucleosynthetic process (*r* process). This often occurs in a dynamically evolving environment associated with astrophysical explosions, where matter expands from high density (baryonic mass density  $\rho \gtrsim \mathcal{O}(10^{10}) \text{ g cm}^{-3}$ ) and/or high temperature ( $k_B T \gtrsim \mathcal{O}(1) \text{ MeV}$ ) (Cowan et al., 2021). Due to expansion, the nuclear composition of matter drops out of reaction equilibrium, allowing nuclear transmutation to occur. At the beginning of the *r* process, the number density of free neutrons in the environment not only needs to be much higher than that of “seed nuclei” (nuclei whose mass number is  $A \sim 50\text{--}100$ ), but also high enough so that a number of neutron captures by the seed nuclei can take place before the produced unstable nuclei undergo  $\beta$ -decay. Through the nuclear transmutation sequence consisting of neutron captures followed by  $\beta$ -decays, very neutron-rich heavy nuclei up to  $A \sim 300$  can be synthesised until nuclear fission prevents further build-up of even heavier nuclei. The *r* process ends when the free neutron number density becomes too low, so that neutron captures become inefficient compared to nuclear decays. From that point onward, the produced *r*-process unstable nuclei gradually decay back toward nuclear stability, forming the heavy isotopes that are eventually identified at Earth, in meteorites, and in stars.

Although the basic theoretical understanding of how an *r* process occurs outlined above is rather well established, key questions regarding exact astrophysical sites and the associated conditions, as well as the involved nuclear physics properties, remain to be answered (Cowan et al., 2021). Among all proposed astrophysical sites (see Tab. 5), including the BNSMs (Eichler et al., 1989), neutron star (NS)–BH mergers (Lattimer and Schramm, 1974), neutrino-driven winds from ccSNe (Woosley et al., 1994), magneto-rotational supernovae (MRSNe) (Winteler et al., 2012), phase-transition supernovae (PTSNe) (Fischer et al., 2020), common envelope jet supernovae (CEJSNe) (Grichener and Soker, 2019), collapsars (Siegel et al., 2019), and more recently magnetar giant flares (GFs) (Cehula et al., 2024), the BNSMs are the only unambiguously confirmed sources through the multimessenger detection of gravitational waves,  $\gamma$ -rays, and the kilonova emissions associated with the GW170817 event at  $\sim 40 \text{ Mpc}$  away in 2017 (Abbott et al., 2017a,b). This confirmation is primarily based on the large opacity required to account for the infrared kilonova emissions on a timescale of  $\sim \mathcal{O}(10) \text{ d}$  after the merger. Advancements in extracting specific emission and absorption features associated with particular *r* process elements have been made in recent years (e.g., Watson et al., 2019; Domoto et al., 2022; Sneppen and Watson, 2023; Gillanders et al., 2024; Hotokezaka et al., 2023). However, they are still subject to large theoretical uncertainties originating from the complicated spatial and temporal evolution of the merger ejecta as well as the associated modelling of radiative transfer. A potential production of *r*-process elements in the magnetar GF SGR 1806-20 has been recently proposed (Patel et al., 2025). This claim is based on the observed late-time MeV emission peaked at  $\sim 10^3 \text{ s}$  after the prompt  $\gamma$ -ray spike. The late-time emission may be powered by the  $\gamma$ -rays from the radioactive decay of *r*-process nuclei from  $\sim 10^{-6} \text{ M}_\odot$ .

of material with velocities around  $\sim 0.15c$  ejected by crustal shocks (Winteler et al., 2012). If such an association is confirmed in the future, magnetar GFs may contribute up to  $\sim 10\%$  to the Galactic  $r$ -process inventory.

The  $\gamma$ -ray or X-ray lines emitted from decay of  $r$  process nuclei in live  $r$ -process producing events or in their remnants, if detected when the environment become  $\gamma$ -ray transparent, will not only be able to offer definitive proof of  $r$  process production within these sites, but also provide an independent tool to probe the nucleosynthesis conditions (Meyer and Howard, 1991; Qian et al., 1998, 1999; Ripley et al., 2014; Hotokezaka et al., 2016; Li, 2019; Wu et al., 2019; Korobkin et al., 2019; Wang et al., 2020; Chen et al., 2021; Terada et al., 2022; Chen et al., 2022; Vassh et al., 2024; Chen et al., 2024; Amend et al., 2025; Patel et al., 2025; Liu et al., 2025). In the following sections, we briefly summarise the most prominent  $r$ -process  $\gamma$ -ray lines from the decay of  $r$ -process nuclei from different sources, and discuss their implications.

### 2.5.2 $\gamma$ -Rays from Individual $r$ -Process Sources

For a single  $r$ -process source located at a distance  $d$  from Earth, the  $\gamma$ -ray line flux from the decay of a single radioactive nuclear species  $i$  with life time  $\tau_i$  at a post-production time  $t \ll \tau_i$  is given by Eq. (15), such that

$$F_\gamma^s \simeq 10^{-7} \text{ ph cm}^{-2} \text{ s}^{-1} I_\gamma \left( \frac{M_i}{3 \times 10^{-4} M_\odot} \right) \left( \frac{d}{10 \text{ kpc}} \right)^{-2} \left( \frac{\tau_i}{10^5 \text{ yr}} \right)^{-1}, \quad (43)$$

where  $I_\gamma$  is the  $\gamma$ -ray emission intensity at a specific energy,  $N_A$  is Avogadro's number, and  $M_i$  is the mass of the species  $i$ , assuming  $A_i \sim 100$ .

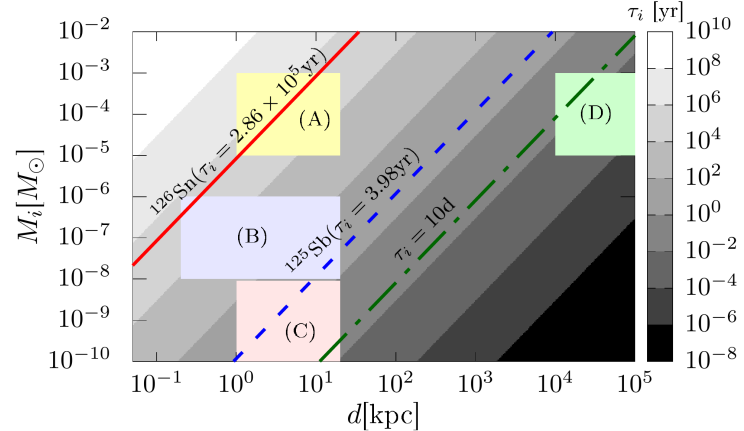


**Fig. 20** Contour plot of  $\tau_i(M_i, d)$  obtained using Eq. (43) for  $F_\gamma^s = 10^{-7} \text{ ph cm}^{-2} \text{ s}^{-1}$ . The red solid, blue dashed, and green dash-dotted lines are for the nuclei  $^{126}\text{Sn}$ ,  $^{125}\text{Sb}$ , and an assumed one with  $\tau_i = 10 \text{ d}$ , respectively. The yellow, blue, pink, and green shaded areas indicate the possible range of source distances and the amount of  $\gamma$ -ray emitting nuclei produced in (A) Galactic BNSM remnants, (B) Galactic ccSNe, (C) Galactic magnetar GFs, and (d) extragalactic BNSMs.

Fig. 20 shows the contour plot of  $\tau_i(M_i, d)$  obtained using Eq. (43) for  $F_\gamma^s = 10^{-7} \text{ ph cm}^{-2} \text{ s}^{-1}$ . Also plotted are the curves from considering particular  $\gamma$ -ray emitting nuclei:  $^{126}\text{Sn}$  ( $\tau_i = 2.9 \times 10^5 \text{ yr}$ ),  $^{125}\text{Sb}$  ( $\tau_i = 4 \text{ yr}$ ), and an assumed nucleus with  $\tau_i = 10 \text{ d}$ . The shaded rectangle areas indicate the approximate estimated range of source distances and the amount of  $\gamma$ -ray emitting nuclei that may be produced in Galactic and extragalactic BNSMs (Wu et al., 2019), ccSNe (Qian et al., 1998), and Galactic magnetar GFs (Patel et al., 2025). Clearly, for nuclei with  $\tau_i \sim \mathcal{O}(1) \text{ yr}$ , it requires a Galactic event that produces  $M_i \gtrsim 10^{-8} M_\odot$  to reach a line flux above  $10^{-7} \text{ ph cm}^{-2} \text{ s}^{-1}$ , overlapping with the potential production sources of ccSNe and nearby magnetar GFs. For nuclei with a longer lifetime of  $\tau_i \sim \mathcal{O}(10^5) \text{ yr}$ , the required mass needs to be proportionally higher, reaching  $M_i \sim \mathcal{O}(10^{-4}) M_\odot$  to satisfy the same criteria. Since the maximal value of  $M_i$  is typically smaller than  $\sim 0.1 M_{\text{ej}}^r$ , only BNSMs, NS-BH mergers, CEJSNe, and collapsars that may produce large enough value of  $M_{\text{ej}}^r$  are good candidates (Tab. 5).

For an extragalactic event with  $d \sim \mathcal{O}(10 - 100) \text{ Mpc}$ ,  $\gamma$ -ray emissions from nuclei with  $\tau_i \lesssim \mathcal{O}(10) \text{ days}$  in BNSM ejecta or NS-BH mergers may reach the level of  $F_\gamma \sim \mathcal{O}(10^{-7}) \text{ ph cm}^{-2} \text{ s}^{-1}$ . However, due to the high velocity of merger ejecta reaching  $\mathcal{O}(10^{-1}) c$  as well as the many lines from  $\mathcal{O}(10-30)$  different species of nuclei that can decay to produce  $\gamma$ -rays across a wide energy range, the lines are expected to be broadened and mixed into a continuum (e.g., Hotokezaka et al., 2016; Li, 2019; Korobkin et al., 2019). For other sources associated with massive stars that may produce large enough amount of  $M_{\text{ej}}^{(r)}$ , the ejecta environments are not expected to become  $\gamma$ -ray transparent yet in days.

After the multimessenger detection of GW170817 (Abbott et al., 2017a,b), confirming that BNSMs are likely the dominant source for the  $r$ -process inventory, particular attention has been paid to the potential detectability of  $\gamma$ -rays lines from the decay of  $^{126}\text{Sn}$  at 414.7, 666.3 and 695.0 keV in BNSM remnants whose ages are around  $\sim \mathcal{O}(10^5) \text{ yr}$  in the Milky Way (Wu et al., 2019; Terada et al., 2022; Patel et al., 2025). These studies were done by sampling over assumed occurring frequency of mergers as well as their spatial distributions in the Milky Way (cf. Sec. 2.1). Despite different assumptions made for the spatial distributions and the nuclear composition of the merger ejecta, they all suggest that it will require a wide field of view  $\gamma$ -ray mission with a line sensitivity reaching the level of  $10^{-7} \text{ ph cm}^{-2} \text{ s}^{-1}$  in order to have a non-negligible chance to detect the  $^{126}\text{Sn}$  decay  $\gamma$ -rays from at least one merger remnant in Milky Way. However, it should be noted that it may remain possible that one or a few recorded nearby ( $\lesssim 3 \text{ kpc}$ ) or young ( $\lesssim 10^4 \text{ yr old}$ ) “SN remnants” are in fact disguised merger remnants. In this case, a potential discovery may be possible with a line sensitivity of  $\sim 10^{-6} \text{ ph cm}^{-2} \text{ s}^{-1}$  (Wu et al., 2019; Korobkin et al., 2019; Terada et al., 2022; Chen et al., 2024). The co- or non-detection of the  $\gamma$ -ray lines at 351.9 and 609.3 keV from the decay chain of  $^{230}\text{Th}$  ( $\tau_i = 1.1 \times 10^5 \text{ yr}$ ) or the hard X-rays at 74.7 keV from the decay chain of  $^{243}\text{Am}$  ( $\tau_i = 1.1 \times 10^4 \text{ yr}$ ) can possibly offer unique insights on the nucleosynthesis condition associated with the remnant (Wu et al., 2019; Terada et al., 2022). The amount of the actinide production in any  $r$ -process sites sensitively depends on the neutron richness of the ejecta. Moreover, a co- or non-detection

of the 1332 keV line from the decay of  $^{60}\text{Co}$  may further help reveal the nature of the progenitor events (Ripley et al., 2014; Liu et al., 2025).

If the line sensitivity of  $\gamma$ -rays in future missions can be much improved to reach the level of  $10^{-8} \text{ ph cm}^{-2} \text{ s}^{-1}$ , then it should be possible to detect the  $^{126}\text{Sn}$  emission from  $\gtrsim \mathcal{O}(10)$  merger remnants (Wu et al., 2019). Such detections could provide important clues on the property of NS binaries that eventually lead to detectable mergers, and probe the variation of the nucleosynthesis conditions in  $r$ -process sites. With such a much improved sensitivity, one can expect to answer whether  $\gamma$ -ray emitting  $r$ -process nuclei are produced in the next Galactic ccSN explosion (Qian et al., 1998) or even in magnetar GFs.

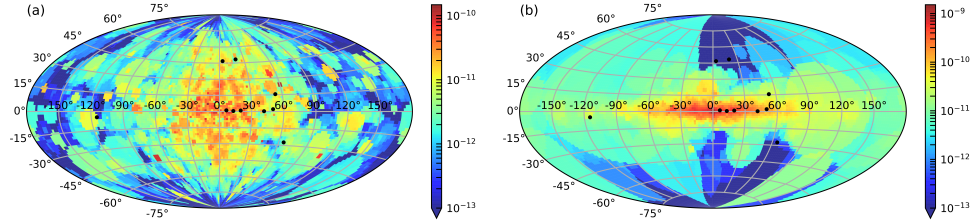


**Fig. 21** Example flux map from the 1.121 MeV decay line of  $^{182}\text{Hf}$  (in units of  $\text{ph cm}^{-2} \text{ s}^{-1} \text{ deg}^{-2}$ ), shown separately for (a) remnant location sampled by following a drift distance distribution similar to known short  $\gamma$ -ray bursts, and (b) following stellar density distributions (from Wu et al., 2019).

### 2.5.3 Diffuse Extended $r$ -Process $\gamma$ -Ray Emission

For the Galactic  $\gamma$ -ray sources, if the lifetime of a specific nucleus  $\tau_i$  is much longer than the inverse of the occurring frequency of the source in the Milky Way  $f_{\text{MW}}^{-1}$ , emissions from individual sources may no longer be separated, due to the fact that many sources are contributing at the same time, similar to the case of  $^{26}\text{Al}$  in massive stars or  $^{22}\text{Na}$  in CNe. In this scenario, the corresponding emission can be considered as “diffuse” emission (Qian et al., 1998; Wu et al., 2019). Since  $f_{\text{MW}}^{-1} \ll \tau_i$ , the total amount of decaying nuclei in the Milky Way at any given moment can be estimated by  $N_d \approx \bar{N}_s \tau_i f_{\text{MW}}$ , where  $\bar{N}_s = N_A \bar{M}_i / A_i$  is the average amount produced per source. Taking  $\bar{d}$  as the average source distance, the diffuse  $\gamma$ -ray flux integrated over the full sky can be estimated by

$$F_\gamma^d \simeq 10^{-7} \text{ ph cm}^{-2} \text{ s}^{-1} I_\gamma \left( \frac{\bar{M}_i}{3 \times 10^{-4} \text{ M}_\odot} \right) \left( \frac{f_{\text{MW}}}{10^5 \text{ yr}} \right), \quad (44)$$

for  $A_i = 100$  and  $\bar{d} = 10 \text{ kpc}$ .

Looking at Eq. (44), it readily tells us an interesting fact that the diffuse flux does not depend on the lifetime of the nuclei, but is mainly determined by the produced amount per source and the occurring source frequency. Moreover, it implies an even more interesting point as follows: Assuming that one unknown single source class dominates the production of the  $r$ -process nuclei in the Milky Way, but all possible

sources' occurring frequency satisfy  $\tau_i \gg f_{\text{MW}}^{-1}$ , then the all-sky diffuse  $\gamma$ -ray flux from nucleus  $i$  will be nearly independent of the nature of the source. This is because  $\bar{M}_i f_{\text{MW}}$  is nearly a constant, which is constrained by the known amount of all  $r$ -process elements produced over the lifetime of Milky Way. This is precisely the case for the diffuse  $\gamma$ -rays from the decay of  $^{182}\text{Hf}$  with a lifetime of  $1.3 \times 10^7$  yr, much longer than the estimated  $f_{\text{MW}}^{-1}$  for most of the  $r$ -process sources listed in Tab. 5. Thus, the estimated all-sky  $^{182}\text{Hf}$   $\gamma$ -ray line flux from, for example, ccSNe (Qian et al., 1998) and from BNSMs (Wu et al., 2019) at 0.270 or 1.121 MeV both range around  $10^{-8} \text{ ph cm}^{-2} \text{ s}^{-1}$ .

On the other hand, the spatial distribution of the  $r$ -process sources intuitively affects the angular distribution of the diffuse flux. For sources that track the stellar density profile of Milky Way, such as ccSNe and collapsars, the resulting diffuse sky maps should concentrate in the region of the Milky Way's disk, similar to the measured emission from  $^{26}\text{Al}$  and  $^{60}\text{Fe}$ . If BNSMs are the dominant source of the  $r$  process and the progenitor NS binaries had received substantial kick velocities at birth, then the corresponding diffuse sky map can extend to high latitude (see Fig. 21).

For  $^{126}\text{Sn}$  decay  $\gamma$ -ray lines, they are considered the best target to detect individual  $r$ -process sources if they were produced in BNSMs. However, if a much more frequent source such as ccSNe can produce them with much smaller amount in each, their all-sky  $\gamma$ -ray flux may be able to reach the level of  $10^{-7} \text{ ph cm}^{-2} \text{ s}^{-1}$  (Qian et al., 1998) if ccSNe account for the majority of  $r$ -process abundances in the Milky Way. Although such a scenario is currently disfavoured (Cowan et al., 2021), this argument indicates that such a consideration may be used to set an independent and meaningful limit on the amount of  $r$ -process production from ccSNe by the non-detection of diffuse  $\gamma$ -ray line emissions from  $^{126}\text{Sn}$  in the future, before the next Galactic ccSN happens.

**Table 4** Selected list of relevant  $\gamma$ -ray or hard X-ray lines from  $r$ -process nuclei mentioned in this work. For lines produced via shorter-lived nuclei inside the decay sequences from a parent isotope, the name of those nuclei are given inside the parenthesis next to the line energy (see Qian et al., 1998; Wu et al., 2019; Terada et al., 2022, for complete lists of potentially relevant nuclei).

Isotope	Decay channel	$\tau_i$ (yr)	Line energy [keV]	Intensity (%)
$^{125}\text{Sb}$	$\beta$ to $^{125}\text{Te}$	3.98	427.9	29.6
$^{243}\text{Am}$	$\alpha\beta$ to $^{239}\text{Pu}$	$1.06 \times 10^4$	74.7	67.2
$^{230}\text{Th}$	$\alpha\beta$ to $^{208}\text{Pb}$	$1.09 \times 10^5$	351.9 ( $^{214}\text{Pb}$ ) 609.3 ( $^{214}\text{Bi}$ )	35.6 45.5
$^{126}\text{Sn}$	$\beta$ to $^{126}\text{Te}$	$2.86 \times 10^5$	414.7 ( $^{126}\text{Sb}$ ) 666.3 ( $^{126}\text{Sb}$ ) 695.0 ( $^{126}\text{Sb}$ )	98.0 100.0 97.0
$^{182}\text{Hf}$	$\beta$ to $^{182}\text{W}$	$1.28 \times 10^7$	270.4 1121.3 ( $^{182}\text{Ta}$ )	79.0 35.2

**Table 5** Possible astrophysical  $r$ -process sources, the estimated  $r$ -process masses in the ejecta per event  $M_{\text{ej}}$ , and the estimated occurring rate in the Milky Way (MW)  $f_{\text{MW}}$ . Among these proposed sites, only the BNSMs are unambiguously confirmed by the GW170817 observation (Abbott et al., 2017a,b). Patel et al. (2025) recently proposed the observation of SGR 1806-20 in 2004 as evidence of  $r$  process production in magnetar GFs. All other sites remain speculative and the quoted amount of  $M_{\text{ej}}$  should be treated as upper limits.

	$M_{\text{ej}} [M_{\odot}]$	$f_{\text{MW}} [\text{Myr}^{-1}]$	Confirmation?
<b>BNSMs</b>	$\mathcal{O}(10^{-3} - 10^{-2})$ (Shibata and Hotokezaka, 2019)	$\sim 30$ (Terada et al., 2022)	GW170817
NS-BH mergers	$\lesssim \mathcal{O}(10^{-1})$ (Shibata and Hotokezaka, 2019)	$\lesssim \mathcal{O}(10)$ (Mandel and Broekgaarden, 2022)	X
ccSNe $\nu$ wind	$\lesssim \mathcal{O}(10^{-4})$ (Goriely and Janka, 2016)	$\sim 10^4$ (Rozwadowska et al., 2021)	X
ccSNe $\nu$ wind	$\lesssim \mathcal{O}(10^{-3})$ (Goriely and Janka, 2016)	?	X
MRSNe	$\lesssim \mathcal{O}(10^{-3})$ (Whitelock et al., 2012)	?	X
PTSNs	$\lesssim \mathcal{O}(10^{-3})$ (Fischer et al., 2020)	?	X
CEJSNe	$\lesssim \mathcal{O}(10^{-2})$ (Grichener and Soker, 2019)	$\lesssim \mathcal{O}(10)$ (Grichener and Soker, 2019)	X
Collapsars	$\lesssim \mathcal{O}(10^{-1})$ (Siegel et al., 2019)	$\lesssim \mathcal{O}(10)$ (Siegel et al., 2019)	X
Magnetar GFs	$\lesssim \mathcal{O}(10^{-6})$ (Patel et al., 2025)	$\sim 10^5$ (Patel et al., 2025)	SGR 1806-20?

## 2.6 Nuclear De-Excitation $\gamma$ -Ray Lines from Low-Energy Cosmic Rays

*Written by Vincent Tatischeff*

### 2.6.1 Utilising Low-Energy Cosmic Rays

The interaction of accelerated nuclei of kinetic energy  $E_{\text{kin}} \gtrsim 1 \text{ MeV/nucleon}$  with ambient matter can produce a wealth of  $\gamma$ -ray lines with energies ranging from tens of keV to about 10 MeV. This non-thermal  $\gamma$ -ray line emission is often observed from the Sun during strong solar flares (e.g., Smith et al., 2003; Kiener et al., 2006, see also Sec. 2.7). It has furnished valuable information on solar ambient abundances, density and temperature, as well as on accelerated particle composition, spectra and transport in the solar atmosphere (e.g., Türler et al., 2021). Similarly, interactions of Galactic CR ions with interstellar matter should produce a diffuse  $\gamma$ -ray line emission that can shed new light on the sources of LECRs ( $E_{\text{kin}} \lesssim 1 \text{ GeV/nucleon}$ ) in the Galaxy and the isotopic composition of the ISM.

LECRs are thought to be responsible for the nucleosynthesis of the light elements lithium, beryllium and boron (LiBeB) from spallation nuclear reactions with nuclei of the ISM. This process is important to explain the observed evolution of the abundances of the LiBeB isotopes throughout the lifetime of the Galaxy. Remarkably, the observed quasi-linear increase of the  $^9\text{Be}$  abundances measured in stellar atmospheres with the star metallicity provides evidence for the existence of a significant component of LECR nuclei in the Galaxy. This has to be in addition to the standard CRs thought to be produced by diffusive shock acceleration in SN remnants (Tatischeff and Gabici, 2018).

LECRs are also thought to play a key role in the chemistry and dynamics of the ISM. They are a primary source of ionisation of heavily shielded, dense molecular clouds and the resulting ionisation fraction conditions both a rich ion-neutral chemistry in these regions and the coupling of the gas with the ambient magnetic field. LECRs also represent an important source of heating that contribute to hold molecular cores in equilibrium against gravitational forces. Hence, LECRs play a central role in the process of star formation. Despite LECRs being a fundamental component of the Galactic ecosystem, their composition and flux are very uncertain Galaxy-wide. They are better known in the local ISM thanks to the valuable CR measurements of the Voyager 1 and Voyager 2 probes as they crossed the heliopause into interstellar space (Cummings et al., 2016; Stone et al., 2019). But the total CR ionisation rate of atomic hydrogen resulting from the measured CR spectra,  $\zeta_{\text{H}} = (1.51-1.64) \times 10^{-17} \text{ s}^{-1}$ , is a factor  $> 10$  lower than the average CR ionisation rate measured in clouds across the Galactic disk using Herschel observations,  $\zeta_{\text{H}} = 1.78 \times 10^{-16} \text{ s}^{-1}$  (Indriolo et al., 2015). This suggests that LECRs are relatively less abundant in the local ISM than elsewhere in the Galaxy. Observations of  $\text{H}_3^+$  in diffuse clouds show indeed that the density of LECRs can strongly vary from one region to another in the Galactic disk (Indriolo and McCall, 2012).

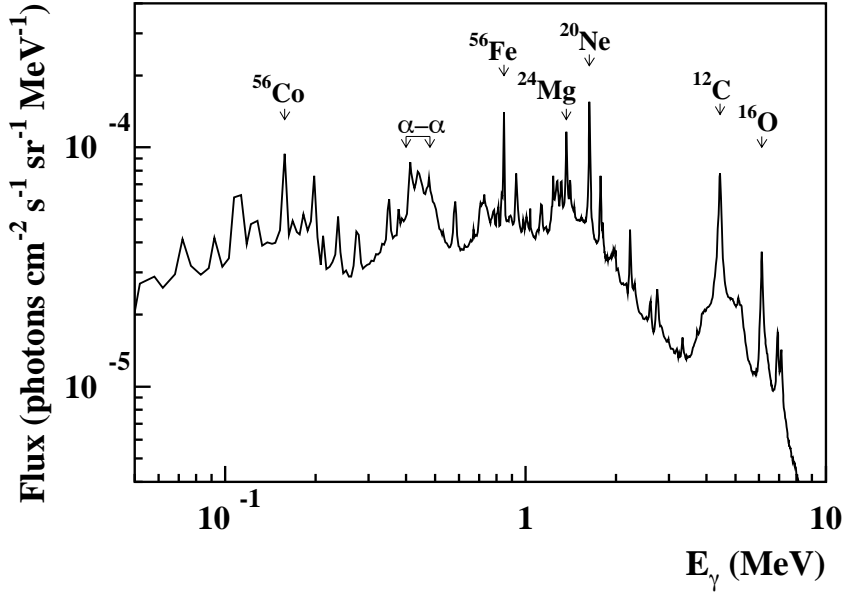


**Fig. 22** Calculated  $\gamma$ -ray line emission produced by LECRs in the inner Galaxy (longitude  $300^\circ < \ell < 60^\circ$ , latitude  $|b| < 10^\circ$ ). For some of the most significant lines, the emitting nuclei are indicated. The broad feature at  $\sim 450$  keV is called the  $\alpha$ - $\alpha$  line and is mainly produced by  $\alpha + {}^4\text{He}$  fusion reactions (adapted from Tatischeff and Kiener, 2011).

## 2.6.2 MeV $\gamma$ -Ray Line Observations and Predictions

### 2.6.2.1 Diffuse Emission – The Galactic Plane

MeV  $\gamma$ -ray astronomy can provide the most direct way of studying the density and effects of LECRs in the ISM, through the observation of nuclear de-excitation lines. Fig. 22 shows a calculated  $\gamma$ -ray line spectrum from LECR interactions with ambient matter in the inner Galaxy, based on Eq. (17). The density and energy spectrum of LECRs have been set to produce the mean ionisation rate of diffuse molecular clouds in the inner Galaxy (see Tatischeff and Kiener, 2011, and references therein). We can see in Fig. 22 a number of relatively narrow lines, which are mainly produced by excitation of abundant heavy nuclei of the ISM, such as  ${}^{12}\text{C}$ ,  ${}^{16}\text{O}$ ,  ${}^{20}\text{Ne}$ ,  ${}^{24}\text{Mg}$ , and  ${}^{56}\text{Fe}$ , by CR protons and alpha particles of kinetic energies between a few MeV/nucleon and a few hundred MeV/nucleon. The emitting nuclei are mainly excited by inelastic scattering or spallation reactions, but some lines are also produced by charge-exchange reactions, such as the one at 158 keV produced by the reaction  ${}^{56}\text{Fe}(p,n){}^{56}\text{Co}_{158}^*$  (see Ramaty et al., 1979; Murphy et al., 2009, for a compilation of the most significant  $\gamma$ -ray lines produced by nuclear collisions, with the involved nuclear reactions and their cross sections). Besides strong narrow lines, the total nuclear line emission is also composed of broad lines produced by interaction of CR heavy ions with ambient H and He, and of thousands of weaker lines that together form a quasi-continuum in the range  $E_\gamma \sim 0.1\text{--}10$  MeV (Murphy et al., 2009; Benhabiles-Mezhoud et al., 2013). The  $\alpha$ - $\alpha$  line feature at  $\sim 0.45$  MeV mainly results from the merging of two prompt lines from

the reactions  ${}^4\text{He}(\alpha, n\gamma_{429}){}^7\text{Be}$  and  ${}^4\text{He}(\alpha, p\gamma_{478}){}^7\text{Li}$  and the delayed line at 478 keV from  ${}^7\text{Be}$  decay ( $T_{1/2} = 53.3$  d).

The narrow lines produced in a gaseous ambient medium are generally broadened by the recoil velocity of the excited nucleus and their **FWHM** is about 0.5–5% of the transition energy. However, some lines produced in interstellar dust grains can be very narrow, because some of the excited nuclei can stop in solid materials before emitting  $\gamma$ -rays (Tatischeff and Kiener, 2004). The most promising of such lines are from the de-excitation of the level of  ${}^{56}\text{Fe}$  at 847 keV ( $T_{1/2} = 6.1$  ps), of  ${}^{24}\text{Mg}$  at 1369 keV ( $T_{1/2} = 1.35$  ps), of  ${}^{28}\text{Si}$  at 1.779 keV ( $T_{1/2} = 475$  fs) and of  ${}^{16}\text{O}$  at 6.129 keV ( $T_{1/2} = 18.4$  ps)<sup>5</sup>. Most of the interstellar Fe, Mg and Si are contained in dust grains, whereas about 30% of the interstellar O could be in grains (Jones et al., 2017).

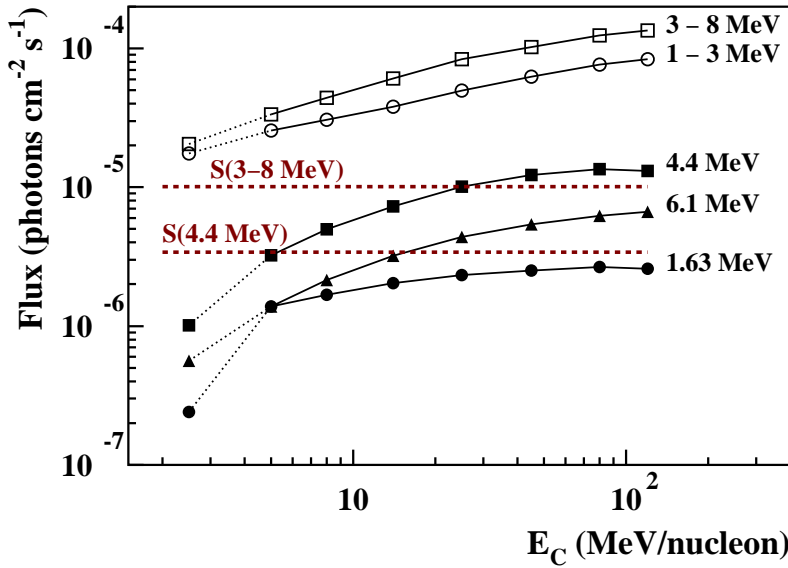


**Fig. 23** Calculated narrow-line fluxes of the 1.63 MeV ( ${}^{20}\text{Ne}$ ; filled circles), 6.1 MeV ( ${}^{16}\text{O}$ ; triangles) and 4.4 MeV lines ( ${}^{12}\text{C}$ ; filled squares), and integrated fluxes in the 1–3 MeV range (open circles) and 3–8 MeV range (open squares), from **LECRs** in the inner Galaxy (see also Fig. 22), as a function of the cut-off energy of the **CR** source spectrum (Eq. (45)). The fluxes given at  $E_C = 2.5$  MeV/nucleon are produced by a **CR** population consistent with the measurements of the Voyager probes in the local **ISM**. The other data points assume an additional **LECR** component accounting for the mean ionisation rate of diffuse clouds in the inner Galaxy deduced from  $\text{H}_3^+$  observations (see text). The red dashed lines show the e-ASTROGAM sensitivity in two years of survey observations for the diffuse emissions in the 4.4 MeV line and the 3–8 MeV range (see de Angelis et al., 2018).

In Fig. 22, the most intense narrow lines, in descending order, are the 4.4 MeV line mainly from  ${}^{12}\text{C}$  (with a contribution from  ${}^{11}\text{B}$  produced by spallation), the 6.1 MeV line mainly from  ${}^{16}\text{O}$  (with a contribution from  ${}^{15}\text{N}$  and  ${}^{15}\text{O}$ ) and the 1.63 MeV line from  ${}^{20}\text{Ne}$ . Calculated fluxes in these three lines are shown in Fig. 23, together with

<sup>5</sup>The effect of **ISM** grains is not taken into account in Fig. 22.

integrated fluxes in the energy ranges 1–3 MeV and 3–8 MeV, as a function of the cut-off energy  $E_C$  of the **LECR** source spectrum. Here, it is assumed to be the same for all species and to result from diffusive shock acceleration (see [Benhabiles-Mezhoud et al., 2013](#)):

$$\frac{dN_i}{dt}(E) = \frac{C_i R_i^{-s}}{\beta} e^{-E/E_C}, \quad (45)$$

where  $C_i$  is the abundance of nuclei of type  $i$  in the **LECR** composition,  $R_i$  is the particle rigidity and  $\beta = v/c$  the particle velocity in units of the speed of light. We see in Fig. 23 that a future  $\gamma$ -ray observatory such as e-ASTROGAM, which was proposed for ESA’s M5 mission ([de Angelis et al., 2018](#)), could detect the characteristic bump between 3 and 8 MeV (see Fig. 22) independent of the actual density of **LECRs** in the inner Galaxy. The detection of individual  $\gamma$ -ray lines, such as the one of  $^{12}\text{C}$  at 4.4 MeV, also seems feasible if low-energy protons contribute significantly to the ionisation of diffuse molecular clouds. The diffuse  $\gamma$ -ray line emission from **LECRs** is expected to be concentrated in the Galactic plane, similar to the high-energy diffuse emission observed by *Fermi*-LAT, of which approximately 60% of the total intensity is within a band of  $\pm 1.5^\circ$  in latitude. The inverse Compton radiation from accelerated electrons, which is also expected to contribute significantly to the diffuse Galactic emission in the MeV range, is predicted to be much more extended, to latitudes  $|b| > 10^\circ$  ([Ackermann et al., 2012](#)). Such a difference in spatial distribution should help to identify the nuclear  $\gamma$ -ray line component within the total Galactic diffuse emission. A Compton-imaging instrument such as e-ASTROGAM, having an angular resolution of  $0.7^\circ$  FWHM at 5 MeV, seems appropriate for such a detection.

Also here, it is interesting to note that a small fraction, up to several percent, of the 1.8 MeV  $\gamma$ -ray line flux may actually come from **LECR** excitation of stable  $^{26}\text{Mg}$  in the Galaxy ([Weinberger, 2021](#)).

#### 2.6.2.2 Point Sources – Supernova Remnants

The **CR** ionisation rates in dense molecular clouds close to **SN** remnants can be very high – more than 100 times the standard value in average molecular clouds. This has been evidenced by measurements of molecular abundance ratios such as  $\text{DCO}^+/\text{HCO}^+$  and  $\text{HCO}^+/\text{CO}$  in clouds near the **SN** remnants W51C ([Ceccarelli et al., 2011](#)), W28 ([Vaupré et al., 2014](#)), and W49B ([Zhou et al., 2022](#)). This suggests that intense fluxes of **LECRs** could escape **SN** remnants and interact with neighbouring molecular clouds, thus producing a potentially observable emission of nuclear  $\gamma$ -ray lines. The young **SN** remnant **Cas A** also appears to be a promising source, as it is the remnant of a massive star explosion  $\sim 350$  yr ago where accelerated nuclei could still interact with an ambient gas enriched in heavy ions from the progenitor winds and the **SN** ejecta ([Summa et al., 2011](#)). Predicted fluxes in the 4.4 and 6.1 MeV lines strongly depend on model assumptions on the accelerated particle spectrum and ambient medium composition, and they could be within the reach of the next generation of MeV  $\gamma$ -ray observatories in certain cases ([Liu et al., 2023](#)).

## 2.7 Solar Flare $\gamma$ -Rays

Written by Gerald H. Share

### 2.7.1 Particle Acceleration in Flares

Electron and ion acceleration to MeV energies and above occurs in settings throughout the Universe. These particles interact with matter, magnetic fields, and electromagnetic radiation to produce  $\gamma$ -rays that enable studies of explosive phenomena that occurred up to billions of years ago. As this volume focuses on the Universe at MeV energies, it is helpful to understand what we have learned when we look at our closest explosive neighbour, the Sun, in this band of the electromagnetic spectrum. The

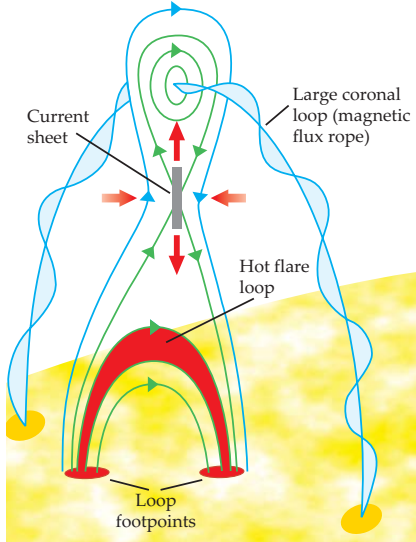


**Fig. 24** Cartoon depicting how reconnecting Solar magnetic field lines provide energy to accelerate particles to relativistic energies and release coronal mass ejections (CMEs) (from Holman, 2012).

Sun accelerates particles in eruptions and flares as a result of energy produced by the reconnection of coronal magnetic fields (Chen et al., 2020). The highest magnetic field strengths at the Sun are a few thousand Gauss, as compared with the  $10^{15}$  G fields that accelerate particles in pulsars. Fig. 24 is a simple picture of the Solar phenomenon in which reconnecting magnetic fields energise the coronal plasma to accelerate electrons and ions that become trapped in magnetic loops reaching into the Solar atmosphere where they interact at the flare foot points to produce hard X-rays and  $\gamma$ -rays (Vilmer et al., 2011). Ions and electrons from the same acceleration process can be ejected into interplanetary space as impulsive Solar energetic particles (SEPs) (Reames, 2021). The flare energisation process also forms magnetic flux ropes that erupt in mountain-sized CMEs. Shocks from these  $\gtrsim 500 \text{ km s}^{-1}$  CMEs can further accelerate supra-thermal ions from the flare and in the Solar wind to GeV energies (Reames, 2021). These SEPs also reach interplanetary space and Earth where they can be hazardous for astronauts, spacecraft systems, and passengers on aircraft flying polar routes.

### 2.7.2 The Solar $\gamma$ -Ray Spectrum

To understand the acceleration of electrons and ions with energies higher than a few hundred keV at the Sun, it is necessary to study the  $\gamma$ -ray spectra observed during Solar flares. In addition to the high-resolution  $\gamma$ -ray spectra measured by the germanium detectors on the Reuven Ramaty High Energy Solar Spectroscopic Imager (**RHESSI**) (Smith et al., 2002), some of the best Solar flare spectra were made with moderate resolution NaI detectors flown on the **SMM/GRS** (Forrest et al., 1980). Its excellent spectral stability allowed us to sum up spectra from 19 large Solar flares from 0.3 to 8.5 MeV that were observed over a nine-year period from 1980 to 1989. We show this summed spectrum in Fig. 25. It reveals the significant continuum and line features of  $\gamma$ -rays emitted in Solar flares. Note that because this is the raw count spectrum, it contains not only the lines but also the escape peaks and low-energy continua from partial energy losses in the instrument. Using seven years of data from the same spectrometer, Harris et al. (1992) showed the Galactic spectrum in the direction of the Galactic Centre, revealing a striking power-law continuum and the annihilation and  $^{26}\text{Al}$  lines. The spectral index of the continuum plotted in their Fig. 3 is consistent with more recent measurements (e.g., Siegert et al., 2022).

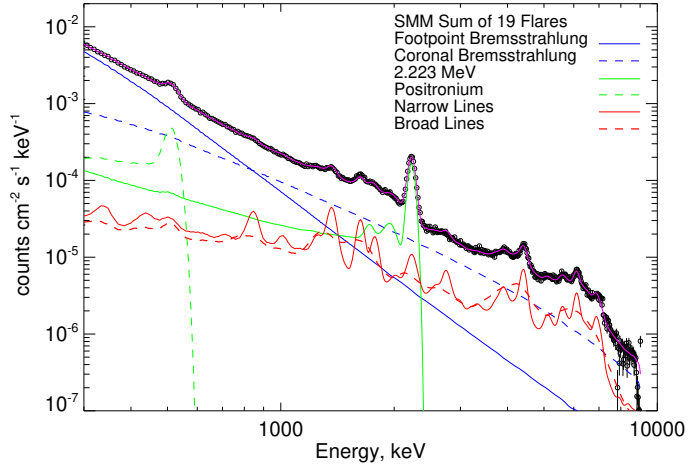


**Fig. 25** Summed background-subtracted spectrum from 19 Solar flares observed by **SMM/GRS**.

### 2.7.3 The $\gamma$ -Ray Continuum from Electrons

The electron-produced Solar  $\gamma$ -ray continuum is comprised of at least two components (Share et al., 2025): The solid blue curve represents the bremsstrahlung from the flare foot points produced by a power-law distribution of electrons. This radiation is anisotropic and can extend up to tens of MeV in some flares. The dashed blue curve represents the hard emission from a recently discovered population of electrons that peaks at energies between 3–5 MeV if they radiate by bremsstrahlung. If the electrons

radiate by inverse Compton scattering of soft flare X-ray photons, their spectrum is flat and extends up to 10–20 MeV. This hard component of electrons, is observed in flares 10–100 times weaker than the 19 nuclear-line flares whose summed spectrum is plotted in Fig. 25. In contrast to the electrons in the power-law component interacting at the foot points, these electrons appear to be isotropic and radiate from the Solar corona.

#### 2.7.4 Neutron-Capture and Annihilation Lines

The 2.223 MeV line (green solid curve) is the most striking line feature in the flare spectrum shown in Fig. 25. It is formed when neutrons, produced when flare-accelerated ions interact in the Solar atmosphere, slow down and are captured by hydrogen to produce deuterium with the binding energy appearing as a few eV wide line (Hua and Lingefelter, 1987). The resulting delay in emission of the line is dependent of the abundance of  $^3\text{He}$  because it also captures neutrons, but without emitting radiation (Wang and Ramaty, 1974). Measurement of the  $^3\text{He}/^1\text{H}$  ratio in the Sun using the 2.223 MeV time history is uncertain, ranging from  $(0.5\text{--}10) \times 10^{-5}$  (Murphy et al., 2003), compared with the  $1 \times 10^{-5}$  primordial ratio (Bania and Balser, 2021). Because the 2.223 MeV line is formed near photospheric depths, it is strongly attenuated for flares near the Solar limb. A Compton-scattered continuum from the  $\gamma$ -ray line emission leaving the Solar atmosphere is detectable by instruments with large photopeak efficiencies (Murphy et al., 2025, in prep.).

RHESSI imaging of the foot points of the electron bremsstrahlung and the neutron-capture line reveals that flare-accelerated ions and electrons interact at the same location (Battaglia and Krucker, 2025) in at least one flare. The close correlation between the  $\gtrsim 300$  keV bremsstrahlung fluence and the 2.223 MeV line fluence over three orders of magnitude indicates that hundreds of keV electrons and  $\gtrsim 5$  MeV protons have a related origin (Shih et al., 2009). Share et al. (2025) have used the relatively weak 2.223 MeV line flux in flares  $\sim 100$  times less intense than the nuclear-line flares to conclude that the accelerated ion spectra are significantly softer in these flares. From upper limits on the quiescent 2.223 MeV line flux, it was found that the Solar corona is not heated by  $\gtrsim 1$  MeV protons in microflares (Harris et al., 1992). The authors set a limit on tritium production at the Sun, and proved that large nuclear line flares are not the result of storage of quiescently accelerated protons in coronal magnetic fields.

The second most striking feature in the flare spectrum is the 511 keV line and lower energy continuum (green dashed curve) formed when positrons produced in  $\beta^+$ -decays of excited nuclei and  $\pi^+$ -decays annihilate with ambient electrons producing two or three  $\gamma$ -rays (Murphy et al., 2005). RHESSI high-resolution measurements of the 511 keV line width and Ps fraction provide information on the conditions of the ambient environment where the positrons annihilate (Share et al., 2004). There are times during the flares observed on 2002 July 23, 2003 October 28, 2003 November 2, and 2005 January 20 in which the Solar 511 keV line is significantly broadened. These measurements suggest that the ambient chromosphere at densities of  $\sim 10^{15} \text{ cm}^{-3}$  may, at times, be heated to temperatures reaching  $\sim 5 \times 10^5 \text{ K}$  during Solar flares.

There is also a variable **Ps** continuum observed in flares measured by the **RHESSI** and **SMM/GRS** spectrometers.

### 2.7.5 Nuclear De-Excitation Lines

A variety of nuclear lines is produced when flare-accelerated protons,  $\alpha$ -particles, and heavier ions interact with ambient elements in the Sun's chromosphere (Ramaty et al., 1979). The dominant ambient elements responsible for the lines are helium, carbon, nitrogen, oxygen, neon, magnesium, silicon, and iron. Fusion of  $\alpha$ -particles and He produce detectable Be and Li lines between 431 and 478 keV, respectively. Interactions of protons and  $\alpha$ -particles with ambient nuclei impart momentum to them producing Doppler-broadened and -shifted narrow lines (solid red curves). The widths (FWHM) of these lines range from  $\sim 8$  keV for the iron line at 847 keV to  $\sim 100$  keV for the carbon line at 4.43 MeV. Interactions of accelerated heavy ions with chromospheric hydrogen and helium produce significantly more shifted and broadened lines (dashed red curves). The widths of these lines range from  $\sim 80$  keV for iron to  $\sim 500$  keV for carbon. The most significant narrow lines found in the **SMM** spectrum and shown in Fig. 25 are listed in Tab. 6 (see also Murphy et al., 2009). The interactions producing these lines mostly occur at chromospheric depths. For comparison with celestial line

Line Energy [MeV]	Target Nucleus	Excited Nucleus
0.339	$^{56}\text{Fe}$	$^{59}\text{Ni}$
0.431	$^4\text{He}$	$^7\text{Be}$
0.478	$^4\text{He}$	$^7\text{Li}$
0.847	$^{56}\text{Fe}$	$^{56}\text{Fe}$
1.014	$^{24}\text{Mg}, ^{28}\text{Si}$	$^{27}\text{Al}$
1.022	$^{12}\text{C}, ^{16}\text{O}$	$^{10}\text{B}$
1.238	$^{56}\text{Fe}$	$^{56}\text{Fe}$
1.369	$^{24}\text{Mg}$	$^{24}\text{Mg}$
1.634	$^{20}\text{Ne}$	$^{20}\text{Ne}$
1.779	$^{28}\text{Si}$	$^{28}\text{Si}$
2.313	$^{14}\text{N}$	$^{14}\text{N}$
2.754	$^{24}\text{Mg}$	$^{24}\text{Mg}$
4.439	$^{12}\text{C}$	$^{12}\text{C}$
6.129	$^{16}\text{O}$	$^{16}\text{O}$
6.176	$^{16}\text{O}$	$^{16}\text{O}$
6.917	$^{16}\text{O}$	$^{16}\text{O}$
15.111	$^{12}\text{C}$	$^{12}\text{C}$

**Table 6** Prominent Solar Nuclear De-excitation Lines.

studies, using over nine years of data from **SMM/GRS**, Harris et al. (1995) has set a  $3\sigma$  limit of  $8.7 \times 10^{-5} \text{ ph cm}^{-2} \text{ s}^{-1} \text{ rad}^{-1}$  on the summed  $^{12}\text{C}$  plus  $^{16}\text{O}$  narrow-line flux from the Galactic Centre region. This limit is as much as a factor ten higher than that calculated from CR interactions with interstellar carbon (Ramaty et al., 1979).

There have been many spectroscopic studies of nuclear de-excitation lines in Solar-flare spectra based on observations by **SMM/GRS**, Yohkoh, Konus-Wind, **CGRO**, **RHESSI**, CORONAS-F/SONG, and Fermi/GBM (e.g., Share and Murphy, 1995; Ramaty et al., 1996; Murphy et al., 1997; Mandzhavidze et al., 1999; Mandzhavidze

and Ramaty, 2000; Smith et al., 2002; Vilmer et al., 2011; Ackermann et al., 2012; Lysenko et al., 2019; Yushkov et al., 2023). These studies addressed ambient abundances where flare-accelerated ions interacted, and the spectra and composition of these ions. Unfortunately, the results obtained were of limited accuracy because the spectra were typically fit by a single electron-produced continuum and by Gaussian fits to the narrow and broad de-excitation lines. What is needed to obtain accurate information on the ambient composition where flare-accelerated particles interact and the abundances of these particles are calculated nuclear  $\gamma$ -ray line spectra for a variety of accelerated particle spectra and compositions, and ambient abundances. Murphy et al. (1991) performed a limited analysis of this type for the 1981 April 27 flare observed by SMM using the seminal work of Ramaty et al. (1979).

Significant improvement in our knowledge about the Solar nuclear lines has come with detailed studies of particle acceleration onto magnetic loops (Hua et al., 1989; Murphy et al., 2007) and from accurate knowledge of the production of broad and narrow nuclear de-excitation lines and unresolved continuum (Kozlovsky et al., 2002; Murphy et al., 2009, 2016; Tusnski et al., 2019). The end product of this work is an array of nuclear  $\gamma$ -ray spectral templates for each of the processes for different ambient and accelerated particle abundances, flare locations, and ion spectral indices. Access to these templates is provided by OSPEX<sup>6</sup> that is available in the SSW IDL software depository<sup>7</sup>. We have also identified issues with how the original SMM/GRS and RHESSI detector response matrices accounted for  $\gamma$ -rays that do not lose all of their energy in the instrument. The response matrices of both instruments have been corrected and incorporated into OSPEX (Share et al., 2025).

There are some studies that were not as dependent on improvements in the analysis techniques discussed above. Kiener et al. (2006); Kiener (2019) analysed INTEGRAL high-resolution measurements of the 4.43 MeV  $^{12}\text{C}$  line in the 2003 October 28 Solar flare and found that relatively narrow-downward directed distributions of accelerated protons and  $\alpha$ -particles provided the best fits. Assuming a model where particles are trapped in magnetic loops with mirroring and pitch angle scattering, the best fitting parameter,  $\lambda$  (the scattering mean free path divided by the half-length of the coronal segment of the magnetic loop), was consistent with a value of 30 and not with a value of 300. This is a somewhat narrower angular distribution of particles than found in Doppler red-shift measurements of the centroids of the high-first ionisation potential (FIP) lines with heliocentric angle in SMM flares (Share et al., 2002) and from RHESSI measurements of the  $\alpha$ - $^{4}\text{He}$  (Share et al., 2003) and de-excitation lines (Smith et al., 2003) in the 2002 July 23 flare. The latter observation and later INTEGRAL observations (Harris et al., 2007) suggested that the Solar magnetic loops were tilted by as much as 40° from the normal. Kiener (2019) also derived an accelerated  $\alpha/p$  ratio of  $0.22^{+0.20}_{-0.13}$ , consistent with SMM measurements (Share and Murphy, 1997). We note that a comparison of the fluxes in the 339 and 847 keV lines provide a direct measurement of the  $\alpha/p$  ratio because the 339 keV line is produced by  $\alpha$ -particle interactions.

---

<sup>6</sup>Object Spectral Executive: [https://hesperia.gsfc.nasa.gov/ssw/packages/spex/doc/ospex\\_explanation.htm](https://hesperia.gsfc.nasa.gov/ssw/packages/spex/doc/ospex_explanation.htm)

<sup>7</sup>[http://www.lmsal.com/solarsoft/ssw\\_whatitis.html](http://www.lmsal.com/solarsoft/ssw_whatitis.html).

A study of the global energetics of Solar eruptions (Emslie et al., 2012) revealed that “*the energy content in flare-accelerated electrons and ions is sufficient to supply the bolometric energy radiated across all wavelengths throughout the event*” and that “*the energy contents of flare-accelerated electrons and ions are comparable*”. This is a significant finding as it shows how important particle acceleration is in the release of energy in flares. We note that the ion energies were only calculated above  $\sim 1$  MeV, therefore, the estimated energy in ions may be significantly higher if the emission extends to lower energies. Determining the spectra of interacting flare-accelerated protons below 1 MeV appears to be a formidable problem (Share et al., 2001).

With our increased understanding of the  $\gamma$ -radiation produced by ion interactions in the chromosphere, Murphy et al. (2016) has provided an example of what can now be achieved in planned studies. They used  $\gamma$ -ray line flux ratios determined from an archival fit to the summed spectrum plotted in Fig. 25 to conclude that there is only a  $10^{-3}$  probability that the  $^3\text{He}$  abundance in flare-accelerated particles could be as small as that found in the Sun’s photosphere. They obtained  $^3\text{He}/\alpha$  ratios ranging from 0.05 to 0.3, depending on the assumed accelerated  $\alpha/p$  ratio. With the improvements in our analysis of Solar flares discussed above, we have analysed the spectra from the 19 SMM flares and the 2002 July 23 flare observed by RHESSI. Planned studies include: (1) elemental composition of high-FIP elements,  $^{12}\text{C}$ ,  $^{14}\text{N}$ ,  $^{16}\text{O}$ , and  $^{20}\text{Ne}$ , (2) composition and variability of the low-FIP elements,  $^{24}\text{Mg}$ ,  $^{28}\text{Si}$ , and  $^{56}\text{Fe}$ , and (3) spectral variations and abundances of accelerated particles, including  $^3\text{He}$ .

*My thanks to Brian Dennis and Ronald Murphy for reviewing the manuscript.*

## 2.8 Solar System Bodies and their $\gamma$ -Ray Albedos

Written by Thomas Siegert

Solid bodies, with or without atmospheres, acquire a  $\gamma$ -ray albedo when bombarded by CRs. When LECRs ( $\lesssim 1$  GeV) interact with nuclei, the nuclei become excited and almost immediately de-excite by emitting characteristic  $\gamma$ -rays (see Eq. (17) and Sec. 1.2.2). In solid bodies, unlike in the ISM, the penetration depth of LECRs and the resulting opacity for the emitted  $\gamma$ -rays must be considered. Thus, not every LECR produces a measurable photon, and the overall  $\gamma$ -ray spectrum is soft (Moskalenko and Porter, 2007). Fig. 26 (top left) illustrates the production mechanisms for  $\gamma$ -ray photons, particularly  $\gamma$ -ray lines. Natural radioactivity is generally observed from  $^{40}\text{K}$  (1460.8 keV,  $\tau = 1.8$  Gyr) and, in heavier materials, from actinide alpha decay chains; elements such as U, Th, and Sm and Gd (as fission products) are dominant  $\gamma$ -ray line emitters in Moon rock (Prettyman et al., 2006). Most Th and U lines occur below 3 MeV. When a CR impacts a solid body, it produces secondary particles such as fast neutrons, pions, and electron-positron pairs. The pions quickly decay into either  $\gamma$ -ray photons or charged muons, which then decay into electrons and positrons, resulting in positron annihilation and bremsstrahlung. Pair annihilation mainly occurs via Ps formation, producing both the 511 keV line and the ortho-Ps continuum. Fast neutrons may escape the surface, undergo inelastic scattering (nuclear excitation), or be captured by the material, also leading to nuclear excitation. Thus, measuring the  $\gamma$ -rays lines allows us to study the surface composition of solid bodies. Fig. 26 (bottom left) displays the Moon's Th surface concentration as measured by the Lunar Prospector (LP) mission (Prettyman et al., 2006). The figure shows the measurement from a  $\gamma$ -ray spectrometer orbiting the Moon at 100 km. In the following, we briefly describe how these  $\gamma$ -ray (line) albedos are calculated, review observed sources, and discuss the cumulative effect of all small bodies (asteroids and trojans) in the Solar System.

### 2.8.1 Calculations of $\gamma$ -Ray Albedos

Eq. (17) provides the general formula for  $\gamma$ -ray production from CRs interacting with matter. The challenge lies not in the equation's complexity but in the many particle species, competing processes (nuclear excitation, elastic scattering, spallation, pair production), and secondary interactions involved. Therefore, Monte Carlo simulations tailored to specific compositions and CR spectra are the preferred method. In detailed 3D models, penetration depth and  $\gamma$ -ray escape in solid bodies and atmospheres are automatically accounted for. Cosmic photon interactions with solids and atmospheres also produce a  $\gamma$ -ray albedo, mostly Compton-scattered to lower energies, though if the pair creation threshold is reached, the 511 keV line reappears in the continuum. This effect is important for CGB measurements since planetary atmospheres and solid bodies both reprocess  $\gamma$ -ray emission (e.g., Siegert et al., 2024; Churazov et al., 2007; Sazonov et al., 2007).

Moskalenko and Porter (2007); Moskalenko et al. (2008); Moskalenko and Porter (2009) employed the GEometry ANd Tracking 4 (GEANT4) Monte Carlo generator (Agostinelli et al., 2003) to calculate the Moon's  $\gamma$ -ray albedo, then extrapolated their

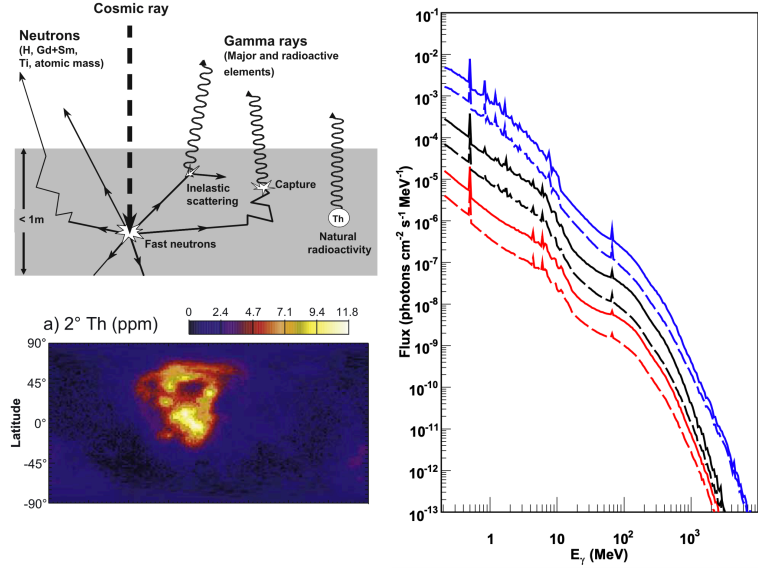


**Fig. 26** Top left: Expected processes leading to  $\gamma$ -ray emission from the Lunar or asteroids surfaces (from Prettyman et al., 2006); in atmospheres, the processes are similar. Bottom left: *Measured* natural radioactivity from the Lunar surface in Th lines from the LP mission (from Prettyman et al., 2006). Right: Expected  $\gamma$ -ray spectrum from a Moon-sized body at the distance of the Moon with different compositions (black: Moon rock; blue: iron  $\times 10$ ; red: water ice  $\times 0.1$ ) for two different modulation potentials (solid: no modulation; dashed: 1500 MV) (from Moskalenko et al., 2008).

results to all small Solar System bodies. Fig. 26 (right) shows the simulated  $\gamma$ -ray albedo from a Moon-sized body at Lunar distance. As expected, the spectrum is very soft with an index of  $-1.0$  below  $\sim 10$  MeV, and it breaks according to the material's composition, density, and the Solar modulation potential.

#### 2.8.1.1 Cosmic-Ray Induced $\gamma$ -Ray Lines

On top of the mainly bremsstrahlung continuum, several  $\gamma$ -rays lines are visible, depending on the material's composition. The absolute continuum flux remains similar for comparable modulation potentials, while the  $\gamma$ -ray lines appear more sensitive to changes. By measuring these line fluxes, one can distinguish asteroid compositions: “dirty snowballs” (ices from water, carbon dioxide, ammonia; Whipple, 1950) show strong oxygen lines (red), pure iron bodies (blue) exhibit lines similar to those in SNe (e.g., 847 and 1238 keV), and Moon rock-like materials display a blend of lines (Al, O, Fe, Mg, Ti, Si). The most intriguing aspect is that these  $\gamma$ -ray lines and the continuum allow the determination of the LECR spectrum in the Solar System as a function of distance, thereby revealing the Solar modulation potential and the Sun's magnetic activity. Major asteroid populations include the Main Belt Asteroids (MBAs) between Mars and Jupiter (2.8 AU), the Jovian Trojans (JTs) at the Jupiter-Sun Lagrange points L4 and L5 (5.2 AU), the Neptunian Trojans (NTs) (28 AU), and the Kuiper Belt Objects (KBOs) as another belt reaching from 40–100 AU. Since the CR spectrum and its intensity vary with distance from the Sun, different objects will exhibit

distinct  $\gamma$ -ray albedos. De-excitation  $\gamma$ -ray line fluxes are expected to be on the order of  $\lesssim 10^{-6} \text{ ph cm}^{-2} \text{ s}^{-1}$ , as estimated by [Moskalenko and Porter \(2007\)](#); [Moskalenko et al. \(2008\)](#); [Moskalenko and Porter \(2009\)](#). Next generation telescopes should take these lines into account, most certainly the 511 keV line.

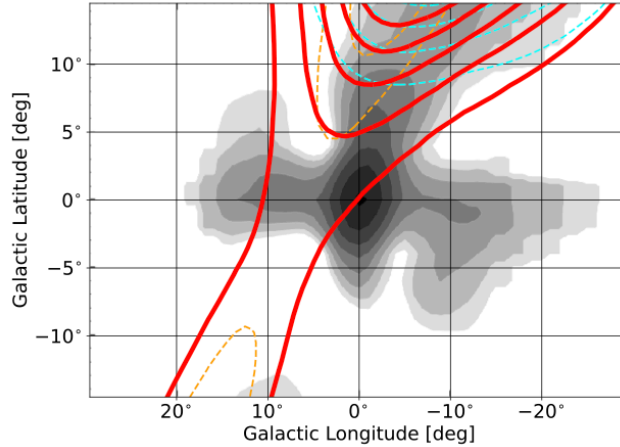


**Fig. 27** Oriented Scintillation Spectrometer Experiment (OSSE) 511 keV map by [Purcell et al. \(1997\)](#), together with the cumulative contributions from the JT<sub>s</sub> (orange) and NT<sub>s</sub> (cyan) from 1990-01-01 to 1997-12-31, and the combined model (red). The “OSSE fountain” was a serendipitous and, so far, never observed afterwards, positive latitude enhancement (from [Siegert et al., 2024](#)).

### 2.8.1.2 Time-Variable $\gamma$ -Ray Foreground

However, the 511 keV line from the asteroids is expected to be significantly stronger, with a flux of  $(1\text{--}4) \times 10^{-4} \text{ ph cm}^{-2} \text{ s}^{-1}$  along the Solar System ecliptic. Since the ecliptic is crossing the Galactic plane around the Galactic bulge region, the contribution of the 511 keV line flux in the bulge from the asteroids is on the order of  $2 \times 10^{-5} \text{ ph cm}^{-2} \text{ s}^{-1}$ , that is, about 2% of the total (see Sec. 2.9). The interesting effect with the JT<sub>s</sub> and NT<sub>s</sub>, and to a lesser extent also with the MBAs, is that their positions on the sky change with time. This will lead to an effective time-variable diffuse  $\gamma$ -ray foreground to Galactic measurements in the 511 keV (and other, weaker lines, as well as the continuum). The ecliptic band in the MeV would then be similar to the zodiac light in the infrared. However, the JT and NT regions may be populated by a much larger number of objects than currently known (only km sized objects are known), so that they may stick out of the ecliptic  $\gamma$ -ray band. This might be measurable already now even though the exposure of, for example, INTEGRAL/SPI is mostly concentrated in the Galactic bulge. A variation of 2% of the flux from the spatial variance alone might not be visible, but the effect of the solar cycle in addition might lead to measurable effects on the time scale of several years. Considering the long exposure times of MeV  $\gamma$ -ray missions, the cumulative effect of these trojan asteroid accumulations over time may lead to asymmetric features, such as seen in the “OSSE 511 keV Galactic fountain” ([Purcell et al., 1997](#)). [Siegert et al. \(2024\)](#) attempts to explain the

OSSE fountain by the cumulative effect of the **JTs** and **NTs** and shows that within the observation period of **CGRO/OSSE** in this study, between 1991 and 1997, the “fountain” matches the cumulative distribution of **JTs** and **NTs**. In Fig. 27, we show the spatial overlap of the “OSSE 511 keV fountain” with the cumulative effect of the **JTs**.

## 2.8.2 $\gamma$ -Ray Measurements of Solar System Objects

There have been several measurements of  $\gamma$ -ray lines from different Solar System objects – not necessarily with MeV telescopes, but with  $\gamma$ -ray spectrometers onboard probes that flew to the objects. We will give a short overview here and some details for individual objects in the following.

Ceres and Vesta are the largest asteroids in the Solar System with radii of 473 and 263 km, respectively, and have been visited by the Dawn spacecraft (Peplowski et al., 2013; Lawrence et al., 2018). Dawn’s Gamma Ray and Neutron Detector (**GRaND**) measured the surface composition of both asteroids, viz. dwarf planets. Other atmosphere-free objects whose surface composition has been measured by  $\gamma$ -ray observations in-situ are Mercury (Evans et al., 2012), the Mars moon Phobos (Lawrence et al., 2019), the asteroid 433 Eros (see Sec. 2.8.2.2), as well as the Moon (see Sec. 2.8.2.1, see also Fig. 26, bottom left). Solar System objects with atmosphere that have  $\gamma$ -ray measurements include the Earth (Sec. 2.8.2.3) and the Sun. However, for the quiet Sun, only upper limits in the MeV range exist up to 200 keV (Hannah et al., 2007).

### 2.8.2.1 The Moon

Besides the natural radioactivity (Fig. 26, bottom left), Prettyman et al. (2006) disentangled more  $\gamma$ -ray lines from the surface survey of the Moon than could be expected from the measurements with BGO crystals and an energy resolution of 12%. Besides Th, the **LP** mission created  $\gamma$ -ray surface maps of the Moon also in the elements of K, Fe, O, Al, Ti, Mg, and Si (mostly in oxide form) at resolutions of 2–20°. In fact, they also measured the 511 keV line but given the scientific purpose of the **LP** mission, this line was disregarded in their study. At an orbit of 100 km above the Lunar surface, their fluxes range from about  $10^{-3}$  ph cm $^{-2}$  s $^{-1}$  at 9 MeV to more than  $10^{-1}$  ph cm $^{-2}$  s $^{-1}$  around 0.5 MeV. Clearly, this is integrating over a large solid angle of 2–20°, and also on top of a 10–90% background from the instrument and bremsstrahlung component. Moskalenko and Porter (2007) estimated a 511 keV flux from the Moon of  $2.4 \times 10^{-5}$  ph cm $^{-2}$  s $^{-1}$  at a distance of 384000 km, which would be equivalent to a differential flux per  $(10^\circ)^2$ -pixel of  $5.2 \times 10^{-2}$  ph cm $^{-2}$  s $^{-1}$ . This appears reasonable, though is on the high side of the Prettyman et al. (2006) measurements. Using this value as a reference, we can estimate the fluxes of some other nuclear de-excitation lines from the Moon if it was observed from a satellite around Earth. For example, the most prominent Fe, Si, and O lines are all be on the order of  $(1-10) \times 10^{-4}$  ph cm $^{-2}$  s $^{-1}$  at a distance of **LP** mission, so that the total surface flux at Earth would be at most a few  $10^{-7}$  ph cm $^{-2}$  s $^{-1}$ . While this is not an extremely strong foreground, next-to-next generation telescopes should take also these lines into account – however certainly the 511 keV line.

### 2.8.2.2 Named Asteroids

Asteroid 433 Eros was measured by the Near Earth Asteroid Rendezvous (NEAR) probe which had a closest approach to the asteroid of about 35 km (Peplowski, 2016). It could measure the nuclear de-excitation of elements like Fe, Mg, K, Si, Al, C, and O, as well as the 511 keV line. Extrapolating NEAR's  $\gamma$ -ray spectrum from 433 Eros towards the entire population of asteroids in all accumulations in the Solar System is difficult, if not meaningless, as there are hardly any other measurements in soft  $\gamma$ -rays for individual asteroids, and especially not at smaller sizes. The smaller asteroids would be required because most induced  $\gamma$ -ray emission from LECR interactions come from grazing angles, that is, the rim of the objects (Moskalenko et al., 2008). If, however, the objects are too small to develop a full particle cascade when hit, the resulting spectrum might differ from the expectations of Moskalenko et al. (2008, see also Fig. 26, right). The number of small objects ( $\lesssim 1$  m) in the Solar System is not known but is expected to exceed that of the known ones by several orders of magnitude (Dohnanyi, 1969), making them the most luminous component in total, even when considering the incomplete particle cascades. A measurement of the cumulative effect of asteroids in the Solar System with next-generation telescopes will help to understand the distribution – and formation – of small-sized bodies and in how far they contribute to the  $\gamma$ -ray foreground albedo.

### 2.8.2.3 Earth

It appears surprising that  $\gamma$ -ray line observations of Earth are rare. While it is important for, for example,  $\gamma$ -ray burst observations to include the reflection from the atmosphere into the satellite instrument (e.g., Kippen et al., 2007), many observatories strictly avoid observing Earth because it is large (no star tracker information) and bright (detector saturation). Especially at MeV energies, there are only a few Earth  $\gamma$ -ray albedo measurements, of which Share and Murphy (2001) provide the most useful. The authors used SMM/GRS observations of Earth in low-Earth orbit with and without a solar particle event. Despite the 5% resolution of the seven NaI detectors, it was possible to identify the major  $\gamma$ -ray lines coming from nuclear excitation and spallation of Earth's atmosphere. Among others, the strongest line blends are around 4.4 MeV with, for example,  $^{12}\text{C}$  (4439 keV) and  $^{11}\text{B}$  (4444 keV), around 7 MeV with  $^{16}\text{O}$  (6917, 7115 keV) and  $^{14}\text{C}$  (7010 keV), and from 3.1–3.7 MeV with  $^{14}\text{N}$  (3073, 3378, 3384 keV) and  $^{13}\text{C}$  (3089 keV) (see Share and Murphy, 2001, Tab. 1). Most of the lines appear broadened up to several 100 keV (FWHM) and at blend flux levels on the order of  $(5\text{--}10) \times 10^{-3} \text{ ph cm}^{-2} \text{ s}^{-1}$ . The strongest line, however, is at 511 keV with a flux level of several  $10^{-2} \text{ ph cm}^{-2} \text{ s}^{-1}$  and hardly broadened with respect to instrumental resolution. These measurements are important to gauge simulations of the  $\gamma$ -ray albedo of Earth, for example for measurements of the CGB that rely on Earth occultation measurements (e.g., Sazonov et al., 2007; Churazov et al., 2007, 2008; Türler et al., 2010). Unless these measurements are validated, any measurement of the CGB beyond a few 100 keV from Earth occultation is highly uncertain. We note that in the case of a Solar particle event, the atmospheric 511 keV line reaches fluxes levels in low-Earth orbit of  $\gtrsim 1 \text{ ph cm}^{-2} \text{ s}^{-1}$  (Share and Murphy, 2001).

## 2.9 The Positron Annihilation Line at 511 keV

Written by Thomas Siegert

### 2.9.1 Overview of 511 keV Observations

#### 2.9.1.1 Historical Observations

The 511 keV line from electron positron annihilation has first been detected by [Johnson and Haymes \(1973\)](#) during balloon flights in 1970–1971. In fact, the line was already indicated in [Haymes et al. \(1969\)](#) at the  $2\sigma$  level during a balloon flight in April 1968. At first, it was not clear whether the line-like feature was actually due to positron annihilation because the centroid was found to be  $476 \pm 24$  keV, which is closer to the  $^{7}\text{Be}$  decay line at 478 keV (see Sec. 2.3). However, with better spectral resolution using Ge detectors on a balloon flight in 1977, [Leventhal et al. \(1978\)](#) unambiguously found that the  $\gamma$ -ray line from the direction of the Galactic centre was indeed at 511 keV and therefore due to the annihilation of positrons.

After this initial detection, several other balloon-borne  $\gamma$ -ray detectors as well as satellite-based observations led to a conundrum about the flux of the 511 keV line: Even the same instruments (e.g., [HEAO 3](#), [SMM](#), [Riegler et al., 1981](#); [Share et al., 1988](#)) found different fluxes, ranging between  $(0.4\text{--}6.0) \times 10^{-3} \text{ ph cm}^{-2} \text{ s}^{-1}$ , on timescales of years. This surprisingly strong variability turned out to be a misconception of what was actually observed – not a single variable point source, but diffuse extended emission. After [Lingenfelter and Ramaty \(1989\)](#) found a strong correlation of the observed 511 keV flux with the field of view (FoV) of the instrument used, [Purcell et al. \(1997\)](#) was finally able to reconstruct the first image of the annihilation line using [CGRO/OSSE](#). The [OSSE](#) image included a strong bulge component with a radial extent of  $5^\circ\text{--}8^\circ$ , a weak disk that only extended out to longitudes  $|\ell| \lesssim 20^\circ$ , and a positive latitude enhancement that was dubbed the “[OSSE](#) 511 keV fountain” (see Fig. 27).

With these findings, it was clear that this strongest  $\gamma$ -ray line detected was the first one from outside the Solar System. Furthermore, it was not only the 511 keV line that was detected, but also the ortho-[Ps](#) continuum below the line that shows a turnover of the falling Inverse Compton (IC) spectrum around 350 keV after which the differential spectrum is, in fact, rising as a function of energy (e.g., [Share et al., 1988](#); [Purcell et al., 1997](#)). Beyond the 511 keV line at which the [Ps](#)-decay spectrum peaks with the para-[Ps](#) line, there is a sharp drop and the Galactic ridge continuum spectrum continues. Newer observations, however, did not find all the structures observed with [OSSE](#).

#### 2.9.1.2 Recent Observations with [INTEGRAL/SPI](#)

With the launch of [INTEGRAL](#), the spectrometer [SPI](#) could do both at unprecedented accuracy – imaging and spectroscopy. The two seminal papers by [Knöldlseder et al. \(2005\)](#) and [Jean et al. \(2006\)](#) consider the imaging and the spectral analysis of positron annihilation using 1.5 yr of [SPI](#) data, respectively. The central parts of the Galaxy were found to be explained by a 2D Gaussian with a spherical shape of radius  $8^\circ$  (FWHM). These values are completely consistent with the previous [OSSE](#) study. However, neither the disk was seen significantly nor the positive latitude enhancement.

Later studies by Weidenspointner et al. (2008), Bouchet et al. (2010), Skinner et al. (2014), and Siegert et al. (2016, 2019, 2022), all found a disk in 511 keV with sizes confirming OSSE, or even more extended in longitude and latitude. The initial extremely high bulge-to-disk flux ratios from SPI and OSSE observations of 0.2–3.3, corresponding to luminosity ratios of up to 9, were then step-by-step decreased by including more exposure over the timescale of the INTEGRAL mission (see Fig. 28). The more or less accepted value for the bulge-to-disk luminosity ratio is now “below 1.0”, which however, depends on the effective distances to bulge and disk, which scale the measured fluxes of  $F_{\text{bulge}} = (0.9\text{--}1.2) \times 10^{-3} \text{ ph cm}^{-3} \text{ s}^{-1}$  and  $F_{\text{disk}} = (1.4\text{--}2.0) \times 10^{-3} \text{ ph cm}^{-3} \text{ s}^{-1}$ . The most recent image reconstruction from INTEGRAL/SPI has been performed by Yoneda et al. (2025) with more than 20 yr of data. This newest image (Fig. 29) shows the same regions as before and might finally reveal sub-structures, such as from massive star groups.

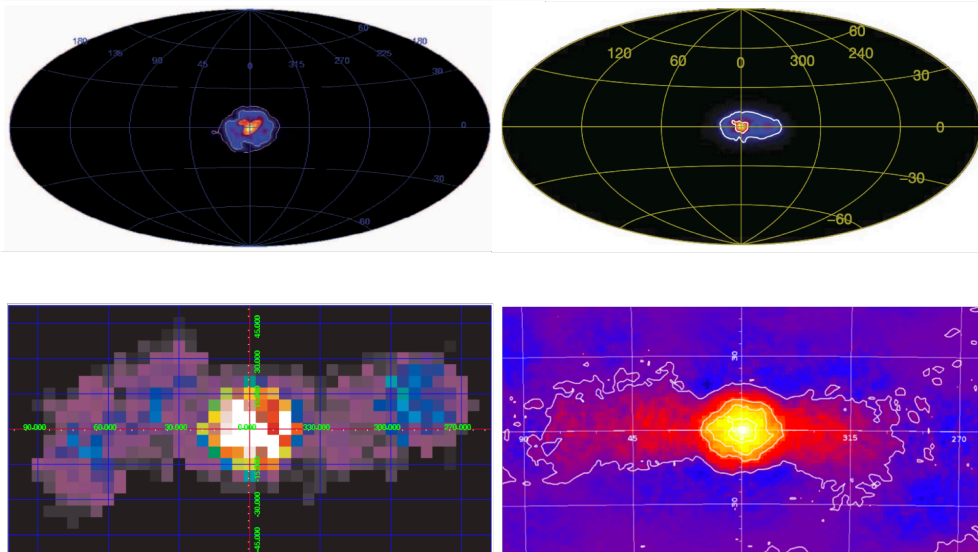


**Fig. 28** Reconstructed images of the 511 keV line with SPI throughout the INTEGRAL mission with different exposure times and algorithms. Top left: 1.5 yr (from Knöldlseder et al., 2005, using Richardson-Lucy). Top right: 3.5 yr (from Weidenspointner et al., 2008, using Richardson-Lucy). Bottom left: 7.5 yr (from Bouchet et al., 2010, using Maximum Likelihood). Bottom right: 10.5 yr (from Siegert, 2017, using Maximum Entropy).

The spectral analysis with SPI revealed the positron annihilation *conditions*, that is, not their sources but their sinks. It was found that positrons mostly annihilate in warm (7000–40000 K) and partly ionised (0.01–0.25%) phases of the ISM (Jean et al., 2006; Churazov et al., 2005) or in a cooling phase (Churazov et al., 2011) (Fig. 30). Given the spectral resolution of SPI of 2.1 keV at 511 keV (FWHM), it was possible to find both, a narrow line with a width of 0.9–1.7 keV, and a broad line with 4–11 keV in the bulge region of the Milky Way (Jean et al., 2006; Siegert et al., 2019).

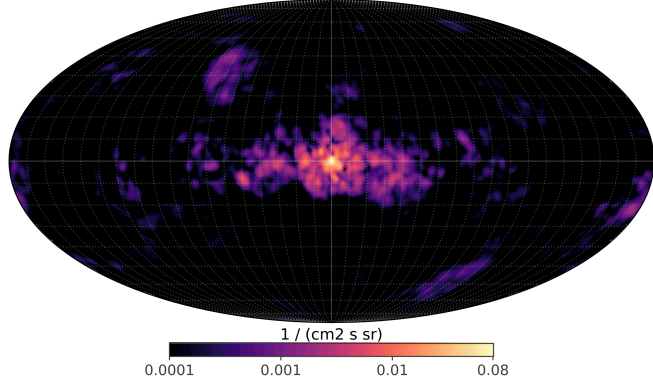


**Fig. 29** Richardson-Lucy image reconstruction of the 511 keV line emission from 20.5 yr of INTEGRAL/SPI data (from [Yoneda et al., 2025](#)).

The annihilation conditions also imprint in the **Ps** fraction,  $f_{\text{Ps}}$ , which, however, is difficult to determine across the Galaxy, or even for different spatial components (e.g., [Siegert et al., 2016](#)). In an attempt to construct a 511 keV longitude-velocity diagram to reveal the internal dynamics of positron annihilation in the Galaxy, similar the  $^{26}\text{Al}$  case ([Kretschmer et al., 2013](#), see also Sec. 2.1), [Siegert et al. \(2019\)](#) found a velocity gradient along the inner  $\pm 30^\circ$  of  $4 \pm 6 \text{ km s}^{-1} \text{ deg}^{-1}$ . This is consistent with zero rotation, consistent with the Galactic rotation speed from CO measurements ( $2\text{--}3 \text{ km s}^{-1} \text{ deg}^{-1}$ ), and also with the 1.8 MeV  $^{26}\text{Al}$  measurement of  $7.5\text{--}9.5 \text{ km s}^{-1} \text{ deg}^{-1}$ . Statistically, it appeared that none of the spectral parameters of the 511 keV line, nor the **Ps** fraction change as a function of longitude. However, a slight, insignificant positive latitude enhancement in the line flux was found, reminiscent of the **OSSE** fountain measurement ([Purcell et al., 1997](#)). Systematic, astrophysical variations with longitude are, nevertheless, possible as discussed in much detail in the appendix of [Siegert et al. \(2019\)](#).

Given 10.5 yr of observations, [Skinner et al. \(2014\)](#) and [Siegert et al. \(2016\)](#) performed an analysis to determine the size of the 511 keV disk (see Fig. 31). While [Skinner et al. \(2014\)](#) used a single energy bin from 508–514 keV, [Siegert et al. \(2016\)](#) used 0.5 keV bins from 490–530 keV to estimate the extent and flux of the disk. Both works assumed the same empirical three-component model for the bulge. Here, [Skinner et al. \(2014\)](#) found a point-like source in the 508–514 keV bin at the position of the Galactic centre, which was then shown to be a 511 keV line and not just continuum by the spectral analysis in [Siegert et al. \(2016\)](#). For the disk, the two approaches led to similar line fluxes, from  $(1.4\text{--}2.0) \times 10^{-3} \text{ ph cm}^{-2} \text{ s}^{-1}$ , but from vastly different scale heights: The single bin from [Skinner et al. \(2014\)](#) seems to prefer a thin disk ( $\sim 3^\circ$ ), while [Siegert et al. \(2016\)](#) found a thick disk ( $\sim 10^\circ$ ). The statistical uncertainties in both cases are rather small, so that the tension between the two studies using the same dataset is about  $3\text{--}4\sigma$ . Significant differences in how the instrumental background is treated probably leads to a stark contrast in how the disk is emerging from the likelihood fits, so that most of the difference here is likely of systematic nature. One method may prefer narrower components, while the other could maybe

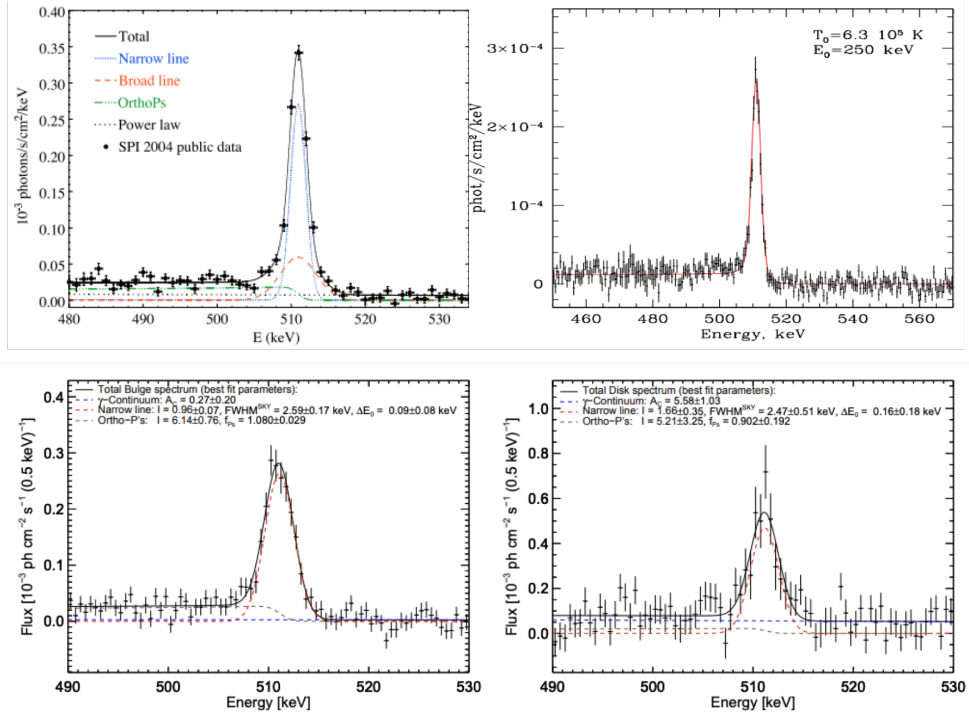


**Fig. 30** Spectra of the 511 keV line in the Galaxy with different exposure times and analysis methods (see main text). Top left: Bulge, 1.5 yr (from Jean et al., 2006). Top right: Bulge, 8.5 yr (from Churazov et al., 2011). Bottom left: Bulge, 10.5 yr (from Siegert et al., 2016). Bottom right: Disk, 10.5 yr (from Siegert et al., 2016).

identify also dimmer, more extended components. Astrophysically, both scenarios can make sense because a thin disk would represent the dense gas distribution of the Milky Way in which positrons may be expected to annihilate quickly, and a thick disk may show positrons on their way propagating from their sources in a partly ionised ISM. Since both may be true, the 511 keV disk is likely thin *and* thick.

Finally, from these and similar studies, a Galactic-wide positron annihilation rate can be inferred, given some educated guesses on the effective distances to the observed components. The observed Milky Way positron annihilation rate is therefore on the order of  $5 \times 10^{43} \text{ e}^+ \text{ s}^{-1}$ , of which 30–40% can be attributed to the bulge, and the remaining annihilation to the disk. A fraction of 10% of the bulge annihilation rate may be assigned to a point-like source in the Galactic centre, consistent with the position of the supermassive BH Sagittarius A\*, but also consistent with the size of the entire Central Molecular Zone given SPI’s angular resolution of  $2.7^\circ$ . While the bulge values are less prone to systematics and statistical uncertainties, the disk annihilation rate may be uncertain by a factor of two. This uncertainty includes the unknown effective distance, the vertical extent, and the possibility that there could be a halo component which is hard to detect for SPI (see, e.g., Purcell et al., 1997; Kinzer et al.,

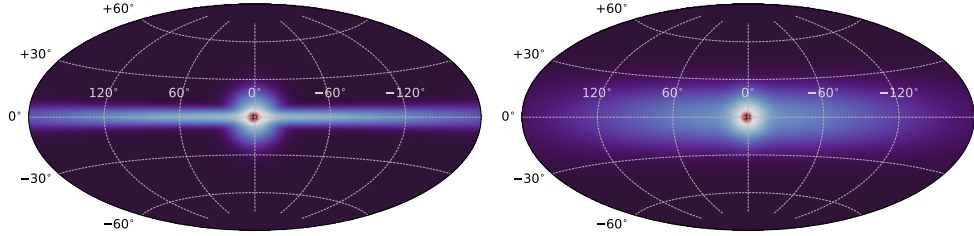


**Fig. 31** Maximum likelihood solutions of fits to the same 10.5 yr INTEGRAL/SPI dataset. Left: Thin disk model with vertical extent of  $\sim 3^\circ$  (from [Skinner et al., 2014](#), using a single 508–514 keV bin). Right: Thick disk model with vertical extent of  $\sim 10^\circ$  (from [Siegert et al., 2016](#), using 0.5 keV bins from 490–530 keV).

[2001](#)). In fact, an (almost) isotropic contribution to the 511 keV line would be entirely invisible for coded mask instruments because it would be disregarded as instrumental background in the data analysis ([Siegert et al., 2022](#)). Such a component might be very large compared to the Galactic contribution and renewed measurements of the [CGB](#) are required to fill this information gap.

A focus study of the bulge region to obtain the best-fitting *astrophysical* components rather than empirical ones, found – and corroborated ([Knöldlseder et al., 2005](#)) – that the 511 keV line and the [ortho-Ps](#) continuum trace the old stellar population in the Milky Way ([Siegert et al., 2022](#), see also Fig. 33). With a 3D smoothing kernel, it was then determined how far from these “sources”, whatever they are (see Sec. 2.9.2), positrons could actually propagate. The characteristic length scale is here  $150 \pm 50$  pc, which would either be close to annihilation *in-situ* at the astrophysical sources which may have been kicked at formation, or the consensus model that requires propagation of positrons away from their sources. The former would suggest kick velocities on the order of  $\gtrsim 50 \text{ km s}^{-1}$  within the Galactic nucleus but  $\lesssim 15 \text{ km s}^{-1}$  in the broad bulge. Positron propagation could explain the overall picture of the 511 keV signal, however only if the injection energies are below 1.4 keV, which may point to a pure nucleosynthesis origin.

Several other authors studied the positron annihilation signal in the Milky Way or tried to set limits on extragalactic objects. Non-Galactic observations can be summarised as finding only upper limits, such as for early observations of individual globular clusters and some extragalactic objects ([Knöldlseder et al., 2005](#)) or dwarf galaxies ([Siegert et al., 2016, 2022](#)).

### 2.9.2 Possible Positron Sources

In the following, we will provide a brief overview of possible and frequently discussed positrons sources. Individual source types might fill entire chapters of books, so that we will only show the most relevant points in the context of future observations. A detailed overview can be found in [Prantzos et al. \(2011\)](#) or [Siegert \(2023\)](#). A summary of the contribution of *possible* sources, including many uncertainties of both theoretical and observational studies, is shown in Fig. 32. It should be noted that this figure is, in some sense, ignorant about circumstantial (and anecdotal) evidence: some sources, such as

SNeIa, may be much weaker than shown in Fig. 32 but not necessarily contribute nothing – the figure is merely a showcase of possibilities.

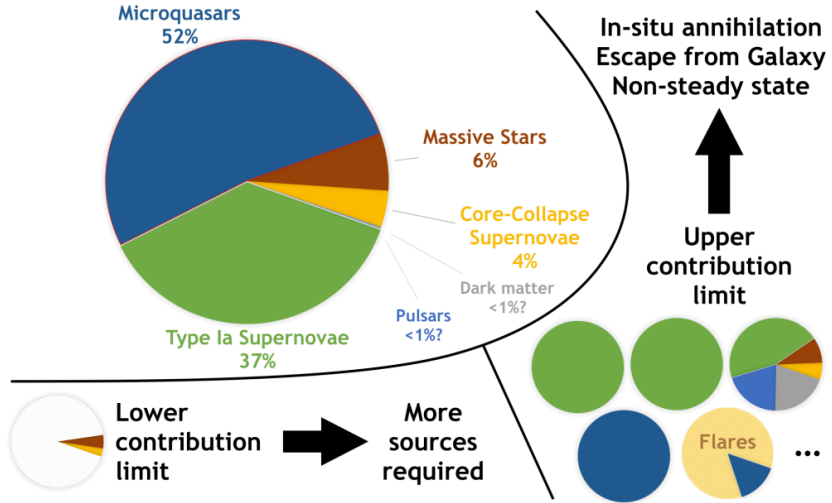


**Fig. 32** Positron production rate in the Milky Way. Top left: About 105% of positrons *seen to annihilate* can be explained by nucleosynthesis sources and microquasars. Other sources might not contribute at all to the 511 keV line (but could contribute to positron annihilation, see Sec. 2.9.4). Bottom left and right: Taking into account measurement uncertainties in production, annihilation, population sizes, and model variants. Both extreme ends would point to a non-steady-state solution of positron annihilation in the Galaxy (from Siegert, 2023).

### 2.9.2.1 Massive Stars and Supernovae

Massive stars and SNe are the only unambiguously confirmed sources of positrons in the Milky Way. Given that  $\gamma$ -rays of  $\beta^+$ -unstable radioactive isotopes have been measured ( $^{26}\text{Al}$ ,  $^{56}\text{Co}$ ,  $^{44}\text{Ti}$ ), the expected contribution, that is, the production rate from these isotopes, can be estimated. However it must be noted that there is so far no one-to-one correspondence of these radioactive isotopes and the 511 keV line, as could be expected from point-like sources such as SNRs ( $^{56}\text{Co}$ ,  $^{44}\text{Ti}$ ) or slightly extended sources such as superbubbles ( $^{26}\text{Al}$ ). These nucleosynthesis positrons are typically ejected with kinetic energies of a few hundred keV up to 1 MeV, depending on the isotope, at the position of the mother nucleus' decay. This means that one positron source map would be equivalent to the  $^{26}\text{Al}$  map of the Galaxy, or the  $^{44}\text{Ti}$  hotspots within SNRs. But since the ejection energy is mildly relativistic, the sink distribution of positrons, that is, where they annihilate, could be significantly different, given the propagation conditions in the ISM. This applies to all source types described below.

With the measured quasi-persistent  $^{26}\text{Al}$  mass in the Milky Way, the observed SNRs in  $^{44}\text{Ti}$ , and the *detected* positron annihilation flux, about  $11 \pm 3\%$  of positrons would originate in these isotopes, taking into account measurement uncertainties in the radioactivity  $\gamma$ -ray lines. In the case of  $^{56}\text{Co}$  as a daughter of  $^{56}\text{Ni}$  in both ccSNe

and **SNe Ia**, the short lifetime of the isotopes makes it difficult to estimate the escape from these sources. There are no solid measurements of the 511 keV line from **ccSNe** or **SNe Ia** directly, but infrared measurements of late lightcurves of **SNe Ia** suggest an escape fraction of positrons of 1–5% (Milne et al., 2001). This would make a contribution of **SNe Ia** to the positron annihilation budget of the Milky Way of 3–17% for an **SN Ia** rate of 0.25 per century. Given the measurements of SN2014J in M82, Siegert (2017) found an escape fraction of  $0.06^{+0.33}_{-0.06}$ , which, at face value, might explain even more than the total annihilation budget of the Galaxy.

### 2.9.2.2 Classical Novae

In **CNe**, two channels can be expected to produce positrons: either by the radioactive decays of  $^{22}\text{Na}$  and  $^{26}\text{Al}$  after the material has been ejected, or by the “annihilation flash” from  $^{15}\text{N}$  and  $^{18}\text{F}$  at the time of explosive burning on the surface of the **WD** (see Sec. 2.3). The case of  $^{26}\text{Al}$  is difficult to calibrate because the consensus model of  $^{26}\text{Al}$  only invokes massive stars to explain the 1.8 MeV signal, so that **CN** contributions are ignored. They may, however, be on the order of a few per cent, or even dominating the  $^{26}\text{Al}$ . In case of positron annihilation, this will not change the total budget, because it is the same amount of  $^{26}\text{Al}$  in the Galaxy but only assigned to different sources. For  $^{22}\text{Na}$ , a measurement of the diffuse 1275 keV line would directly calibrate the positron production rate from this isotope. However, the line has never been detected and only upper limits on the line flux, integrated over the whole Galaxy and recent ONe novae, lead to an upper limit on the positron production rate of  $\lesssim 10\%$  (Siegert et al., 2021).

The case of the “annihilation flash” is also difficult to gauge because it has also never been measured. It is expected that most, if not all, positrons annihilate directly in the expanding **CN** shell, which may result in an approximately one hour long  $\gamma$ -ray signal from positron annihilation. Estimates find a peak 511 keV flux on the order of  $10^{-3}\text{--}10^{-2}\text{ ph cm}^{-2}\text{ s}^{-1}$  for **CNe** at a distance of 1 kpc. With an effective distance to **CNe** of 5 kpc, and a **CN** rate of  $50\text{ yr}^{-1}$ , one expects to not see a quasi-persistent flux from these sources, but rather individual points from time to time. If, by some mechanism, the positrons would escape, they would only make a contribution on the order of  $10^{-5}$  of the total Galactic annihilation budget.

### 2.9.2.3 Cosmic Rays

The **CR** interactions with molecular clouds lead to the production of positively charged pions and other mesons that, at some point, will decay into positrons, however with larger energies than the nucleosynthesis positrons. It has been suggested that these positrons do not contribute to the Galactic annihilation signal because their energies are too large to be slowed down efficiently. Early studies of the in-flight annihilation spectrum in the Milky Way find limits on the injection energy of positrons on the order of 3–7 MeV (e.g., Sizun et al., 2006; Beacom and Yüksel, 2006; Churazov et al., 2011). However, these studies assume knowledge about the underlying Galactic diffuse continuum from **IC** scattering and bremsstrahlung which in themselves are barely understood (Siegert et al., 2022). It is clear that if the assumptions on the Galactic diffuse emission are relaxed, much higher injection energies, up to several tens or hundreds of MeV, are possible (Siegert, 2023). By estimates of the average **CR** spectrum

throughout the Galaxy by GeV observations, it was found that on the order of 3–10% of the positrons *seen to annihilate* may originate in CR interactions (e.g., Aharonian and Atoyan, 2000; Porter et al., 2008). The GeV map of the Galaxy, showing dense gas regions, would be the starting point of these higher-energy positrons.

#### 2.9.2.4 Pulsars

Through interactions of particles and photons with magnetic fields, pulsars, millisecond pulsars, and magnetars, could produce high-energy electron-positron pairs (see Prantzos et al., 2011; Siegert, 2023, for discussion). Also here, no measurement actually confirms the logical sequence of production in pulsars, followed by slowing down in the ISM, and final annihilation at a distance, nor the also plausible path of in-situ annihilation near the pulsar, for example in pulsar wind nebulae. Given the consensus model of pulsar emission, pair production is inevitable, and the positron production rate of all types of pulsars may be on the order of 10% for the entire Milky Way. However, also here, the energy considerations and propagation through the ISM with possible in-flight annihilation, must be considered. Individual pulsars are currently too dim to be observable at 511 keV.

#### 2.9.2.5 Black Holes

Like pulsars, the strong gravity around accreting BHs may lead to photon-photon pair production, ejection, or in-situ annihilation. There are three historical measurements that claim to have seen an annihilation feature (*not necessarily* a 511 keV line) from microquasars (Bouchet et al., 1991; Sunyaev et al., 1991, 1992; Siegert et al., 2016) – all of which are contested. Pair production in highly compact objects is inevitable whenever the pair creation threshold is met. It is then expected that an electron-positron pair-plasma is ejected, which may be related to jets observed at radio frequencies. The pair-plasma is unstable and would annihilate quickly with itself, resulting in potentially erratic Doppler-blue-shifted and Doppler-broadened features of thermal pair annihilation (Svensson, 1983; Beloborodov, 1999). However, it may also be the case that the pairs do not annihilate in-situ but rather propagate in the ISM and only annihilate later at a distance to their sources, similar to the nucleosynthesis case. Both scenarios appear plausible and would make microquasars a strong contributor to the Galactic positron budget, given that each year about one accreting BH is in outburst. The uncertainties in the total population of microquasars make estimates difficult but their total production rate may range around 50% with large systematics. Also quiescent or weakly active BHs may lead to a quasi-steady production of positrons (Bartels et al., 2018), but this population is even more uncertain than the measurable outbursts.

#### 2.9.2.6 Stellar Flares

The Sun is the only star for which we have measurements of the 511 keV line during a flare (e.g., Murphy et al., 2005, see also Sec. 2.7). The Sun is also expected to have a quasi-steady flux at 511 keV from CR interactions with the Solar atmosphere (Frost et al., 1966; Mazziotta et al., 2020) and photon-photon pair production followed by IC cooling. With the more than  $10^{11}$  stars in the Milky Way, one can therefore expect

to see a quasi-persistent flux at 511 keV that may directly follow the old stellar population. With rough assumptions, it was estimated that this quasi-persistent flux could make up to 100% of the bulge luminosity at 511 keV [Bisnovatyi-Kogan and Pozanenko \(2017\)](#). However, since the 511 keV line and the 2.2 MeV line from neutron capture on protons are almost one-to-one correlated in Solar flares, it would be expected that a diffuse 2.2 MeV line is visible in the same region with the same flux, but which is not the case (e.g., [Harris et al., 1991](#); [McConnell et al., 1997](#)). Given the upper limits on the 2.2 MeV line, the quasi-persistent flux of the 511 keV line from normal flaring stars must be on the order of 10% or less in the bulge region.

#### 2.9.2.7 *Nearby Objects*

The interactions of [CRs](#) with asteroids in the Solar System also lead to a 511 keV line (e.g., [Moskalenko and Porter, 2007](#); [Moskalenko et al., 2008](#); [Moskalenko and Porter, 2009](#)). Individual asteroids have been observed at MeV  $\gamma$ -ray energies, but an extrapolation to the entire population of the expectedly more than  $10^{20}$  objects inside the Solar System is difficult. From [GEANT4](#) simulations, a flux contribution of the asteroids towards the bulge region may be on the order of 2%, so that the entire ecliptic should show a flux of  $4 \times 10^{-4} \text{ ph cm}^{-2} \text{ s}^{-1}$ . This flux is difficult to measure with [INTEGRAL/SPI](#) because it rarely observed the ecliptic. However, since the signal is expected to be variable in time, because objects and accumulations move with respect to Earth, the bulge signal may be variable in time at this per cent level. A strong reduction of the total annihilation rate is not plausible because otherwise the asteroids accumulations would have been found already. In fact, the “[OSSE](#) 511 keV fountain” may be the cumulative effect of such asteroids integrated over several years ([Siegert et al., 2024](#)). Future observations and analyses are required to gauge the local contribution.

#### 2.9.2.8 *Dark Matter*

The case of [DM](#) will be discussed in more detail in the outlook Sec. 3.2.2. In principle, [DM](#) can explain the entire 511 keV signal statistically. But astrophysically, this would imply that other objects should be much brighter than they are: the dwarf galaxies should be visible, the halo of M31, and galaxy clusters should all show a sizeable 511 keV signal, which is not the case, limiting the power of this explanation vastly.

### 2.9.3 The Positron Puzzle

The description above can be summarised into the “Positron Puzzle”, which poses one of the biggest unsolved problems in astronomy:

1. What do we see?
2. Why does it look like that?
3. Where do the positrons come from?

While we believe to understand what we actually observe in terms of positron annihilation, that is, the 511 keV  $\gamma$ -ray line and the ortho-[Ps](#) continuum, it is, in fact, not clear how the line is formed: The line shape is the cumulative effect of [LoS](#) integrals which would weight different phases of the [ISM](#) with the emissivity from

annihilation of different channels, of positrons being slowed down by continuous and catastrophic energy losses, having propagated through the same phases according to a rather unknown diffusion coefficient (tensor)  $D_{\mu\mu}$  (e.g., [Spanier et al., 2022](#)). The lack of angular resolution in combination with MeV instrument sensitivities allows us to only probe an average spectrum across large regions in the sky and of the Milky Way. In fact, we cannot even say for certain that the observed emission features are Galactic or very nearby – clearly the spatial coincidence with the Galactic centre and the Galactic plane make this plausible, but no kinematic measurement could prove or provide the assumed distances to the celestial positron annihilation. It is again the epistemic problem of astronomy that there is no inherent distance information, and detailed modelling always carries an enormous uncertainty. In what follows, we will discuss different parts of the more extended “Positron Puzzle” briefly.

#### **2.9.3.1 Positron Transport in the Interstellar Medium?**

The distribution of annihilating positrons as a function of time, position and momentum should be described as the steady-state solution of a suitable Fokker-Planck-equation. Such a diffusion-loss treatment should include drift (re-acceleration, convection, advection, energy losses), diffusion (coefficients due to transport mode and conditions), sources (see above), and sinks (annihilation rates, cross sections, escape, leakage timescales). The problem in such a treatment is that it requires realistic 3D distributions of both, positron sources and the [ISM](#), proper injection spectra and considering turbulent magnetic fields, different transport modes and corresponding diffusion coefficients. Most of these input parameters and distributions are very uncertain, so that other treatments, such as Monte Carlo simulations of individual positrons experiencing possible interactions, have been used in the past.

In [Jean et al. \(2009\)](#), such Monte Carlo simulations have been performed based on a thorough recapitulation of possible transport modes. In collisional transport, for example, positrons propagate almost ballistically and are guided by the large-scale magnetic field in the Galaxy. Through pitch-angle scatterings in a turbulent magnetic field, the generic stopping distance for MeV positrons in typical [ISM](#) conditions is only reduced by 25%, resulting in an effective distance of  $10(n/\text{cm}^{-3})^{-1}$  kpc. This appears very large compared to the intuitive case of positrons annihilating whenever they enter dense regions. Such a treatment, however, cannot reproduce the observed features in the Galaxy: In [Alexis et al. \(2014\)](#), first nucleosynthesis sources only have been used as starting distribution to explain emission after propagation, but those fail to explain the large bulge flux, and also predict a spiral arm structure at 511 keV, but which is not seen. However, with a single Galactic outburst a few Myr ago from the direction of the Galactic centre, the tension between the production channels, propagation, and annihilation is not as severe. Certainly, this topics require more attention also for future observations.

#### **2.9.3.2 Smooth or Structured 511 keV Image?**

Most analyses of the 511 keV line as well as the [ortho-Ps](#) assume spatial models for which the spectra are extracted. This forward-folding approach has the advantage that the response function is properly included and that the uncertainties of the models

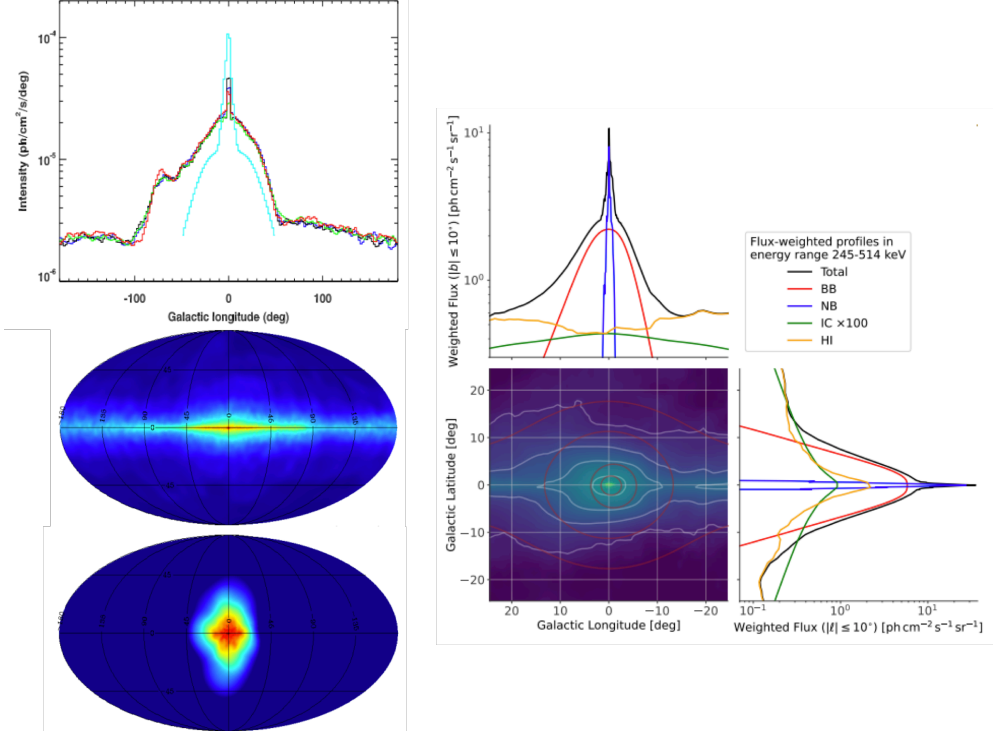


**Fig. 33** Astrophysical modelling of the 511 keV line. Left: Monte Carlo simulations of positron transport in the ISM. Top: Expected profile from only nucleosynthesis sources (colours) compared to the measured longitude profile (cyan). Middle: Expected sky map from only nucleosynthesis sources. Bottom: Simulated outburst of  $^{26}\text{Al}$  positrons in the Central Molecular Zone after 2 Myrs (from Alexis et al., 2014). Right: Best-fit model of astrophysical components of positron annihilation (ortho-Ps + 511 keV line) in the bulge region of the Galaxy. Top: Longitudinal profile. Right: Latitudinal profile. Bottom left: Combination of sky maps (coloured) compared to best-fit maximum likelihood fit (red).

used can be easily estimated by likelihood profiles. As described above, the entire Milky Way in positron annihilation (line + ortho-Ps; see also Sec. 2.9.4) can be modelled by 3–4 Gaussian-shaped components – three for bulge, and one for the disk (e.g., Skinner et al., 2014; Siegert et al., 2016). These models can be replaced by three or more astrophysically-motivated components, such as the infrared bulge and the nuclear stellar cluster, the HI or CO disk, or by DM annihilation models, on top of some IC continuum, which is always present. Astrophysical models that describe the Galaxy by the old stellar population only require a weak disk component (Siegert et al., 2022), but avoid the need for a DM halo component altogether when both the 511 keV line and the ortho-Ps component is considered (Fig. 33). The 511 keV line alone only makes less than 20% of positron annihilation in the Galaxy, so that it must not be considered by theoretical models and data analyses separately. However, due to computational constraints and the fact that the ortho-Ps continuum quickly becomes sub-dominant

towards lower energies, it is typically treated separately, especially because also the IC continuum has its own large uncertainties.

The problem with this approach is that it always includes smooth models without structure or template maps whose meanings can be interpreted in different, non-unique ways. Therefore, image reconstructions are used to obtain a possibly less-biased view of the MeV sky. But image reconstruction can come with artefacts due to improper modelling of instrumental background, for example, low-number statistics, small exposure regions, strong gradients in exposure, extremely long datasets, and changes in the imaging and spectral response. Therefore, one must take a large number of possible reconstruction algorithms and study the emerging features. The uncertainties per pixel or per region are then not trivially determined – a possible way is bootstrapping of the dataset so that individual emission features can be validated. This again is computationally very expensive and only a few tens or hundred realisations of one and the same method can be achieved unless high-performance computers are available.

The image reconstructions of the 511 keV line (e.g., Knölseder et al., 2005; Weidenspointner et al., 2008; Bouchet et al., 2010) always resulted in the bulge region, plus some more features with increasing exposure, that resulted in the 511 keV disk. An important effect of imaging the sky with an instrument like SPI that “only” sees about 1% of the sky at any given time (FoV), is that one can only see photons from direction where the instrument was actually pointed to. This trivial statement, however, has the effect of dark regions in the sky whenever there was only weak exposure. All-sky maps should therefore always be compared to the exposure maps of the respective instrument, so that also artefacts at exposure edges could easily be identified and not misinterpreted.

A truly smooth image could mean annihilation in gas, nearby objects, or stars. A structured image could show a link to point sources of 511 keV emission, similar to the case of the Cosmic X-Ray Background (CXB) that was finally resolved by ROSAT observations to be due to active galactic nuclei. Only with more than one robustly identified positron annihilation source can this part of the puzzle actually be solved.

#### 2.9.3.3 More Positrons Injected than Observed?

Given the large uncertainties in measuring positron sources, and the fact that some sources have not been identified as sources even though it is suggested (CNe, SNe Ia, etc.), there is a possibility that more positrons are created than observed to annihilate. This could be due to an observational bias with coded mask telescopes that cannot observe isotropic emission (Sieger et al., 2022). As has been suggested by OSSE observations, there could be a much stronger halo, which however would be difficult to identify with SPI. In fact, there could be an almost or entirely isotropic component of positron annihilation that would make up some part of the CGB. By previous measurements, such a scenario is not excluded as most CGB measurements above 200 keV and below 30 MeV are notoriously uncertain and not highly resolved. With occultation observations or with a dedicated Compton telescope that sees large parts of the sky and with high spectral resolution, such a measurement could be made possible.

The observed *annihilation rate* (of the Milky Way) is on the order of  $5 \times 10^{43} \text{ e}^+ \text{ s}^{-1}$  – the potential positron *production rate*, taking into account uncertainties in models,

observations, cross sections, etc., could be a factor of five higher (Siegert, 2023, see also Fig. 32). Observations of another Milky-Way-like galaxy, such as M31, could gauge this number because the entire galaxy would be in the FoV and the distance-question would not be much of an issue. However, if the *production rate* is significantly higher than the *annihilation rate*, where do the remaining positrons go? A possible solution would be the escape into intergalactic medium in which highly relativistic positrons would potentially take Gyrs to cool to produce a 511 keV line, so that their contribution to the CGB spectrum might be small. On the other hand, since this effect might have occurred already over the time scale of the Galaxy, the intergalactic positrons may also have relaxed to a sizeable steady-state annihilation rate.

#### 2.9.3.4 In-Flight Annihilation?

So far, no firm detection of in-flight annihilation has been detected. Previous limits for the injection energy are on the order of only 3–7 MeV (e.g., Sizun et al., 2006; Beacom and Yüksel, 2006) which is at odds with the high-energy positrons observed at GeV energies. Siegert (2023) contested these values by re-investigating the data analysis: Given that the IC continuum is uncertain in itself and that the combination of different instruments that measured at two different epochs with different apertures is delicate, and given updated measurements from SPI that finally superseded the accuracy of the COMPTEL data points (Siegert et al., 2022), injection energies of up to 100 MeV suddenly appeared possible. If this analysis turns out to be accurate, it would open up space for even more sources, which have previously been rejected because of too high injection energies, such as pulsars, CRs, weakly interacting massive particles (WIMPs), or  $\gamma$ -ray bursts.

Two recent studies investigate the possibility of in-flight annihilation in the Galactic bulge region. While Knöldlseder et al. (2025) focus on a re-analysis of the energy range of 0.7–30 MeV with CGRO/COMPTEL, Das et al. (2025) combined the most recent INTEGRAL/SPI analysis (Siegert et al., 2022; Berteaud et al., 2022), and data from CGRO. The paper by Knöldlseder et al. (2025) claims to have detected positron annihilation in flight, and sets a strict injection energy of positrons of  $\approx 2$  MeV. This would rule out positrons from radioactive decays ( $\lesssim 1$  MeV) and from CR secondaries ( $\gtrsim 100$  MeV). The work by Das et al. (2025) finds less stringent bounds on the injection energy of positrons up to  $\sim 100$  MeV, which would allow more source types to contribute, such as pulsars and CR positron production. Das et al. (2025) make the important remark that the excess found may not necessarily be due to positrons annihilating in flight, but that a population of electrons with a cut-off around an energy of 100 MeV would show a similar spectrum from bremsstrahlung. The authors find that the bremsstrahlung component would always be dominant, except for photon energies close to the cut-off. The spectrum of Knöldlseder et al. (2025) in Fig. 34, top, shows only the excess component, the authors find above the Galactic ridge, which already includes the bremsstrahlung of CR electrons. The bottom spectrum of Fig. 34 shows the total Galactic spectrum in circular a 9°-radius region around the Galactic centre from Das et al. (2025). While the spectral analyses and models differ in detail, it becomes clear that with improved analysis techniques, a long-sought component could finally be studied in detail.

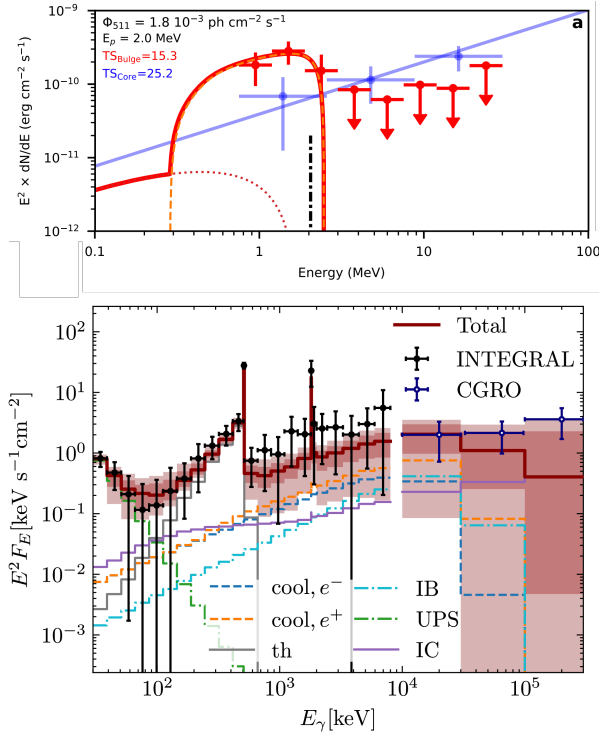


**Fig. 34** Measured continuum spectrum in the Milky Way bulge region. Top: CGRO/COMPTEL analysis (red data points: bulge, blue data points: centre) with spectral fit of in-flight annihilation of positrons with an injection energy of 2 MeV (dashed orange) and bremsstrahlung (dotted) (adapted from Knöldlseder et al., 2025). Bottom: INTEGRAL (black data points) and CGRO (blue data points) analysis of a circular  $9^{\circ}$ -radius region around the Galactic centre, together with a multi-component fit and 1 and  $2\sigma$  (shaded red) bands (from Das et al., 2025).

### 2.9.3.5 Similarities to Infrared Emission and Dark Matter

*Old stars.* Fitting full-sky maps of other wavelengths to the raw  $\gamma$ -ray data results typically in bad fits. This is true except for the maps around 1.25–4.9 micron, i.e. at infrared wavelengths that mostly show starlight. This points to the or an old population of stars, as opposed to the case of  $^{26}\text{Al}$  from young massive stars, but which has been proven to a positron source. However, alternative explanations for this match may come from flaring stars. As described above, Bisnovatyi-Kogan and Pozanenko (2017) suggest that all the *annihilating* positrons in the Milky Way come from main sequence and evolved stars. While this study probably predicts too much 511 keV flux, it would naturally explain the morphology and the spectrum, and would not require a lot of positron propagation. Good candidates to further test this scenario are globular clusters to identify point-like enhancements above the diffuse emission. Alternatively, satellite and other galaxies should then show a 511 keV flux that only scales with stellar mass. Only future observations with improved sensitivity or detailed analyses with the 22 yr of INTEGRAL/SPI observations could verify such a scenario.

*Dark matter.* Navarro-Frenk-White (NFW) profiles squared can replace the bulge components unless other physically motivated templates are used, again pointing to an old stellar population (see above). If the 511 keV emission *and* the ortho-Ps continuum *and* the inflight annihilation continuum all point to DM, it potentially points to a DM particle in the MeV mass range (De la Torre Luque et al., 2024a,b, 2025). However then, the annihilation cross section would be extremely large compared to the thermal relic cross section (Slatyer and Wu, 2017). Other sources would then be required to explain the data. It is not formally ruled out that some positrons are due to DM, but there are always other sources to explain the signal. DM, be it in the MeV mass range or GeV–TeV, would always add more difficulties than solutions because suddenly other objects should be visible. More details about the DM case can be found in Sec. 3.2.2.

#### 2.9.4 Positron Annihilation is not Always a 511 keV Line

As already mentioned several times in the previous sections, *positron annihilation does not always result in a 511 keV line*. In fact, the 511 keV line is the rarer case in the ISM, given that most positrons form Ps with a fraction of 90–100%. This means that at least 3.1, up to maximally 4.5, times the flux of the 511 keV is found in the ortho-Ps continuum. Solving Eq. (23) for the ratio  $R_{32}$  of ortho-Ps continuum vs. 511 keV line flux sets the *total annihilation flux of thermalised positrons* to

$$F_{\text{ann}}^{\text{th}} \approx (1 + R_{32})F_{511}. \quad (46)$$

Furthermore, the in-flight annihilation spectrum of mildly and strongly relativistic positrons would add a continuum that depends strongly on the injection energy and the exact cooling conditions. The survival probability,

$$P \equiv P(E_{\text{kin}}, m_e) = \exp \left( -n_X \int_{m_e}^{E_{\text{kin}}} dE \frac{\sigma(E)}{\left| \frac{dE(E, n_X)}{dx} \right|} \right), \quad (47)$$

where  $\sigma(E)$  is the total annihilation cross section, and  $\left| \frac{dE(E, n_X)}{dx} \right|$  is the stopping power (energy loss rate, cooling function) of a positron propagating in a medium with density  $n_X$ , suggests that the *total annihilation flux* can be expressed as

$$F_{\text{ann}}^{\text{tot}} = (1 + R_{32} + R_{\text{IA}})F_{511}. \quad (48)$$

Here, the ratio of the in-flight annihilation flux and 511 keV line flux,  $R_{\text{IA}}$ , is given by

$$R_{\text{IA}} = \frac{1}{1 - \frac{3}{4}f_{\text{Ps}}} \frac{1 - P}{P}. \quad (49)$$

With typical values of  $P$  in the ISM of 80–95% (e.g., Beacom and Yüksel, 2006; Siegert et al., 2022), the in-flight annihilation continuum is expected to be on the order of 20%–100% of the 511 keV line flux. However, since the spectrum is spread out to energies equivalent to the injection energies of positrons, the in-flight annihilation

spectrum is notoriously difficult to detect. In fact, so far all studies failed to uniquely identify positron annihilation in flight as an additional component above the Galactic diffuse emission. Given Eq. (48), it is clear that the 511 keV line is just one part of the *positron annihilation spectrum*, and certainly not the strongest one.

It should be noted here that there are also other positron annihilation spectra:

1. The “accelerator case” in which relativistic positrons interact and potentially annihilate with relativistic electrons can lead to doubly peaked or singly peaked spectra, depending on the kinetic energies.
2. “Thermal pair plasma” annihilation happens when an electron-positron pair-plasma, for example as ejected in jets of microquasars or active galactic nuclei, is relaxing. Here, the relativistic Doppler effects broadens and blue-shifts the annihilation feature (Svensson, 1983). *In general, there is no narrow 511 keV “line” in microquasars unless there are very specific circumstances (Mirabel et al., 1992).*
3. The “narrow 511 keV line” from the Galactic bulge region is actually broadened. The true width depends on the **ISM** conditions such as temperature, composition, and ionisation state. There is also a “broad 511 keV line” from the same region.
4. Positron annihilation in dense material, such as atmospheres, rocks, asteroids, dust, etc., will inevitably lead to a “narrow 511 keV line”.

### 3 Outlook

*Written by Thomas Siegert, with contributions from multiple authors (see below)*

#### 3.1 Laboratory Measurements for the Production of $\gamma$ -Ray Emitters

*Written by Nicolas de Séréville*

The MeV band, covering two energy decades, is particularly interesting as it corresponds to the energy range of atomic nuclear transitions, where MeV  $\gamma$ -rays are produced either during nuclear processes or interactions. Observations in this spectral range provide a unique window to directly study nucleosynthesis by measuring the abundance of radionuclides, rather than inferring elemental abundances from observations at other wavelengths. Comparing observed abundances with those predicted by astrophysical models is essential for understanding astrophysical objects. These models incorporate multiple ingredients, and abundance predictions are closely tied to thermonuclear reaction rates.

##### 3.1.1 Reaction Rates, Nuclear Cross-Sections and Their Determination

In a stellar plasma where the kinetic energy of nuclei is given by the thermal agitation velocity, and for a non-degenerate perfect gas where the velocity follows the Maxwell-Boltzmann distribution, thermonuclear reaction rates are defined per particle pair (in units of  $\text{cm}^3 \text{s}^{-1}$ ) as (Iliadis, 2015):

$$\langle \sigma v \rangle = \sqrt{\frac{8}{\pi \mu}} \cdot \frac{1}{(k_B T)^{3/2}} \int_0^\infty \sigma(E) E e^{-E/k_B T} dE, \quad (50)$$

where  $\mu$  is the reduced mass of the interacting nuclei,  $k_B$  is the Boltzmann constant,  $T$  is the temperature at which the reaction rate is evaluated, and  $\sigma(E)$  is the energy-dependent cross-section of the reaction. Thermonuclear reaction rates are crucial inputs to stellar models, with cross-sections being the fundamental physical quantities that need to be determined, either through theoretical calculations or experimental measurements. However, the experimental determination of cross-sections of nuclear reactions relevant to astrophysics presents significant challenges.

In astrophysical environments, and for interacting charged-particles, nuclear reactions occur at low relative energies in the so-called Gamow peak, located around typical energies of a few tens to a few hundreds of keV in quiescent burning environments, and around several hundreds of keV to a few MeV during explosive nucleosynthesis. The Gamow peak (Fig. 35) results from the product of the terms present in the integrand of Eq. (50). Indeed, cross-sections drop exponentially at low energies because of the Coulomb (in case of charged particles) and centrifugal barriers (given by the relative angular momentum of interacting nuclei), while the Maxwell-Boltzmann distribution approaches zero for large energies.

There are two experimental approaches for measuring cross-sections relevant to astrophysics. In direct measurements, the cross-section of the astrophysical reaction

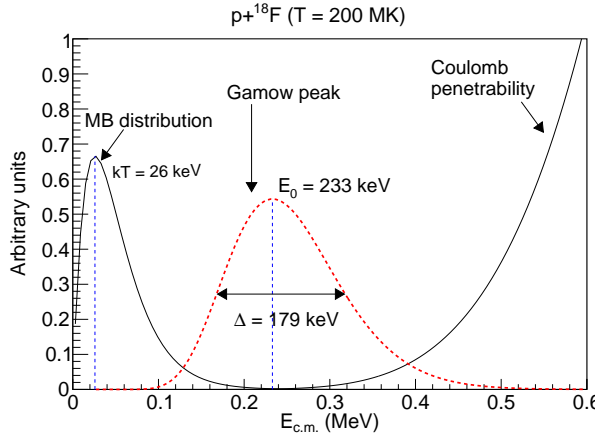


**Fig. 35** Maxwell-Boltzmann distribution, Coulomb penetrability and Gamow peak for the  $p + {}^{18}\text{F}$  system at  $2 \times 10^8$  K relevant for the  ${}^{18}\text{F}(p, \alpha){}^{15}\text{O}$  reaction and the prediction of the  $\gamma$ -ray emission at  $\leq 511$  keV in CNe.

is the one which is measured in the laboratory, at the lowest energy possible. However, because the cross-sections are extremely small, and well below the Coulomb and centrifugal barriers, dedicated facilities and experimental setups are used to suppress background signals which would otherwise prevent the measurement at the lowest energies. These measurements include the use of recoil separators (e.g., DRAGON (D'Auria and DRAG. O. N. Collaboration, 2002), St Georges (Couder et al., 2008), SECAR (Berg et al., 2018)), coincidence detection systems (e.g., STELLA Heine et al., 2018), and underground laboratories (e.g., LUNA (Greife et al., 1994), JUNA (Liu et al., 2016), Felsenkeller (Szucs et al., 2019)), among others. When direct measurements are not feasible, indirect techniques such as transfer reaction method, Coulomb dissociation method, surrogate reactions and Trojan Horse Method are good alternatives (see Hammache and de Sérerville, 2021, and references therein). In these approaches the experiments are usually performed at energies above the Coulomb barrier where cross-sections are significantly higher than in direct measurements. However, since the reactions studied in the laboratory differ from the astrophysically ones, the extraction of the relevant information, and the link with the cross-section of interest, rely on nuclear theory. Moreover, many astrophysical processes involve unstable nuclei, which presents additional challenges for experimental measurements, further complicating the determination of reliable cross-sections.

### 3.1.2 Observed $\gamma$ -Ray Emitters

The  $\gamma$ -ray emission of only a few limited number of radionuclides has been observed in the Milky Way by balloon-borne and space-borne instruments so far. Here, we recapitulate on the detected ones and then give details on their nuclear structure and laboratory measurements. The isotope  ${}^{26}\text{Al}$  undergoes  $\beta^+$ -decay to the first excited state of  ${}^{26}\text{Mg}$ , followed by de-excitation to the ground state that produces a  $\gamma$ -ray line at 1809 keV (see Sec. 2.1). This  $\gamma$ -ray emission is observed in the Galactic plane

and is mainly associated to the population of massive stars during their core-collapse and/or during their Wolf-Rayet phase for the most massive ones. **AGB** stars and **CNe** are also expected to contribute to the  $^{26}\text{Al}$  budget. In these astrophysical sites,  $^{26}\text{Al}$  is mainly produced by radiative proton capture on  $^{25}\text{Mg}$ . The most influential resonances above the  $p+^{25}\text{Mg}$  threshold are located at  $E_r^{\text{c.m.}} = 59$ -, 93-, 191- and 305- keV, the lowest two dominating the  $^{25}\text{Mg}(\text{p},\gamma)^{26}\text{Al}$  reaction rate in the temperature region  $(0.02\text{--}0.15) \times 10^9 \text{ K}$ , and the other two above. The strength of the highest three resonances has been measured directly at LUNA (Limata et al., 2010; Strieder et al., 2012), and at JUNA for the  $E_r^{\text{c.m.}} = 93$  keV one (Su et al., 2022). For the lowest resonance at  $E_r^{\text{c.m.}} = 59$  keV its energy is too low for direct measurements and its resonance strength is computed using the proton width deduced from one-proton transfer reactions such as  $(^3\text{He},\text{d})$  (Champagne et al., 1989; Rollefson et al., 1990) and more recently  $(^7\text{Li},^6\text{He})$  (Li et al., 2020). The resonance strengths agree within uncertainty when several determinations have been reported, and the thermonuclear  $^{25}\text{Mg}(\text{p},\gamma)^{26}\text{Al}$  reaction rate has in the end an uncertainty smaller than 20% over the whole temperature range covered by the different astrophysical sites producing  $^{26}\text{Al}$ .

The main destruction mode of  $^{26}\text{Al}$  in stellar environments is either through proton or neutron capture. During core H-burning in massive stars and in **AGB** stars,  $^{26}\text{Al}$  is destroyed through the  $^{26}\text{Al}(\text{p},\gamma)^{27}\text{Si}$  reaction whose rate is dominated by a single  $\ell_p = 0$  resonance at  $E_r^{\text{c.m.}} = 128$  keV. Transfer reactions have been used to determine the single-particle width of its associated state in  $^{27}\text{Si}$  (Vogelaar et al., 1996) and of its analogue in  $^{27}\text{Al}$  (Pain et al., 2015; Lotay et al., 2020). These two approaches are in disagreement by a factor of four, which could be solved with a direct measurement of the resonance strength when more intense  $^{26}\text{Al}$  beams become available. At higher temperatures in **CNe**, the destruction of  $^{26}\text{Al}$  is dominated by the  $E_r^{\text{c.m.}} = 188$  keV resonance. While its spin and parity are now confirmed to be  $11/2^-$ , its precise energy is still not accurately determined, and differs by 5 keV between DRAGON measurement (Ruiz et al., 2006) and  $\gamma$ -ray studies (Lotay et al., 2009). During hydrostatic C-shell and explosive Ne/C-shell burning phases in massive stars,  $^{26}\text{Al}$  is destroyed by neutron capture. Spectroscopic information on  $^{27}\text{Al}$  is needed up to 500 keV above the  $n+^{26}\text{Al}$  threshold, but the data remain incomplete. Direct measurements have been performed using the high neutron flux beam-line EAR-2 at n\_TOF CERN, and at the GELINA facility (Lederer-Woods et al., 2021a,b) allowing cross-sections determination up to about 150 keV above the  $n+^{26}\text{Al}$  threshold. Even though indirect measurements identified  $^{27}\text{Al}$  levels up to 500 keV above the  $n+^{26}\text{Al}$  threshold (Benamara et al., 2014), the resonance strength are not yet determined. The isomeric  $^{26m}\text{Al}$  state has a short lifetime of about 6 s, allowing rapid thermal equilibration with the ground state under typical stellar temperatures. Its presence slightly alters the effective destruction and production rates of  $^{26}\text{Al}$  in stellar interiors because thermal coupling can shift population between the two levels. In laboratory measurements, however, the isomer decays before significant reactions can occur, so experimental cross sections generally probe only the ground-state behaviour. Further information concerning the nuclear aspects of  $^{26}\text{Al}$  nucleosynthesis including also the isomeric state at 228 keV can be found in recent reviews (e.g., Diehl et al., 2021; Laird et al., 2023).

The isotope  $^{60}\text{Fe}$  decays via the chain  $^{60}\text{Fe} \rightarrow ^{60}\text{Co} \rightarrow ^{60}\text{Ni}$ , producing two  $\gamma$ -ray lines at 1173 and 1332 keV that have been observed in the Galactic plane by **INTEGRAL/SPI** and **RHESSI** (see Sec. 2.2). The  $^{60}\text{Fe}$  radionuclide is produced in massive stars and intermediate-mass thermal-pulsating **AGB** stars during the *s*-process which results from a competition between slow radiative neutron captures and  $\beta^-$ -decays.  $^{60}\text{Fe}$  nucleosynthesis occurs for temperatures greater than  $5 \times 10^8$  K and neutron densities on the order of  $\sim 10^{10-12} \text{ cm}^{-3}$  (Limongi and Chieffi, 2006). For temperatures smaller than  $2 \times 10^9$  K,  $^{60}\text{Fe}$  is mainly produced by neutron capture on the unstable nucleus  $^{59}\text{Fe}$  and destroyed by the  $(n, \gamma)$  reaction. Indeed, the destruction of  $^{60}\text{Fe}$  by neutron capture is always faster than the  $\beta^-$ -decay of  $^{60}\text{Fe}$  for which the terrestrial lifetime is now well determined as  $\tau = (3.78 \pm 0.06)$  Myr (Rugel et al., 2009). The Maxwellian averaged  $^{60}\text{Fe}(n, \gamma)^{61}\text{Fe}$  cross-section at  $k_B T = 25$  keV has been measured by activation and is  $9.9_{-1.4(\text{stat})}^{+2.8(\text{syst})}$  mbarn (Uberseder et al., 2009), confirming that the resonant capture is dominant (Giron et al., 2017). The main nuclear uncertainty comes from  $^{60}\text{Fe}$  production which requires the nuclear flow to bypass the  $^{59}\text{Fe}$  bottleneck. The stellar lifetime of  $^{59}\text{Fe}$  is much shorter than its terrestrial lifetime ( $\tau = 64.2$  d) because of the thermal excitation of its excited state at 472 keV which decays more favourably to the ground state of its daughter nucleus. The effect of this excited state has only been recently studied experimentally at NSCL using the charge exchange  $^{59}\text{Co}(t, ^3\text{He})^{59}\text{Fe}$  reaction (Gao et al., 2021). The obtained stellar lifetime is in agreement with the latest theoretical estimates (Li et al., 2016), but a factor 3.5 larger than the  $^{59}\text{Fe}$  decay rate used in stellar models (Langanke and Martínez-Pinedo, 2001), leading to a decrease by 40% of the  $^{60}\text{Fe}$  production yield for a  $18 M_\odot$  star of Solar metallicity (Gao et al., 2021). Due to the unstable nature of  $^{59}\text{Fe}$ , the  $^{59}\text{Fe}(n, \gamma)^{60}\text{Fe}$  cross-section has been the focus of several indirect experimental studies. Earlier studies relying on the Coulomb dissociation method (Uberseder et al., 2014) and the surrogate method (Yan et al., 2021) agree within uncertainty. However, a recent work using the  $\beta$ -Oslo method finds a significant enhancement of the  $\gamma$ -ray strength function at low energies, increasing the Maxwellian averaged cross-section by a factor of 1.6–2.1, leading to an increase of almost a factor of two of  $^{60}\text{Fe}$  yields for Solar metallicity stars of  $15-25 M_\odot$  initial mass (Spyrou et al., 2024).

Other astrophysical  $\gamma$ -ray emitters are  $^{44}\text{Ti}$  and  $^{56}\text{Co}$  produced by **SNe** (see Sec. 2.4).  $^{44}\text{Ti}$  has been observed in SN 1987A (Grebenev et al., 2012; Boggs et al., 2015) and **Cas A** (Grefenstette et al., 2014; Weinberger et al., 2020) **ccSNe**. The  $\gamma$ -ray lines associated to the  $^{56}\text{Ni}$  decay chain have been observed in the **SN Ia** SN 2014J (Churazov et al., 2014; Diehl et al., 2015, 2014; Isern et al., 2016). The nucleosynthesis of  $^{44}\text{Ti}$  and  $^{56}\text{Ni}$  happen during  $\alpha$ -rich freeze-out in the deepest layers of a massive star during its core-collapse, providing the opportunity to constrain properties of **ccSN** explosions. Because the temperatures are typically between 4 and  $10 \times 10^9$  K, the nucleosynthesis network is extended and involves many nuclei, charged particle and weak reaction rates. Several sensitivity studies have been conducted (e.g., Magkotsios et al., 2010; Subedi et al., 2020; Hermansen et al., 2020) to assess the rates impacting the most  $^{44}\text{Ti}$  and  $^{56}\text{Ni}$  nucleosynthesis, pointing out a dozen of key reactions including  $(\alpha, p)$  and  $(p, \gamma)$ .

### 3.1.3 Yet to be Observed $\gamma$ -ray Emitters

Several nuclear  $\gamma$ -ray lines have yet to be observed. A few of them originate from CNe which results from a thermonuclear runaway at the surface of an accreting WD powered by explosive hydrogen burning (see Sec. 2.3). The main  $\gamma$ -ray emitters produced are  $^{7}\text{Be}$ ,  $^{13}\text{N}$ ,  $^{18}\text{F}$ ,  $^{22}\text{Na}$  and  $^{26}\text{Al}$ .

Even though the 1.8 MeV  $\gamma$ -ray line is mostly associated with massive stars and ccSNe, the contribution of CNe is not well known (Vasini et al., 2025) and could be 12% or higher (e.g., Laird et al., 2023; Vasini et al., 2025). In this context, the  $^{25}\text{Al}(\text{p},\gamma)^{26}\text{Si}$  reaction producing  $^{26}\text{Si}$ , which decays to  $^{26}\text{Al}$ , is the last reaction for which the uncertainty still needs to be reduced. The reaction rate uncertainty at  $10^8$  K of a factor of ten is associated with the lack of spectroscopic information for  $^{26}\text{Si}$  states, mainly the  $E_r^{\text{c.m.}} = 163$  keV resonance. This situation arises from the difficulty to produce intense radioactive  $^{25}\text{Al}$  beams, so that several properties have to be estimated using theoretical shell model calculations or properties of analogous levels in the mirror nucleus  $^{26}\text{Mg}$ . A recent experiment was performed at FRIB using the GRETINA  $\gamma$ -ray array and the S800 magnetic spectrometer with the goal to measure the strength of  $^{26}\text{Si}$  resonant states (Fougères et al.).

The 1275 keV  $\gamma$ -ray line associated with the  $^{22}\text{Na}$  decay is particularly interesting since it could be used as a proxy to the CN rate in the Milky Way because the lifetime of  $^{22}\text{Na}$  ( $\tau = 3.75$  yr) is much longer than the time interval between two outbursts (CN rate  $\sim 50_{-23}^{+31}$  yr $^{-1}$  (Shafter, 2017)). The main nuclear uncertainty used to come from  $^{22}\text{Na}(\text{p},\gamma)^{23}\text{Mg}$  whose reaction rate is dominated by the  $E_r^{\text{c.m.}} = 204$  keV resonance. On the one hand, direct determinations of the resonance strength disagree at the  $5\sigma$  level by at least a factor of four (Seuthe et al., 1990; Stegmüller et al., 1996; Sallaska et al., 2010). On the other hand, indirect measurements give a resonance strength at least five times smaller than the direct ones. This tension was alleviated by a recent study of the  $^{3}\text{He}(^{24}\text{Mg},^{4}\text{He})^{23}\text{Mg}$  reaction at GANIL, where the strength of the  $E_r^{\text{c.m.}} = 204$  keV resonance was determined using the AGATA  $\gamma$ -ray array together with the VAMOS magnetic spectrometer, and the SPIDER silicon detector (Fougères et al., 2023). In this approach, both the lifetime ( $\tau = 11_{-5}^{+7}$  fs) and proton branching ratio ( $\text{BR}_p = 0.68 \pm 0.17$ ) were determined, which, combined with existing measurements, give a consolidated resonance strength  $\omega\gamma = 0.24_{-0.04}^{+0.11}$  meV, consistent with indirect measurements. The uncertainty on the  $^{22}\text{Na}(\text{p},\gamma)^{23}\text{Mg}$  reaction rate is now reduced to 10–40% at the CN peak temperature, resulting in an uncertainty of 1.4 in the estimated  $^{22}\text{Na}$  yield (Fougères et al., 2023).

The  $\gamma$ -ray emission at and below 511 keV is produced by positrons, coming mostly from the  $\beta^+$ -decay of  $^{18}\text{F}$ , annihilating in the material ejected by the outburst. This emission happens before the visual peak luminosity of the CN, which makes it a difficult observational target. However, its observation would bring very valuable information on the nucleosynthesis and on the dynamic of the ejection since the lifetime of  $^{18}\text{F}$  ( $\tau = 159$  min) is similar to the characteristic time for the envelope to become transparent to  $\gamma$ -rays. The main remaining nuclear uncertainty for  $^{18}\text{F}$  nucleosynthesis comes from its destruction path through the  $^{18}\text{F}(\text{p},\alpha)^{15}\text{O}$  reaction. This reaction is still the focus of many experimental studies despite efforts over more than two decades (de Oliveira Santos, 2025). It represents a complex case where the number and

energy of  $\ell = 0$   $^{19}\text{Ne}$  states in the vicinity of the  $p+^{18}\text{F}$  threshold are not yet firmly established. Direct measurements focused on the determination of the cross-section at low-energy (de Sérerville et al., 2009; Beer et al., 2011), with the goal to constrain the sign of interferences between  $s$ -wave states, whose effect is maximum in the Gamow peak. A wide variety of indirect methods (see, e.g., de Oliveira Santos, 2025, and references therein) have also been used to determine the properties of individual states in the compound nucleus  $^{19}\text{Ne}$  above and below the proton threshold. However, the current understanding is still incomplete mainly due to missing properties of  $\ell = 0$  states below the proton threshold, the sign of their interference with other  $s$ -wave states above the proton threshold, for which their  $\alpha$ -particle width is unknown. This situation leads to an uncertainty on the  $^{18}\text{F}(p,\alpha)^{15}\text{O}$  reaction rate about a factor of three, which translates to a  $^{18}\text{F}$  yield uncertain by more than a factor of ten (Kahl et al., 2021).

Massive stars during their core-collapse produce a large number of nuclides, and the characteristic  $\gamma$ -ray lines of a few of them have been observed (see previous sections). With improved line sensitivity in future MeV observatories other  $\gamma$ -ray emitters such as  $^{43}\text{K}$ ,  $^{48}\text{Cr}$ ,  $^{48}\text{V}$ ,  $^{52}\text{Mn}$ ,  $^{44,47}\text{Sc}$ ,  $^{47}\text{Ca}$ ,  $^{51}\text{Cr}$  and  $^{59}\text{Fe}$  could potentially become observable (Timmes et al., 2019). Many of these nuclides have lifetimes from a few hours to a few days, requiring a fast mixing of material to the outer layers where the  $\gamma$ -rays can escape. A recent sensitivity study focusing on the explosive silicon burning phase in a  $12\text{ M}_\odot$  massive star has identified key reaction rates that influence the synthesis of these nuclides (Hermansen et al., 2020).

### 3.1.4 Perspectives

Predictions of elemental and isotopic yields are strongly linked to nuclear cross-sections and thermonuclear reaction rates. Yet, their determination remains very challenging due to the low, sub-Coulomb reaction energies and the radioactive nature of the species involved. On the one hand, next generation facilities such as FRIB (FRIB) and RAON (Kim, 2020), equipped with state of the art detection systems, should significantly improve cross-sections determination, leading to more reliable predictions of  $\gamma$ -ray emitters production. On the other hand, future MeV  $\gamma$ -ray missions such as COSI (Kierans et al., 2017), AMEGO (AMEGO) or newASTROGAM (ASTROGAM) will observe these  $\gamma$ -ray lines with unprecedented sensitivity. Combined with other multi-messenger instruments, they will also be able to detect  $\gamma$ -rays from BNSMs and trace  $r$ -process nucleosynthesis (Hotokezaka et al., 2016) (see Sec. 2.5). The interplay between laboratory measurements and  $\gamma$ -ray observations are here at the heart of nuclear astrophysics and more collaboration should be encouraged on all levels.

## 3.2 Quo Vadis, $\gamma$ -Ray Line Science?

### 3.2.1 Neutron Capture Line: 2223 keV

*Written by Thomas Siegert*

The 2223 keV line from the neutron capture on protons to form deuterium is particularly strong in Solar flares (Sec. 2.7). But besides the detection from the Sun and a few

rare terrestrial cases, the 2.2 MeV has not been observed from outside the Solar System. It has, however, the potential to revolutionise MeV  $\gamma$ -ray astrophysics because it relates to more than stellar flares. In the following, we will present three cases for how a detection of the 2.2 MeV might contribute to our understanding of difference sources.

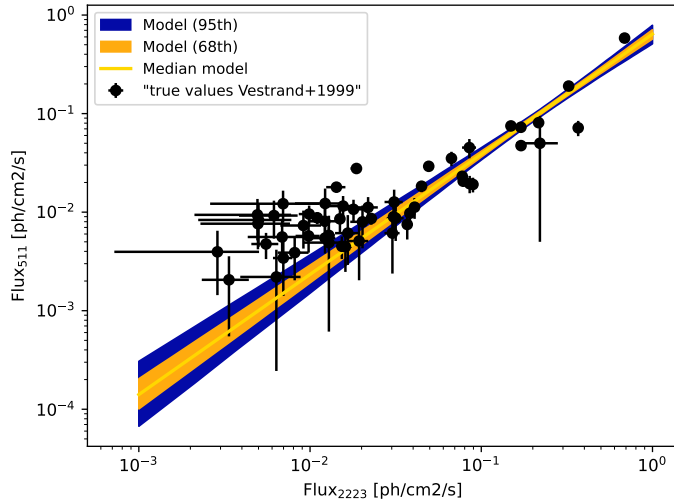


**Fig. 36** Correlation between the prompt 511 keV line due to electron-positron annihilation and the 2.2 MeV line due to neutron capture in Solar flares. Shown are data from [Vestrand et al. \(1999\)](#) ([Mittal et al. \[2025; in prep.\]](#)).

### 3.2.1.1 Stellar Flares and the 511 keV Line

As mentioned before in Secs. 2.7 & 2.9.2, the Sun is known to flare with a certain flare-energy frequency distribution that often results in two prominent  $\gamma$ -ray lines – the 511 keV line from positron annihilation and the 2.2 MeV line from neutron capture. In fact, there is a strong one-to-one correlation between the fluxes of both lines in the Sun (Fig. 36). This means that if parts of the Galactic 511 keV line are due to one hundred billion intermittently flaring stars ([Bisnovatyi-Kogan and Pozanenko, 2017](#)), a similar flux would be expected at 2.2 MeV. As it turns out, only up to 10% of the annihilation line can potentially be explained by flaring stars as otherwise, a diffuse 2.2 MeV line would have already been detected ([McConnell et al., 1997](#)). From a bottom-up model of flaring stars, extrapolating from the Sun as the best-studied star, a diffuse extended 2.2 MeV line with a flux level of  $10^{-6}$ – $10^{-4}$  ph cm $^{-2}$  s $^{-1}$ , distributed identical to the 511 keV line, would be expected. This is certainly within the range of future MeV observatories. A detection of the 2.2 MeV line co-spatial with the 511 keV line would be a spectacular result that would solve large parts of the “Positron Puzzle”, even though only 10% at most can be explained. But it would point to a possibility that there is, indeed, in-situ annihilation happening – and maybe in more than one source type.

### 3.2.1.2 A Relic 2.2 MeV Background? – The ‘Hydrogen Calorimeter’

After early measurement of the [CGB](#), such as by the Apollo 15 mission, a suspicious ‘bump’ around 1–2 MeV was claimed. [Leventhal \(1973\)](#) speculated that this emission feature may be due to deuterium formation in a warm Galactic halo. In fact, [CR](#) spallation will inevitably lead to free neutrons in the [ISM](#) and the intergalactic medium. If the thermalisation time scale of the neutrons is faster, or at least not much longer, than the neutron decay time, they might be captured by protons and emit a 2.2 MeV photon. While this process is the general production channel in Solar flares, [Ramaty and Lingenfelter \(1980\)](#) pointed out that the thermalisation time scale might be on the order of  $10^4$  s for a  $1\text{ cm}^{-3}$  [ISM](#), while the neutron decay time is 880 s. This means that only a few per cent of neutrons will be captured. However, this would mean that the 2.2 MeV brightness would integrate the *entire* sub-GeV [CR](#) power and act as a ‘hydrogen calorimeter’ in the Galaxy – in fact in all galaxies. A formal estimate of the expected 2.2 MeV line flux is given nowhere in the literature, but measurements are available: [COMPTEL](#) and [SMM](#) provided narrow line upper limit fluxes of  $\lesssim 10^{-4}\text{ ph cm}^{-2}\text{ s}^{-1}$  ([Harris et al., 1991](#); [McConnell et al., 1997](#)). It is up to the next generation of soft  $\gamma$ -ray telescopes to improve upon these limits and decipher if a diffuse 2.2 MeV line traces the dense gas in the Milky Way or even its halo.

### 3.2.1.3 Accretion Flow Around Compact Objects

There are several scenarios that could produce a 2.2 MeV line in accreting [NSs](#) or [BHs](#). Neutron capture within the accretion flow is one possibility. Neutron capture in a [NS](#)’s atmosphere is another. Neutrons escaping the accretion flow and being captured in the companion star comprise a third scenario. Finally, a beam of accelerated particles striking the companion can induce neutron capture, analogous to the 2.2 MeV line observed in Solar flares. We will briefly summarise these ideas:

*Neutron capture within the accretion flow.* Accretion onto a compact object heats ions to 100 MeV, enough to spallate heavy nuclei and release neutrons. Energetic protons on  $^4\text{He}$  dominate neutron production at Solar abundances. Some neutrons could capture on protons in the flow, yielding a 2.2 MeV line, but this demands proton densities of  $\gtrsim 10^{16}\text{ cm}^{-3}$ . Even then, neutrons more often escape than capture ([Guessoum and Dermer, 1988](#)), and captures in hot plasma produce extremely broad lines ([Aharonian and Sunyaev, 1984](#)). Therefore, detectable 2.2 MeV emission from within the accretion flow is improbable.

*Neutron capture in a neutron star atmosphere.* Again, accreting matter onto the [NS](#) surface can spallate  $^4\text{He}$ , releasing neutrons ([Shvartsman, 1970](#)). Thermalised neutrons may again recombine radiatively with protons to emit a 2.2 MeV photon or non-radiatively with  $^3\text{He}$ . Predicted fluxes reach  $2 \times 10^{-5}\text{ cm}^{-2}\text{ s}^{-1}$  for heavy-element-rich accreting sources, such as 4U 1916-05, 4U 1626-67 or 4U 1820-30 ([Bildsten et al., 1992](#)). Since this emission originates near the surface, the 2.2 MeV line may be gravitationally redshifted to  $\gtrsim 1.76$  MeV.

*Neutron capture in the companion star.* Neutrons produced in the accretion flow can escape the compact object’s gravity and reach the companion’s atmosphere. Thermalised neutrons captured by protons there emit again a 2.2 MeV line. Close binaries

are more likely sources, as neutron decay limits travel distance and a small separation increases the companion's solid angle. Emission arises from the companion's irradiated face and is modulated by the orbital period, peaking near the X-ray maximum. [Guessoum and Dermer \(1988\)](#) predict fluxes up to  $\sim 10^{-5} \text{ cm}^{-2} \text{ s}^{-1}$  for Cygnus X-1. [Jean and Guessoum \(2001\)](#) revised the work of [Guessoum and Dermer \(1988\)](#) and computed this emission for different accretion disk models and two kinds of companion stars. Later, [Guessoum and Jean \(2002\)](#) calculated the 2.2 MeV line emission characteristics for several nearby X-ray binary sources, as a function of their accretion rate and accretion disk models. The authors obtained fluxes of  $\lesssim 10^{-5} \text{ ph cm}^{-2} \text{ s}^{-1}$ .

*Neutron capture from a beam dump in the companion star.* Very high-energy photons ( $E \gtrsim 10^{12} \text{ eV}$ ) detected from accreting sources like Cygnus X-3, Vela X-1, and Hercules X-1 imply proton beam acceleration. Beams striking the companion produce neutrons that capture on protons, analogous to Solar flares. This yields a narrow and unshifted 2.2 MeV line that varies with orbital phase. [Vestrand \(1990\)](#) predicts peak fluxes for Cygnus X-3 on the order of  $\sim 10^{-4} \text{ cm}^{-2} \text{ s}^{-1}$ , but which has already been excluded by [COMPTEL](#) measurements ([McConnell et al., 1997](#)).

*Summary.* In any of these cases, the emission map would probably reveal individual point sources, such as the attempt by [McConnell et al. \(1997\)](#) who found one intriguing hotspot in the 2.2 MeV map from [COMPTEL](#). Later this point-like emission feature was interpreted as the highly magnetised [WD RE J0317-853](#) at a distance of only 35 pc. However, the gravitational red-shift of a [WD](#) would result in a line around  $\gtrsim 1.9 \text{ MeV}$  and not necessarily at 2.2 MeV. For [NSs](#), a measurement of a red-shifted neutron capture line would immediately provide an *equation of state* by disentangling the parameter combination  $M(R)/R$  as exactly this the gravitational red-shift will be identified. The need for better measurements is therefore clear: high spectral resolution in combination with at least one order of magnitude better sensitivity.

### 3.2.2 Dark Matter and other Beyond-Standard-Model Candidates

*Written by Francesca Calore*

The MeV domain in [γ-ray](#) astronomy offers a unique observational window for [BSM](#) physics, especially in the search for light [DM](#) candidates and other feebly interacting particles, with masses in the keV to sub-GeV range. In this energy regime, narrow [γ-ray](#) lines and distinctive continuum features may act as smoking guns for [DM](#) decay or annihilation, standing out against smoother astrophysical backgrounds mostly from faint, unresolved point sources and [IC](#) photons from [CR](#) electrons interacting with the stellar radiation field of the Galaxy. Several [BSM](#) scenarios predict such signals, ranging from thermal relic [DM](#) below the GeV scale to non-thermal candidates like sterile neutrinos, axion-like particles ([ALPs](#)), and other light weakly interacting slim particles ([WISPs](#)), not necessarily linked to the cosmological [DM](#).

Importantly, the cosmological viability of these scenarios – especially light thermal relics – is tightly constrained by observations of the Cosmic Microwave Background ([CMB](#)) and by Big Bang Nucleosynthesis ([BBN](#)). In general, thermal production through the freeze-out mechanism is possible from eV up to GeV masses. However, below 1 MeV, light [DM](#) modifies predictions for light-element abundances during [BBN](#)

and thermal production is therefore strongly constrained (Sabti et al., 2020). Above 1 MeV, **DM** annihilation during the recombination epoch injects energy that alters the ionisation history, which is stringently constrained by Planck data (Slatyer, 2016). As a result, thermal annihilation cross sections compatible with a relic abundance are often excluded for sub-GeV **DM** with velocity-independent annihilation rate, that is, elastic *s*-wave annihilation into non-neutrino Standard Model final states. The relevant annihilation cross section is typically the one into electron-positron pairs. **CMB** and **BBN** constraints leave room for other **DM** types, with late-time velocity suppression or secluded annihilation channels, like the one found in rich dark sectors with vector mediators (Antel et al., 2023). Besides, other production mechanisms can be invoked such as freeze-in at low re-heating temperatures, or dark phase transitions at low temperatures (Krnjaic and McDermott, 2020).

### 3.2.2.1 Dark Matter $\gamma$ -Ray Lines

Monochromatic  $\gamma$ -ray lines are among the most striking and least ambiguous spectral features that could arise from **DM** decay or annihilation. In the MeV regime and depending on the centre-of-mass energy<sup>8</sup>, such lines would typically originate from two-body final states like  $\chi(\chi) \rightarrow \gamma X$ , where  $\chi$  indicates the **DM** candidate, and  $X$  is another neutral particle (e.g., another photon, a neutrino or a light boson if kinematically allowed). For example, for annihilation into two photons, the  $\gamma$ -ray spectrum  $dN_\gamma/dE$  is equal to  $2\delta(E - Nm_\chi/2)$  (see Sec. 1.2.4).

Sterile neutrinos provide a textbook example (Boyarsky et al., 2019): Their radiative decay channel,  $\nu_s \rightarrow \nu\gamma$ , leads to a sharp line at half the mass of the sterile neutrino. Though keV-mass sterile neutrinos have received attention as warm **DM** candidates, heavier versions in the MeV regime have been explored as unstable **DM** producing  $\gamma$ -ray lines in this range. However, such candidates are often in tension with cosmological constraints or decay too rapidly to contribute substantially to today's **DM** density. **ALPs**, on the other hand, may decay to photon pairs ( $a \rightarrow \gamma\gamma$ ), producing a characteristic line at  $m_a/2$ . The **ALPs** spontaneous decay rate is proportional to  $m_a^3 g_{a\gamma}^2$ , with  $g_{a\gamma}$  the fundamental **ALP**-photon coupling. This makes MeV-mass **ALPs** with weak couplings long-lived on cosmological timescales.

The differential  $\gamma$ -ray flux from a given direction in the sky, identified by Galactic coordinates  $(\ell, b)$ , due to **DM** decay or annihilation, has been introduced by Eqs. (26)–(29), and is repeated here for convenience:

$$\frac{d\Phi_\gamma}{dE}(\ell, b) = \mathcal{A}(\theta_\chi) \times \frac{dN_\gamma}{dE} \times \int_{\text{l.o.s.}} \rho_\chi^N(s, \ell, b) ds, \quad (51)$$

where  $\theta_\chi = \{\Gamma_\gamma, m_\chi\}$  for decay, and  $\theta_\chi = \{\langle\sigma v\rangle, m_\chi^2\}$  for annihilation. The **LoS** integral reflects the **DM** distribution in the target, such as a galactic halo. In the Milky Way, the **DM** profile is constrained at large radii via the rotation curve, but its inner structure, especially near the Galactic centre, relies on semi-analytic models or cosmological simulations. Common choices include the **NFW** profile, although theoretical

---

<sup>8</sup>In the Galactic halo, **DM** is non-relativistic today so that the centre-of-mass energy simply connects to the **DM** mass,  $E_{\text{cm}} = Nm_\chi$ , where  $N = 1$  for decay and 2 for annihilation.

uncertainties near the centre are large. This significantly impacts flux predictions, particularly for annihilation scenarios, where the flux scales with the square of the **DM** density. The  $\gamma$ -rays from **DM** can be expected in the continuum, diffuse  $\gamma$ -ray emission of the Galaxy, or from specific targets like dwarf galaxies or the Galactic centre.

*Current constraints.* A recent reanalysis of 16 yr of **INTEGRAL/SPI** data has significantly improved our understanding of the Galactic diffuse emission up to 8 MeV, superseding the two-decade-old **COMPTEL** results (Siegert et al., 2022). This updated measurement offers critical insights not only into **CR** propagation in the MeV range but also provides sensitivity to exotic emission processes, including those associated with particle and non-particle **DM**. Currently, these observations set the among some of the highest sensitivities available in this energy band. For annihilation, the bounds on the two-photon final state are superseding the limits from the **CMB** in the range from 50 keV up to  $\sim$ 3 MeV, showing the potential future MeV missions will have in probing light **DM**. These analyses currently provide also some among the strongest constraints on light decaying **DM** in the 0.1–10 MeV.

In addition to the diffuse Galactic background, targeted observations of **DM**-dominated systems, such as dwarf spheroidal galaxies, offer complementary constraints. For instance, **SPI** data from a 1.5 Ms exposure toward the Reticulum II dwarf galaxy has been analysed in Siegert et al. (2022), setting competitive limits despite the shorter exposure time.

### 3.2.2.2 The 511 keV Line and Dark Matter

The bright 511 keV  $\gamma$ -ray line from the Galactic bulge (see Sec. 2.9) has long puzzled astrophysicists. Its interpretation as arising from positron annihilation implies the existence of a large and concentrated source of low-energy positrons in the inner Galaxy, with little corresponding emission from the disk (Siegert et al., 2016, 2021). While astrophysical sources remain viable explanations, **DM** has been presented as a compelling alternative, especially given the spatial morphology of the signal (Prantzos et al., 2011).

*A DM explanation of the 511 keV line.* Sub-GeV **DM** annihilating or decaying into  $e^+e^-$  pairs has been proposed as a mechanism to generate these positrons. For example, MeV-scale scalar or vector **DM** particles could annihilate via  $\chi\chi \rightarrow e^+e^-$  or decay through suppressed channels into leptonic final states. The subsequent positron annihilation with electrons in the **ISM** would produce a 511 keV line, accompanied by a low-energy continuum from **Ps** formation and in-flight annihilation. However, such scenarios are constrained by both cosmology and  $\gamma$ -ray data. As seen above, annihilating **DM** in this mass range must have suppressed late-time cross sections (e.g., *p*-wave annihilation) to evade **CMB** constraints on energy injection during recombination. Similarly, the injection of positrons must be soft and spatially confined to avoid overproducing in-flight  $\gamma$ -rays or breaching bounds from diffuse MeV backgrounds (e.g., De la Torre Luque et al., 2025). Candidates that can potentially match both the morphology and flux of the 511 keV line include asymmetric **DM** and secluded annihilation models. In particular, annihilations or decays into intermediate metastable states, which subsequently decay into  $e^+e^-$  with delayed injection, provide a plausible

mechanism. These models can evade stringent cosmological bounds (e.g., allowing for neutrino injection from **DM** annihilation in the early Universe (Sabti et al., 2020)), while naturally explaining the spatial profile of the signal. A recent model has been proposed by Aghaie et al. (2025) where MeV-scale Dirac **DM** annihilates into **ALPs**: *p*-wave annihilation into two **ALPs** set the relic abundance, whereas *s*-wave annihilation into three **ALPs** later decaying into electron-positron pairs is responsible for the line intensity.

*Current constraints on dark matter.* Sub-GeV **DM** particles producing electron-positron pairs and form **Ps** after thermalisation are strongly constrained by **INTEGRAL/SPI** observations. A first conservative bound can be set by requiring that the **DM** annihilation/decay rate should not overproduce the positrons necessary to sustain the line observation. This argument gave a bound of  $\langle\sigma v\rangle \sim 5 \times 10^{-31} \text{ cm}^3 \text{ s}^{-1}$  at 3 MeV, for an **NFW** profile **DM** density distribution (Vincent et al., 2012). Including the effects of positron propagation in the Galaxy, most notably diffusion, and fully exploiting the spatial distribution of the observed signal, De la Torre Luque et al. (2024a) set the currently leading constraints for masses in the range 1–300 (1000) MeV for annihilation (decay), touching values of  $\langle\sigma v\rangle \sim 10^{-32} \text{ cm}^3 \text{ s}^{-1}$  at 1 MeV for electron-positron annihilation. Theoretical uncertainties related to positrons propagation and thermalisation requires further investigation (see Sec. 2.9.3).

In this context, we stress that for velocity-dependent annihilation scenarios with *p*-wave cross sections (scaling as  $v^2$ ), constraints from the **CMB** are significantly weakened due to the low relative velocities of **DM** at recombination ( $v_{\text{CMB}} \lesssim 10^{-5} \text{ c}$ ) (Liu et al., 2016). In contrast, present-day indirect detection probes remain sensitive, since Galactic **DM** particles today move with  $v_0 \lesssim 10^{-3} \text{ c}$ . Consequently, for *p*-wave models, the strongest constraints come from the MeV diffuse  **$\gamma$ -ray** background and 511 keV line, touching upon the expected *p*-wave vanilla cross section. The relic abundance condition for *p*-wave annihilating **DM** indeed – set at freeze-out when  $v_{\text{f.o.}} \sim 0.15 \text{ c}$  – requires a cross section of  $\sim 10^{-26} \text{ cm}^3 \text{ s}^{-1}$  (Diamanti et al., 2014). Extrapolating to today’s velocities, the expected thermal cross section becomes  $\langle\sigma v\rangle_0^{\text{f.o.}} \sim 10^{-32} \text{ cm}^3 \text{ s}^{-1}$  (Bartels et al., 2017), potentially in the reach of current indirect detection efforts.

*Current constraints on other **WISPs**.* **ALPs**, as other **WISPs** like dark photons and sterile neutrinos, can also be produced in stars, and especially in **ccSNe** (Carenza et al., 2025). **ALPs** production in **SN** cores is due to the coupling with nucleons, whereas, if coupled also to electrons, for suitable masses and couplings, these particles escape from the **SN** and decay into positrons. Those then eventually annihilate with electrons in the **ISM**. The resulting signal is a 511 keV annihilation line. However, the spatial distribution of the 511 keV line signal would be dramatically different than the observed one and correlated with the Galactic disk, allowing to set strong constraints on **ALP**-electron coupling. In Calore et al. (2021), using the **INTEGRAL/SPI** observation of this  **$\gamma$ -ray** line, a wide range of the axion-electron couplings has been excluded,  $10^{-19} \lesssim g_{ae} \lesssim 10^{-11}$ , for  $g_{\text{ap}} \sim 10^{-9}$ . Also, **ALPs** from extragalactic **SNe** decaying into electron-positron pairs contribute to the **CXB**, leading to constraints down to  $g_{ae} \sim 10^{-20}$ . These argument allow us to set stringent limits on the mixing parameters, in a region not accessible by current and planned laboratory experiments, and competitive with cosmological bounds. The 511 keV observations were shown to

be the most constraining observable among many others in X- and  $\gamma$ -rays (e.g., De la Torre Luque et al., 2024b).

We stress again that these bounds rely on the modelling of the positrons propagation and thermalisation in the ISM where improvement is warranted. A better treatment of these aspects would strengthen the confidence in the results, and might also allow to tighten the limits via a detailed modelling of the signal morphology.

### 3.2.2.3 In-Flight Annihilation of Positrons

A crucial consequence of positron injection at MeV energies is the generation of “in-flight annihilation”  $\gamma$ -rays. These arise when positrons annihilate before thermalising with the ambient ISM, producing a broad spectral feature above 511 keV – and not a  $\gamma$ -ray line (see Sec. 2.9.4). The resulting emission can conflict with observed diffuse  $\gamma$ -ray data if the positron injection energy is too high or the rate too large. In-flight annihilation constraints, derived from SPI and COMPTEL data, severely limit models that inject positrons with energies above a few MeV. For instance, decaying DM models with mass  $m_\chi \gtrsim 10$  MeV decaying to  $e^+e^-$  pairs are strongly constrained by this effect. Only scenarios where the positron injection energy is below a few MeV, or where most positrons annihilate after slowing down, remain viable (De la Torre Luque et al., 2025). As a result, viable models must finely balance the need to reproduce the observed 511 keV signal while suppressing the in-flight annihilation component. We note that the joint analysis of  $\gamma$ -ray instruments decades apart might invoke some bias and that a wrong inter-calibration might lead to stronger effects than what is actually happening (Siegert, 2023).

### 3.2.2.4 Smoking-Gun Observables and Future Prospects

Identifying a “smoking gun” signature of MeV DM requires observations that are both spectrally distinctive and spatially correlated with plausible DM distributions. The most promising signatures include:

- Narrow  $\gamma$ -ray lines from decaying or annihilating DM, e.g.,  $\chi \rightarrow \gamma\nu$  or  $a \rightarrow \gamma\gamma$ , especially if observed from regions of high DM density like the Galactic centre, dwarf spheroidal galaxies or other nearby galaxies.
- The 511 keV line with a morphology consistent with DM-induced positron injection, ideally confirmed with improved angular resolution and spectral modelling.
- Possibly suppressed in-flight annihilation emission, confirming that positrons annihilate after thermalisation and thus match the spectral constraints.

To detect such signatures, dedicated MeV  $\gamma$ -ray telescopes with high spectral and angular resolution are essential. In the near future, COSI is scheduled for launch in 2027 following multiple balloon campaigns. It will operate in the 0.2–5.0 MeV range and is expected to significantly enhance current limits on light dark matter decay or annihilation (e.g., Aramaki et al., 2022; Caputo et al., 2022). The proposed GECCO mission (Galactic Explorer with a Coded Aperture Mask Compton Telescope) aims to extend coverage up to 10 MeV, offering improved angular and energy resolution (Coogan et al., 2021). To probe DM masses beyond this range, broader-band missions

reaching  $\sim 100$  MeV are required, such as GRAMS, APT, AMEGO-X, and all-sky-ASTROGAM. These instruments would be crucial to close the sensitivity gap at intermediate energies. For a comprehensive overview of planned MeV  $\gamma$ -ray missions, see [Aramaki et al. \(2022\)](#). Future detectors are projected to tighten existing constraints by at least an order of magnitude. Combining such observations with [CMB](#) and [BBN](#) constraints, and modelling of astrophysical foregrounds, will be key to disentangling [DM](#) signals from standard astrophysical backgrounds. Besides the discovery potential, the MeV band holds unique promise to *exclude* some among the most well-motivated extensions of the minimal [DM](#) model, namely dark sectors with vector- or scalar-type mediators which possess, in most cases, velocity-suppressed cross sections. Excluding a sizeable part of  $p$ -wave cross section is in the reach of these future instruments for a large range of [DM](#) masses.

### 3.3 What is Needed? – A New MeV $\gamma$ -Ray Mission

*Written by Thomas Sieger*

From all the considerations above, the summary of this chapter is the following: *We need a better soft  $\gamma$ -ray telescope.*

But the path is not straight-forward. Some science cases require accurate spatial resolution but may ignore the spectral requirements of others. Some need a smooth and all-sky covering exposure with a large [FoV](#), others need a focussing aperture to detect extragalactic sources. For  $\gamma$ -ray line science – as is true for all other observations – a sensitivity improvement should be the major driver for any new observatory. Modern data analysis tools can then still be applied to mediocre spatial and spectral resolution, but identifications of more sources and different lines should be in the focus of future developments. MeV telescopes should be built for dedicated purposes as either of the common apertures, coded masks, Compton telescopes, and Laue lenses (concentrators), have their ups and downs – *there is no one-fits-it-all solution.*

## **Declarations**

Conflict of interest statement: Not applicable.

## References

Ramaty, R., Lingenfelter, R.E.: Gamma-ray line astronomy. *Nature* **278**, 127–132 (1979) <https://doi.org/10.1038/278127a0>

Schönfelder, V.: The Universe in Gamma Rays. *Astronomy and Astrophysics Library*. Springer, ??? (2001). <https://doi.org/10.1007/978-3-662-04593-0>

Diehl, R., Hartmann, D.H., Prantzos, N.: *Astronomy with Radioactivities I: Radioactivities and Other Tracers of the Stellar Cycle. Space Sciences Series of ISSI*. Springer, Cham, Switzerland (2018). <https://doi.org/10.1007/978-94-024-0848-1>

Lingenfelter, R.E., Ramaty, R.: Gamma-ray line astrophysics. In: Shen, B.S.P. (ed.) *Theoretical Nuclear Reaction Astrophysics*, p. . Benjamin/Cummings, ??? (1986). NASA NTRS Report 19860022013. <https://ntrs.nasa.gov/api/citations/19860022013/downloads/19860022013.pdf>

Prantzos, N., Boehm, C., Bykov, A.M., Diehl, R., Ferrière, K., Guessoum, N., Jean, P., Knölseder, J., Marcowith, A., Moskalenko, I.V., Strong, A., Weidenspointner, G.: The 511 keV emission from positron annihilation in the Galaxy. *Reviews of Modern Physics* **83**(3), 1001–1056 (2011) <https://doi.org/10.1103/RevModPhys.83.1001> [arXiv:1009.4620](https://arxiv.org/abs/1009.4620) [astro-ph.HE]

Lewin, J.D., Smith, P.F.: Review of mathematics, numerical factors, and corrections for dark matter experiments based on elastic nuclear recoil. *Astroparticle Physics* **6**(1), 87–112 (1996) [https://doi.org/10.1016/S0927-6505\(96\)00047-3](https://doi.org/10.1016/S0927-6505(96)00047-3)

Bergström, L., Ullio, P., Buckley, J.H.: Observability of  $\gamma$  rays from dark matter neutralino annihilations in the Milky Way halo. *Astroparticle Physics* **9**(2), 137–162 (1998) [https://doi.org/10.1016/S0927-6505\(98\)00015-2](https://doi.org/10.1016/S0927-6505(98)00015-2) [arXiv:astro-ph/9712318](https://arxiv.org/abs/astro-ph/9712318) [astro-ph]

Krane, K.S.: *Introductory Nuclear Physics*. John Wiley & Sons, New York (1987). 2nd edition

Ferrière, K.M.: The interstellar environment of our galaxy. *Reviews of Modern Physics* **73**(4), 1031–1066 (2001) <https://doi.org/10.1103/RevModPhys.73.1031> [arXiv:astro-ph/0106359](https://arxiv.org/abs/astro-ph/0106359) [astro-ph]

Chan, L.W., Lingenfelter, R.E.: Calculated Gamma-Ray Line Fluxes from the Type II Supernova 1987A. *ApJL* **318**, 51 (1987) <https://doi.org/10.1086/184936>

Knoll, G.F.: *Radiation Detection and Measurement*, (2000)

Diehl, R., Siegert, T., Greiner, J., Krause, M., Kretschmer, K., Lang, M., Pleintinger, M., Strong, A.W., Weinberger, C., Zhang, X.: INTEGRAL/SPI  $\gamma$ -ray line spectroscopy. Response and background characteristics. *A&A* **611**, 12 (2018) <https://doi.org/10.1051/0004-6361/201731440>

<https://doi.org/10.1051/0004-6361/201731815> arXiv:1710.10139 [astro-ph.IM]

Pendleton, G.N., Paciesas, W.S., Mallozzi, R.S., Koshut, T.M., Fishman, G.J., Meegan, C.A., Wilson, R.B., Horack, J.M., Lestrade, J.P.: The detector response matrices of the burst and transient source experiment (BATSE) on the Compton Gamma Ray Observatory. Nuclear Instruments and Methods in Physics Research A **364**, 567–577 (1995) [https://doi.org/10.1016/0168-9002\(95\)00448-3](https://doi.org/10.1016/0168-9002(95)00448-3)

Sieger, T., Horan, D., Kanbach, G.: Telescope Concepts in Gamma-Ray Astronomy. In: Bambi, C., Sanganelo, A. (eds.) Handbook of X-ray and Gamma-ray Astrophysics, p. 80 (2022). [https://doi.org/10.1007/978-981-16-4544-0\\_43-1](https://doi.org/10.1007/978-981-16-4544-0_43-1)

Clayton, D.D.: Principles of Stellar Evolution and Nucleosynthesis. University of Chicago Press, Chicago (1968). Classic textbook on nuclear astrophysics

Woosley, S.E., Weaver, T.A.: The Evolution and Explosion of Massive Stars. II. Explosive Hydrodynamics and Nucleosynthesis. ApJS **101**, 181 (1995) <https://doi.org/10.1086/192237>

Kozlovsky, B., Murphy, R.J., Ramaty, R.: Nuclear Deexcitation Gamma-Ray Lines from Accelerated Particle Interactions. ApJS **141**(2), 523–541 (2002) <https://doi.org/10.1086/340545>

Share, G.H., Murphy, R.J.: Gamma-Ray Measurements of Flare-to-Flare Variations in Ambient Solar Abundances. ApJ **452**, 933 (1995) <https://doi.org/10.1086/176360>

Hua, X.-M., Lingenfelter, R.E.: Solar flare neutron production and the angular dependence of the capture gamma-ray emission. Solar Physics **107**, 351–383 (1987) <https://doi.org/10.1007/BF00152031>

Aharonian, F.A., Sunyaev, R.A.: Gamma-ray line emission, nuclear destruction and neutron production in hot astrophysical plasmas. The deuterium boiler as a gamma-ray source. MNRAS **210**, 257–277 (1984) <https://doi.org/10.1093/mnras/210.2.257>

Yoneda, H., Aharonian, F., Coppi, P., Sieger, T., Takahashi, T.: Line profile of nuclear de-excitation gamma-ray emission from very hot plasma. MNRAS **526**(1), 1460–1470 (2023) <https://doi.org/10.1093/mnras/stad2780> arXiv:2309.05426 [astro-ph.HE]

Guessoum, N., Jean, P., Gillard, W.: The lives and deaths of positrons in the interstellar medium. A&A **436**(1), 171–185 (2005) <https://doi.org/10.1051/0004-6361:20042454> arXiv:astro-ph/0504186 [astro-ph]

Ore, A., Powell, J.L.: Three-photon annihilation of an electron-positron pair. Phys. Rev. **75**, 1696–1699 (1949) <https://doi.org/10.1103/PhysRev.75.1696>

Aharonian, F.A., Atoyan, A.M.: Cosmic gamma-rays associated with annihilation of

relativistic  $e^+$  - $e^-$  pairs. Physics Letters B **99**(3), 301–304 (1981) [https://doi.org/10.1016/0370-2693\(81\)91130-8](https://doi.org/10.1016/0370-2693(81)91130-8)

Aharonian, F.A., Atoyan, A.M.: Broad-band diffuse gamma ray emission of the galactic disk. A&A **362**, 937–952 (2000) <https://doi.org/10.48550/arXiv.astro-ph/0009009> [astro-ph]

Svensson, R.: Electron-Positron Pair Equilibria in Relativistic Plasmas. ApJ **258**, 335 (1982) <https://doi.org/10.1086/160082>

Svensson, R.: The thermal pair annihilation spectrum - A detailed balance approach. ApJ **270**, 300–304 (1983) <https://doi.org/10.1086/161122>

Deutsch, M.: Evidence for the Formation of Positronium in Gases. Physical Review **82**, 455–456 (1951) <https://doi.org/10.1103/PhysRev.82.455>

Deutsch, M.: Observation of the Long-Lived Positronium State. Physical Review **83**, 866–868 (1951) <https://doi.org/10.1103/PhysRev.83.866>

Guessoum, N., Ramaty, R., Lingenfelter, R.E.: Positron Annihilation in the Interstellar Medium. ApJ **378**, 170 (1991) <https://doi.org/10.1086/170417>

Guessoum, N., Jean, P., Gillard, W.: The lives and deaths of positrons in the interstellar medium. A&A **436**(1), 171–185 (2005) <https://doi.org/10.1051/0004-6361:20042454> arXiv:astro-ph/0504186 [astro-ph]

Guessoum, N., Jean, P., Gillard, W.: Positron annihilation on polycyclic aromatic hydrocarbon molecules in the interstellar medium. MNRAS **402**(2), 1171–1178 (2010) <https://doi.org/10.1111/j.1365-2966.2009.15954.x> arXiv:0911.0582 [astro-ph.HE]

Siebert, T.: The Positron Puzzle. Ap&SS **368**(4), 27 (2023) <https://doi.org/10.1007/s10509-023-04184-4> arXiv:2303.15582 [astro-ph.HE]

Leventhal, M., MacCallum, C.J., Stang, P.D.: Detection of 511 keV positron annihilation radiation from the galactic center direction. ApJL **225**, 11–14 (1978) <https://doi.org/10.1086/182782>

Churazov, E., Sunyaev, R., Sazonov, S., Revnivtsev, M., Varshalovich, D.: Positron annihilation spectrum from the Galactic Centre region observed by SPI/INTEGRAL. MNRAS **357**(4), 1377–1386 (2005) <https://doi.org/10.1111/j.1365-2966.2005.08757.x> arXiv:astro-ph/0411351 [astro-ph]

Jean, P., Knöldlseder, J., Gillard, W., Guessoum, N., Ferrière, K., Marcowith, A., Lonjou, V., Roques, J.P.: Spectral analysis of the Galactic  $e^+e^-$  annihilation emission. A&A **445**(2), 579–589 (2006) <https://doi.org/10.1051/0004-6361:20053765> arXiv:astro-ph/0509298 [astro-ph]

Siebert, T.: Positron-Annihilation Spectroscopy throughout the Milky Way. PhD thesis, Max-Planck-Institute for Extraterrestrial Physics, Garching (February 2017)

Abazajian, K., Fuller, G.M., Patel, M.: Sterile neutrino hot, warm, and cold dark matter. *Phys. Rev. D* **64**(2), 023501 (2001) <https://doi.org/10.1103/PhysRevD.64.023501> arXiv:astro-ph/0101524 [astro-ph]

Jungman, G., Kamionkowski, M., Griest, K.: Supersymmetric dark matter. *Phys. Rep.* **267**, 195–373 (1996) [https://doi.org/10.1016/0370-1573\(95\)00058-5](https://doi.org/10.1016/0370-1573(95)00058-5) arXiv:hep-ph/9506380 [hep-ph]

Evans, L.G., Peplowski, P.N., Rhodes, E.A., Lawrence, D.J., McCoy, T.J., Nittler, L.R., Solomon, S.C., Sprague, A.L., Stockstill-Cahill, K.R., Starr, R.D., Weider, S.Z., Boynton, W.V., Hamara, D.K., Goldsten, J.O.: Major-element abundances on the surface of Mercury: Results from the MESSENGER Gamma-Ray Spectrometer. *Journal of Geophysical Research (Planets)* **117**, 00–07 (2012) <https://doi.org/10.1029/2012JE004178>

Steigman, G., Dasgupta, B., Beacom, J.F.: Precise relic WIMP abundance and its impact on searches for dark matter annihilation. *Phys. Rev. D* **86**(2), 023506 (2012) <https://doi.org/10.1103/PhysRevD.86.023506> arXiv:1204.3622 [hep-ph]

Rybicki, G.B., Lightman, A.P.: Radiative Processes in Astrophysics, (1979)

Morrison, R., McCammon, D.: Interstellar photoelectric absorption cross sections, 0.03–10 keV. *ApJ* **270**, 119–122 (1983) <https://doi.org/10.1086/161102>

Pinto, P.A., Woosley, S.E.: The theory of gamma-ray emergence in supernova 1987A. *Nature* **333**(6173), 534–537 (1988) <https://doi.org/10.1038/333534a0>

Milne, P.A., Hungerford, A.L., Fryer, C.L., Evans, T.M., Urbatsch, T.J., Boggs, S.E., Isern, J., Bravo, E., Hirschmann, A., Kumagai, S., Pinto, P.A., The, L.-S.: Unified One-Dimensional Simulations of Gamma-Ray Line Emission from Type Ia Supernovae. *ApJ* **613**(2), 1101–1119 (2004) <https://doi.org/10.1086/423235> arXiv:astro-ph/0406173 [astro-ph]

Mahoney, W.A., Ling, J.C., Wheaton, W.A., Jacobson, A.S.: HEAO 3 discovery of Al-26 in the interstellar medium. *ApJ* **286**, 578–585 (1984) <https://doi.org/10.1086/162632>

Teegarden, B.J., Barthelmy, S.D., Gehrels, N., Tueller, J., Leventhal, M., MacCallum, C.J.: GRIS Observations of 26Al Gamma-Ray Line Emission from Two Points in the Galactic Plane. *ApJL* **375**, 9 (1991) <https://doi.org/10.1086/186076>

Endt, P.M.: Energy levels of  $A = 21\text{--}44$  nuclei (VII). *Nucl. Phys. A* **521**, 1–400 (1990) [https://doi.org/10.1016/0375-9474\(90\)90598-G](https://doi.org/10.1016/0375-9474(90)90598-G)

Iliadis, C., Champagne, A., Chieffi, A., Limongi, M.: The Effects of Thermonuclear Reaction Rate Variations on  $^{26}\text{Al}$  Production in Massive Stars: A Sensitivity Study. *ApJS* **193**(1), 16 (2011) <https://doi.org/10.1088/0067-0049/193/1/16> [arXiv:1101.5553](https://arxiv.org/abs/1101.5553) [astro-ph.SR]

Pleintinger, M.M.M.: Star Groups and their Nucleosynthesis. PhD thesis, Max-Planck-Institute for Extraterrestrial Physics, Garching (November 2020)

Rugel, G., Fästermann, T., Knie, K., Korschinek, G., Poutivtsev, M., Schumann, D., Kivel, N., Günther-Leopold, I., Weinreich, R., Wohlmuther, M.: New Measurement of the  $\text{Fe}60$  Half-Life. *Phys. Rev. Lett.* **103**(7), 072502 (2009) <https://doi.org/10.1103/PhysRevLett.103.072502>

Meynet, G., Arnould, M., Prantzos, N., Paulus, G.: Contribution of Wolf-Rayet stars to the synthesis of  $^{26}\text{Al}$ . I. The  $\gamma$ -ray connection. *A&A* **320**, 460–468 (1997)

José, J., Hernanz, M.: Nucleosynthesis in Classical Novae: CO versus ONe White Dwarfs. *ApJ* **494**(2), 680–690 (1998) <https://doi.org/10.1086/305244> [arXiv:astro-ph/9709153](https://arxiv.org/abs/astro-ph/9709153) [astro-ph]

Vasini, A., Spitoni, E., Matteucci, F., Cescutti, G., Della Valle, M.: Tracing the Milky Way spiral arms with  $^{26}\text{Al}$ : The role of nova systems in the 2D distribution of  $^{26}\text{Al}$ . *A&A* **693**, 37 (2025) <https://doi.org/10.1051/0004-6361/202451630> [arXiv:2407.16765](https://arxiv.org/abs/2407.16765) [astro-ph.GA]

Mowlavi, N., Meynet, G.: Aluminum 26 production in asymptotic giant branch stars. *A&A* **361**, 959–976 (2000)

Clayton, D.D.: Al-26 in the interstellar medium. *ApJ* **280**, 144–149 (1984) <https://doi.org/10.1086/161978>

Knöldlseder, J., Bennett, K., Bloemen, H., Diehl, R., Hermsen, W., Oberlack, U., Ryan, J., Schönfelder, V., von Ballmoos, P.: A multiwavelength comparison of COMPTEL 1.8 MeV  $^{26}\text{Al}$  line data. *A&A* **344**, 68–82 (1999)

Diehl, R., Halloin, H., Kretschmer, K., Lichti, G.G., Schönfelder, V., Strong, A.W., von Kienlin, A., Wang, W., Jean, P., Knöldlseder, J., Roques, J.-P., Weidenspointner, G., Schanne, S., Hartmann, D.H., Winkler, C., Wunderer, C.: Radioactive  $^{26}\text{Al}$  from massive stars in the Galaxy. *Nature* **439**(7072), 45–47 (2006) <https://doi.org/10.1038/nature04364> [arXiv:astro-ph/0601015](https://arxiv.org/abs/astro-ph/0601015) [astro-ph]

Diehl, R., Dupraz, C., Bennett, K., Bloemen, H., Hermsen, W., Knöldlseder, J., Lichti, G., Morris, D., Ryan, J., Schönfelder, V., Steinle, H., Strong, A., Swanenburg, B., Varendorff, M., Winkler, C.: COMPTEL observations of Galactic  $^{26}\text{Al}$  emission. *A&A* **298**, 445 (1995)

Oberlack, U., Bennett, K., Bloemen, H., Diehl, R., Dupraz, C., Hermsen, W.,

Knöldlseder, J., Morris, D., Schönfelder, V., Strong, A., Winkler, C.: The COMPTEL 1.809MeV all-sky image. *A&AS* **120**, 311–314 (1996)

del Rio, E., von Ballmoos, P., Bennett, K., Bloemen, H., Diehl, R., Hermsen, W., Knöldlseder, J., Oberlack, U., Ryan, J., Schönfelder, V., Winkler, C.: 1.8 MeV line emission from the Cygnus region. *A&A* **315**, 237–242 (1996)

Knöldlseder, J., Bennett, K., Bloemen, H., Diehl, R., Hermsen, W., Oberlack, U., Ryan, J., Schönfelder, V.: 1.8 MeV emission from the Carina region. *A&AS* **120**, 327–330 (1996) <https://doi.org/10.48550/arXiv.astro-ph/9604054> arXiv:astro-ph/9604054 [astro-ph]

Diehl, R., Bennett, K., Bloemen, H., Dupraz, C., Hermsen, W., Knöldlseder, J., Lichten, G., Morris, D., Oberlack, U., Ryan, J., Schönfelder, V., Steinle, H., Varendorff, M., Winkler, C.: 1.809 MeV gamma-rays from the VELA region. *A&A* **298**, 25 (1995)

Plüschke, S., Diehl, R., Schönfelder, V., Bloemen, H., Hermsen, W., Bennett, K., Winkler, C., McConnell, M., Ryan, J., Oberlack, U., Knöldlseder, J.: The COMPTEL 1.809 MeV survey. In: Gimenez, A., Reglero, V., Winkler, C. (eds.) Exploring the Gamma-Ray Universe. ESA Special Publication, vol. 459, pp. 55–58 (2001). <https://doi.org/10.48550/arXiv.astro-ph/0104047>

Bouchet, L., Jourdain, E., Roques, J.-P.: The Galactic  $^{26}\text{Al}$  Emission Map as Revealed by INTEGRAL SPI. *ApJ* **801**(2), 142 (2015) <https://doi.org/10.1088/0004-637X/801/2/142> arXiv:1501.05247 [astro-ph.HE]

Siegert, T., Pleintinger, M.M.M., Diehl, R., Krause, M.G.H., Greiner, J., Weinberger, C.: Galactic population synthesis of radioactive nucleosynthesis ejecta. *A&A* **672**, 54 (2023) <https://doi.org/10.1051/0004-6361/202244457> arXiv:2301.10192 [astro-ph.GA]

Martin, P., Knöldlseder, J., Diehl, R., Meynet, G.: New estimates of the gamma-ray line emission of the Cygnus region from INTEGRAL/SPI observations. *A&A* **506**(2), 703–710 (2009) <https://doi.org/10.1051/0004-6361/200912178> arXiv:1001.1521 [astro-ph.HE]

Diehl, R., Lang, M.G., Martin, P., Ohlendorf, H., Preibisch, T., Voss, R., Jean, P., Roques, J.-P., von Ballmoos, P., Wang, W.: Radioactive  $^{26}\text{Al}$  from the Scorpius-Centaurus association. *A&A* **522**, 51 (2010) <https://doi.org/10.1051/0004-6361/201014302> arXiv:1007.4462 [astro-ph.HE]

Krause, M.G.H., Burkert, A., Diehl, R., Fierlinger, K., Gaczkowski, B., Kröll, D., Ngoumou, J., Roccatagliata, V., Siegert, T., Preibisch, T.: Surround and Squash: the impact of superbubbles on the interstellar medium in Scorpius-Centaurus OB2. *A&A* **619**, 120 (2018) <https://doi.org/10.1051/0004-6361/201732416> arXiv:1808.04788 [astro-ph.GA]

Kretschmer, K., Diehl, R., Krause, M., Burkert, A., Fierlinger, K., Gerhard, O., Greiner, J., Wang, W.: Kinematics of massive star ejecta in the Milky Way as traced by  $^{26}\text{Al}$ . *A&A* **559**, 99 (2013) <https://doi.org/10.1051/0004-6361/201322563> arXiv:1309.4980 [astro-ph.HE]

Krause, M.G.H., Diehl, R., Bagetakos, Y., Brinks, E., Burkert, A., Gerhard, O., Greiner, J., Kretschmer, K., Siegert, T.:  $^{26}\text{Al}$  kinematics: superbubbles following the spiral arms?. Constraints from the statistics of star clusters and HI supershells. *A&A* **578**, 113 (2015) <https://doi.org/10.1051/0004-6361/201525847> arXiv:1504.03120 [astro-ph.GA]

Siegert, T., Diehl, R.: The  $^{26}\text{Al}$  Gamma-ray Line from Massive-Star Regions. In: Kubono, S., Kajino, T., Nishimura, S., Isobe, T., Nagataki, S., Shima, T., Takeda, Y. (eds.) 14th International Symposium on Nuclei in the Cosmos (NIC2016), p. 020305 (2017). <https://doi.org/10.7566/JPSCP.14.020305>

Pleintinger, M.M.M., Diehl, R., Siegert, T., Greiner, J., Krause, M.G.H.:  $^{26}\text{Al}$  gamma rays from the Galaxy with INTEGRAL/SPI. *A&A* **672**, 53 (2023) <https://doi.org/10.1051/0004-6361/202245069> arXiv:2212.11228 [astro-ph.HE]

Parikh, A., José, J., Karakas, A., Ruiz, C., Wimmer, K.: Strength of the  $E_R=127$  keV,  $\text{Al}26(p,\gamma)\text{Si}27$  resonance. *Phys. Rev. C* **90**(3), 038801 (2014) <https://doi.org/10.1103/PhysRevC.90.038801> arXiv:1408.5227 [astro-ph.SR]

Prantzos, N., Diehl, R.: Radioactive  $^{26}\text{Al}$  in the galaxy: observations versus theory. *Phys. Rep.* **267**, 1–69 (1996) [https://doi.org/10.1016/0370-1573\(95\)00055-0](https://doi.org/10.1016/0370-1573(95)00055-0)

Lugaro, M., Ott, U., Keresztfuri, Á.: Radioactive nuclei from cosmochronology to habitability. *Progress in Particle and Nuclear Physics* **102**, 1–47 (2018) <https://doi.org/10.1016/j.ppnp.2018.05.002> arXiv:1808.00233 [astro-ph.SR]

Sieverding, A., Martínez-Pinedo, G., Langanke, K., Heger, A.: Neutrino Induced Nucleosynthesis of Radioactive Nuclei in Core-Collapse Supernovae. In: Kubono, S., Kajino, T., Nishimura, S., Isobe, T., Nagataki, S., Shima, T., Takeda, Y. (eds.) 14th International Symposium on Nuclei in the Cosmos (NIC2016), p. 020701 (2017). <https://doi.org/10.7566/JPSCP.14.020701>

Karakas, A.I., Lattanzio, J.C.: The Dawes Review 2: Nucleosynthesis and Stellar Yields of Low- and Intermediate-Mass Single Stars. *PASA* **31**, 030 (2014) <https://doi.org/10.1017/pasa.2014.21> arXiv:1405.0062 [astro-ph.SR]

Starrfield, S., Bose, M., Iliadis, C., Hix, W.R., Woodward, C.E., Wagner, R.M.: Carbon-Oxygen Classical Novae Are Galactic  $^7\text{Li}$  Producers as well as Potential Supernova Ia Progenitors. *ApJ* **895**(1), 70 (2020) <https://doi.org/10.3847/1538-4357/ab8d23> arXiv:1910.00575 [astro-ph.SR]

Pleintinger, M.M.M., Siegert, T., Diehl, R., Fujimoto, Y., Greiner, J., Krause,

M.G.H., Krumholz, M.R.: Comparing simulated  $^{26}\text{Al}$  maps to gamma-ray measurements. *A&A* **632**, 73 (2019) <https://doi.org/10.1051/0004-6361/201935911> [arXiv:1910.06112](https://arxiv.org/abs/1910.06112) [astro-ph.HE]

Limongi, M., Chieffi, A.: Presupernova Evolution and Explosive Nucleosynthesis of Rotating Massive Stars in the Metallicity Range  $-3 \leq [\text{Fe}/\text{H}] \leq 0$ . *ApJS* **237**(1), 13 (2018) <https://doi.org/10.3847/1538-4365/aacb24> [arXiv:1805.09640](https://arxiv.org/abs/1805.09640) [astro-ph.SR]

Janka, H.-T.: Explosion Mechanisms of Core-Collapse Supernovae. Annual Review of Nuclear and Particle Science **62**(1), 407–451 (2012) <https://doi.org/10.1146/annurev-nucl-102711-094901> [arXiv:1206.2503](https://arxiv.org/abs/1206.2503) [astro-ph.SR]

Sukhbold, T., Ertl, T., Woosley, S.E., Brown, J.M., Janka, H.-T.: Core-collapse Supernovae from 9 to 120 Solar Masses Based on Neutrino-powered Explosions. *ApJ* **821**(1), 38 (2016) <https://doi.org/10.3847/0004-637X/821/1/38> [arXiv:1510.04643](https://arxiv.org/abs/1510.04643) [astro-ph.HE]

Licquia, T.C., Newman, J.A.: Improved Estimates of the Milky Way's Stellar Mass and Star Formation Rate from Hierarchical Bayesian Meta-Analysis. *ApJ* **806**(1), 96 (2015) <https://doi.org/10.1088/0004-637X/806/1/96> [arXiv:1407.1078](https://arxiv.org/abs/1407.1078) [astro-ph.GA]

Mel'nik, A.M., Dambis, A.K.: Kinematics of OB-associations in Gaia epoch. *MNRAS* **472**(4), 3887–3904 (2017) <https://doi.org/10.1093/mnras/stx2225> [arXiv:1708.08337](https://arxiv.org/abs/1708.08337) [astro-ph.GA]

Schulreich, M.M., Feige, J., Breitschwerdt, D.: Numerical studies on the link between radioisotopic signatures on Earth and the formation of the Local Bubble. II. Advanced modelling of interstellar  $^{26}\text{Al}$ ,  $^{53}\text{Mn}$ ,  $^{60}\text{Fe}$ , and  $^{244}\text{Pu}$  influxes as traces of past supernova activity in the solar neighbourhood. *A&A* **680**, 39 (2023) <https://doi.org/10.1051/0004-6361/202347532> [arXiv:2309.13983](https://arxiv.org/abs/2309.13983) [astro-ph.SR]

Siegert, T., Horan, D., Kanbach, G.: Telescope Concepts in Gamma-Ray Astronomy. In: Bambi, C., Sanganello, A. (eds.) *Handbook of X-ray and Gamma-ray Astrophysics*, p. 80 (2022). [https://doi.org/10.1007/978-981-16-4544-0\\_43-1](https://doi.org/10.1007/978-981-16-4544-0_43-1)

Siegert, T., Schulreich, M.M., Bauer, N., Reinhardt, R., Mittal, S., Yoneda, H.: Gamma-ray line emission from the Local Bubble. *A&A* **689**, 2 (2024) <https://doi.org/10.1051/0004-6361/202450310> [arXiv:2405.15262](https://arxiv.org/abs/2405.15262) [astro-ph.HE]

Limongi, M., Chieffi, A.: The Nucleosynthesis of  $^{26}\text{Al}$  and  $^{60}\text{Fe}$  in Solar Metallicity Stars Extending in Mass from 11 to 120  $\text{M}_{\text{solar}}$ : The Hydrostatic and Explosive Contributions. *ApJ* **647**(1), 483–500 (2006) <https://doi.org/10.1086/505164> [arXiv:astro-ph/0604297](https://arxiv.org/abs/astro-ph/0604297) [astro-ph]

Brinkman, H.E., Doherty, C.L., Pols, O.R., Li, E.T., Côté, B., Lugaro, M.: Aluminium-26 from Massive Binary Stars. I. Nonrotating Models. *ApJ* **884**(1), 38 (2019) <https://doi.org/10.3847/1538-4357/ab0a20>

<https://doi.org/10.3847/1538-4357/ab40ae> arXiv:1909.04433 [astro-ph.SR]

Oberlack, U., Wessolowski, U., Diehl, R., Bennett, K., Bloemen, H., Hermsen, W., Knöldlseder, J., Morris, D., Schönfelder, V., von Ballmoos, P.: COMPTEL limits on  $^{26}\text{Al}$  1.809 MeV line emission from gamma $^2$  Velorum. *A&A* **353**, 715–721 (2000) <https://doi.org/10.48550/arXiv.astro-ph/9910555> arXiv:astro-ph/9910555 [astro-ph]

Smartt, S.J.: Progenitors of Core-Collapse Supernovae. *ARA&A* **47**(1), 63–106 (2009) <https://doi.org/10.1146/annurev-astro-082708-101737> arXiv:0908.0700 [astro-ph.SR]

Weaver, R., McCray, R., Castor, J., Shapiro, P., Moore, R.: Interstellar bubbles. II. Structure and evolution. *ApJ* **218**, 377–395 (1977) <https://doi.org/10.1086/155692>

Fujimoto, Y., Krumholz, M.R., Tachibana, S.: Short-lived radioisotopes in meteorites from Galactic-scale correlated star formation. *MNRAS* **480**(3), 4025–4039 (2018) <https://doi.org/10.1093/mnras/sty2132> arXiv:1802.08695 [astro-ph.GA]

Rodgers-Lee, D., Krause, M.G.H., Dale, J., Diehl, R.: Synthetic  $^{26}\text{Al}$  emission from galactic-scale superbubble simulations. *MNRAS* **490**(2), 1894–1912 (2019) <https://doi.org/10.1093/mnras/stz2708> arXiv:1909.10978 [astro-ph.GA]

Krause, M., Diehl, R., Böhringer, H., Freyberg, M., Lubos, D.: Feedback by massive stars and the emergence of superbubbles. II. X-ray properties. *A&A* **566**, 94 (2014) <https://doi.org/10.1051/0004-6361/201423871> arXiv:1405.0037 [astro-ph.GA]

Burrows, D.N., Singh, K.P., Nousek, J.A., Garmire, G.P., Good, J.: A Multiwavelength Study of the Eridanus Soft X-Ray Enhancement. *ApJ* **406**, 97 (1993) <https://doi.org/10.1086/172423>

Smartt, S.J.: Observational Constraints on the Progenitors of Core-Collapse Supernovae: The Case for Missing High-Mass Stars. *PASA* **32**, 016 (2015) <https://doi.org/10.1017/pasa.2015.17> arXiv:1504.02635 [astro-ph.SR]

Martinet, S., Meynet, G., Nandal, D., Ekström, S., Georgy, C., Haemmerlé, L., Hirschi, R., Yusof, N., Gounelle, M., Dwarkadas, V.: Very massive star winds as sources of the short-lived radioactive isotope  $^{26}\text{Al}$ . *A&A* **664**, 181 (2022) <https://doi.org/10.1051/0004-6361/202243474> arXiv:2205.15184 [astro-ph.SR]

Sana, H., de Mink, S.E., de Koter, A., Langer, N., Evans, C.J., Gieles, M., Gosset, E., Izzard, R.G., Le Bouquin, J.-B., Schneider, F.R.N.: Binary Interaction Dominates the Evolution of Massive Stars. *Science* **337**(6093), 444 (2012) <https://doi.org/10.1126/science.1223344> arXiv:1207.6397 [astro-ph.SR]

Brinkman, H.E., den Hartogh, J.W., Doherty, C.L., Pignatari, M., Lugaro, M.:  $^{26}\text{Al}$  from Massive Binary Stars. II. Rotating Single Stars Up to Core

Collapse and Their Impact on the Early Solar System. *ApJ* **923**(1), 47 (2021) <https://doi.org/10.3847/1538-4357/ac25ea> arXiv:2109.05842 [astro-ph.SR]

Brinkman, H.E., Doherty, C., Pignatari, M., Pols, O., Lugaro, M.: Aluminium-26 from Massive Binary Stars. III. Binary Stars up to Core Collapse and Their Impact on the Early Solar System. *ApJ* **951**(2), 110 (2023) <https://doi.org/10.3847/1538-4357/acd7ea> arXiv:2305.16787 [astro-ph.SR]

Paxton, B., Bildsten, L., Dotter, A., Herwig, F., Lesaffre, P., Timmes, F.: Modules for Experiments in Stellar Astrophysics (MESA). *ApJS* **192**(1), 3 (2011) <https://doi.org/10.1088/0067-0049/192/1/3> arXiv:1009.1622 [astro-ph.SR]

Kamiński, T., Tylenda, R., Menten, K.M., Karakas, A., Winters, J.M., Breier, A.A., Wong, K.T., Giesen, T.F., Patel, N.A.: Astronomical detection of radioactive molecule  $^{26}\text{AlF}$  in the remnant of an ancient explosion. *Nature Astronomy* **2**, 778–783 (2018) <https://doi.org/10.1038/s41550-018-0541-x> arXiv:1807.10647 [astro-ph.SR]

Knödlseder, J.:  $^{26}\text{Al}$  Sources in the Galaxy as Seen in the 1. 809 MeV Gamma-Ray Line. In: Diehl, R., Hartmann, D. (eds.) *Astronomy with Radioactivities*, vol. 274, p. 43 (1999). <https://doi.org/10.48550/arXiv.astro-ph/9912132>

Limongi, M., Chieffi, A.: Evolution, Explosion, and Nucleosynthesis of Core-Collapse Supernovae. *ApJ* **592**(1), 404–433 (2003) <https://doi.org/10.1086/375703> arXiv:astro-ph/0304185 [astro-ph]

Pignatari, M., Herwig, F., Hirschi, R., Bennett, M., Rockefeller, G., Fryer, C., Timmes, F.X., Ritter, C., Heger, A., Jones, S., Battino, U., Dotter, A., Trappitsch, R., Diehl, S., Frischknecht, U., Hungerford, A., Magkotsios, G., Travaglio, C., Young, P.: NuGrid Stellar Data Set. I. Stellar Yields from H to Bi for Stars with Metallicities  $Z = 0.02$  and  $Z = 0.01$ . *ApJS* **225**(2), 24 (2016) <https://doi.org/10.3847/0067-0049/225/2/24> arXiv:1307.6961 [astro-ph.SR]

Jones, S.W., Möller, H., Fryer, C.L., Fontes, C.J., Trappitsch, R., Even, W.P., Couture, A., Mumpower, M.R., Safi-Harb, S.:  $^{60}\text{Fe}$  in core-collapse supernovae and prospects for X-ray and gamma-ray detection in supernova remnants. *MNRAS* **485**(3), 4287–4310 (2019) <https://doi.org/10.1093/mnras/stz536> arXiv:1902.05980 [astro-ph.SR]

Wanajo, S., Janka, H.-T., Müller, B.: Electron-capture Supernovae as Sources of  $^{60}\text{Fe}$ . *ApJL* **774**(1), 6 (2013) <https://doi.org/10.1088/2041-8205/774/1/L6> arXiv:1307.3319 [astro-ph.SR]

Wanajo, S., Müller, B., Janka, H.-T., Heger, A.: Nucleosynthesis in the Innermost Ejecta of Neutrino-driven Supernova Explosions in Two Dimensions. *ApJ* **852**(1), 40 (2018) <https://doi.org/10.3847/1538-4357/aa9d97> arXiv:1701.06786 [astro-ph.SR]

Jones, S., Röpke, F.K., Pakmor, R., Seitenzahl, I.R., Ohlmann, S.T., Edelmann,

P.V.F.: Do electron-capture supernovae make neutron stars?. First multidimensional hydrodynamic simulations of the oxygen deflagration. *A&A* **593**, 72 (2016) <https://doi.org/10.1051/0004-6361/201628321> arXiv:1602.05771 [astro-ph.SR]

Jones, S., Röpke, F.K., Fryer, C., Ruiter, A.J., Seitenzahl, I.R., Nittler, L.R., Ohlmann, S.T., Reifarth, R., Pignatari, M., Belczynski, K.: Remnants and ejecta of thermonuclear electron-capture supernovae. Constraining oxygen-neon deflagrations in high-density white dwarfs. *A&A* **622**, 74 (2019) <https://doi.org/10.1051/0004-6361/201834381> arXiv:1812.08230 [astro-ph.SR]

Lugardo, M., Doherty, C.L., Karakas, A.I., Maddison, S.T., Liffman, K., García-Hernández, D.A., Siess, L., Lattanzio, J.C.: Short-lived radioactivity in the early solar system: The Super-AGB star hypothesis. *Meteorit. Planet. Sci.* **47**(12), 1998–2012 (2012) <https://doi.org/10.1111/j.1945-5100.2012.01411.x> arXiv:1208.5816 [astro-ph.SR]

Woosley, S.E.: Neutron-rich Nucleosynthesis in Carbon Deflagration Supernovae. *ApJ* **476**(2), 801–810 (1997) <https://doi.org/10.1086/303650>

Wallner, A., Bichler, M., Buczak, K., Dressler, R., Fifield, L.K., Schumann, D., Sterba, J.H., Tims, S.G., Wallner, G., Kutschera, W.: Settling the Half-Life of  $^{60}\text{Fe}$ : Fundamental for a Versatile Astrophysical Chronometer. *Phys. Rev. Lett.* **114**(4), 041101 (2015) <https://doi.org/10.1103/PhysRevLett.114.041101>

Ostdiek, K.M.C.: Measurement of the half-life of  $^{60}\text{Fe}$  for stellar and early solar system models using the direct decay of  $^{60m}\text{Co}$  and accelerator mass spectrometry. PhD thesis, University of Notre Dame, Indiana (January 2016)

Knie, K., Korschinek, G., Fästermann, T., Dorfi, E.A., Rugel, G., Wallner, A.:  $^{60}\text{Fe}$  Anomaly in a Deep-Sea Manganese Crust and Implications for a Nearby Supernova Source. *Phys. Rev. Lett.* **93**(17), 171103 (2004) <https://doi.org/10.1103/PhysRevLett.93.171103>

Wallner, A., Feige, J., Kinoshita, N., Paul, M., Fifield, L.K., Golser, R., Honda, M., Linnemann, U., Matsuzaki, H., Merchel, S., Rugel, G., Tims, S.G., Steier, P., Yamagata, T., Winkler, S.R.: Recent near-Earth supernovae probed by global deposition of interstellar radioactive  $^{60}\text{Fe}$ . *Nature* **532**(7597), 69–72 (2016) <https://doi.org/10.1038/nature17196>

Wallner, A., Fröhlich, M.B., Hotchkis, M.A.C., Kinoshita, N., Paul, M., Martschini, M., Pavetich, S., Tims, S.G., Kivel, N., Schumann, D., Honda, M., Matsuzaki, H., Yamagata, T.:  $^{60}\text{Fe}$  and  $^{244}\text{Pu}$  deposited on Earth constrain the r-process yields of recent nearby supernovae. *Science* **372**(6543), 742–745 (2021) <https://doi.org/10.1126/science.aax3972>

Fimiani, L., Cook, D.L., Fästermann, T., Gómez-Guzmán, J.M., Hain, K., Herzog,

G., Knie, K., Korschinek, G., Ludwig, P., Park, J., Reedy, R.C., Rugel, G.: Interstellar  $\gamma$ -ray line emission from  $^{60}\text{Fe}$  on the Surface of the Moon. *Phys. Rev. Lett.* **116**(15), 151104 (2016) <https://doi.org/10.1103/PhysRevLett.116.151104>

Binns, W.R., Israel, M.H., Christian, E.R., Cummings, A.C., de Nolfo, G.A., Lave, K.A., Leske, R.A., Mewaldt, R.A., Stone, E.C., von Rosenvinge, T.T., Wiedenbeck, M.E.: Observation of the  $^{60}\text{Fe}$  nucleosynthesis-clock isotope in galactic cosmic rays. *Science* **352**(6286), 677–680 (2016) <https://doi.org/10.1126/science.aad6004>

Wang, W., Harris, M.J., Diehl, R., Halloin, H., Cordier, B., Strong, A.W., Kretschmer, K., Knölseder, J., Jean, P., Lichten, G.G., Roques, J.P., Schanne, S., von Kienlin, A., Weidenspointner, G., Wunderer, C.: SPI observations of the diffuse  $^{60}\text{Fe}$  emission in the Galaxy. *A&A* **469**(3), 1005–1012 (2007) <https://doi.org/10.1051/0004-6361:20066982> arXiv:0704.3895 [astro-ph]

Wang, W., Siegert, T., Dai, Z.G., Diehl, R., Greiner, J., Heger, A., Krause, M., Lang, M., Pleintinger, M.M.M., Zhang, X.L.: Gamma-Ray Emission of  $^{60}\text{Fe}$  and  $^{26}\text{Al}$  Radioactivity in Our Galaxy. *ApJ* **889**(2), 169 (2020) <https://doi.org/10.3847/1538-4357/ab6336> arXiv:1912.07874 [astro-ph.HE]

Leising, M.D., Share, G.H.: Gamma-Ray Limits on Galactic  $^{60}\text{Fe}$  and  $^{44}\text{Ti}$  Nucleosynthesis. *ApJ* **424**, 200 (1994) <https://doi.org/10.1086/173883>

Harris, M.J., Purcell, W.R., McNaron-Brown, K., Murphy, R.J., Grove, J.E., Johnson, W.N., Kinzer, R.L., Kurfess, J.D., Share, G.H., Jung, G.V.: OSSE results on Galactic  $\gamma$ -ray line emission. In: Dermer, C.D., Strickman, M.S., Kurfess, J.D. (eds.) *Proceedings of the Fourth Compton Symposium*. American Institute of Physics Conference Series, vol. 410, pp. 1079–1083. AIP, ??? (1997). <https://doi.org/10.1063/1.54086>

Diehl, R., Wesselowski, U., Oberlack, U., Bloemen, H., Georgii, R., Iyudin, A., Knölseder, J., Lichten, G., Hermsen, W., Morris, D., Ryan, J., Schönfelder, V., Strong, A., von Ballmoos, P., Winkler, C.:  $^{26}\text{Al}$  and the COMPTEL  $^{60}\text{Fe}$  data. In: Dermer, C.D., Strickman, M.S., Kurfess, J.D. (eds.) *Proceedings of the Fourth Compton Symposium*. American Institute of Physics Conference Series, vol. 410, pp. 1109–1113. AIP, ??? (1997). <https://doi.org/10.1063/1.54176>

Smith, D.M.: Gamma-Ray Line Observations with RHESSI. In: Schönfelder, V., Lichten, G., Winkler, C. (eds.) *5th INTEGRAL Workshop on the INTEGRAL Universe*. ESA Special Publication, vol. 552, p. 45 (2004). <https://doi.org/10.48550/arXiv.astro-ph/0404594>

Pelgrims, V., Ferrière, K., Boulanger, F., Lallement, R., Montier, L.: Modeling the magnetized Local Bubble from dust data. *A&A* **636**, 17 (2020) <https://doi.org/10.1051/0004-6361/201937157> arXiv:1911.09691 [astro-ph.GA]

Zucker, C., Goodman, A.A., Alves, J., Bialy, S., Foley, M., Speagle, J.S., Großschedl, J., Finkbeiner, D.P., Burkert, A., Khimey, D., Swiggum, C.: Star formation near the Sun is driven by expansion of the Local Bubble. *Nature* **601**(7893), 334–337 (2022) <https://doi.org/10.1038/s41586-021-04286-5> arXiv:2201.05124 [astro-ph.GA]

Timmes, F.X., Woosley, S.E., Hartmann, D.H., Hoffman, R.D., Weaver, T.A., Matteucci, F.: 26Al and 60Fe from Supernova Explosions. *ApJ* **449**, 204 (1995) <https://doi.org/10.1086/176046> arXiv:astro-ph/9503120 [astro-ph]

Rauscher, T., Heger, A., Hoffman, R.D., Woosley, S.E.: Nucleosynthesis in Massive Stars with Improved Nuclear and Stellar Physics. *ApJ* **576**(1), 323–348 (2002) <https://doi.org/10.1086/341728> arXiv:astro-ph/0112478 [astro-ph]

Prantzos, N.: Radioactive  $^{26}\text{Al}$  and  $^{60}\text{Fe}$  in the Milky Way: Implications of the RHESSI detection of  $^{60}\text{Fe}$ . *A&A* **420**, 1033–1037 (2004) <https://doi.org/10.1051/0004-6361:20035766> arXiv:astro-ph/0402198 [astro-ph]

Woosley, S.E., Heger, A.: Nucleosynthesis and remnants in massive stars of solar metallicity. *Phys. Rep.* **442**(1-6), 269–283 (2007) <https://doi.org/10.1016/j.physrep.2007.02.009> arXiv:astro-ph/0702176 [astro-ph]

Tur, C., Heger, A., Austin, S.M.: Production of  $^{26}\text{Al}$ ,  $^{44}\text{Ti}$ , and  $^{60}\text{Fe}$  in Core-collapse Supernovae: Sensitivity to the Rates of the Triple Alpha and  $^{12}\text{C}(\alpha, \gamma)^{16}\text{O}$  Reactions. *ApJ* **718**(1), 357–367 (2010) <https://doi.org/10.1088/0004-637X/718/1/357> arXiv:0908.4283 [astro-ph.SR]

Austin, S.M., West, C., Heger, A.: Reducing Uncertainties in the Production of the Gamma-emitting Nuclei  $^{26}\text{Al}$ ,  $^{44}\text{Ti}$ , and  $^{60}\text{Fe}$  in Core-collapse Supernovae by Using Effective Helium Burning Rates. *ApJL* **839**(1), 9 (2017) <https://doi.org/10.3847/2041-8213/aa68e7> arXiv:1704.01240 [astro-ph.SR]

Bouchet, L., Strong, A.W., Porter, T.A., Moskalenko, I.V., Jourdain, E., Roques, J.-P.: Diffuse Emission Measurement with the SPectrometer on INTEGRAL as an Indirect Probe of Cosmic-Ray Electrons and Positrons. *ApJ* **739**(1), 29 (2011) <https://doi.org/10.1088/0004-637X/739/1/29> arXiv:1107.0200 [astro-ph.HE]

Leising, M.D., Clayton, D.D.: Angular distribution of interstellar Al-26. *ApJ* **294**, 591–598 (1985) <https://doi.org/10.1086/163326>

José, J., Hernanz, M., Coc, A.: New Results on  $^{26}\text{Al}$  Production in Classical Novae. *ApJL* **479**(1), 55–58 (1997) <https://doi.org/10.1086/310575> arXiv:astro-ph/9701181 [astro-ph]

Bennett, M.B., Wrede, C., Chipps, K.A., José, J., Liddick, S.N., Santia, M., Bowe, A., Chen, A.A., Cooper, N., Irvine, D., McNeice, E., Montes, F., Naqvi, F., Ortez, R., Pain, S.D., Pereira, J., Prokop, C., Quaglia, J., Quinn, S.J., Schwartz, S.B., Shanab, S., Simon, A., Spyrou, A., Thiagalingam, E.: Classical-Nova Contribution to the

Milky Way's Al26 Abundance: Exit Channel of the Key Al25( $p, \gamma$ )Si26 Resonance. Phys. Rev. Lett. **111**(23), 232503 (2013) <https://doi.org/10.1103/PhysRevLett.111.232503> arXiv:1312.3668 [nucl-ex]

Clayton, D.D., Hoyle, F.: Gamma-Ray Lines from Novae. ApJL **187**, 101 (1974) <https://doi.org/10.1086/181406>

Clayton, D.D.: Li-7 gamma-ray lines from novae. ApJL **244**, 97 (1981) <https://doi.org/10.1086/183488>

Hernanz, M.: Gamma-ray Emission from Nova Outbursts. In: Woudt, P.A., Ribeiro, V.A.R.M. (eds.) Stellar Novae: Past and Future Decades. Astronomical Society of the Pacific Conference Series, vol. 490, p. 319 (2014). <https://doi.org/10.48550/arXiv.1305.0769>

Hernanz, M., José, J.: Radioactivities from novae. NewAR **50**(7-8), 504–508 (2006) <https://doi.org/10.1016/j.newar.2006.06.012>

Leising, M.D., Clayton, D.D.: Positron Annihilation Gamma Rays from Novae. ApJ **323**, 159 (1987) <https://doi.org/10.1086/165816>

Gómez-Gomar, J., Hernanz, M., Jose, J., Isern, J.: Gamma-ray emission from individual classical novae. MNRAS **296**(4), 913–920 (1998) <https://doi.org/10.1046/j.1365-8711.1998.01421.x> arXiv:astro-ph/9711322 [astro-ph]

Hernanz, M., José, J., Coc, A., Gómez-Gomar, J., Isern, J.: Gamma-Ray Emission from Novae Related to Positron Annihilation: Constraints on its Observability Posed by New Experimental Nuclear Data. ApJL **526**(2), 97–100 (1999) <https://doi.org/10.1086/312372> arXiv:astro-ph/9910111 [astro-ph]

Leung, S.-C., Siegert, T.: Gamma-ray light curves and spectra of classical novae. MNRAS **516**(1), 1008–1021 (2022) <https://doi.org/10.1093/mnras/stac1672> arXiv:2112.06893 [astro-ph.HE]

Leising, M.D., Share, G.H., Chupp, E.L., Kanbach, G.: Gamma-Ray Limits on  $^{22}\text{Na}$  Production in Novae. ApJ **328**, 755 (1988) <https://doi.org/10.1086/166334>

Iyudin, A.F., Bennett, K., Bloemen, H., Diehl, R., Hermsen, W., Lichti, G.G., Morris, D., Ryan, J., Schönfelder, V., Steinle, H., Strong, A., Varendorff, M., Winkler, C.: COMPTEL search for  $^{22}\text{Na}$  line emission from recent novae. A&A **300**, 422 (1995)

Siegert, T., Ghosh, S., Mathur, K., Spraggan, E., Yeddanapudi, A.: Nucleosynthesis constraints through  $\gamma$ -ray line measurements from classical novae. Hierarchical model for the ejecta of  $^{22}\text{Na}$  and  $^7\text{Be}$ . A&A **650**, 187 (2021) <https://doi.org/10.1051/0004-6361/202140300>

Jean, P., Hernanz, M., Gómez-Gomar, J., José, J.: Galactic 1.275-MeV emission from

ONe novae and its detectability by INTEGRAL/SPI. MNRAS **319**(2), 350–364 (2000) <https://doi.org/10.1046/j.1365-8711.2000.03587.x> arXiv:astro-ph/0004126 [astro-ph]

Shafter, A.W.: The Galactic Nova Rate Revisited. ApJ **834**(2), 196 (2017) <https://doi.org/10.3847/1538-4357/834/2/196> arXiv:1606.02358 [astro-ph.SR]

Higdon, J.C., Fowler, W.A.: Gamma-Ray Constraints on  $^{22}\text{Na}$  Yields in Nova Explosions. ApJ **317**, 710 (1987) <https://doi.org/10.1086/165317>

Mahoney, W.A., Ling, J.C., Jacobson, A.S., Lingenfelter, R.E.: Diffuse galactic gamma-ray line emission from nucleosynthetic Fe-60, Al-26, and Na-22 - Preliminary limits from HEAO 3. ApJ **262**, 742–748 (1982) <https://doi.org/10.1086/160469>

Jean, P., Knöldlseder, J., von Ballmoos, P., Gómez-Gomar, J., Hernanz, M., José, J.: Upper limits of the  $^{22}\text{Na}$  yield from O-Ne nova. In: Gimenez, A., Reglero, V., Winkler, C. (eds.) Exploring the Gamma-Ray Universe. ESA Special Publication, vol. 459, pp. 73–77 (2001). <https://doi.org/10.48550/arXiv.astro-ph/0106340>

Fougères, C., de Oliveira Santos, F., José, J., Michelagnoli, C., Clément, E., Kim, Y.H., Lemasson, A., Guimaraes, V., Barrientos, D., Bemmerer, D., Benzoni, G., Boston, A.J., Böttger, R., Boulay, F., Bracco, A., Čeliković, I., Cederwall, B., Ciemala, M., Delafosse, C., Domingo-Pardo, C., Dudouet, J., Eberth, J., Fülop, Z., González, V., Gottardo, A., Goupi, J., Hess, H., Jungclaus, A., Kaşkaş, A., Korichi, A., Lenzi, S.M., Leoni, S., Li, H., Ljungvall, J., Lopez-Martens, A., Menegazzo, R., Mengoni, D., Million, B., Mrázek, J., Napoli, D.R., Navin, A., Nyberg, J., Podolyák, Z., Pullia, A., Quintana, B., Ralet, D., Redon, N., Reiter, P., Rezynkina, K., Saillant, F., Salsac, M.-D., Sánchez-Benítez, A.M., Sanchis, E., Şenyiğit, M., Siciliano, M., Smirnova, N.A., Sohler, D., Stanoi, M., Theisen, C., Valiente-Dobón, J.J., Ujić, P., Zielińska, M.: Search for  $^{22}\text{Na}$  in novae supported by a novel method for measuring femtosecond nuclear lifetimes. Nature Communications **14**, 4536 (2023) <https://doi.org/10.1038/s41467-023-40121-3> arXiv:2212.06302 [nucl-ex]

Knöldlseder, J., Bennett, K., Bloemen, H., Diehl, R., Hermsen, W., Oberlack, U., Ryan, J., Schönfelder, V., von Ballmoos, P.: A multiwavelength comparison of COMPTEL 1.8 MeV  $\{\text{26Al}\}$  line data. A&A **344**, 68–82 (1999)

Canete, L., Doherty, D.T., Lotay, G., Seweryniak, D., Campbell, C.M., Carpenter, M.P., Catford, W.N., Chipps, K.A., Henderson, J., Izzard, R.G., Janssens, R.V.F., Jayatissa, H., José, J., Kennington, A.R.L., Kondev, F.G., Korichi, A., Lauritsen, T., Müller-Gatermann, C., Paxman, C., Podolyák, Z., Reed, B.J., Regan, P.H., Revol, W., Siciliano, M., Wilson, G.L., Yates, R., Zhu, S.: Confirmation of a new resonance in  $^{26}\text{Si}$  and contribution of classical novae to the galactic abundance of  $^{26}\text{Al}$ . Phys. Rev. C **108**(3), 035807 (2023) <https://doi.org/10.1103/PhysRevC.108.035807>

Harris, M.J., Leising, M.D., Share, G.H.: A Search for the 478 keV Line from the Decay of Nucleosynthetic  $^{7}\text{Be}$ . ApJ **375**, 216 (1991) <https://doi.org/10.1086/170183>

Siebert, T., Coc, A., Delgado, L., Diehl, R., Greiner, J., Hernanz, M., Jean, P., José, J., Molaro, P., Pleintinger, M.M.M., Savchenko, V., Starrfield, S., Tatischeff, V., Weinberger, C.: Gamma-ray observations of Nova Sgr 2015 No. 2 with INTEGRAL. *A&A* **615**, 107 (2018) <https://doi.org/10.1051/0004-6361/201732514> arXiv:1803.06888 [astro-ph.HE]

Izzo, L., Siebert, T., Jean, P., Molaro, P., Bonifacio, P., Della Valle, M., Parsotan, T.: Possible evidence for the 478 keV emission line from  ${}^7\text{Be}$  decay during the outburst phases of V1369 Cen. arXiv e-prints, 2504–20866 (2025) <https://doi.org/10.48550/arXiv.2504.20866> arXiv:2504.20866 [astro-ph.HE]

Tajitsu, A., Sadakane, K., Naito, H., Arai, A., Kawakita, H., Aoki, W.: The  ${}^7\text{Be}$  II Resonance Lines in Two Classical Novae V5668 Sgr and V2944 Oph. *ApJ* **818**(2), 191 (2016) <https://doi.org/10.3847/0004-637X/818/2/191> arXiv:1601.05168 [astro-ph.SR]

Molaro, P., Izzo, L., Bonifacio, P., Hernanz, M., Selvelli, P., della Valle, M.: Search for  ${}^7\text{Be}$  in the outbursts of four recent novae. *MNRAS* **492**(4), 4975–4985 (2020) <https://doi.org/10.1093/mnras/stz3587> arXiv:1912.13281 [astro-ph.GA]

Jean, P., Gómez-Gomar, J., Hernanz, M., José, J., Isern, J., Vedrenne, G., Mandrou, P., Schönfelder, V., Lichti, G.G., Georgii, R.: Possibility of the Detection of Classical Novae with the Shield of the Integral Spectrometer SPI. *Astrophysical Letters and Communications* **38**, 421 (1999) <https://doi.org/10.48550/arXiv.astro-ph/9903015> arXiv:astro-ph/9903015 [astro-ph]

Hernanz, M., Smith, D.M., Fishman, J., Harmon, A., Gómez-Gomar, J., José, J., Isern, J., Jean, P.: BATSE observations of classical novae. In: McConnell, M.L., Ryan, J.M. (eds.) The Fifth Compton Symposium. American Institute of Physics Conference Series, vol. 510, pp. 82–86. AIP, ??? (2000). <https://doi.org/10.1063/1.1303179>

Harris, M.J., Teegarden, B.J., Cline, T.L., Gehrels, N., Palmer, D.M., Ramaty, R., Seifert, H.: Transient Gamma-Ray Spectrometer Observations of Gamma-Ray Lines from Novae. II. Constraining the Galactic Nova Rate from a Survey of the Southern Sky during 1995–1997. *ApJ* **542**(2), 1057–1063 (2000) <https://doi.org/10.1086/317022> arXiv:astro-ph/0004167 [astro-ph]

Senziani, F., Skinner, G.K., Jean, P., Hernanz, M.: Detectability of gamma-ray emission from classical novae with Swift/BAT. *A&A* **485**(1), 223–231 (2008) <https://doi.org/10.1051/0004-6361:200809863> arXiv:0804.4791 [astro-ph]

Tomsick, J., Boggs, S., Zoglauer, A., Hartmann, D.H., Ajello, M., Burns, E., Fryer, C., Karwin, C., Kierans, C., Lowell, A., Malzac, J., Roberts, J., Saint-Hilaire, P., Shih, A., Siebert, T., Sleator, C., Takahashi, T., Tavecchio, F., Wulf, E., Beechert, J., Gulick, H., Joens, A., Lazar, H., Neights, E., Martinez Oliveros, J.C., Matsumoto, S., Melia, T., Yoneda, H., Amman, M., Bal, D., von Ballmoos, P., Bates, H., Böttcher, M., Bulgarelli, A., Cavazzuti, E., Chang, H.K., Chen, C., Chu, C.Y., Ciabattoni,

A., Costamante, L., Dreyer, L., Fioretti, V., Fenu, F., Gallego, S., Ghirlanda, G., Grove, E., Huang, C.Y., Jean, P., Khatiya, N., Knödlseder, J., Kraus, M., Leising, M., Lewis, T., Lommler, J., Marcotulli, L., Martinez Castellanos, I., Mittal, S., Negro, M., Al Nussirat, S., Nakazawa, K., Oberlack, U., Palmore, D., Panebianco, G., Parmiggiani, N., Pike, S., Rogers, F., Schutte, H., Sheng, Y., Smale, A., Smith, J.R., Trigg, A., Venter, T., Watanabe, Y., Zhang, H.: The Compton Spectrometer and Imager. In: 38th International Cosmic Ray Conference, p. 745 (2024). <https://doi.org/10.48550/arXiv.2308.12362>

Burbidge, E.M., Burbidge, G.R., Fowler, W.A., Hoyle, F.: Synthesis of the Elements in Stars. *Reviews of Modern Physics* **29**(4), 547–650 (1957) <https://doi.org/10.1103/RevModPhys.29.547>

Colgate, S.A., White, R.H.: The Hydrodynamic Behavior of Supernovae Explosions. *ApJ* **143**, 626 (1966) <https://doi.org/10.1086/148549>

Andrews, S., Fryer, C., Even, W., Jones, S., Pignatari, M.: The Nucleosynthetic Yields of Core-collapse Supernovae: Prospects for the Next Generation of Gamma-Ray Astronomy. *ApJ* **890**(1), 35 (2020) <https://doi.org/10.3847/1538-4357/ab64f8> [arXiv:1912.10542](https://arxiv.org/abs/1912.10542) [astro-ph.HE]

Stritzinger, M., Mazzali, P.A., Sollerman, J., Benetti, S.: Consistent estimates of  $^{56}\text{Ni}$  yields for type Ia supernovae. *A&A* **460**(3), 793–798 (2006) <https://doi.org/10.1051/0004-6361:20065514> [arXiv:astro-ph/0609232](https://arxiv.org/abs/astro-ph/0609232) [astro-ph]

Weinberger, C., Diehl, R., Pleintinger, M.M.M., Siegert, T., Greiner, J.:  $^{44}\text{Ti}$  ejecta in young supernova remnants. *A&A* **638**, 83 (2020) <https://doi.org/10.1051/0004-6361/202037536> [arXiv:2004.12688](https://arxiv.org/abs/2004.12688) [astro-ph.HE]

Magkotsios, G., Timmes, F.X., Hungerford, A.L., Fryer, C.L., Young, P.A., Wiescher, M.: Trends in  $^{44}\text{Ti}$  and  $^{56}\text{Ni}$  from Core-collapse Supernovae. *ApJS* **191**(1), 66–95 (2010) <https://doi.org/10.1088/0067-0049/191/1/66> [arXiv:1009.3175](https://arxiv.org/abs/1009.3175) [astro-ph.SR]

Prantzos, N.: Nucleosynthesis and gamma-ray lines. arXiv e-prints, 1101–2112 (2011) <https://doi.org/10.48550/arXiv.1101.2112> [arXiv:1101.2112](https://arxiv.org/abs/1101.2112) [astro-ph.HE]

Prantzos, N.: An Introduction to Galactic Chemical Evolution. In: Charbonnel, C., Zahn, J.-P. (eds.) EAS Publications Series. EAS Publications Series, vol. 32, pp. 311–356 (2008). <https://doi.org/10.1051/eas:0832009>

Kobayashi, C., Karakas, A.I., Lugaro, M.: The Origin of Elements from Carbon to Uranium. *ApJ* **900**(2), 179 (2020) <https://doi.org/10.3847/1538-4357/abae65> [arXiv:2008.04660](https://arxiv.org/abs/2008.04660) [astro-ph.GA]

Vasini, A., Matteucci, F., Spitoni, E.: Chemical evolution of  $^{26}\text{Al}$  and  $^{60}\text{Fe}$  in the Milky Way. *MNRAS* **517**(3), 4256–4264 (2022) <https://doi.org/10.1093/mnras/stac2981> [arXiv:2204.00510](https://arxiv.org/abs/2204.00510) [astro-ph.GA]

Fu, A., Arnett, W.D.: The Late Behavior of Supernova 1987A. II. Gamma-Ray Transparency of the Ejecta. *ApJ* **340**, 414 (1989) <https://doi.org/10.1086/167403>

Grebenev, S.A., Syunyaev, R.A.: The Expected X-Ray Emission from Supernova 1987A - Monte-Carlo Calculations. *Soviet Astronomy Letters* **13**, 397 (1987)

Palmer, D.M., Schindler, S.M., Cook, W.R., Grunsfeld, J.M., Heindl, W.A., Prince, T.A., Stone, E.C.: Gamma-Ray Continuum and Line Observations of SN 1987A. *ApJ* **412**, 203 (1993) <https://doi.org/10.1086/172912>

Leising, M.D., Share, G.H.: The Gamma-Ray Light Curves of SN 1987A. *ApJ* **357**, 638 (1990) <https://doi.org/10.1086/168952>

Iyudin, A.F., Diehl, R., Bloemen, H., Hermsen, W., Lichti, G.G., Morris, D., Ryan, J., Schönfelder, V., Steinle, H., Varendorff, M., de Vries, C., Winkler, C.: COMPTEL observations of  $^{44}\text{Ti}$  gamma-ray line emission from Cas A. *A&A* **284**, 1–4 (1994)

The, L.-S., Leising, M.D., Kurfess, J.D., Johnson, W.N., Hartmann, D.H., Gehrels, N., Grove, J.E., Purcell, W.R.: CGRO/OSSE observations of the Cassiopeia A SNR. *A&AS* **120**, 357–360 (1996)

Vink, J., Laming, J.M., Kaastra, J.S., Bleeker, J.A.M., Bloemen, H., Oberlack, U.: Detection of the 67.9 and 78.4 keV Lines Associated with the Radioactive Decay of  $^{44}\text{Ti}$  in Cassiopeia A. *ApJL* **560**(1), 79–82 (2001) <https://doi.org/10.1086/324172> [arXiv:astro-ph/0107468](https://arxiv.org/abs/astro-ph/0107468) [astro-ph]

Renaud, M., Vink, J., Decourchelle, A., Lebrun, F., den Hartog, P.R., Terrier, R., Couvreur, C., Knödlseder, J., Martin, P., Prantzos, N., Bykov, A.M., Bloemen, H.: The Signature of  $^{44}\text{Ti}$  in Cassiopeia A Revealed by IBIS/ISGRI on INTEGRAL. *ApJL* **647**(1), 41–44 (2006) <https://doi.org/10.1086/507300> [arXiv:astro-ph/0606736](https://arxiv.org/abs/astro-ph/0606736) [astro-ph]

Grefenstette, B.W., Harrison, F.A., Boggs, S.E., Reynolds, S.P., Fryer, C.L., Madsen, K.K., Wik, D.R., Zoglauer, A., Ellinger, C.I., Alexander, D.M., An, H., Barret, D., Christensen, F.E., Craig, W.W., Forster, K., Giommi, P., Hailey, C.J., Hornstrup, A., Kaspi, V.M., Kitaguchi, T., Koglin, J.E., Mao, P.H., Miyasaka, H., Mori, K., Perri, M., Pivovaroff, M.J., Puccetti, S., Rana, V., Stern, D., Westergaard, N.J., Zhang, W.W.: Asymmetries in core-collapse supernovae from maps of radioactive  $^{44}\text{Ti}$  in Cassiopeia A. *Nature* **506**(7488), 339–342 (2014) <https://doi.org/10.1038/nature12997> [arXiv:1403.4978](https://arxiv.org/abs/1403.4978) [astro-ph.HE]

Siegert, T., Diehl, R., Krause, M.G.H., Greiner, J.: Revisiting INTEGRAL/SPI observations of  $^{44}\text{Ti}$  from Cassiopeia A. *A&A* **579**, 124 (2015) <https://doi.org/10.1051/0004-6361/201525877> [arXiv:1505.05999](https://arxiv.org/abs/1505.05999) [astro-ph.HE]

Motizuki, Y., Kumagai, S.:  $^{44}\text{Ti}$  radioactivity in young supernova remnants: Cas A and SN 1987A. *NewAR* **48**(1-4), 69–73 (2004) <https://doi.org/10.1016/j.newar.2003.11>

009 arXiv:astro-ph/0311080 [astro-ph]

Clayton, D.D., Colgate, S.A., Fishman, G.J.: Gamma-Ray Lines from Young Supernova Remnants. *ApJ* **155**, 75 (1969) <https://doi.org/10.1086/149849>

Matz, S.M., Share, G.H.: A Limit on the Production of  $^{56}\text{Ni}$  in a Type I Supernova. *ApJ* **362**, 235 (1990) <https://doi.org/10.1086/169259>

Churazov, E., Sunyaev, R., Isern, J., Knöldlseder, J., Jean, P., Lebrun, F., Chugai, N., Grebenev, S., Bravo, E., Sazonov, S., Renaud, M.: Cobalt-56  $\gamma$ -ray emission lines from the type Ia supernova 2014J. *Nature* **512**(7515), 406–408 (2014) <https://doi.org/10.1038/nature13672> arXiv:1405.3332 [astro-ph.HE]

Lichti, G.G., Bennett, K., den Herder, J.W., Diehl, R., Morris, D., Ryan, J., Schönfelder, V., Steinle, H., Strong, A.W., Winkler, C.: COMPTEL upper limits on gamma-ray line emission from Supernova 1991T. *A&A* **292**, 569 (1994)

Leising, M.D., Johnson, W.N., Kurfess, J.D., Clayton, D.D., Grabelsky, D.A., Jung, G.V., Kinzer, R.L., Purcell, W.R., Strickman, M.S., The, L.-S., Ulmer, M.P.: Compton Gamma Ray Observatory OSSE Observations of SN 1991T. *ApJ* **450**, 805 (1995) <https://doi.org/10.1086/176185>

Georgii, R., Plüschke, S., Diehl, R., Lichti, G.G., Schönfelder, V., Bloemen, H., Hermsen, W., Ryan, J., Bennett, K.: COMPTEL upper limits for the  $^{56}\text{Co}$  gamma-ray emission from SN1998bu. *A&A* **394**, 517–523 (2002) <https://doi.org/10.1051/0004-6361:20021133> arXiv:astro-ph/0208152 [astro-ph]

Isern, J., Jean, P., Bravo, E., Diehl, R., Knöldlseder, J., Domingo, A., Hirschmann, A., Höflich, P., Lebrun, F., Renaud, M., Soldi, S., Elias-Rosa, N., Hernanz, M., Kulebi, B., Zhang, X., Badenes, C., Domínguez, I., Garcia-Senz, D., Jordi, C., Lichti, G., Vedrenne, G., Von Ballmoos, P.: Observation of SN2011fe with INTEGRAL. I. Pre-maximum phase. *A&A* **552**, 97 (2013) <https://doi.org/10.1051/0004-6361/201220303> arXiv:1302.3381 [astro-ph.HE]

Churazov, E., Sunyaev, R., Isern, J., Bikmaev, I., Bravo, E., Chugai, N., Grebenev, S., Jean, P., Knöldlseder, J., Lebrun, F., Kuulkers, E.: Gamma-rays from Type Ia Supernova SN2014J. *ApJ* **812**(1), 62 (2015) <https://doi.org/10.1088/0004-637X/812/1/62> arXiv:1502.00255 [astro-ph.HE]

Diehl, R., Siegert, T., Hillebrandt, W., Krause, M., Greiner, J., Maeda, K., Röpke, F.K., Sim, S.A., Wang, W., Zhang, X.: SN2014J gamma rays from the  $^{56}\text{Ni}$  decay chain. *A&A* **574**, 72 (2015) <https://doi.org/10.1051/0004-6361/201424991> arXiv:1409.5477 [astro-ph.HE]

Diehl, R., Siegert, T., Hillebrandt, W., Grebenev, S.A., Greiner, J., Krause, M., Kromer, M., Maeda, K., Röpke, F., Taubenberger, S.: Early  $^{56}\text{Ni}$  decay gamma rays from SN2014J suggest an unusual explosion. *Science* **345**(6201), 1162–1165 (2014)

<https://doi.org/10.1126/science.1254738> arXiv:1407.3061 [astro-ph.HE]

Isern, J., Jean, P., Bravo, E., Knölseder, J., Lebrun, F., Churazov, E., Sunyaev, R., Domingo, A., Badenes, C., Hartmann, D.H., Höflich, P., Renaud, M., Soldi, S., Elias-Rosa, N., Hernanz, M., Domínguez, I., García-Senz, D., Lichten, G.G., Vedrenne, G., Von Ballmoos, P.: Gamma-ray emission from SN2014J near maximum optical light. *A&A* **588**, 67 (2016) <https://doi.org/10.1051/0004-6361/201526941> arXiv:1602.02918 [astro-ph.HE]

The, L.-S., Burrows, A.: Expectations for the Hard X-Ray Continuum and Gamma-Ray Line Fluxes from the Type Ia Supernova SN 2014J in M82. *ApJ* **786**(2), 141 (2014) <https://doi.org/10.1088/0004-637X/786/2/141> arXiv:1402.4806 [astro-ph.HE]

Nomoto, K., Thielemann, F.-K., Yokoi, K.: Accreting white dwarf models for type I supernovae. III. Carbon deflagration supernovae. *ApJ* **286**, 644–658 (1984) <https://doi.org/10.1086/162639>

Burrows, A., The, L.-S.: X- and Gamma-Ray Signatures of Type IA Supernovae. *ApJ* **360**, 626 (1990) <https://doi.org/10.1086/169150>

Müller, E., Höflich, P., Khokhlov, A.: Type IA supernovae : gamma-rays as predicted by delayed detonation models and SN 1991T. *A&A* **249**, 1 (1991)

Höflich, P., Wheeler, J.C., Khokhlov, A.: Hard X-Rays and Gamma Rays from Type IA Supernovae. *ApJ* **492**(1), 228–245 (1998) <https://doi.org/10.1086/305018> arXiv:astro-ph/9709033 [astro-ph]

Gómez-Gomar, J., Isern, J., Jean, P.: Prospects for Type IA supernova explosion mechanism identification with gamma-rays. *MNRAS* **295**, 1–9 (1998) <https://doi.org/10.1046/j.1365-8711.1998.29511115.x> arXiv:astro-ph/9709048 [astro-ph]

Sim, S.A., Mazzali, P.A.: On the  $\gamma$ -ray emission of Type Ia supernovae. *MNRAS* **385**(4), 1681–1690 (2008) <https://doi.org/10.1111/j.1365-2966.2008.12600.x> arXiv:0710.3313 [astro-ph]

Maeda, K., Terada, Y., Kasen, D., Röpke, F.K., Bamba, A., Diehl, R., Nomoto, K., Kromer, M., Seitenzahl, I.R., Yamaguchi, H., Tamagawa, T., Hillebrandt, W.: Prospect of Studying Hard X- and Gamma-Rays from Type Ia Supernovae. *ApJ* **760**(1), 54 (2012) <https://doi.org/10.1088/0004-637X/760/1/54> arXiv:1208.2094 [astro-ph.HE]

Summa, A., Ulyanov, A., Kromer, M., Boyer, S., Röpke, F.K., Sim, S.A., Seitenzahl, I.R., Fink, M., Mannheim, K., Pakmor, R., Ciaraldi-Schoolmann, F., Diehl, R., Maeda, K., Hillebrandt, W.: Gamma-ray diagnostics of Type Ia supernovae. Predictions of observables from three-dimensional modeling. *A&A* **554**, 67 (2013) <https://doi.org/10.1051/0004-6361/201220972> arXiv:1304.2777 [astro-ph.SR]

Wang, L., Wheeler, J.C.: Spectropolarimetry of supernovae. *ARA&A* **46**, 433–474 (2008) <https://doi.org/10.1146/annurev.astro.46.060407.145139> arXiv:0811.1054 [astro-ph]

Porter, A.L., Leising, M.D., Williams, G.G., Milne, P., Smith, P., Smith, N., Bilinski, C., Hoffman, J.L., Huk, L., Leonard, D.C.: Asymmetries in SN 2014J near Maximum Light Revealed through Spectropolarimetry. *ApJ* **828**(1), 24 (2016) <https://doi.org/10.3847/0004-637X/828/1/24> arXiv:1605.03994 [astro-ph.HE]

Cikota, A., Patat, F., Wang, L., Wheeler, J.C., Bulla, M., Baade, D., Höflich, P., Cikota, S., Clocchiatti, A., Maund, J.R., Stevance, H.F., Yang, Y.: Linear spectropolarimetry of 35 Type Ia supernovae with VLT/FORS: an analysis of the Si II line polarization. *MNRAS* **490**(1), 578–599 (2019) <https://doi.org/10.1093/mnras/stz2322> arXiv:1908.07526 [astro-ph.HE]

Höflich, P., Yang, Y., Baade, D., Cikota, A., Maund, J.R., Mishra, D., Patat, F., Patra, K.C., Wang, L., Wheeler, J.C., Filippenko, A.V., Gal-Yam, A., Schulze, S.: The core normal Type Ia supernova 2019np - an overall spherical explosion with an aspherical surface layer and an aspherical  $^{56}\text{Ni}$  core. *MNRAS* **520**(1), 560–582 (2023) <https://doi.org/10.1093/mnras/stad172> arXiv:2301.04721 [astro-ph.SR]

Röpke, F.K.: Following multi-dimensional type Ia supernova explosion models to homologous expansion. *A&A* **432**(3), 969–983 (2005) <https://doi.org/10.1051/0004-6361:20041700> arXiv:astro-ph/0408296 [astro-ph]

Diamond, T.R., Höflich, P., Gerardy, C.L.: Late-time Near-infrared Observations of SN 2005df. *ApJ* **806**(1), 107 (2015) <https://doi.org/10.1088/0004-637X/806/1/107> arXiv:1410.6759 [astro-ph.SR]

Leising, M.D.: Deriving Thermonuclear Supernova Properties from Gamma-Ray Line Measurements. *ApJ* **932**(1), 63 (2022) <https://doi.org/10.3847/1538-4357/ac6efa> arXiv:2205.06348 [astro-ph.HE]

Tiwari, V., Graur, O., Fisher, R., Seitenzahl, I., Leung, S.-C., Nomoto, K., Perets, H.B., Shen, K.: The late-time light curves of Type Ia supernovae: confronting models with observations. *MNRAS* **515**(3), 3703–3715 (2022) <https://doi.org/10.1093/mnras/stac1618> arXiv:2206.02812 [astro-ph.HE]

Troja, E., Segreto, A., La Parola, V., Hartmann, D., Baumgartner, W., Markwardt, C., Barthelmy, S., Cusumano, G., Gehrels, N.: Swift/BAT Detection of Hard X-Rays from Tycho's Supernova Remnant: Evidence for Titanium-44. *ApJL* **797**(1), 6 (2014) <https://doi.org/10.1088/2041-8205/797/1/L6> arXiv:1411.0991 [astro-ph.HE]

Lopez, L.A., Grefenstette, B.W., Reynolds, S.P., An, H., Boggs, S.E., Christensen, F.E., Craig, W.W., Eriksen, K.A., Fryer, C.L., Hailey, C.J., Harrison, F.A., Madsen, K.K., Stern, D.K., Zhang, W.W., Zoglauer, A.: A Spatially Resolved Study

of the Synchrotron Emission and Titanium in Tycho's Supernova Remnant Using NuSTAR. *ApJ* **814**(2), 132 (2015) <https://doi.org/10.1088/0004-637X/814/2/132> [arXiv:1504.07238](https://arxiv.org/abs/1504.07238) [astro-ph.HE]

Woosley, S.E., Taam, R.E., Weaver, T.A.: Models for Type I Supernova. I. Detonations in White Dwarfs. *ApJ* **301**, 601 (1986) <https://doi.org/10.1086/163926>

Leung, S.-C., Nomoto, K.: Explosive Nucleosynthesis in Sub-Chandrasekhar-mass White Dwarf Models for Type Ia Supernovae: Dependence on Model Parameters. *ApJ* **888**(2), 80 (2020) <https://doi.org/10.3847/1538-4357/ab5c1f> [arXiv:1901.10007](https://arxiv.org/abs/1901.10007) [astro-ph.HE]

Roy, N.C., Tiwari, V., Bobrick, A., Kosakowski, D., Fisher, R., Perets, H.B., Kashyap, R., Lorén-Aguilar, P., García-Berro, E.: 3D Hydrodynamical Simulations of Helium-ignited Double-degenerate White Dwarf Mergers. *ApJL* **932**(2), 24 (2022) <https://doi.org/10.3847/2041-8213/ac75e7> [arXiv:2204.09683](https://arxiv.org/abs/2204.09683) [astro-ph.SR]

Panther, F.H., Seitenzahl, I.R., Ruiter, A.J., Siegert, T., Sim, S., Crocker, R.M.: Prospects of direct detection of  $^{48}\text{V}$  gamma-rays from thermonuclear supernovae. *MNRAS* **508**(2), 1590–1598 (2021) <https://doi.org/10.1093/mnras/stab2701> [arXiv:2103.16840](https://arxiv.org/abs/2103.16840) [astro-ph.HE]

Sim, S.A., Fink, M., Kromer, M., Röpke, F.K., Ruiter, A.J., Hillebrandt, W.: 2D simulations of the double-detonation model for thermonuclear transients from low-mass carbon-oxygen white dwarfs. *MNRAS* **420**(4), 3003–3016 (2012) <https://doi.org/10.1111/j.1365-2966.2011.20162.x> [arXiv:1111.2117](https://arxiv.org/abs/1111.2117) [astro-ph.HE]

Kinzer, R.L., Jung, G.V., Gruber, D.E., Matteson, J.L., Peterson, L. E.: Diffuse Cosmic Gamma Radiation Measured by HEAO 1. *ApJ* **475**(1), 361–372 (1997) <https://doi.org/10.1086/303507>

Gruber, D.E., Matteson, J.L., Peterson, L.E., Jung, G.V.: The Spectrum of Diffuse Cosmic Hard X-Rays Measured with HEAO-1. *ApJ* **520**, 124–129 (1999) <https://doi.org/10.1086/307450>

Watanabe, K., Leising, M.D., Share, G.H., Kinzer, R.L.: The MeV cosmic gamma-ray background measured with SMM. *AIP Conference Proceedings* **510**, 471–475 (2000) <https://doi.org/10.1063/1.1290203>

Weidenspointner, G., Varendorff, M., Oberlack, U., Morris, D., Plüschke, S., Diehl, R., Kappadath, S.C., McConnell, M.L., Ryan, J., Schönfelder, V., Steinle, H.: The cosmic diffuse gamma-ray background spectrum between 0.8 and 30 MeV measured with COMPTEL. *AIP Conference Proceedings* **510**, 467–471 (2000) <https://doi.org/10.1063/1.1290201>

Churazov, E., Sunyaev, R., Revnivtsev, M., Sazonov, S., Yao, Y., Ubertini, P., Lebrun,

F., Terrier, R., Broderick, J.W., Shtykovskiy, P., Jourdain, E., Natalucci, L.: INTEGRAL observations of the cosmic X-ray background in the 5–100 keV range via occultation by the Earth. *A&A* **467**, 529–540 (2007) <https://doi.org/10.1051/0004-6361:20066230>

Türler, M., Chernyakova, M., Courvoisier, T.J.-L., Lubinski, P., Neronov, A., Produit, N., Walter, R.: INTEGRAL hard X-ray spectra of the cosmic X-ray background and Galactic ridge emission. *A&A* **512**, 49 (2010) <https://doi.org/10.1051/0004-6361/200913072> arXiv:1001.2110 [astro-ph.CO]

The, L.-S., Leising, M.D., Clayton, D.D.: The Cosmic Gamma-Ray Background from Type IA Supernovae. *ApJ* **403**, 32 (1993) <https://doi.org/10.1086/172180>

Ueda, Y., Akiyama, M., Ohta, K., Miyaji, T.: Cosmological Evolution of the Hard X-Ray Active Galactic Nucleus Luminosity Function and the Origin of the Hard X-Ray Background. *ApJ* **598**(2), 886–908 (2003) <https://doi.org/10.1086/378940> arXiv:astro-ph/0308140 [astro-ph]

Inoue, Y.: Cosmic Gamma-ray Background Radiation. arXiv e-prints, 1412–3886 (2014) <https://doi.org/10.48550/arXiv.1412.3886> arXiv:1412.3886 [astro-ph.HE]

Chugai, N.N.: Cosmic Abundance of Iron. *Astronomy Letters* **49**(5), 209–215 (2023) <https://doi.org/10.1134/S1063773723050018> arXiv:2307.00944 [astro-ph.HE]

Ruiz-Lapuente, P., Korobkin, O.: Gamma-Rays from Kilonovae and the Cosmic Gamma-Ray Background. *ApJ* **892**(1), 45 (2020) <https://doi.org/10.3847/1538-4357/ab744e> arXiv:1912.11974 [astro-ph.HE]

Lacki, B.C., Horiuchi, S., Beacom, J.F.: The Star-forming Galaxy Contribution to the Cosmic MeV and GeV Gamma-Ray Background. *ApJ* **786**(1), 40 (2014) <https://doi.org/10.1088/0004-637X/786/1/40> arXiv:1206.0772 [astro-ph.HE]

Iguaz, J., Serpico, P.D., Siegert, T.: Isotropic x-ray bound on primordial black hole dark matter. *Phys. Rev. D* **103**(10), 103025 (2021) <https://doi.org/10.1103/PhysRevD.103.103025> arXiv:2104.03145 [astro-ph.CO]

Arnett, W.D.: Analytic solutions for the early part of the light curve of Type I supernovae. *Astrophysical Journal* **253**, 785–797 (1982) <https://doi.org/10.1086/159681>

Phillips, M.M.: The Absolute Magnitudes of Type Ia Supernovae. *Astrophysical Journal Letters* **413**, 105–108 (1993) <https://doi.org/10.1086/186970>

Timmes, F.X., Woosley, S.E.: The metagalactic gamma-ray background from Type Ia supernovae. *ApJ* **403**, 32–46 (1993) <https://doi.org/10.1086/172185>

Watanabe, K., Hartmann, D.H., Leising, M.D., The, L.-S.: The Diffuse Gamma-Ray Background from Supernovae. *ApJ* **516**(1), 285–296 (1999) <https://doi.org/10.1086/307110> [arXiv:astro-ph/9809197](https://arxiv.org/abs/astro-ph/9809197) [astro-ph]

Ahn, K., Komatsu, E., Höflich, P.: Cosmic gamma-ray background from type Ia supernovae reexamined: Evidence for missing gamma rays at MeV energy. *Phys. Rev. D* **71**(12), 121301 (2005) <https://doi.org/10.1103/PhysRevD.71.121301> [arXiv:astro-ph/0506126](https://arxiv.org/abs/astro-ph/0506126) [astro-ph]

Lien, A., Fields, B.D.: The Diffuse Gamma-Ray Background from Type Ia Supernovae. *ApJ* **747**(2), 120 (2012) <https://doi.org/10.1088/0004-637X/747/2/120> [arXiv:1201.3447](https://arxiv.org/abs/1201.3447) [astro-ph.CO]

Ruiz-Lapuente, P., The, L.-S., Hartmann, D.H., Ajello, M., Canal, R., Röpke, F.K., Ohlmann, S.T., Hillebrandt, W.: The Origin of the Cosmic Gamma-ray Background in the MeV Range. *ApJ* **820**(2), 142 (2016) <https://doi.org/10.3847/0004-637X/820/2/142> [arXiv:1502.06116](https://arxiv.org/abs/1502.06116) [astro-ph.HE]

Breitschwerdt, D., Egger, R., Freyberg, M.J., Frisch, P.C., Vallerga, J.V.: The Local Bubble Origin and Evolution. *Space Sci. Rev.* **78**(1-2), 183–198 (1996) <https://doi.org/10.1007/BF00170805>

Ramaty, R., Lingenfelter, R.E.: Interpretations and Implications of Gamma Ray Lines from Solar Flares, the Galactic Center and Gamma Ray Transients., (1980)

Green, D.A.: A revised catalogue of 294 Galactic supernova remnants. *Journal of Astrophysics and Astronomy* **40**(4), 36 (2019) <https://doi.org/10.1007/s12036-019-9601-6> [arXiv:1907.02638](https://arxiv.org/abs/1907.02638) [astro-ph.GA]

Boggs, S.E., Harrison, F.A., Miyasaka, H., Grefenstette, B.W., Zoglauer, A., Fryer, C.L., Reynolds, S.P., Alexander, D.M., An, H., Barret, D., Christensen, F.E., Craig, W.W., Forster, K., Giommi, P., Hailey, C.J., Hornstrup, A., Kitaguchi, T., Koglin, J.E., Madsen, K.K., Mao, P.H., Mori, K., Perri, M., Pivovaroff, M.J., Puccetti, S., Rana, V., Stern, D., Westergaard, N.J., Zhang, W.W.:  $^{44}\text{Ti}$  gamma-ray emission lines from SN1987A reveal an asymmetric explosion. *Science* **348**(6235), 670–671 (2015) <https://doi.org/10.1126/science.aaa2259>

The, L.-S., Clayton, D.D., Diehl, R., Hartmann, D.H., Iyudin, A.F., Leising, M.D., Meyer, B.S., Motizuki, Y., Schönfelder, V.: Are  $^{44}\text{Ti}$ -producing supernovae exceptional? *A&A* **450**(3), 1037–1050 (2006) <https://doi.org/10.1051/0004-6361:20054626> [arXiv:astro-ph/0601039](https://arxiv.org/abs/astro-ph/0601039) [astro-ph]

Englhauser, J., Dobereiner, S., Pietsch, W., Reppin, C., Trumper, J., Kendziorra, E., Maisack, M., Mony, B., Staubert, R., Efremov, V., Kaniovsky, A., Kuznetsov, A., Sunyaev, R.: Mir-Kvant HEXE Hard X-Ray Lightcurve of Supernova 1987A. In: Hunt, J., Battrick, B. (eds.) Two Topics in X-Ray Astronomy, Volume 1: X Ray Binaries. Volume 2: AGN and the X Ray Background. ESA Special Publication,

vol. 1, p. 397 (1989)

Sunyaev, R.A., Efremov, V., Kaniovsky, A., Stepanov, D., Unin, S., Kuznetsov, A., Loznikov, V., McLioransky, A., Prudkoglyad, A., Grebenev, S., Reppin, C., Pietsch, W., Englhauser, J., Trümper, J., Voges, W., Kendziorra, E., Bezler, M., Staubert, R.: Hard x-rays from supernova 1987a. *Advances in Space Research* **10**(2), 47–53 (1990) [https://doi.org/10.1016/0273-1177\(90\)90117-I](https://doi.org/10.1016/0273-1177(90)90117-I)

Matz, S.M., Share, G.H., Leising, M.D., Chupp, E.L., Vestrand, W.T., Purcell, W.R., Strickman, M.S., Reppin, C.: Gamma-ray line emission from SN1987A. *Nature* **331**(6155), 416–418 (1988) <https://doi.org/10.1038/331416a0>

Sunyaev, R., Kaniovsky, A., Efremov, V., Gilfanov, M., Churazov, E., Grebenev, S., Kuznetsov, A., Melioranskiy, A., Yamburenko, N., Yunin, S., Stepanov, D., Chulkov, I., Pappe, N., Boyarskiy, M., Gavrilova, E., Loznikov, V., Prudkoglyad, A., Rodin, V., Reppin, C., Pietsch, W., Engelhauser, J., Trümper, J., Voges, W., Kendziorra, E., Bezler, M., Staubert, R., Brinkman, A.C., Heise, J., Mels, W.A., Jager, R., Skinner, G.K., Al-Emam, O., Patterson, T.G., Willmore, A.P., Gilfanov, M., Churazov, E.: Discovery of hard X-ray emission from supernova 1987A. *Nature* **330**, 227–229 (1987) <https://doi.org/10.1038/330227a0>

Shigeyama, T., Nomoto, K.: Theoretical Light Curve of SN 1987A and Mixing of Hydrogen and Nickel in the Ejecta. *ApJ* **360**, 242 (1990) <https://doi.org/10.1086/169114>

Arnett, W.D., Bahcall, J.N., Kirshner, R.P., Woosley, S.E.: Supernova 1987A. *ARA&A* **27**, 629–700 (1989) <https://doi.org/10.1146/annurev.aa.27.090189.003213>

Bussard, R.W., Burrows, A., The, L.S.: SN 1987A Gamma-Ray Line Profiles and Fluxes. *ApJ* **341**, 401 (1989) <https://doi.org/10.1086/167503>

Li, T.-P., Ma, Y.-Q.: Analysis methods for results in gamma-ray astronomy. *ApJ* **272**, 317–324 (1983) <https://doi.org/10.1086/161295>

Vianello, G.: The Significance of an Excess in a Counting Experiment: Assessing the Impact of Systematic Uncertainties and the Case with a Gaussian Background. *ApJS* **236**(1), 17 (2018) <https://doi.org/10.3847/1538-4365/aab780> [arXiv:1712.00118](https://arxiv.org/abs/1712.00118) [physics.data-an]

Thielemann, F.-K., Hashimoto, M.-A., Nomoto, K.: Explosive Nucleosynthesis in SN 1987A. II. Composition, Radioactivities, and the Neutron Star Mass. *ApJ* **349**, 222 (1990) <https://doi.org/10.1086/168308>

Woosley, S.E., Hoffman, R.D.:  $^{57}\text{Co}$  and  $^{44}\text{Ti}$  Production in SN 1987A. *ApJL* **368**, 31 (1991) <https://doi.org/10.1086/185941>

Wang, T., Burrows, A.: Insights into the Production of  $^{44}\text{Ti}$  and Nickel Isotopes

in Core-collapse Supernovae. *ApJ* **974**(1), 39 (2024) <https://doi.org/10.3847/1538-4357/ad6983> arXiv:2406.13746 [astro-ph.HE]

Clayton, D.D., Leising, M.D., The, L.-S., Johnson, W.N., Kurfess, J.D.: The 57 CO Abundance in SN 1987A. *ApJL* **399**, 141 (1992) <https://doi.org/10.1086/186627>

Kurfess, J.D., Johnson, W.N., Kinzer, R.L., Kroeger, R.A., Strickman, M.S., Grove, J.E., Leising, M.D., Clayton, D.D., Grabelsky, D.A., Purcell, W.R., Ulmer, M.P., Cameron, R.A., Jung, G.V.: Oriented Scintillation Spectrometer Experiment Observations of 57Co in SN 1987A. *ApJL* **399**, 137 (1992) <https://doi.org/10.1086/186626>

Seitenzahl, I.R., Timmes, F.X., Magkotsios, G.: The Light Curve of SN 1987A Revisited: Constraining Production Masses of Radioactive Nuclides. *ApJ* **792**(1), 10 (2014) <https://doi.org/10.1088/0004-637X/792/1/10> arXiv:1408.5986 [astro-ph.SR]

Grebenev, S.A., Lutovinov, A.A., Tsygankov, S.S., Winkler, C.: Hard-X-ray emission lines from the decay of  $^{44}\text{Ti}$  in the remnant of supernova 1987A. *Nature* **490**(7420), 373–375 (2012) <https://doi.org/10.1038/nature11473> arXiv:1211.2656 [astro-ph.HE]

Alarie, A., Bilodeau, A., Drissen, L.: A hyperspectral view of Cassiopeia A. *MNRAS* **441**(4), 2996–3008 (2014) <https://doi.org/10.1093/mnras/stu774>

Eriksen, K.A., Arnett, D., McCarthy, D.W., Young, P.: The Reddening Toward Cassiopeia A’s Supernova: Constraining the  $^{56}\text{Ni}$  Yield. *ApJ* **697**(1), 29–36 (2009) <https://doi.org/10.1088/0004-637X/697/1/29> arXiv:0902.4029 [astro-ph.SR]

Tsygankov, S.S., Krivonos, R.A., Lutovinov, A.A., Revnivtsev, M.G., Churazov, E.M., Sunyaev, R.A., Grebenev, S.A.: Galactic survey of  $^{44}\text{Ti}$  sources with the IBIS telescope onboard INTEGRAL. *MNRAS* **458**(4), 3411–3419 (2016) <https://doi.org/10.1093/mnras/stw549> arXiv:1603.01264 [astro-ph.HE]

Wang, W., Li, Z.: Hard X-Ray Emissions from Cassiopeia A Observed by INTEGRAL. *ApJ* **825**(2), 102 (2016) <https://doi.org/10.3847/0004-637X/825/2/102> arXiv:1605.00360 [astro-ph.HE]

Grefenstette, B.W., Fryer, C.L., Harrison, F.A., Boggs, S.E., DeLaney, T., Laming, J.M., Reynolds, S.P., Alexander, D.M., Barret, D., Christensen, F.E., Craig, W.W., Forster, K., Giommi, P., Hailey, C.J., Hornstrup, A., Kitaguchi, T., Koglin, J.E., Lopez, L., Mao, P.H., Madsen, K.K., Miyasaka, H., Mori, K., Perri, M., Pivovaroff, M.J., Puccetti, S., Rana, V., Stern, D., Westergaard, N.J., Wik, D.R., Zhang, W.W., Zoglauer, A.: The Distribution of Radioactive  $^{44}\text{Ti}$  in Cassiopeia A. *ApJ* **834**(1), 19 (2017) <https://doi.org/10.3847/1538-4357/834/1/19> arXiv:1612.02774 [astro-ph.HE]

Weinberger, C.: Supernova Diagnostics from Gamma-Ray Lines in the Young Remnant Phase. PhD thesis, Max-Planck-Institute for Extraterrestrial Physics, Garching (February 2021). <https://mediatum.ub.tum.de/1609856>

Summa, A., Elsässer, D., Mannheim, K.: Nuclear de-excitation line spectrum of Cassiopeia A. *A&A* **533**, 13 (2011) <https://doi.org/10.1051/0004-6361/201117267> [arXiv:1107.4331](https://arxiv.org/abs/1107.4331) [astro-ph.HE]

Liu, B., Yang, R.-z., He, X.-y., Aharonian, F.: New estimation of the nuclear de-excitation line emission from the supernova remnant Cassiopeia A. *MNRAS* **524**(4), 5248–5253 (2023) <https://doi.org/10.1093/mnras/stad2165> [arXiv:2307.08967](https://arxiv.org/abs/2307.08967) [astro-ph.HE]

McKinnon, R., Torrey, P., Vogelsberger, M.: Dust formation in Milky Way-like galaxies. *MNRAS* **457**(4), 3775–3800 (2016) <https://doi.org/10.1093/mnras/stw253> [arXiv:1505.04792](https://arxiv.org/abs/1505.04792) [astro-ph.GA]

Iyudin, A.F., Müller, E., Obergaulinger, M.: Titanium hidden in dust. *MNRAS* **485**(3), 3288–3295 (2019) <https://doi.org/10.1093/mnras/stz419> [arXiv:1902.02249](https://arxiv.org/abs/1902.02249) [astro-ph.HE]

Vance, G.S., Young, P.A., Fryer, C.L., Ellinger, C.I.: Titanium and Iron in the Cassiopeia A Supernova Remnant. *ApJ* **895**(2), 82 (2020) <https://doi.org/10.3847/1538-4357/ab8ade> [arXiv:2005.03777](https://arxiv.org/abs/2005.03777) [astro-ph.HE]

Orlando, S., Wongwathanarat, A., Janka, H.-T., Miceli, M., Ono, M., Nagataki, S., Bocchino, F., Peres, G.: The fully developed remnant of a neutrino-driven supernova. Evolution of ejecta structure and asymmetries in SNR Cassiopeia A. *A&A* **645**, 66 (2021) <https://doi.org/10.1051/0004-6361/202039335> [arXiv:2009.01789](https://arxiv.org/abs/2009.01789) [astro-ph.HE]

Wongwathanarat, A., Janka, H.-T., Müller, E., Plumbi, E., Wanajo, S.: Production and Distribution of  $^{44}\text{Ti}$  and  $^{56}\text{Ni}$  in a Three-dimensional Supernova Model Resembling Cassiopeia A. *ApJ* **842**(1), 13 (2017) <https://doi.org/10.3847/1538-4357/aa72de> [arXiv:1610.05643](https://arxiv.org/abs/1610.05643) [astro-ph.HE]

Hwang, U., Laming, J.M., Badenes, C., Berendse, F., Blondin, J., Cioffi, D., DeLaney, T., Dewey, D., Fesen, R., Flanagan, K.A., Fryer, C.L., Ghavamian, P., Hughes, J.P., Morse, J.A., Plucinsky, P.P., Petre, R., Pohl, M., Rudnick, L., Sankrit, R., Slane, P.O., Smith, R.K., Vink, J., Warren, J.S.: A Million Second Chandra View of Cassiopeia A. *ApJL* **615**(2), 117–120 (2004) <https://doi.org/10.1086/426186> [arXiv:astro-ph/0409760](https://arxiv.org/abs/astro-ph/0409760) [astro-ph]

Maeda, K., Nomoto, K.: Bipolar Supernova Explosions: Nucleosynthesis and Implications for Abundances in Extremely Metal-Poor Stars. *ApJ* **598**(2), 1163–1200 (2003) <https://doi.org/10.1086/378948> [arXiv:astro-ph/0304172](https://arxiv.org/abs/astro-ph/0304172) [astro-ph]

Seitenzahl, I.R., Ciaraldi-Schoolmann, F., Röpke, F.K., Fink, M., Hillebrandt, W., Kromer, M., Pakmor, R., Ruiter, A.J., Sim, S.A., Taubenberger, S.: Three-dimensional delayed-detonation models with nucleosynthesis for Type Ia supernovae. *MNRAS* **429**(2), 1156–1172 (2013) <https://doi.org/10.1093/mnras/sts402> [arXiv:1211.3015](https://arxiv.org/abs/1211.3015) [astro-ph.SR]

Fink, M., Röpke, F.K., Hillebrandt, W., Seitenzahl, I.R., Sim, S.A., Kromer, M.: Double-detonation sub-Chandrasekhar supernovae: can minimum helium shell masses detonate the core? *A&A* **514**, 53 (2010) <https://doi.org/10.1051/0004-6361/200913892> [arXiv:1002.2173](https://arxiv.org/abs/1002.2173) [astro-ph.SR]

Fink, M., Kromer, M., Seitenzahl, I.R., Ciaraldi-Schoolmann, F., Röpke, F.K., Sim, S.A., Pakmor, R., Ruiter, A.J., Hillebrandt, W.: Three-dimensional pure deflagration models with nucleosynthesis and synthetic observables for Type Ia supernovae. *MNRAS* **438**(2), 1762–1783 (2014) <https://doi.org/10.1093/mnras/stt2315> [arXiv:1308.3257](https://arxiv.org/abs/1308.3257) [astro-ph.SR]

Anders, E., Grevesse, N.: Abundances of the elements: Meteoritic and solar. *Geochim. Cosmochim. Acta* **53**(1), 197–214 (1989) [https://doi.org/10.1016/0016-7037\(89\)90286-X](https://doi.org/10.1016/0016-7037(89)90286-X)

Cowan, J.J., Sneden, C., Lawler, J.E., Aprahamian, A., Wiescher, M., Langanke, K., Martínez-Pinedo, G., Thielemann, F.-K.: Origin of the heaviest elements: The rapid neutron-capture process. *Rev. Mod. Phys.* **93**(1), 15002 (2021) <https://doi.org/10.1103/RevModPhys.93.015002> [arXiv:1901.01410](https://arxiv.org/abs/1901.01410) [astro-ph.HE]

Eichler, D., Livio, M., Piran, T., Schramm, D.N.: Nucleosynthesis, Neutrino Bursts and Gamma-Rays from Coalescing Neutron Stars. *Nature* **340**, 126–128 (1989) <https://doi.org/10.1038/340126a0>

Lattimer, J.M., Schramm, D.N.: Black-hole-neutron-star collisions. *Astrophys. J. Lett.* **192**, 145 (1974) <https://doi.org/10.1086/181612>

Woosley, S.E., Wilson, J.R., Mathews, G.J., Hoffman, R.D., Meyer, B.S.: The r process and neutrino heated supernova ejecta. *Astrophys. J.* **433**, 229–246 (1994) <https://doi.org/10.1086/174638>

Winteler, C., Kaeppli, R., Perego, A., Arcones, A., Vasset, N., Nishimura, N., Liebendörfer, M., Thielemann, F.-K.: Magneto-rotationally driven Supernovae as the origin of early galaxy r-process elements? *Astrophys. J. Lett.* **750**, 22 (2012) <https://doi.org/10.1088/2041-8205/750/1/L22> [arXiv:1203.0616](https://arxiv.org/abs/1203.0616) [astro-ph.SR]

Fischer, T., Wu, M.-R., Wehmeyer, B., Bastian, N.-U.F., Martínez-Pinedo, G., Thielemann, F.-K.: Core-collapse Supernova Explosions Driven by the Hadron-quark Phase Transition as a Rare *r*-process Site. *Astrophys. J.* **894**(1), 9 (2020) <https://doi.org/10.3847/1538-4357/ab86b0> [arXiv:2003.00972](https://arxiv.org/abs/2003.00972) [astro-ph.HE]

Grichener, A., Soker, N.: The Common Envelope Jet Supernova (CEJSN) r-process Scenario. *Astrophys. J.* **878**(1), 24 (2019) <https://doi.org/10.3847/1538-4357/ab1d5d> [arXiv:1810.03889](https://arxiv.org/abs/1810.03889) [astro-ph.SR]

Siegel, D.M., Barnes, J., Metzger, B.D.: Collapsars as a major source of r-process elements. *Nature* **569**, 241 (2019) <https://doi.org/10.1038/s41586-019-1136-0> [arXiv:1810.00098](https://arxiv.org/abs/1810.00098) [astro-ph.HE]

Cehula, J., Thompson, T.A., Metzger, B.D.: Dynamics of baryon ejection in magnetar giant flares: implications for radio afterglows, r-process nucleosynthesis, and fast radio bursts. *Mon. Not. Roy. Astron. Soc.* **528**(3), 5323–5345 (2024) <https://doi.org/10.1093/mnras/stae358> [arXiv:2311.05681](https://arxiv.org/abs/2311.05681) [astro-ph.HE]

Abbott, B.P., *et al.*: GW170817: Observation of Gravitational Waves from a Binary Neutron Star Inspiral. *Phys. Rev. Lett.* **119**(16), 161101 (2017) <https://doi.org/10.1103/PhysRevLett.119.161101> [arXiv:1710.05832](https://arxiv.org/abs/1710.05832) [gr-qc]

Abbott, B.P., *et al.*: Multi-messenger Observations of a Binary Neutron Star Merger. *Astrophys. J. Lett.* **848**(2), 12 (2017) <https://doi.org/10.3847/2041-8213/aa91c9> [arXiv:1710.05833](https://arxiv.org/abs/1710.05833) [astro-ph.HE]

Watson, D., *et al.*: Identification of strontium in the merger of two neutron stars. *Nature* **574**(7779), 497–500 (2019) <https://doi.org/10.1038/s41586-019-1676-3> [arXiv:1910.10510](https://arxiv.org/abs/1910.10510) [astro-ph.HE]

Domoto, N., Tanaka, M., Kato, D., Kawaguchi, K., Hotokezaka, K., Wanajo, S.: Lanthanide Features in Near-infrared Spectra of Kilonovae. *Astrophys. J.* **939**(1), 8 (2022) <https://doi.org/10.3847/1538-4357/ac8c36> [arXiv:2206.04232](https://arxiv.org/abs/2206.04232) [astro-ph.HE]

Sneppen, A., Watson, D.: Discovery of a 760 nm P Cygni line in AT2017gfo: Identification of yttrium in the kilonova photosphere. *Astron. Astrophys.* **675**, 194 (2023) <https://doi.org/10.1051/0004-6361/202346421> [arXiv:2306.14942](https://arxiv.org/abs/2306.14942) [astro-ph.HE]

Gillanders, J.H., Sim, S.A., Smartt, S.J., Goriely, S., Bauswein, A.: Modelling the spectra of the kilonova AT2017gfo – II. Beyond the photospheric epochs. *Mon. Not. Roy. Astron. Soc.* **529**(3), 2918–2945 (2024) <https://doi.org/10.1093/mnras/stad3688> [arXiv:2306.15055](https://arxiv.org/abs/2306.15055) [astro-ph.HE]

Hotokezaka, K., Tanaka, M., Kato, D., Gaigalas, G.: Tellurium emission line in kilonova AT 2017gfo. *Mon. Not. Roy. Astron. Soc.* **526**(1), 155–159 (2023) <https://doi.org/10.1093/mnrasl/slad128> [arXiv:2307.00988](https://arxiv.org/abs/2307.00988) [astro-ph.HE]

Patel, A., Metzger, B.D., Cehula, J., Burns, E., Goldberg, J.A., Thompson, T.A.: Direct evidence for r-process nucleosynthesis in delayed MeV emission from the SGR 1806-20 magnetar giant flare (2025) [arXiv:2501.09181](https://arxiv.org/abs/2501.09181) [astro-ph.HE]

Meyer, B.S., Howard, W.M.: Possible gamma-ray signatures of an r-process event. In:

Woosley, S.E. (ed.) *Supernovae*, pp. 630–632. Springer, New York, NY (1991)

Qian, Y.Z., Vogel, P., Wasserburg, G.J.: Supernovae as the site of the r process: Implications for gamma-ray astronomy. *Astrophys. J.* **506**, 868–873 (1998) <https://doi.org/10.1086/306285> arXiv:astro-ph/9803300

Qian, Y.Z., Vogel, P., Wasserburg, G.J.: Probing r-process production of nuclei beyond bi209 with gamma-rays. *Astrophys. J.* **524**, 213–219 (1999) <https://doi.org/10.1086/307805> arXiv:astro-ph/9905387

Ripley, J.L., Metzger, B.D., Arcones, A., Martinez-Pinedo, G.: X-ray Decay Lines from Heavy Nuclei in Supernova Remnants as a Probe of the r-Process Origin and the Birth Periods of Magnetars. *Mon. Not. Roy. Astron. Soc.* **438**(4), 3243–3254 (2014) <https://doi.org/10.1093/mnras/stt2434> arXiv:1310.2950 [astro-ph.HE]

Hotokezaka, K., Wanajo, S., Tanaka, M., Bamba, A., Terada, Y., Piran, T.: Radioactive decay products in neutron star merger ejecta: heating efficiency and  $\gamma$ -ray emission. *Mon. Not. Roy. Astron. Soc.* **459**(1), 35–43 (2016) <https://doi.org/10.1093/mnras/stw404> arXiv:1511.05580 [astro-ph.HE]

Li, L.-X.: Radioactive Gamma-Ray Emissions from Neutron Star Mergers. *Astrophys. J.* **872**(1), 19 (2019) <https://doi.org/10.3847/1538-4357/aaf961> arXiv:1808.09833 [astro-ph.HE]

Wu, M.-R., Banerjee, P., Metzger, B.D., Martínez-Pinedo, G., Aramaki, T., Burns, E., Hailey, C.J., Barnes, J., Karagiorgi, G.: Finding the remnants of the Milky Way’s last neutron star mergers. *Astrophys. J.* **880**(1), 23 (2019) <https://doi.org/10.3847/1538-4357/ab2593> arXiv:1905.03793 [astro-ph.HE]

Korobkin, O., et al.: Gamma-rays from kilonova: a potential probe of r-process nucleosynthesis (2019) <https://doi.org/10.3847/1538-4357/ab64d8> arXiv:1905.05089 [astro-ph.HE]

Wang, X., Vassh, N., Sprouse, T., Mumpower, M., Vogt, R., Randrup, J., Surman, R.: MeV Gamma Rays from Fission: A Distinct Signature of Actinide Production in Neutron Star Mergers. *Astrophys. J. Lett.* **903**(1), 3 (2020) <https://doi.org/10.3847/2041-8213/abbe18> arXiv:2008.03335 [astro-ph.HE]

Chen, M.-H., Li, L.-X., Lin, D.-B., Liang, E.-W.: Gamma-Ray Emission Produced by r-process Elements from Neutron Star Mergers. *Astrophys. J.* **919**(1), 59 (2021) <https://doi.org/10.3847/1538-4357/ac1267> arXiv:2107.02982 [astro-ph.HE]

Terada, Y., Miwa, Y., Ohsumi, H., Fujimoto, S.-i., Katsuda, S., Bamba, A., Yamazaki, R.: Gamma-ray Diagnostics of r-process Nucleosynthesis in the Remnants of Galactic Binary Neutron-Star Mergers. *Astrophys. J.* **933**(1), 111 (2022) <https://doi.org/10.3847/1538-4357/ac721f> arXiv:2205.05407 [astro-ph.HE]

Chen, M.-H., Hu, R.-C., Liang, E.-W.: Radioactively Powered Gamma-Ray Transient Associated with a Kilonova from Neutron Star Merger. *Astrophys. J. Lett.* **932**(1), 7 (2022) <https://doi.org/10.3847/2041-8213/ac7470> arXiv:2204.13269 [astro-ph.HE]

Vassh, N., Wang, X., Lariviere, M., Sprouse, T., Mumpower, M.R., Surman, R., Liu, Z., McLaughlin, G.C., Denissenkov, P., Herwig, F.: Thallium-208: A Beacon of In Situ Neutron Capture Nucleosynthesis. *Phys. Rev. Lett.* **132**(5), 052701 (2024) <https://doi.org/10.1103/PhysRevLett.132.052701> arXiv:2311.10895 [nucl-th]

Chen, M.-H., Li, L.-X., Liang, E.-W.: Radioactive Gamma-Ray Lines from Long-lived Neutron Star Merger Remnants. *Astrophys. J.* **971**(2), 143 (2024) <https://doi.org/10.3847/1538-4357/ad65ec> arXiv:2407.14762 [astro-ph.HE]

Amend, B., Fryer, C.L., Mumpower, M.R., Korobkin, O.: Spatial Models of R-process Remnants and their  $\gamma$ -Ray Detectability. *ApJ* **991**(2), 216 (2025) <https://doi.org/10.3847/1538-4357/adfdde> arXiv:2412.05424 [astro-ph.HE]

Liu, Z., Grohs, E., Lund, K.A., McLaughlin, G.C., Reichert, M., Röderer, I.U., Surman, R., Wang, X.: Gamma rays as a signature of r-process producing supernovae: remnants and future Galactic explosions (2025) arXiv:2506.14991 [astro-ph.HE]

Patel, A., Metzger, B.D., Goldberg, J.A., Cehula, J., Thompson, T.A., Renzo, M.: r-Process Nucleosynthesis and Radioactively Powered Transients from Magnetar Giant Flares (2025) arXiv:2501.17253 [astro-ph.HE]

Shibata, M., Hotokezaka, K.: Merger and Mass Ejection of Neutron-Star Binaries. *Ann. Rev. Nucl. Part. Sci.* **69**, 41–64 (2019) <https://doi.org/10.1146/annurev-nucl-101918-023625> arXiv:1908.02350 [astro-ph.HE]

Mandel, I., Broekgaarden, F.S.: Rates of compact object coalescences. *Living Rev. Rel.* **25**(1), 1 (2022) <https://doi.org/10.1007/s41114-021-00034-3> arXiv:2107.14239 [astro-ph.HE]

Goriely, S., Janka, H.-T.: Solar r-process-constrained actinide production in neutrino-driven winds of supernovae. *Mon. Not. Roy. Astron. Soc.* **459**(4), 4174–4182 (2016) <https://doi.org/10.1093/mnras/stw946> arXiv:1603.04282 [astro-ph.SR]

Rozwadowska, K., Vissani, F., Cappellaro, E.: On the rate of core collapse supernovae in the milky way. *New Astron.* **83**, 101498 (2021) <https://doi.org/10.1016/j.newast.2020.101498> arXiv:2009.03438 [astro-ph.HE]

Smith, D.M., Share, G.H., Murphy, R.J., Schwartz, R.A., Shih, A.Y., Lin, R.P.: High-Resolution Spectroscopy of Gamma-Ray Lines from the X-Class Solar Flare of 2002 July 23. *ApJL* **595**(2), 81–84 (2003) <https://doi.org/10.1086/378173> arXiv:astro-ph/0306292 [astro-ph]

Kiener, J., Gros, M., Tatischeff, V., Weidenspointner, G.: Properties of the energetic

particle distributions during the October 28, 2003 solar flare from INTEGRAL/SPI observations. *A&A* **445**(2), 725–733 (2006) <https://doi.org/10.1051/0004-6361:20053665> arXiv:astro-ph/0511091 [astro-ph]

Türler, M., Tatischeff, V., Beckmann, V., Churazov, E.: INTEGRAL serendipitous observations of solar and terrestrial X-rays and gamma rays. *NewAR* **93**, 101616 (2021) <https://doi.org/10.1016/j.newar.2021.101616> arXiv:2104.06073 [astro-ph.HE]

Tatischeff, V., Gabici, S.: Particle Acceleration by Supernova Shocks and Spallogenic Nucleosynthesis of Light Elements. *Annual Review of Nuclear and Particle Science* **68**(1), 377–404 (2018) <https://doi.org/10.1146/annurev-nucl-101917-021151> arXiv:1803.01794 [astro-ph.HE]

Cummings, A.C., Stone, E.C., Heikkila, B.C., Lal, N., Webber, W.R., Jóhannesson, G., Moskalenko, I.V., Orlando, E., Porter, T.A.: Galactic Cosmic Rays in the Local Interstellar Medium: Voyager 1 Observations and Model Results. *ApJ* **831**(1), 18 (2016) <https://doi.org/10.3847/0004-637X/831/1/18>

Stone, E.C., Cummings, A.C., Heikkila, B.C., Lal, N.: Cosmic ray measurements from Voyager 2 as it crossed into interstellar space. *Nature Astronomy* **3**, 1013–1018 (2019) <https://doi.org/10.1038/s41550-019-0928-3>

Indriolo, N., Neufeld, D.A., Gerin, M., Schilke, P., Benz, A.O., Winkel, B., Menten, K.M., Chambers, E.T., Black, J.H., Bruderer, S., Falgarone, E., Godard, B., Goicoechea, J.R., Gupta, H., Lis, D.C., Ossenkopf, V., Persson, C.M., Sonnentrucker, P., van der Tak, F.F.S., van Dishoeck, E.F., Wolfire, M.G., Wyrowski, F.: Herschel Survey of Galactic OH<sup>+</sup>, H<sub>2</sub>O<sup>+</sup>, and H<sub>3</sub>O<sup>+</sup>: Probing the Molecular Hydrogen Fraction and Cosmic-Ray Ionization Rate. *ApJ* **800**(1), 40 (2015) <https://doi.org/10.1088/0004-637X/800/1/40> arXiv:1412.1106 [astro-ph.GA]

Indriolo, N., McCall, B.J.: Investigating the Cosmic-Ray Ionization Rate in the Galactic Diffuse Interstellar Medium through Observations of H<sup>+</sup>. *ApJ* **745**(1), 91 (2012) <https://doi.org/10.1088/0004-637X/745/1/91> arXiv:1111.6936 [astro-ph.GA]

Tatischeff, V., Kiener, J.: Nuclear interactions of low-energy cosmic rays with the interstellar medium. *Mem. Soc. Astron. Ital.* **82**, 903 (2011) <https://doi.org/10.48550/arXiv.1109.1672> arXiv:1109.1672 [astro-ph.HE]

Ramaty, R., Kozlovsky, B., Lingenfelter, R.E.: Nuclear gamma-rays from energetic particle interactions. *ApJS* **40**, 487–526 (1979) <https://doi.org/10.1086/190596>

Murphy, R.J., Kozlovsky, B., Kiener, J., Share, G.H.: Nuclear Gamma-Ray De-Excitation Lines and Continuum from Accelerated-Particle Interactions in Solar Flares. *ApJS* **183**(1), 142–155 (2009) <https://doi.org/10.1088/0067-0049/183/1/142>

Benhabiles-Mezhoud, H., Kiener, J., Tatischeff, V., Strong, A.W.: De-excitation Nuclear Gamma-Ray Line Emission from Low-energy Cosmic Rays in the Inner Galaxy. *ApJ* **763**(2), 98 (2013) <https://doi.org/10.1088/0004-637X/763/2/98> [arXiv:1212.1622](https://arxiv.org/abs/1212.1622) [astro-ph.HE]

Tatischeff, V., Kiener, J.:  $\gamma$ -ray lines from cosmic-ray interactions with interstellar dust grains. *NewAR* **48**(1-4), 99–103 (2004) <https://doi.org/10.1016/j.newar.2003.11.013> [arXiv:astro-ph/0310827](https://arxiv.org/abs/astro-ph/0310827) [astro-ph]

Jones, A.P., Köhler, M., Ysard, N., Bocchio, M., Verstraete, L.: The global dust modelling framework THEMIS. *A&A* **602**, 46 (2017) <https://doi.org/10.1051/0004-6361/201630225> [arXiv:1703.00775](https://arxiv.org/abs/1703.00775) [astro-ph.GA]

de Angelis, A., Tatischeff, V., Grenier, I.A., McEnery, J., Mallamaci, M., Tavani, M., Oberlack, U., Hanlon, L., Walter, R., Argan, A., von Ballmoos, P., Bulgarelli, A., Bykov, A., Hernanz, M., Kanbach, G., Kuvvetli, I., Pearce, M., Zdziarski, A., Conrad, J., Ghisellini, G., Harding, A., Isern, J., Leising, M., Longo, F., Madejski, G., Martinez, M., Mazziotta, M.N., Paredes, J.M., Pohl, M., Rando, R., Razzano, M., Aboudan, A., Ackermann, M., Addazi, A., Ajello, M., Albertus, C., Álvarez, J.M., Ambrosi, G., Antón, S., Antonelli, L.A., Babic, A., Baibussinov, B., Balbo, M., Baldini, L., Balman, S., Bambi, C., Barres de Almeida, U., Barrio, J.A., Bartels, R., Bastieri, D., Bednarek, W., Bernard, D., Bernardini, E., Bernasconi, T., Bertucci, B., Biland, A., Bissaldi, E., Böttcher, M., Bonvicini, V., Bosch-Ramon, V., Bottacini, E., Bozhilov, V., Bretz, T., Branchesi, M., Brdar, V., Bringmann, T., Brogna, A., Budtz Jørgensen, C., Busetto, G., Buson, S., Busso, M., Caccianiga, A., Camera, S., Campana, R., Caraveo, P., Cardillo, M., Carlson, P., Celestin, S., Cermeño, M., Chen, A., Cheung, C.C., Churazov, E., Ciprini, S., Coc, A., Colafrancesco, S., Coleiro, A., Collmar, W., Coppi, P., Curado da Silva, R., Cutini, S., D’Ammando, F., de Lotto, B., de Martino, D., De Rosa, A., Del Santo, M., Delgado, L., Diehl, R., Dietrich, S., Dolgov, A.D., Domínguez, A., Dominis Prester, D., Donnarumma, I., Dorner, D., Doro, M., Dutra, M., Elsässer, D., Fabrizio, M., Fernández-Barral, A., Fioretti, V., Foffano, L., Formato, V., Fornengo, N., Foschini, L., Franceschini, A., Franckowiak, A., Funk, S., Fuschino, F., Gaggero, D., Galanti, G., Gargano, F., Gasparini, D., Gehrz, R., Giannaria, P., Giglietto, N., Giommi, P., Giordano, F., Giroletti, M., Ghirlanda, G., Godinovic, N., Gouiffés, C., Grove, J.E., Hamadache, C., Hartmann, D.H., Hayashida, M., Hryczuk, A., Jean, P., Johnson, T., José, J., Kaufmann, S., Khelifi, B., Kiener, J., Knödlseder, J., Kole, M., Kopp, J., Kozhuharov, V., Labanti, C., Lalkovski, S., Laurent, P., Limousin, O., Linares, M., Lindfors, E., Lindner, M., Liu, J., Lombardi, S., Loparco, F., López-Coto, R., López Moya, M., Lott, B., Lubrano, P., Malyshev, D., Mankuzhiyil, N., Mannheim, K., Marchā, M.J., Marcianò, A., Marcote, B., Mariotti, M., Marisaldi, M., McBreen, S., Mereghetti, S., Merle, A., Mignani, R., Minervini, G., Moiseev, A., Morselli, A., Moura, F., Nakazawa, K., Nava, L., Nieto, D., Orienti, M., Orio, M., Orlando, E., Orleanski, P., Paiano, S., Paoletti, R., Papitto, A., Pasquato, M., Patricelli, B., Pérez-García, M.Á., Persic, M., Piano, G., Pichel, A., Pimenta, M.,

Pittori, C., Porter, T., Poutanen, J., Prandini, E., Prantzos, N., Produit, N., Profumo, S., Queiroz, F.S.: Science with e-ASTROGAM. A space mission for MeV-GeV gamma-ray astrophysics. *Journal of High Energy Astrophysics* **19**, 1–106 (2018) <https://doi.org/10.1016/j.jheap.2018.07.001> arXiv:1711.01265 [astro-ph.HE]

Ackermann, M., Ajello, M., Atwood, W.B., Baldini, L., Ballet, J., Barbiellini, G., Bastieri, D., Bechtol, K., Bellazzini, R., Berenji, B., Blandford, R.D., Bloom, E.D., Bonamente, E., Borgland, A.W., Brandt, T.J., Bregeon, J., Brigida, M., Bruel, P., Buehler, R., Buson, S., Caliandro, G.A., Cameron, R.A., Caraveo, P.A., Cavazzuti, E., Cecchi, C., Charles, E., Chekhtman, A., Chiang, J., Ciprini, S., Claus, R., Cohen-Tanugi, J., Conrad, J., Cutini, S., de Angelis, A., de Palma, F., Dermer, C.D., Digel, S.W., Silva, E.d.C.e., Drell, P.S., Drlica-Wagner, A., Falletti, L., Favuzzi, C., Fegan, S.J., Ferrara, E.C., Focke, W.B., Fortin, P., Fukazawa, Y., Funk, S., Fusco, P., Gaggero, D., Gargano, F., Germani, S., Giglietto, N., Giordano, F., Giroletti, M., Glanzman, T., Godfrey, G., Grove, J.E., Guiriec, S., Gustafsson, M., Hadash, D., Hanabata, Y., Harding, A.K., Hayashida, M., Hays, E., Horan, D., Hou, X., Hughes, R.E., Jóhannesson, G., Johnson, A.S., Johnson, R.P., Kamae, T., Katagiri, H., Kataoka, J., Knöldlseder, J., Kuss, M., Lande, J., Latronico, L., Lee, S.-H., Lemoine-Goumard, M., Longo, F., Loparco, F., Lott, B., Lovellette, M.N., Lubrano, P., Mazziotta, M.N., McEnery, J.E., Michelson, P.F., Mitthumsiri, W., Mizuno, T., Monte, C., Monzani, M.E., Morselli, A., Moskalenko, I.V., Murgia, S., Naumann-Godo, M., Norris, J.P., Nuss, E., Ohsugi, T., Okumura, A., Omodei, N., Orlando, E., Ormes, J.F., Paneque, D., Panetta, J.H., Parent, D., Pesce-Rollins, M., Pierbattista, M., Piron, F., Pivato, G., Porter, T.A., Rainò, S., Rando, R., Razzano, M., Razzaque, S., Reimer, A., Reimer, O., Sadrozinski, H.F.-W., Sgrò, C., Siskind, E.J., Spandre, G., Spinelli, P., Strong, A.W., Suson, D.J., Takahashi, H., Tanaka, T., Thayer, J.G., Thayer, J.B., Thompson, D.J., Tibaldo, L., Tinivella, M., Torres, D.F., Tosti, G., Troja, E., Usher, T.L., Vandenbroucke, J., Vasileiou, V., Vianello, G., Vitale, V., Waite, A.P., Wang, P., Winer, B.L., Wood, K.S., Wood, M., Yang, Z., Ziegler, M., Zimmer, S.: Fermi-LAT Observations of the Diffuse  $\gamma$ -Ray Emission: Implications for Cosmic Rays and the Interstellar Medium. *ApJ* **750**(1), 3 (2012) <https://doi.org/10.1088/0004-637X/750/1/3> arXiv:1202.4039 [astro-ph.HE]

Ceccarelli, C., Hily-Blant, P., Montmerle, T., Dubus, G., Gallant, Y., Fiasson, A.: Supernova-enhanced Cosmic-Ray Ionization and Induced Chemistry in a Molecular Cloud of W51C. *ApJL* **740**(1), 4 (2011) <https://doi.org/10.1088/2041-8205/740/1/L4> arXiv:1108.3600 [astro-ph.GA]

Vaupré, S., Hily-Blant, P., Ceccarelli, C., Dubus, G., Gabici, S., Montmerle, T.: Cosmic ray induced ionisation of a molecular cloud shocked by the W28 supernova remnant. *A&A* **568**, 50 (2014) <https://doi.org/10.1051/0004-6361/201424036> arXiv:1407.0205 [astro-ph.GA]

Zhou, P., Zhang, G.-Y., Zhou, X., Arias, M., Koo, B.-C., Vink, J., Zhang, Z.-Y., Sun, L., Du, F.-J., Zhu, H., Chen, Y., Bovino, S., Lee, Y.-H.: Unusually High  $\text{HCO}^+/\text{CO}$  Ratios in and outside Supernova Remnant W49B. *ApJ* **931**(2), 144 (2022) <https://doi.org/10.3847/1538-4357/ac3a2a>

//doi.org/10.3847/1538-4357/ac63b5 arXiv:2203.13111 [astro-ph.GA]

Holman, G.D.: Solar eruptive events. Physics Today **65**(4), 56 (2012) <https://doi.org/10.1063/PT.3.1520>

Chen, B., Shen, C., Gary, D.E., Reeves, K.K., Fleishman, G.D., Yu, S., Guo, F., Krucker, S., Lin, J., Nita, G.M., Kong, X.: Measurement of magnetic field and relativistic electrons along a solar flare current sheet. Nature Astronomy **4**, 1140–1147 (2020) <https://doi.org/10.1038/s41550-020-1147-7> arXiv:2005.12757 [astro-ph.SR]

Vilmer, N., MacKinnon, A.L., Hurford, G.J.: Properties of Energetic Ions in the Solar Atmosphere from  $\gamma$ -Ray and Neutron Observations. Space Sci. Rev. **159**, 167–224 (2011) <https://doi.org/10.1007/s11214-010-9728-x> arXiv:1110.2432 [astro-ph.SR]

Reames, D.V.: Solar Energetic Particles. A Modern Primer on Understanding Sources, Acceleration and Propagation vol. 978, (2021). <https://doi.org/10.1007/978-3-030-66402-2>

Smith, D.M., Lin, R.P., Turin, P., Curtis, D.W., Primbsch, J.H., Campbell, R.D., Abiad, R., Schroeder, P., Cork, C.P., Hull, E.L., Landis, D.A., Madden, N.W., Malone, D., Pehl, R.H., Raudorf, T., Sangsingkeow, P., Boyle, R., Banks, I.S., Shirey, K., Schwartz, R.: The RHESSI Spectrometer. Solar Physics **210**(1), 33–60 (2002) <https://doi.org/10.1023/A:1022400716414>

Forrest, D.J., Chupp, E.L., Ryan, J.M., Cherry, M.L., Gleske, I.U., Reppin, C., Pinkau, K., Rieger, E., Kanbach, G., Kinzer, R.L., Share, G., Johnson, W.N., Kurfess, J.D.: The gamma ray spectrometer for the Solar Maximum Mission. Solar Physics **65**(1), 15–23 (1980) <https://doi.org/10.1007/BF00151381>

Harris, M.J., Share, G.H., Beall, J.H., Murphy, R.J.: Upper limit on the steady emission of the 2.223 MeV neutron capture gamma-ray line from the sun. Solar Physics **142**, 171–185 (1992) <https://doi.org/10.1007/BF00156640>

Siegert, T., Berteaud, J., Calore, F., Serpico, P.D., Weinberger, C.: Diffuse Galactic emission spectrum between 0.5 and 8.0 MeV. A&A **660**, 130 (2022) <https://doi.org/10.1051/0004-6361/202142639> arXiv:2202.04574 [astro-ph.HE]

Share, G.H., Murphy, R.J., Dennis, B.R., Finke, J.D.: Solar Gamma-Ray Evidence for a Distinct Population of  $> 1$  MeV Flare-accelerated Electrons. ApJ **981**(1), 11 (2025) <https://doi.org/10.3847/1538-4357/adac60> arXiv:2412.19586 [astro-ph.SR]

Wang, H.T., Ramaty, R.: Neutron Propagation and 2.2 MeV Gamma-Ray Line Production in the Solar Atmosphere. Solar Physics **36**(1), 129–137 (1974) <https://doi.org/10.1007/BF00151553>

Murphy, R.J., Share, G.H., Hua, X.-M., Lin, R.P., Smith, D.M., Schwartz, R.A.: Physical Implications of RHESSI Neutron-Capture Line Measurements. ApJL **595**(2),

93–96 (2003) <https://doi.org/10.1086/378175>

Bania, T.M., Balser, D.S.: Green Bank Telescope Observations of  ${}^3\text{He}^+$ : Planetary Nebulae. *ApJ* **910**(1), 73 (2021) <https://doi.org/10.3847/1538-4357/abd543> [arXiv:2012.11707](https://arxiv.org/abs/2012.11707) [astro-ph.GA]

Battaglia, A.F., Krucker, S.: New insights into the proton precipitation sites in solar flares. *A&A* **694**, 58 (2025) <https://doi.org/10.1051/0004-6361/202453144> [arXiv:2412.11490](https://arxiv.org/abs/2412.11490) [astro-ph.SR]

Shih, A.Y., Lin, R.P., Smith, D.M.: RHESSI Observations of the Proportional Acceleration of Relativistic  $>0.3$  MeV Electrons and  $>30$  MeV Protons in Solar Flares. *ApJL* **698**(2), 152–157 (2009) <https://doi.org/10.1088/0004-637X/698/2/L152>

Murphy, R.J., Share, G.H., Skibo, J.G., Kozlovsky, B.: The Physics of Positron Annihilation in the Solar Atmosphere. *ApJS* **161**, 495–519 (2005) <https://doi.org/10.1086/452634>

Share, G.H., Murphy, R.J., Smith, D.M., Schwartz, R.A., Lin, R.P.: RHESSI  $e^+e^-$  Annihilation Radiation Observations: Implications for Conditions in the Flaring Solar Chromosphere. *ApJL* **615**(2), 169–172 (2004) <https://doi.org/10.1086/426478>

Ramaty, R., Kozlovsky, B., Lingenfelter, R.E.: Nuclear gamma-rays from energetic particle interactions. *ApJS* **40**, 487–526 (1979) <https://doi.org/10.1086/190596>

Murphy, R.J., Kozlovsky, B., Kiener, J., Share, G.H.: Nuclear Gamma-Ray De-Excitation Lines and Continuum from Accelerated-Particle Interactions in Solar Flares. *ApJS* **183**, 142–155 (2009) <https://doi.org/10.1088/0067-0049/183/1/142>

Harris, M.J., Share, G.H., Messina, D.C.: Limits on Galactic Gamma-Ray Lines at 4.44 MeV and 6.13 MeV from Nuclear De-Excitation. *ApJ* **448**, 157 (1995) <https://doi.org/10.1086/175948>

Share, G.H., Murphy, R.J.: Gamma-Ray Measurements of Flare-to-Flare Variations in Ambient Solar Abundances. *ApJ* **452**, 933 (1995) <https://doi.org/10.1086/176360>

Ramaty, R., Mandzhavidze, N., Kozlovsky, B.: Solar atmospheric abundances from gamma ray spectroscopy. In: Ramaty, R., Mandzhavidze, N., Hua, X.-M. (eds.) American Institute of Physics Conference Series. American Institute of Physics Conference Series, vol. 374, pp. 172–183 (1996). <https://doi.org/10.1063/1.50953>

Murphy, R.J., Share, G.H., Grove, J.E., Johnson, W.N., Kinzer, R.L., Kurfess, J.D., Strickman, M.S., Jung, G.V.: Accelerated Particle Composition and Energetics and Ambient Abundances from Gamma-Ray Spectroscopy of the 1991 June 4 Solar Flare. *ApJ* **490**, 883 (1997) <https://doi.org/10.1086/304902>

Mandzhavidze, N., Ramaty, R., Kozlovsky, B.: Determination of the Abundances

of Subcoronal  $^4\text{He}$  and of Solar Flare-accelerated  $^3\text{He}$  and  $^4\text{He}$  from Gamma-Ray Spectroscopy. *ApJ* **518**(2), 918–925 (1999) <https://doi.org/10.1086/307321>

Mandzhavidze, N., Ramaty, R.: Particle Acceleration and Abundances from Gamma-Ray Line Spectroscopy. In: Ramaty, R., Mandzhavidze, N. (eds.) High Energy Solar Physics Workshop - Anticipating Hess! Astronomical Society of the Pacific Conference Series, vol. 206, p. 64 (2000)

Ackermann, M., Ajello, M., Allafort, A., Atwood, W.B., Baldini, L., Barbiellini, G., Bastieri, D., al.: Fermi Detection of  $\gamma$ -Ray Emission from the M2 Soft X-Ray Flare on 2010 June 12. *ApJ* **745**, 144 (2012) <https://doi.org/10.1088/0004-637X/745/2/144>

Lysenko, A.L., Anfinogentov, S.A., Svinkin, D.S., Frederiks, D.D., Fleishman, G.D.: Gamma-Ray Emission from the Impulsive Phase of the 2017 September 6 X9.3 Flare. *ApJ* **877**(2), 145 (2019) <https://doi.org/10.3847/1538-4357/ab1be0> [arXiv:1904.10017](https://arxiv.org/abs/1904.10017) [astro-ph.HE]

Yushkov, B.Y., Kurt, V.G., Galkin, V.I.: High-Energy Emissions Observed in the Impulsive Phase of the 2001 August 25 Eruptive Flare. *Solar Physics* **298**(2), 31 (2023) <https://doi.org/10.1007/s11207-023-02123-8>

Murphy, R.J., Ramaty, R., Reames, D.V., Kozlovsky, B.: Solar abundances from gamma-ray spectroscopy - Comparisons with energetic particle, photospheric, and coronal abundances. *ApJ* **371**, 793–803 (1991) <https://doi.org/10.1086/169944>

Hua, X.-M., Ramaty, R., Lingenfelter, R.E.: Deexcitation gamma-ray line emission from solar flare magnetic loops. *ApJ* **341**, 516–532 (1989) <https://doi.org/10.1086/167513>

Murphy, R.J., Kozlovsky, B., Share, G.H., Hua, X., Lingenfelter, R.E.: Using Gamma-Ray and Neutron Emission to Determine Solar Flare Accelerated Particle Spectra and Composition and the Conditions within the Flare Magnetic Loop. *ApJS* **168**, 167–194 (2007) <https://doi.org/10.1086/509637>

Murphy, R.J., Kozlovsky, B., Share, G.H.: Evidence for Enhanced  $^3\text{He}$  in Flare-accelerated Particles Based on New Calculations of the Gamma-Ray Line Spectrum. *ApJ* **833**, 196 (2016) <https://doi.org/10.3847/1538-4357/833/2/196>

Tusnski, D.S., Szpigiel, S., Giménez de Castro, C.G., MacKinnon, A.L., Simões, P.J.A.: Self-consistent Modeling of Gamma-ray Spectra from Solar Flares with the Monte Carlo Simulation Package FLUKA. *Solar Physics* **294**(8), 103 (2019) <https://doi.org/10.1007/s11207-019-1499-2> [arXiv:1907.11575](https://arxiv.org/abs/1907.11575) [astro-ph.HE]

Kiener, J., Gros, M., Tatischeff, V., Weidenspointner, G.: Properties of the energetic particle distributions during the October 28, 2003 solar flare from INTEGRAL/SPI observations. *A&A* **445**(2), 725–733 (2006) <https://doi.org/10.1051/0004-6361:20054530>

20053665 arXiv:astro-ph/0511091 [astro-ph]

Kiener, J.: Shape and angular distribution of the 4.439-MeV  $\gamma$ -ray line from proton inelastic scattering off  $^{12}\text{C}$ . *Phys. Rev. C* **99**(1), 014605 (2019) <https://doi.org/10.1103/PhysRevC.99.014605> arXiv:1802.00658 [nucl-ex]

Share, G.H., Murphy, R.J., Kiener, J., de Séerville, N.: Directionality of Solar Flare-accelerated Protons and  $\alpha$ -Particles from  $\gamma$ -Ray Line Measurements. *ApJ* **573**, 464–470 (2002) <https://doi.org/10.1086/340595> astro-ph/0203215

Share, G.H., Murphy, R.J., Smith, D.M., Lin, R.P., Dennis, B.R., Schwartz, R.A.: Directionality of Flare-accelerated  $\alpha$ -Particles at the Sun. *ApJL* **595**(2), 89–92 (2003) <https://doi.org/10.1086/378176>

Smith, D.M., Share, G.H., Murphy, R.J., Schwartz, R.A., Shih, A.Y., Lin, R.P.: High-Resolution Spectroscopy of Gamma-Ray Lines from the X-Class Solar Flare of 2002 July 23. *ApJL* **595**(2), 81–84 (2003) <https://doi.org/10.1086/378173> arXiv:astro-ph/0306292 [astro-ph]

Harris, M.J., Tatischeff, V., Kiener, J., Gros, M., Weidenspointner, G.: High resolution  $\gamma$ -ray spectroscopy of flares on the east and west limbs of the Sun. *A&A* **461**(2), 723–729 (2007) <https://doi.org/10.1051/0004-6361:20066084> arXiv:astro-ph/0610859 [astro-ph]

Share, G.H., Murphy, R.J.: Intensity and Directionality of Flare-accelerated  $\alpha$ -Particles at the Sun. *ApJ* **485**(1), 409–418 (1997) <https://doi.org/10.1086/304407>

Emslie, A.G., Dennis, B.R., Shih, A.Y., Chamberlin, P.C., Mewaldt, R.A., Moore, C.S., Share, G.H., Vourlidas, A., Welsch, B.T.: Global Energetics of Thirty-eight Large Solar Eruptive Events. *ApJ* **759**(1), 71 (2012) <https://doi.org/10.1088/0004-637X/759/1/71> arXiv:1209.2654 [astro-ph.SR]

Share, G.H., Murphy, R.J., Newton, E.K.: Limits on Radiative Capture  $\gamma$ -Ray Lines and Implications for Energy Content in Flare-Accelerated Protons. *Solar Physics* **201**(1), 191–200 (2001) <https://doi.org/10.1023/A:1010333807867>

Moskalenko, I.V., Porter, T.A.: The Gamma-Ray Albedo of the Moon. *ApJ* **670**(2), 1467–1472 (2007) <https://doi.org/10.1086/522828> arXiv:0708.2742 [astro-ph]

Prettyman, T.H., Hagerty, J.J., Elphic, R.C., Feldman, W.C., Lawrence, D.J., McKinney, G.W., Vaniman, D.T.: Elemental composition of the lunar surface: Analysis of gamma ray spectroscopy data from Lunar Prospector. *Journal of Geophysical Research (Planets)* **111**(E12), 12007 (2006) <https://doi.org/10.1029/2005JE002656>

Moskalenko, I.V., Porter, T.A., Digel, S.W., Michelson, P.F., Ormes, J.F.: A Celestial Gamma-Ray Foreground Due to the Albedo of Small Solar System Bodies and a Remote Probe of the Interstellar Cosmic-Ray Spectrum. *ApJ* **681**(2), 1708–1716

(2008) <https://doi.org/10.1086/588425> arXiv:0712.2015 [astro-ph]

Churazov, E., Sunyaev, R., Revnivtsev, M., Sazonov, S., Molkov, S., Grebenev, S., Winkler, C., Parmar, A., Bazzano, A., Falanga, M., Gros, A., Lebrun, F., Natalucci, L., Ubertini, P., Roques, J.-P., Bouchet, L., Jourdain, E., Knöldlseder, J., Diehl, R., Budtz-Jorgensen, C., Brandt, S., Lund, N., Westergaard, N.J., Neronov, A., Türler, M., Chernyakova, M., Walter, R., Produit, N., Mowlavi, N., Mas-Hesse, J.M., Domingo, A., Gehrels, N., Kuulkers, E., Kretschmar, P., Schmidt, M.: INTEGRAL observations of the cosmic X-ray background in the 5-100 keV range via occultation by the Earth. *A&A* **467**(2), 529–540 (2007) <https://doi.org/10.1051/0004-6361:20066230> arXiv:astro-ph/0608250 [astro-ph]

Sazonov, S., Churazov, E., Sunyaev, R., Revnivtsev, M.: Hard X-ray emission of the Earth's atmosphere: Monte Carlo simulations. *MNRAS* **377**(4), 1726–1736 (2007) <https://doi.org/10.1111/j.1365-2966.2007.11746.x> arXiv:astro-ph/0608253 [astro-ph]

Moskalenko, I.V., Porter, T.A.: Isotropic Gamma-Ray Background: Cosmic-Ray-Induced Albedo from Debris in the Solar System? *ApJL* **692**(1), 54–57 (2009) <https://doi.org/10.1088/0004-637X/692/1/L54> arXiv:0901.0304 [astro-ph.HE]

Agostinelli, S., Allison, J., Amako, K., Apostolakis, J., Araujo, H., Arce, P., Asai, M., Axen, D., Banerjee, S., Barrand, G., Behner, F., Bellagamba, L., Boudreau, J., Broglia, L., Brunengo, A., Burkhardt, H., Chauvie, S., Chuma, J., Chytracek, R., Cooperman, G., Cosmo, G., Degtyarenko, P., Dell'Acqua, A., Depaola, G., Dietrich, D., Enami, R., Feliciello, A., Ferguson, C., Fesefeldt, H., Folger, G., Foppiano, F., Forti, A., Garelli, S., Giani, S., Giannitrapani, R., Gibin, D., Gómez Cadenas, J.J., González, I., Gracia Abril, G., Greeniaus, G., Greiner, W., Grichine, V., Grossheim, A., Guatelli, S., Gumplinger, P., Hamatsu, R., Hashimoto, K., Hasui, H., Heikkinen, A., Howard, A., Ivanchenko, V., Johnson, A., Jones, F.W., Kallenbach, J., Kanaya, N., Kawabata, M., Kawabata, Y., Kawaguti, M., Kelner, S., Kent, P., Kimura, A., Kodama, T., Kokoulin, R., Kossov, M., Kurashige, H., Lamanna, E., Lampén, T., Lara, V., Lefebure, V., Lei, F., Liendl, M., Lockman, W., Longo, F., Magni, S., Maire, M., Medernach, E., Minamimoto, K., Mora de Freitas, P., Morita, Y., Murakami, K., Nagamatu, M., Nartallo, R., Nieminen, P., Nishimura, T., Ohtsubo, K., Okamura, M., O'Neale, S., Oohata, Y., Paech, K., Perl, J., Pfeiffer, A., Pia, M.G., Ranjard, F., Rybin, A., Sadilov, S., Di Salvo, E., Santin, G., Sasaki, T., Savvas, N., Sawada, Y., Scherer, S., Sei, S., Sirotenko, V., Smith, D., Starkov, N., Stoecker, H., Sulkimo, J., Takahata, M., Tanaka, S., Tcherniaev, E., Safai Tehrani, E., Tropeano, M., Truscott, P., Uno, H., Urban, L., Urban, P., Verderi, M., Walkden, A., Wander, W., Weber, H., Wellisch, J.P., Wenaus, T., Williams, D.C., Wright, D., Yamada, T., Yoshida, H., Zschiesche, D., G EANT4 Collaboration: G EANT4—a simulation toolkit. *Nuclear Instruments and Methods in Physics Research A* **506**(3), 250–303 (2003) [https://doi.org/10.1016/S0168-9002\(03\)01368-8](https://doi.org/10.1016/S0168-9002(03)01368-8)

Whipple, F.L.: A comet model. I. The acceleration of Comet Encke. *ApJ* **111**, 375–394

(1950) <https://doi.org/10.1086/145272>

Purcell, W.R., Cheng, L.-X., Dixon, D.D., Kinzer, R.L., Kurfess, J.D., Leventhal, M., Saunders, M.A., Skibo, J.G., Smith, D.M., Tueller, J.: OSSE Mapping of Galactic 511 keV Positron Annihilation Line Emission. *ApJ* **491**(2), 725–748 (1997) <https://doi.org/10.1086/304994>

Peplowski, P.N., Lawrence, D.J., Prettyman, T.H., Yamashita, N., Bazell, D., Feldman, W.C., Le Corre, L., McCoy, T.J., Reddy, V., Reedy, R.C., Russell, C.T., Toplis, M.J.: Compositional variability on the surface of 4 Vesta revealed through GRAND measurements of high-energy gamma rays. *Meteorit. Planet. Sci.* **48**(11), 2252–2270 (2013) <https://doi.org/10.1111/maps.12176>

Lawrence, D.J., Peplowski, P.N., Beck, A.W., Feldman, W.C., Prettyman, T.H., Russell, C.T., Toplis, M.J., Wilson, J.T., Ammannito, E., Castillo-Rogez, J.C., Desantis, M.C., Mest, S.C., Neesemann, A.: Compositional variability on the surface of 1 Ceres revealed through GRAND measurements of high-energy gamma rays. *Meteorit. Planet. Sci.* **53**(9), 1805–1819 (2018) <https://doi.org/10.1111/maps.13124>

Lawrence, D.J., Peplowski, P.N., Beck, A.W., Burks, M.T., Chabot, N.L., Cully, M.J., Elphic, R.C., Ernst, C.M., Fix, S., Goldsten, J.O., Hoffer, E.M., Kusano, H., Murchie, S.L., Schratz, B.C., Usui, T., Yokley, Z.W.: Measuring the Elemental Composition of Phobos: The Mars-moon Exploration with GAMMA rays and NEutrons (MEGANE) Investigation for the Martian Moons eXploration (MMX) Mission. *Earth and Space Science* **6**(12), 2605–2623 (2019) <https://doi.org/10.1029/2019EA000811>

Hannah, I.G., Hurford, G.J., Hudson, H.S., Lin, R.P., van Bibber, K.: First Limits on the 3–200 keV X-Ray Spectrum of the Quiet Sun Using RHESSI. *ApJL* **659**(1), 77–80 (2007) <https://doi.org/10.1086/516750> [arXiv:astro-ph/0702726](https://arxiv.org/abs/astro-ph/0702726) [astro-ph]

Peplowski, P.N.: The global elemental composition of 433 Eros: First results from the NEAR gamma-ray spectrometer orbital dataset. *Planet. Space Sci.* **134**, 36–51 (2016) <https://doi.org/10.1016/j.pss.2016.10.006>

Dohnanyi, J.S.: Collisional Model of Asteroids and Their Debris. *J. Geophys. Res.* **74**, 2531–2554 (1969) <https://doi.org/10.1029/JB074i010p02531>

Kippen, R.M., Hoover, A.S., Wallace, M.S., Pendleton, G.N., Meegan, C.A., Fishman, G.J., Wilson-Hodge, C.A., Kouveliotou, C., Lichti, G.G., von Kienlin, A., Steinle, H., Diehl, R., Greiner, J., Preece, R.D., Connaughton, V., Briggs, M.S., Paciesas, W.S., Bhat, P.N.: Instrument Response Modeling and Simulation for the GLAST Burst Monitor. In: Ritz, S., Michelson, P., Meegan, C.A. (eds.) *The First GLAST Symposium*. American Institute of Physics Conference Series, vol. 921, pp. 590–591. AIP, ??? (2007). <https://doi.org/10.1063/1.2757466>

Share, G.H., Murphy, R.J.: Atmospheric gamma rays from solar energetic particles

and cosmic rays penetrating the magnetosphere. *J. Geophys. Res.* **106**(A1), 77–92 (2001) <https://doi.org/10.1029/2000JA002012>

Churazov, E., Sazonov, S., Sunyaev, R., Revnivtsev, M.: Earth X-ray albedo for cosmic X-ray background radiation in the 1-1000 keV band. *MNRAS* **385**(2), 719–727 (2008) <https://doi.org/10.1111/j.1365-2966.2008.12918.x>

Johnson, W.N. III, Haymes, R.C.: Detection of a Gamma-Ray Spectral Line from the Galactic-Center Region. *ApJ* **184**, 103–126 (1973) <https://doi.org/10.1086/152309>

Haymes, R.C., Ellis, D.V., Fishman, G.J., Glenn, S.W., Kurfess, J.D.: Observation of Hard Radiation from the Region of the Galactic Center. *ApJ* **157**, 1455 (1969) <https://doi.org/10.1086/150164>

Riegler, G.R., Ling, J.C., Mahoney, W.A., Wheaton, W.A., Willett, J.B., Jacobson, A.S., Prince, T.A.: Variable positron annihilation radiation from the galactic center region. *ApJL* **248**, 13–16 (1981) <https://doi.org/10.1086/183613>

Share, G.H., Kinzer, R.L., Kurfess, J.D., Messina, D.C., Purcell, W.R., Chupp, E.L., Forrest, D.J., Reppin, C.: SMM Detection of Diffuse Galactic 511 keV Annihilation Radiation. *ApJ* **326**, 717 (1988) <https://doi.org/10.1086/166130>

Lingenfelter, R.E., Ramaty, R.: The Nature of the Annihilation Radiation and Gamma-Ray Continuum from the Galactic Center Region. *ApJ* **343**, 686 (1989) <https://doi.org/10.1086/167740>

Knöldlseder, J., Jean, P., Lonjou, V., Weidenspointner, G., Guessoum, N., Gillard, W., Skinner, G., von Ballmoos, P., Vedrenne, G., Roques, J.-P., Schanne, S., Teegarden, B., Schönfelder, V., Winkler, C.: The all-sky distribution of 511 keV electron-positron annihilation emission. *A&A* **441**(2), 513–532 (2005) <https://doi.org/10.1051/0004-6361:20042063> arXiv:astro-ph/0506026 [astro-ph]

Weidenspointner, G., Skinner, G., Jean, P., Knöldlseder, J., von Ballmoos, P., Bignami, G., Diehl, R., Strong, A.W., Cordier, B., Schanne, S., Winkler, C.: An asymmetric distribution of positrons in the Galactic disk revealed by  $\gamma$ -rays. *Nature* **451**(7175), 159–162 (2008) <https://doi.org/10.1038/nature06490>

Bouchet, L., Roques, J.P., Jourdain, E.: On the Morphology of the Electron-Positron Annihilation Emission as Seen by Spi/integral. *ApJ* **720**(2), 1772–1780 (2010) <https://doi.org/10.1088/0004-637X/720/2/1772> arXiv:1007.4753 [astro-ph.HE]

Skinner, G., Diehl, R., Zhang, X., Bouchet, L., Jean, P.: The Galactic distribution of the 511 keV  $e^+e^-$  annihilation radiation. In: Proceedings of the 10th INTEGRAL Workshop: "A Synergistic View of the High-Energy Sky" (INTEGRAL 2014). 15-19 September 2014. Annapolis, MD, USA. Published Online at [Http://pos.sissa.it/cgi-bin/reader/conf.cgi?confid=228](http://pos.sissa.it/cgi-bin/reader/conf.cgi?confid=228), Id.054, p. 054 (2014)

Siebert, T., Diehl, R., Khachtryan, G., Krause, M.G.H., Guglielmetti, F., Greiner, J., Strong, A.W., Zhang, X.: Gamma-ray spectroscopy of positron annihilation in the Milky Way. *A&A* **586**, 84 (2016) <https://doi.org/10.1051/0004-6361/201527510> [arXiv:1512.00325](https://arxiv.org/abs/1512.00325) [astro-ph.HE]

Siebert, T., Crocker, R.M., Diehl, R., Krause, M.G.H., Panther, F.H., Pleintinger, M.M.M., Weinberger, C.: Constraints on positron annihilation kinematics in the inner Galaxy. *A&A* **627**, 126 (2019) <https://doi.org/10.1051/0004-6361/201833856> [arXiv:1906.00498](https://arxiv.org/abs/1906.00498) [astro-ph.HE]

Siebert, T., Crocker, R.M., Macias, O., Panther, F.H., Calore, F., Song, D., Horiuchi, S.: Measuring the smearing of the Galactic 511-keV signal: positron propagation or supernova kicks? *MNRAS* **509**(1), 11–16 (2022) <https://doi.org/10.1093/mnrasl/slab113> [arXiv:2109.03691](https://arxiv.org/abs/2109.03691) [astro-ph.HE]

Yoneda, H., Siebert, T., Mittal, S.: Imaging the positron annihilation line with 20 years of INTEGRAL/SPI observations. *A&A* **702**, 220 (2025) <https://doi.org/10.1051/0004-6361/202555895> [arXiv:2509.01066](https://arxiv.org/abs/2509.01066) [astro-ph.HE]

Churazov, E., Sazonov, S., Tsygankov, S., Sunyaev, R., Varshalovich, D.: Positron annihilation spectrum from the Galactic Centre region observed by SPI/INTEGRAL revisited: annihilation in a cooling ISM? *MNRAS* **411**(3), 1727–1743 (2011) <https://doi.org/10.1111/j.1365-2966.2010.17804.x> [arXiv:1010.0864](https://arxiv.org/abs/1010.0864) [astro-ph.HE]

Kinzer, R.L., Milne, P.A., Kurfess, J.D., Strickman, M.S., Johnson, W.N., Purcell, W.R.: Positron Annihilation Radiation from the Inner Galaxy. *ApJ* **559**(1), 282–295 (2001) <https://doi.org/10.1086/322371>

Siebert, T., Horan, D., Kanbach, G.: Telescope Concepts in Gamma-Ray Astronomy. In: Bambi, C., Sangangelo, A. (eds.) *Handbook of X-ray and Gamma-ray Astrophysics*, p. 80 (2022). [https://doi.org/10.1007/978-981-16-4544-0\\_43-1](https://doi.org/10.1007/978-981-16-4544-0_43-1)

Siebert, T., Diehl, R., Vincent, A.C., Guglielmetti, F., Krause, M.G.H., Boehm, C.: Search for 511 keV emission in satellite galaxies of the Milky Way with INTEGRAL/SPI. *A&A* **595**, 25 (2016) <https://doi.org/10.1051/0004-6361/201629136> [arXiv:1608.00393](https://arxiv.org/abs/1608.00393) [astro-ph.HE]

Siebert, T., Boehm, C., Calore, F., Diehl, R., Krause, M.G.H., Serpico, P.D., Vincent, A.C.: An INTEGRAL/SPI view of reticulum II: particle dark matter and primordial black holes limits in the MeV range. *MNRAS* **511**(1), 914–924 (2022) <https://doi.org/10.1093/mnras/stac008> [arXiv:2109.03791](https://arxiv.org/abs/2109.03791) [astro-ph.HE]

Milne, P.A., The, L.-S., Leising, M.D.: Late Light Curves of Type Ia Supernovae. *ApJ* **559**(2), 1019–1031 (2001) <https://doi.org/10.1086/322352> [arXiv:astro-ph/0104185](https://arxiv.org/abs/astro-ph/0104185) [astro-ph]

Sizun, P., Cassé, M., Schanne, S.: Continuum  $\gamma$ -ray emission from light dark matter

positrons and electrons. Phys. Rev. D **74**(6), 063514 (2006) <https://doi.org/10.1103/PhysRevD.74.063514> arXiv:astro-ph/0607374 [astro-ph]

Beacom, J.F., Yüksel, H.: Stringent Constraint on Galactic Positron Production. Phys. Rev. Lett. **97**(7), 071102 (2006) <https://doi.org/10.1103/PhysRevLett.97.071102> arXiv:astro-ph/0512411 [astro-ph]

Siegert, T., Berteaud, J., Calore, F., Serpico, P.D., Weinberger, C.: Diffuse Galactic emission spectrum between 0.5 and 8.0 MeV. A&A **660**, 130 (2022) <https://doi.org/10.1051/0004-6361/202142639> arXiv:2202.04574 [astro-ph.HE]

Aharonian, F.A., Atoyan, A.M.: Broad-band diffuse gamma ray emission of the galactic disk. A&A **362**, 937–952 (2000) <https://doi.org/10.48550/arXiv.astro-ph/0009009> arXiv:astro-ph/0009009 [astro-ph]

Porter, T.A., Moskalenko, I.V., Strong, A.W., Orlando, E., Bouchet, L.: Inverse Compton Origin of the Hard X-Ray and Soft Gamma-Ray Emission from the Galactic Ridge. ApJ **682**(1), 400–407 (2008) <https://doi.org/10.1086/589615> arXiv:0804.1774 [astro-ph]

Bouchet, L., Mandrou, P., Roques, J.P., Vedrenne, G., Cordier, B., Goldwurm, A., Lebrun, F., Paul, J., Sunyaev, R., Churazov, E., Gilfanov, M., Pavlinsky, M., Grebenev, S., Babalyan, G., Dekhanov, I., Khavenson, N.: SIGMA Discovery of Variable E + E - Annihilation Radiation from the Near Galactic Center Variable Compact Source 1E 1740.7-2942. ApJL **383**, 45 (1991) <https://doi.org/10.1086/186237>

Sunyaev, R., Churazov, E., Gilfanov, M., Pavlinsky, M., Grebenev, S., Babalyan, G., Dekhanov, I., Khavenson, N., Bouchet, L., Mandrou, P., Roques, J.P., Vedrenne, G., Cordier, B., Goldwurm, A., Lebrun, F., Paul, J.: Three Spectral States of 1E 1740.7-2942: From Standard Cygnus X-1 Type Spectrum to the Evidence of Electron-Positron Annihilation Feature. ApJL **383**, 49 (1991) <https://doi.org/10.1086/186238>

Sunyaev, R., Churazov, E., Gilfanov, M., Dyachkov, A., Khavenson, N., Grebenev, S., Kremnev, R., Sukhanov, K., Goldwurm, A., Ballet, J., Cordier, B., Paul, J., Denis, M., Vedrenne, G., Niel, M., Jourdain, E.: X-Ray Nova in Musca (GRS 1124-68): Hard X-Ray Source with Narrow Annihilation Line. ApJL **389**, 75 (1992) <https://doi.org/10.1086/186352>

Siegert, T., Diehl, R., Greiner, J., Krause, M.G.H., Beloborodov, A.M., Bel, M.C., Guglielmetti, F., Rodriguez, J., Strong, A.W., Zhang, X.: Positron annihilation signatures associated with the outburst of the microquasar V404 Cygni. Nature **531**(7594), 341–343 (2016) <https://doi.org/10.1038/nature16978> arXiv:1603.01169 [astro-ph.HE]

Beloborodov, A.M.: Electron-positron outflows from gamma-ray emitting accretion

discs. MNRAS **305**(1), 181–189 (1999) <https://doi.org/10.1046/j.1365-8711.1999.02384.x> arXiv:astro-ph/9901107 [astro-ph]

Bartels, R., Calore, F., Storm, E., Weniger, C.: Galactic binaries can explain the Fermi Galactic centre excess and 511 keV emission. MNRAS **480**(3), 3826–3841 (2018) <https://doi.org/10.1093/mnras/sty2135> arXiv:1803.04370 [astro-ph.HE]

Murphy, R.J., Share, G.H., Skibo, J.G., Kozlovsky, B.: The Physics of Positron Annihilation in the Solar Atmosphere. ApJS **161**(2), 495–519 (2005) <https://doi.org/10.1086/452634>

Frost, K.J., Rothe, E.D., Peterson, L.E.: A Search for the Quiet-Time Solar Gamma Rays from Balloon Altitudes. J. Geophys. Res. **71**, 4079 (1966) <https://doi.org/10.1029/JZ071i017p04079>

Mazziotta, M.N., Luque, P.D.L.T., Di Venere, L., Fassò, A., Ferrari, A., Loparco, F., Sala, P.R., Serini, D.: Cosmic-ray interactions with the Sun using the FLUKA code. Phys. Rev. D **101**(8), 083011 (2020) <https://doi.org/10.1103/PhysRevD.101.083011> arXiv:2001.09933 [astro-ph.HE]

Bisnovatyi-Kogan, G.S., Pozanenko, A.S.: Can Flare Stars Explain the Annihilation Line from the Galactic Bulge? Astrophysics **60**(2), 223–227 (2017) <https://doi.org/10.1007/s10511-017-9477-6>

McConnell, M., Fletcher, S., Bennett, K., Bloemen, H., Diehl, R., Hermsen, W., Ryan, J., Schönfelder, V., Strong, A., van Dijk, R.: COMPTEL all-sky imaging at 2.2 MeV. In: Dermer, C.D., Strickman, M.S., Kurfess, J.D. (eds.) Proceedings of the Fourth Compton Symposium. American Institute of Physics Conference Series, vol. 410, pp. 1099–1103. AIP, ??? (1997). <https://doi.org/10.1063/1.54175>

Spanier, F., Schreiner, C., Schlickeiser, R.: Determining Pitch-Angle Diffusion Coefficients for Electrons in Whistler Turbulence. Physics **4**(1), 80–103 (2022) <https://doi.org/10.3390/physics4010008> arXiv:2112.03999 [astro-ph.HE]

Alexis, A., Jean, P., Martin, P., Ferrière, K.: Monte Carlo modelling of the propagation and annihilation of nucleosynthesis positrons in the Galaxy. A&A **564**, 108 (2014) <https://doi.org/10.1051/0004-6361/201322393> arXiv:1402.6110 [astro-ph.HE]

Jean, P., Gillard, W., Marcowith, A., Ferrière, K.: Positron transport in the interstellar medium. A&A **508**(3), 1099–1116 (2009) <https://doi.org/10.1051/0004-6361/200809830> arXiv:0909.4022 [astro-ph.HE]

Knöldlseder, J., Sabri, K., Jean, P., von Ballmoos, P., Skinner, G., Collmar, W.: Detection of positron in-flight annihilation from the Galaxy. A&A **700**, 257 (2025) <https://doi.org/10.1051/0004-6361/202556046> arXiv:2506.17427 [astro-ph.HE]

Das, S., Krumholz, M.R., Crocker, R.M., Siegert, T., Eisenberger, L.: Relaxation

of Energy Constraints for Positrons Generating the Galactic Annihilation Signal. arXiv e-prints, 2506–00847 (2025) <https://doi.org/10.48550/arXiv.2506.00847> arXiv:2506.00847 [astro-ph.HE]

Berteaud, J., Calore, F., Iguaz, J., Serpico, P.D., Siegert, T.: Strong constraints on primordial black hole dark matter from 16 years of INTEGRAL/SPI observations. Phys. Rev. D **106**(2), 023030 (2022) <https://doi.org/10.1103/PhysRevD.106.023030> arXiv:2202.07483 [astro-ph.HE]

Torre Luque, P., Balaji, S., Silk, J.: New 511 keV Line Data Provide Strongest sub-GeV Dark Matter Constraints. Astrophys. J. Lett. **973**(1), 6 (2024) <https://doi.org/10.3847/2041-8213/ad72f4> arXiv:2312.04907 [hep-ph]

Torre Luque, P., Balaji, S., Carenza, P.: Multimessenger search for electrophilic feebly interacting particles from supernovae. Phys. Rev. D **109**(10), 103028 (2024) <https://doi.org/10.1103/PhysRevD.109.103028> arXiv:2307.13731 [hep-ph]

Torre Luque, P., Balaji, S., Carenza, P., Mastrototaro, L.:  $\gamma$  rays from in-flight positron annihilation as a probe of new physics. Phys. Rev. D **111**(6), 061303 (2025) <https://doi.org/10.1103/PhysRevD.111.L061303> arXiv:2405.08482 [hep-ph]

Slatyer, T.R., Wu, C.-L.: General Constraints on Dark Matter Decay from the Cosmic Microwave Background. Phys. Rev. D **95**(2), 023010 (2017) <https://doi.org/10.1103/PhysRevD.95.023010> arXiv:1610.06933 [astro-ph.CO]

Mirabel, I.F., Rodriguez, L.F., Cordier, B., Paul, J., Lebrun, F.: A double-sided radio jet from the compact Galactic Centre annihilator 1E1740.7-2942. Nature **358**(6383), 215–217 (1992) <https://doi.org/10.1038/358215a0>

Iliadis, C.: Nuclear Physics of Stars, (2015). <https://doi.org/10.1002/9783527692668>

D'Auria, J.M., DRAG. O. N. Collaboration: Astrophysics with a DRAGON at ISAC. Nucl. Phys. A **701**, 625–631 (2002) [https://doi.org/10.1016/S0375-9474\(01\)01656-6](https://doi.org/10.1016/S0375-9474(01)01656-6)

Couder, M., Berg, G.P.A., Görres, J., LeBlanc, P.J., Lamm, L.O., Stech, E., Wiescher, M., Hinnefeld, J.: Design of the recoil mass separator St. George. Nuclear Instruments and Methods in Physics Research A **587**(1), 35–45 (2008) <https://doi.org/10.1016/j.nima.2007.11.069>

Berg, G.P.A., Couder, M., Moran, M.T., Smith, K., Wiescher, M., Schatz, H., Hager, U., Wrede, C., Montes, F., Perdikakis, G., Wu, X., Zeller, A., Smith, M.S., Bardayan, D.W., Chipps, K.A., Pain, S.D., Blackmon, J., Greife, U., Rehm, K.E., Janssens, R.V.F.: Design of SECAR a recoil mass separator for astrophysical capture reactions with radioactive beams. Nuclear Instruments and Methods in Physics Research A **877**, 87–103 (2018) <https://doi.org/10.1016/j.nima.2017.08.048>

Heine, M., Courtin, S., Fruet, G., Jenkins, D.G., Morris, L., Montanari, D., Rudigier, M., Adsley, P., Curien, D., Della Negra, S., Lesrel, J., Beck, C., Charles, L., Dené, P., Haas, F., Hammache, F., Heitz, G., Krauth, M., Meyer, A., Podolyák, Z., Regan, P.H., Richer, M., de Séreville, N., Stodel, C.: The STELLA apparatus for particle-Gamma coincidence fusion measurements with nanosecond timing. *Nuclear Instruments and Methods in Physics Research A* **903**, 1–7 (2018) <https://doi.org/10.1016/j.nima.2018.06.058> arXiv:1802.07679 [physics.ins-det]

Greife, U., Arpesella, C., Barnes, C.A., Bartolucci, F., Bellotti, E., Broggini, C., Corvisiero, P., Fiorentini, G., Fubini, A., Gervino, G., Gorris, F., Gustavino, C., Junker, M., Kavanagh, R.W., Lanza, A., Mezzorani, G., Prati, P., Quarati, P., Rodney, W.S., Rolfs, C., Schulte, W.H., Trautvetter, H.P., Zahnow, D.: Laboratory for Underground Nuclear Astrophysics (LUNA). *Nuclear Instruments and Methods in Physics Research A* **350**(1-2), 327–337 (1994) [https://doi.org/10.1016/0168-9002\(94\)91182-7](https://doi.org/10.1016/0168-9002(94)91182-7)

Liu, W., Li, Z., He, J., Tang, X., Lian, G., An, Z., Chang, J., Chen, H., Chen, Q., Chen, X., Chen, Z., Cui, B., Du, X., Fu, C., Gan, L., Guo, B., He, G., Heger, A., Hou, S., Huang, H., Huang, N., Jia, B., Jiang, L., Kubono, S., Li, J., Li, K., Li, T., Li, Y., Lugaro, M., Luo, X., Ma, H., Ma, S., Mei, D., Qian, Y., Qin, J., Ren, J., Shen, Y., Su, J., Sun, L., Tan, W., Tanihata, I., Wang, S., Wang, P., Wang, Y., Wu, Q., Xu, S., Yan, S., Yang, L., Yang, Y., Yu, X., Yue, Q., Zeng, S., Zhang, H., Zhang, H., Zhang, L., Zhang, N., Zhang, Q., Zhang, T., Zhang, X., Zhang, X., Zhang, Z., Zhao, W., Zhao, Z., Zhou, C., JUNA Collaboration: Progress of Jinping Underground laboratory for Nuclear Astrophysics (JUNA). *Science China Physics, Mechanics, and Astronomy* **59**(4), 642001 (2016) <https://doi.org/10.1007/s11433-016-5785-9>

Szücs, T., Bemmerer, D., Degering, D., Domula, A., Grieber, M., Ludwig, F., Schmidt, K., Steckling, J., Turkat, S., Zuber, K.: Background in  $\gamma$ -ray detectors and carbon beam tests in the Felsenkeller shallow-underground accelerator laboratory. *European Physical Journal A* **55**(10), 174 (2019) <https://doi.org/10.1140/epja/i2019-12865-4> arXiv:1908.08945 [nucl-ex]

Hammache, F., de Séreville, N.: Transfer reactions as a tool in Nuclear Astrophysics. *Frontiers in Physics* **8**, 630 (2021) <https://doi.org/10.3389/fphy.2020.602920> arXiv:2107.13228 [nucl-ex]

Limata, B., Strieder, F., Formicola, A., Imbriani, G., Junker, M., Becker, H.W., Bemmerer, D., Best, A., Bonetti, R., Broggini, C., Caciolli, A., Corvisiero, P., Costantini, H., Dileva, A., Elekes, Z., Fülöp, Z., Gervino, G., Guglielmetti, A., Gustavino, C., Gyürky, G., Lemut, A., Marta, M., Mazzocchi, C., Menegazzo, R., Prati, P., Roca, V., Rolfs, C., Rossi Alvarez, C., Salvo, C., Somorjai, E., Straniero, O., Terrasi, F., Trautvetter, H.-P.: New experimental study of low-energy  $(p, \gamma)$  resonances in magnesium isotopes. *Phys. Rev. C* **82**(1), 015801 (2010) <https://doi.org/10.1103/PhysRevC.82.015801> arXiv:1006.5281 [nucl-ex]

Strieder, F., Limata, B., Formicola, A., Imbriani, G., Junker, M., Bemmerer, D., Best, A., Broggini, C., Caciolli, A., Corvisiero, P., Costantini, H., DiLeva, A., Elekes, Z., Fülop, Z., Gervino, G., Guglielmetti, A., Gustavino, C., Gyürky, G., Lemut, A., Marta, M., Mazzocchi, C., Menegazzo, R., Prati, P., Roca, V., Rolfs, C., Rossi Alvarez, C., Somorjai, E., Straniero, O., Terrasi, F., Trautvetter, H.P.: The  $^{25}\text{Mg}(\text{p},\gamma)^{26}\text{Al}$  reaction at low astrophysical energies. *Physics Letters B* **707**(1), 60–65 (2012) <https://doi.org/10.1016/j.physletb.2011.12.029>

Su, J., Strieder, F., Formicola, A., Imbriani, G., Junker, M., Becker, H.W., Bemmerer, D., Best, A., Bonetti, R., Broggini, C., Caciolli, A., Corvisiero, P., Costantini, H., Dileva, A., Elekes, Z., Fülop, Z., Gervino, G., Guglielmetti, A., Gustavino, C., Gyürky, G., Lemut, A., Marta, M., Mazzocchi, C., Menegazzo, R., Prati, P., Roca, V., Rolfs, C., Rossi Alvarez, C., Salvo, C., Somorjai, E., Straniero, O., Terrasi, F., Trautvetter, H.-P.: First result from the Jinping Underground Nuclear Astrophysics experiment JUNA: precise measurement of the 92 keV  $^{25}\text{Mg}(\text{p},\gamma)^{26}\text{Al}$ . *Science Bulletin* **67**, 125–132 (2022)

Champagne, A.E., Howard, A.J., Smith, M.S., Magnus, P.V., Parker, P.D.: The effect of weak resonances on the  $^{25}\text{Mg}(\text{p},\gamma)^{26}\text{Al}$  reaction rate. *Nucl. Phys. A* **505**(2), 384–396 (1989) [https://doi.org/10.1016/0375-9474\(89\)90382-5](https://doi.org/10.1016/0375-9474(89)90382-5)

Rollefson, A.A., Wijekumar, V., Browne, C.P., Wiescher, M., Hausman, H.J., Kim, W.Y., Schmalbrock, P.: Spectroscopic factors for proton unbound levels in  $^{26}\text{Al}$  and their influence on stellar reaction rates. *Nucl. Phys. A* **507**(2), 413–425 (1990) [https://doi.org/10.1016/0375-9474\(90\)90301-2](https://doi.org/10.1016/0375-9474(90)90301-2)

Li, Y.J., Li, Z.H., Li, E.T., Li, X.Y., Ma, T.L., Shen, Y.P., Liu, J.C., Gan, L., Su, Y., Qiao, L.H., Han, Z.Y., Zhou, Y., Su, J., Yan, S.Q., Zeng, S., Wang, Y.B., Guo, B., Lian, G., Nan, D., Bai, X.X., Liu, W.P.: Indirect measurement of the 57.7 keV resonance strength for the astrophysical  $\gamma$ -ray source of the  $^{25}\text{Mg}(\text{p},\gamma)^{26}\text{Al}$  reaction. *Phys. Rev. C* **102**(2), 025804 (2020) <https://doi.org/10.1103/PhysRevC.102.025804>

Vogelaar, R.B., Mitchell, L.W., Kavanagh, R.W., Champagne, A.E., Magnus, P.V., Smith, M.S., Howard, A.J., Parker, P.D., O'Brien, H.A.: Constraining  $^{26}\text{Al}+\text{p}$  resonances using  $^{26}\text{Al}(\text{He}^3,\text{d})^{27}\text{Si}$ . *Phys. Rev. C* **53**(4), 1945–1949 (1996) <https://doi.org/10.1103/PhysRevC.53.1945>

Pain, S.D., Bardayan, D.W., Blackmon, J.C., Brown, S.M., Chae, K.Y., Chipps, K.A., Cizewski, J.A., Jones, K.L., Kozub, R.L., Liang, J.F., Matei, C., Matos, M., Moazen, B.H., Nesaraja, C.D., Okołowicz, J., O'Malley, P.D., Peters, W.A., Pittman, S.T., Płoszajczak, M., Schmitt, K.T., Shriner, J.F., Shapira, D., Smith, M.S., Stracener, D.W., Wilson, G.L.: Constraint of the Astrophysical  $^{Al}g_{26}(\text{p},\gamma)$  Destruction Rate at Stellar Temperatures. *Phys. Rev. Lett.* **114**(21), 212501 (2015) <https://doi.org/10.1103/PhysRevLett.114.212501>

Lotay, G., Woods, P.J., Moukaddam, M., Aliotta, M., Christian, G., Davids, B.,

Davinson, T., Doherty, D.T., Howell, D., Margerin, V., Ruiz, C.: High-resolution radioactive beam study of the  $^{26}\text{Al}(\text{d},\text{p})$  reaction and measurements of single-particle spectroscopic factors. European Physical Journal A **56**(1), 3 (2020) <https://doi.org/10.1140/epja/s10050-019-00008-8>

Ruiz, C., Parikh, A., José, J., Buchmann, L., Caggiano, J.A., Chen, A.A., Clark, J.A., Crawford, H., Davids, B., D'Auria, J.M., Davis, C., Deibel, C., Erikson, L., Fogarty, L., Frekers, D., Greife, U., Hussein, A., Hutcheon, D.A., Huyse, M., Jewett, C., Laird, A.M., Lewis, R., Mumby-Croft, P., Olin, A., Ottewell, D.F., Ouellet, C.V., Parker, P., Pearson, J., Ruprecht, G., Trinczek, M., Vockenhuber, C., Wrede, C.: Measurement of the  $E_{c.m.}=184\text{keV}$  Resonance Strength in the  $^{26g}\text{Al}(\text{p},\gamma)^{27}\text{Si}$  Reaction. Phys. Rev. Lett. **96**(25), 252501 (2006) <https://doi.org/10.1103/PhysRevLett.96.252501>

Lotay, G., Woods, P.J., Seweryniak, D., Carpenter, M.P., Janssens, R.V.F., Zhu, S.: Identification of Key Astrophysical Resonances Relevant for the  $^{26g}\text{Al}(\text{p},\gamma)^{27}\text{Si}$  Reaction in Wolf-Rayet Stars, AGB stars, and Classical Novae. Phys. Rev. Lett. **102**(16), 162502 (2009) <https://doi.org/10.1103/PhysRevLett.102.162502>

Lederer-Woods, C., Woods, P.J., Davinson, T., Kahl, D., Lonsdale, S.J., Aberle, O., Amaducci, S., Andrzejewski, J., Audouin, L., Bacak, M., Balibrea, J., Barbagallo, M., Bečvář, F., Berthoumieux, E., Billowes, J., Bosnar, D., Brown, A., Caamaño, M., Calviño, F., Calviani, M., Cano-Ott, D., Cardella, R., Casanovas, A., Cerutti, F., Chen, Y.H., Chiaveri, E., Colonna, N., Cortés, G., Cortés-Giraldo, M.A., Cosentino, L., Cristallo, S., Damone, L.A., Diakaki, M., Domingo-Pardo, C., Dressler, R., Dupont, E., Durán, I., Fernández-Domínguez, B., Ferrari, A., Ferreira, P., Ferrer, F.J., Finocchiaro, P., Furman, V., Göbel, K., García, A.R., Gawlik, A., Gilardoni, S., Glodariu, T., Gonçalves, I.F., González-Romero, E., Griesmayer, E., Guerrero, C., Gunsing, F., Harada, H., Heinitz, S., Heyse, J., Jenkins, D.G., Jericha, E., Käppeler, F., Kadi, Y., Kalamara, A., Kavrigin, P., Kimura, A., Kivel, N., Kokkoris, M., Krtička, M., Kurtulgil, D., Leal-Cidoncha, E., Leeb, H., Lerendegui-Marco, J., Lo Meo, S., Macina, D., Manna, A., Marganiec, J., Martínez, T., Masi, A., Massimi, C., Mastinu, P., Mastromarco, M., Maugeri, E.A., Mazzone, A., Mendoza, E., Mengoni, A., Milazzo, P.M., Mingrone, F., Musumarra, A., Negret, A., Nolte, R., Oprea, A., Patronis, N., Pavlik, A., Perkowski, J., Porras, I., Praena, J., Quesada, J.M., Radeck, D., Rauscher, T., Reifarth, R., Rubbia, C., Ryan, J.A., Sabaté-Gilarte, M., Saxena, A., Schillebeeckx, P., Schumann, D., Sedyshev, P., Smith, A.G., Sosnin, N.V., Stamatopoulos, A., Tagliente, G., Tain, J.L., Tarifeño-Saldivia, A., Tassan-Got, L., Valenta, S., Vannini, G., Variale, V., Vaz, P., Ventura, A., Vlachoudis, V., Vlastou, R., Wallner, A., Warren, S., Weiss, C., Wright, T., Žugec, P., n TOF Collaboration: Destruction of the cosmic  $\gamma$ -ray emitter  $^{26}\text{Al}$  in massive stars: Study of the key  $^{26}\text{Al}(\text{n},\text{p})$  reaction. Phys. Rev. C **104**(2), 022803 (2021) <https://doi.org/10.1103/PhysRevC.104.L022803>

Lederer-Woods, C., Woods, P.J., Davinson, T., Estrade, A., Heyse, J., Kahl, D., Lonsdale, S.J., Paradela, C., Schillebeeckx, P., Aberle, O., Amaducci, S., Andrzejewski,

J., Audouin, L., Bacak, M., Balibrea, J., Barbagallo, M., Bečvář, F., Berthoumieux, E., Billowes, J., Bosnar, D., Brown, A., Caamaño, M., Calviño, F., Calviani, M., Cano-Ott, D., Cardella, R., Casanovas, A., Cerutti, F., Chen, Y.H., Chiaveri, E., Colonna, N., Cortés, G., Cortés-Giraldo, M.A., Cosentino, L., Cristallo, S., Damone, L.A., Diakaki, M., Domingo-Pardo, C., Dressler, R., Dupont, E., Durán, I., Fernández-Domínguez, B., Ferrari, A., Ferreira, P., Ferrer, F.J., Finocchiaro, P., Furman, V., Göbel, K., García, A.R., Gawlik, A., Gilardon, S., Glodariu, T., Gonçalves, I.F., González-Romero, E., Griesmayer, E., Guerrero, C., Gunsing, F., Harada, H., Heinitz, S., Jenkins, D.G., Jericha, E., Käppeler, F., Kadi, Y., Kalamaras, A., Kavrigin, P., Kimura, A., Kivel, N., Kokkoris, M., Krčíčka, M., Kurtulgil, D., Leal-Cidoncha, E., Leeb, H., Lerendegui-Marco, J., Lo Meo, S., Macina, D., Manna, A., Marganiec, J., Martínez, T., Masi, A., Massimi, C., Mastinu, P., Mastro-marco, M., Maugeri, E.A., Mazzone, A., Mendoza, E., Mengoni, A., Milazzo, P.M., Migrone, F., Musumarra, A., Negret, A., Nolte, R., Oprea, A., Patronis, N., Pavlik, A., Perkowski, J., Porras, I., Praena, J., Quesada, J.M., Radeck, D., Rauscher, T., Reifarth, R., Rubbia, C., Ryan, J.A., Sabaté-Gilarte, M., Saxena, A., Schumann, D., Sedyshev, P., Smith, A.G., Sosnin, N.V., Stamatopoulos, A., Tagliente, G., Tain, J.L., Tarifeño-Saldivia, A., Tassan-Got, L., Valenta, S., Vannini, G., Variale, V., Vaz, P., Ventura, A., Vlachoudis, V., Vlastou, R., Wallner, A., Warren, S., Weiss, C., Wright, T., Žugec, P., n TOF Collaboration: Destruction of the cosmic  $\gamma$ -ray emitter  $^{26}\text{Al}$  in massive stars: Study of the key  $^{26}\text{Al}(\text{n},\alpha)$  reaction. *Phys. Rev. C* **104**(3), 032803 (2021) <https://doi.org/10.1103/PhysRevC.104.L032803>

Benamara, S., de Séréville, N., Laird, A.M., Hammache, F., Stefan, I., Roussel, P., Ancelin, S., Assié, M., Coc, A., Deloncle, I., Fox, S.P., Kiener, J., Lefebvre, L., Lefebvre-Schuhl, A., Mavilla, G., Morfouace, P., Sánchez-Benítez, Á.M., Perrot, L., Sinha, M., Tatischeff, V., Vandebruck, M.: Nucleosynthesis of Al26 in massive stars: New Al27 states above  $\alpha$  and neutron emission thresholds. *Phys. Rev. C* **89**(6), 065805 (2014) <https://doi.org/10.1103/PhysRevC.89.065805>

Diehl, R., Lugaro, M., Heger, A., Sieverding, A., Tang, X., Li, K.A., Li, E.T., Doherty, C.L., Krause, M.G.H., Wallner, A., Prantzos, N., Brinkman, H.E., den Hartogh, J.W., Wehmeyer, B., Yagüe López, A., Pleintinger, M.M.M., Banerjee, P., Wang, W.: The radioactive nuclei  $^{26}\text{Al}$  and  $^{60}\text{Fe}$  in the Cosmos and in the solar system. *PASA* **38**, 062 (2021) <https://doi.org/10.1017/pasa.2021.48> arXiv:2109.08558 [astro-ph.HE]

Laird, A.M., Lugaro, M., Kankainen, A., Adsley, P., Bardayan, D.W., Brinkman, H.E., Côté, B., Deibel, C.M., Diehl, R., Hammache, F., den Hartogh, J.W., José, J., Kurtulgil, D., Lederer-Woods, C., Lotay, G., Meynet, G., Palmerini, S., Pignatari, M., Reifarth, R., de Séréville, N., Sieverding, A., Stancliffe, R.J., Trueman, T.C.L., Lawson, T., Vink, J.S., Massimi, C., Mengoni, A.: Progress on nuclear reaction rates affecting the stellar production of  $^{26}\text{Al}$ . *Journal of Physics G Nuclear Physics* **50**(3), 033002 (2023) <https://doi.org/10.1088/1361-6471/ac9cf8>

Uberseder, E., Reifarth, R., Schumann, D., Dillmann, I., Pardo, C.D., Görres, J.,

Heil, M., Käppeler, F., Marganiec, J., Neuhausen, J., Pignatari, M., Voss, F., Walter, S., Wiescher, M.: Measurement of the  $^{60}\text{Fe}(n,\gamma)^{61}\text{Fe}$  Cross Section at Stellar Temperatures. *Phys. Rev. Lett.* **102**(15), 151101 (2009) <https://doi.org/10.1103/PhysRevLett.102.151101>

Giron, S., Hammache, F., de Séerville, N., Roussel, P., Burgunder, J., Moukaddam, M., Beaumel, D., Caceres, L., Duchêne, G., Clément, E., Fernandez-Dominguez, B., Flavigny, F., de France, G., Franchoo, S., Galaviz-Redondo, D., Gasques, L., Gibelin, J., Gillibert, A., Grevy, S., Guillot, J., Heil, M., Kiener, J., Lapoux, V., Maréchal, F., Matta, A., Matea, I., Nalpas, L., Pancin, J., Perrot, L., Obertelli, A., Raabe, R., Scarpaci, J.A., Sieja, K., Sorlin, O., Stefan, I., Stodel, C., Takechi, M., Thomas, J.C., Togano, Y.: Spectroscopy of  $^{61}\text{Fe}$  via the neutron transfer reaction  $^2\text{H}(^{60}\text{Fe},\text{p})^{61}\text{Fe}$ . *Phys. Rev. C* **95**(3), 035806 (2017) <https://doi.org/10.1103/PhysRevC.95.035806>

Gao, B., Giraud, S., Li, K.A., Sieverding, A., Zegers, R.G.T., Tang, X., Ash, J., Ayyad-Limonge, Y., Bazin, D., Biswas, S., Brown, B.A., Chen, J., DeNudt, M., Farris, P., Gabler, J.M., Gade, A., Ginter, T., Grinder, M., Heger, A., Hultquist, C., Hill, A.M., Iwasaki, H., Kwan, E., Li, J., Longfellow, B., Maher, C., Ndayisabye, F., Noji, S., Pereira, J., Qi, C., Rebenstock, J., Revel, A., Rhodes, D., Sanchez, A., Schmitt, J., Sumithrarachchi, C., Sun, B.H., Weisshaar, D.: New  $^{59}\text{Fe}$  Stellar Decay Rate with Implications for the  $^{60}\text{Fe}$  Radioactivity in Massive Stars. *Phys. Rev. Lett.* **126**(15), 152701 (2021) <https://doi.org/10.1103/PhysRevLett.126.152701>

Li, K.A., Lam, Y.H., Qi, C., Tang, X.D., Zhang, N.T.:  $\beta$  -decay rate of  $^{59}\text{Fe}$  in shell burning environment and its influence on the production of  $^{60}\text{Fe}$  in a massive star. *Phys. Rev. C* **94**(6), 065807 (2016) <https://doi.org/10.1103/PhysRevC.94.065807>

Langanke, K., Martínez-Pinedo, G.: Rate Tables for the Weak Processes of pf-SHELL Nuclei in Stellar Environments. *Atomic Data and Nuclear Data Tables* **79**(1), 1–46 (2001) <https://doi.org/10.1006/adnd.2001.0865>

Uberseder, E., Adachi, T., Aumann, T., Beceiro-Novo, S., Boretzky, K., Caesar, C., Dillmann, I., Ershova, O., Estrade, A., Farinon, F., Hagdahl, J., Heftrich, T., Heil, M., Heine, M., Holl, M., Ignatov, A., Johansson, H.T., Kalantar, N., Langer, C., Le Bleis, T., Litvinov, Y.A., Marganiec, J., Movsesyan, A., Najafi, M.A., Nilsson, T., Nociforo, C., Panin, V., Pietri, S., Plag, R., Prochazka, A., Rastrepina, G., Reifarth, R., Ricciardi, V., Rigollet, C., Rossi, D.M., Savran, D., Simon, H., Sonnabend, K., Streicher, B., Terashima, S., Thies, R., Togano, Y., Volkov, V., Wamers, F., Weick, H., Weigand, M., Wiescher, M., Wimmer, C., Winckler, N., Woods, P.J.: First Experimental Constraint on the  $^{59}\text{Fe}(n,\gamma)^{60}\text{Fe}$  Reaction Cross Section at Astrophysical Energies via the Coulomb Dissociation of Fe60. *Phys. Rev. Lett.* **112**(21), 211101 (2014) <https://doi.org/10.1103/PhysRevLett.112.211101>

Yan, S.Q., Li, X.Y., Nishio, K., Lugaro, M., Li, Z.H., Makii, H., Pignatari, M., Wang, Y.B., Orlandi, R., Hirose, K., Tsukada, K., Mohr, P., Li, G.S., Wang, J.G., Gao, B.S., Han, Y.L., Guo, B., Li, Y.J., Shen, Y.P., Sato, T.K., Ito, Y., Suzuki, F., Su,

J., Yang, Y.Y., Wang, J.S., Ma, J.B., Ma, P., Bai, Z., Xu, S.W., Ren, J., Fan, Q.W., Zeng, S., Han, Z.Y., Nan, W., Nan, W.K., Chen, C., Lian, G., Hu, Q., Duan, F.F., Jin, S.Y., Tang, X.D., Liu, W.P.: The  $^{59}\text{Fe}(n,\gamma)^{60}\text{Fe}$  Cross Section from the Surrogate Ratio Method and Its Effect on the  $^{60}\text{Fe}$  Nucleosynthesis. *ApJ* **919**(2), 84 (2021) <https://doi.org/10.3847/1538-4357/ac12ce> [arXiv:2109.12654](https://arxiv.org/abs/2109.12654) [astro-ph.GA]

Spyrou, A., Richman, D., Couture, A., Fields, C.E., Liddick, S.N., Childers, K., Crider, B.P., DeYoung, P.A., Dombos, A.C., Gastis, P., Guttormsen, M., Hermansen, K., Larsen, A.C., Lewis, R., Lyons, S., Midtbø, J.E., Mosby, S., Muecher, D., Naqvi, F., Palmisano-Kyle, A., Perdikakis, G., Prokop, C., Schatz, H., Smith, M.K., Sumithrarachchi, C., Sweet, A.: Enhanced production of  $^{60}\text{Fe}$  in massive stars. *Nature Communications* **15**(1), 9608 (2024) <https://doi.org/10.1038/s41467-024-54040-4> [arXiv:2412.01723](https://arxiv.org/abs/2412.01723) [nucl-ex]

Grefenstette, B.W., Harrison, F.A., Boggs, S.E., Reynolds, S.P., Fryer, C.L., Madsen, K.K., Wik, D.R., Zoglauer, A., Ellinger, C.I., Alexander, D.M., An, H., Barret, D., Christensen, F.E., Craig, W.W., Forster, K., Giommi, P., Hailey, C.J., Hornstrup, A., Kaspi, V.M., Kitaguchi, T., Koglin, J.E., Mao, P.H., Miyasaka, H., Mori, K., Perri, M., Pivovaroff, M.J., Puccetti, S., Rana, V., Stern, D., Westergaard, N.J., Zhang, W.W.: Asymmetries in core-collapse supernovae from maps of radioactive  $^{44}\text{Ti}$  in Cassiopeia A. *Nature* **506**(7488), 339–342 (2014) <https://doi.org/10.1038/nature12997> [arXiv:1403.4978](https://arxiv.org/abs/1403.4978) [astro-ph.HE]

Subedi, S.K., Meisel, Z., Merz, G.: Sensitivity of  $^{44}\text{Ti}$  and  $^{56}\text{Ni}$  Production in Core-collapse Supernova Shock-driven Nucleosynthesis to Nuclear Reaction Rate Variations. *ApJ* **898**(1), 5 (2020) <https://doi.org/10.3847/1538-4357/ab9745> [arXiv:2005.14702](https://arxiv.org/abs/2005.14702) [astro-ph.HE]

Hermansen, K., Couch, S.M., Roberts, L.F., Schatz, H., Warren, M.L.: Reaction Rate Sensitivity of the Production of  $\gamma$ -Ray Emitting Isotopes in Core-collapse Supernovae. *ApJ* **901**(1), 77 (2020) <https://doi.org/10.3847/1538-4357/abaflb> [arXiv:2006.16181](https://arxiv.org/abs/2006.16181) [astro-ph.SR]

Fougères, C., de Oliveira Santos, F., de Séerville, N., Hammache, F.: Experiment e13037 at FRIB

Seuthe, S., Rolfs, C., Schröder, U., Schulte, W.H., Somorjai, E., Trautvetter, H.P., Waanders, F.B., Kavanagh, R.W., Ravn, H., Arnould, M., Paulus, G.: Resonances in the  $^{22}\text{Na}(p, \gamma)^{23}\text{Mg}$  reaction. *Nucl. Phys. A* **514**(3), 471–502 (1990) [https://doi.org/10.1016/0375-9474\(90\)90153-D](https://doi.org/10.1016/0375-9474(90)90153-D)

Stegmüller, F., Rolfs, C., Schmidt, S., Schulte, W.H., Trautvetter, H.P., Kavanagh, R.W.:  $^{22}\text{Na}(p, \gamma)^{23}\text{Mg}$  resonant reaction at low energies. *Nucl. Phys. A* **601**(2), 168–180 (1996) [https://doi.org/10.1016/0375-9474\(96\)00084-X](https://doi.org/10.1016/0375-9474(96)00084-X)

Sallaska, A.L., Wrede, C., García, A., Storm, D.W., Brown, T.A.D., Ruiz, C., Snover, K.A., Ottewell, D.F., Buchmann, L., Vockenhuber, C., Hutz, D.A., Caggiano,

J.A.: Direct Measurements of  $^{22}\text{Na}(\text{p},\gamma)^{23}\text{Mg}$  Resonances and Consequences for  $^{22}\text{Na}$  Production in Classical Novae. *Phys. Rev. Lett.* **105**(15), 152501 (2010) <https://doi.org/10.1103/PhysRevLett.105.152501>

de Oliveira Santos, F.: The  $^{18}\text{F}(\text{p}, \alpha)^{15}\text{O}$  reaction: A textbook case in nuclear astrophysics. *Progress in Particle and Nuclear Physics* **142**, 104154 (2025) <https://doi.org/10.1016/j.ppnp.2025.104154>

de Séerville, N., Angulo, C., Coc, A., Achouri, N.L., Casarejos, E., Davinson, T., Descouvemont, P., Figuera, P., Fox, S., Hammache, F., Kiener, J., Laird, A., Lefebvre-Schuhl, A., Leleux, P., Mumby-Croft, P., Orr, N.A., Stefan, I., Vaughan, K., Tatischeff, V.: Low-energy  $^{18}\text{F}(\text{p}, \alpha)^{15}\text{O}$  cross section measurements relevant to nova  $\gamma$ -ray emission. *Phys. Rev. C* **79**(1), 015801 (2009) <https://doi.org/10.1103/PhysRevC.79.015801>

Beer, C.E., Laird, A.M., Murphy, A.S.J., Bentley, M.A., Buchman, L., Davids, B., Davinson, T., Diget, C.A., Fox, S.P., Fulton, B.R., Hager, U., Howell, D., Martin, L., Ruiz, C., Ruprecht, G., Salter, P., Vockenhuber, C., Walden, P.: Direct measurement of the  $^{18}\text{F}(\text{p}, \alpha)^{15}\text{O}$  reaction at nova temperatures. *Phys. Rev. C* **83**(4), 042801 (2011) <https://doi.org/10.1103/PhysRevC.83.042801>

Kahl, D., José, J., Woods, P.J.: Uncertainties in the  $^{18}\text{F}(\text{p}, \alpha)^{15}\text{O}$  reaction rate in classical novae. *A&A* **653**, 64 (2021) <https://doi.org/10.1051/0004-6361/202140339> [arXiv:2106.02606](https://arxiv.org/abs/2106.02606) [nucl-th]

Timmes, F., Fryer, C., Timmes, F., Hungerford, A.L., Couture, A., Adams, F., Aoki, W., Arcones, A., Arnett, D., Auchettl, K., Avila, M., Badenes, C., Baron, E., Bauswein, A., Beacom, J., Blackmon, J., Blondin, S., Bloser, P., Boggs, S., Boss, A., Brandt, T., Bravo, E., Brown, E., Brown, P., Bruenn, S., Budtz-Jørgensen, C., Burns, E., Calder, A., Caputo, R., Champagne, A., Chevalier, R., Chieffi, A., Chipps, K., Cinabro, D., Clarkson, O., Clayton, D., Coc, A., Connolly, D., Conroy, C., Côté, B., Couch, S., Dauphas, N., deBoer, R.J., Deibel, C., Denisenkov, P., Desch, S., Dessart, L., Diehl, R., Doherty, C., Domínguez, I., Dong, S., Dwarkadas, V., Fan, D., Fields, B., Fields, C., Filippenko, A., Fisher, R., Foucart, F., Fransson, C., Fröhlich, C., Fuller, G., Gibson, B., Giryanskaya, V., Görres, J., Goriely, S., Grebenev, S., Grefenstette, B., Grohs, E., Guillochon, J., Harpole, A., Harris, C., Harris, J.A., Harrison, F., Hartmann, D., Hashimoto, M.-a., Heger, A., Hernanz, M., Herwig, F., Hirschi, R., Hix, W.R., Höflich, P., Hoffman, R., Holcomb, C., Hsiao, E., Iliadis, C., Janiuk, A., Janka, T., Jerkstrand, A., Johns, L., Jones, S., José, J., Kajino, T., Karakas, A., Karpov, P., Kasen, D., Kierans, C., Kippen, M., Korobkin, O., Kobayashi, C., Kozma, C., Krot, S., Kumar, P., Kuvvetli, I., Laird, A., Laming, J.M., Larsson, J., Lattanzio, J., Lattimer, J., Leising, M., Lennarz, A., Lentz, E., Limongi, M., Lippuner, J., Livne, E., Lloyd-Ronning, N., Longland, R., Lopez, L.A., Lugaro, M., Lutovinov, A., Madsen, K., Malone, C., Matteucci, F., McEnery, J., Meisel, Z., Messer, B., Metzger, B., Meyer, B., Meynet, G., Mezzacappa, A., Miller, J., Miller, R., Milne, P., Misch, W., Mitchell, L., Mösta, P.,

Motizuki, Y., Müller, B., Mumpower, M., Murphy, J., Nagataki, S., Nakar, E., Nomoto, K., Nugent, P., Nunes, F., O'Shea, B., Oberlack, U., Pain, S., Parker, L., Perego, A., Pignatari, M., Pinedo, G.M., Plewa, T., Poznanski, D., Priedhorsky, W., Pritychenko, B., Radice, D., Ramirez-Ruiz, E., Rauscher, T., Reddy, S., Rehm, E., Reifarth, R., Richman, D., Ricker, P., Rijal, N., Roberts, L., Röpke, F., Rosswog, S., Ruiter, A.J., Ruiz, C., Savin, D.W., Schatz, H., Schneider, D., Schwab, J., Seitenzahl, I., Shen, K., Siegert, T., Sim, S., Smith, D., Smith, K., Smith, M., Sollerman, J., Sprouse, T., Spyrou, A., Starrfield, S., Steiner, A., Strong, A.W., Sukhbold, T., Suntzeff, N., Surman, R., Tanimori, T., The, L.-S., Thielemann, F.-K., Tolstov, A., Tominaga, N., Tomsick, J., Townsley, D., Tsintari, P., Tsygankov, S., Vartanyan, D., Venters, T.: Catching Element Formation In The Act ; The Case for a New MeV Gamma-Ray Mission: Radionuclide Astronomy in the 2020s. *BAAS* **51**(3), 2 (2019) <https://doi.org/10.48550/arXiv.1902.02915> arXiv:1902.02915 [astro-ph.HE]

FRIB: <https://frib.msu.edu/>. <https://asd.gsfc.nasa.gov/amego/>

Kim, Y.J.: Current status of experimental facilities at RAON. *Nuclear Instruments and Methods in Physics Research B* **463**, 408–414 (2020) <https://doi.org/10.1016/j.nimb.2019.04.041>

Kierans, C.A., Boggs, S.E., Chiu, J.-L., Lowell, A., Sleator, C., Tomsick, J.A., Zoglauer, A., Amman, M., Chang, H.-K., Tseng, C.-H., Yang, C.-Y., Lin, C.-H., Jean, P., von Ballmoos, P.: The 2016 Super Pressure Balloon flight of the Compton Spectrometer and Imager. *arXiv e-prints*, 1701–05558 (2017) <https://doi.org/10.48550/arXiv.1701.05558> arXiv:1701.05558 [astro-ph.IM]

AMEGO: <https://asd.gsfc.nasa.gov/amego/>. <https://asd.gsfc.nasa.gov/amego/>

ASTROGAM: <http://new-astrogam.eu/>. <https://asd.gsfc.nasa.gov/amego/>

Hotokezaka, K., Wanajo, S., Tanaka, M., Bamba, A., Terada, Y., Piran, T.: Radioactive decay products in neutron star merger ejecta: heating efficiency and  $\gamma$ -ray emission. *MNRAS* **459**(1), 35–43 (2016) <https://doi.org/10.1093/mnras/stw404> arXiv:1511.05580 [astro-ph.HE]

Vestrand, W.T., Share, G.H., Murphy, R., Forrest, D.J., Rieger, E., Chupp, E.L., Kanbach, G.: The Solar Maximum Mission Atlas of Gamma-Ray Flares. *ApJS* **120**(2), 409–467 (1999) <https://doi.org/10.1086/313180>

Leventhal, M.: Deuterium Formation Hypothesis for the Diffuse Gamma-ray Excess at 1 MeV. *Nature* **246**(5429), 136–138 (1973) <https://doi.org/10.1038/246136a0>

Guessoum, N., Dermer, C.D.: Properties of hydrogen/helium accretion plasmas. In: Gehrels, N., Share, G.H. (eds.) *Nuclear Spectroscopy of Astrophysical Sources*. American Institute of Physics Conference Series, vol. 170, pp. 332–337. AIP, ??? (1988). <https://doi.org/10.1063/1.37227>

Aharonian, F.A., Sunyaev, R.A.: Gamma-ray line emission, nuclear destruction and neutron production in hot astrophysical plasmas. The deuterium boiler as a gamma-ray source. *MNRAS* **210**, 257–277 (1984) <https://doi.org/10.1093/mnras/210.2.257>

Shvartsman, V.F.: On the generation of relativistic particles by neutron stars in the state of accretion. *Astrofizika* **6**, 309–317 (1970)

Bildsten, L., Salpeter, E.E., Wasserman, I.: The Fate of Accreted CNO Elements in Neutron Star Atmospheres: X-Ray Bursts and Gamma-Ray Lines. *ApJ* **384**, 143 (1992) <https://doi.org/10.1086/170860>

Jean, P., Guessoum, N.: Neutron-capture and 2.22 MeV emission in the atmosphere of the secondary of an X-ray binary. *A&A* **378**, 509–521 (2001) <https://doi.org/10.1051/0004-6361:20011201> arXiv:astro-ph/0109185 [astro-ph]

Guessoum, N., Jean, P.: Detectability and characteristics of the 2.223 MeV line emission from nearby X-ray binaries. *A&A* **396**, 157–169 (2002) <https://doi.org/10.1051/0004-6361:20021376>

Vestrand, W.T.: A New Gamma-Ray Diagnostic for Energetic Ion Distributions: The Compton Tail on the Neutron Capture Line. *ApJ* **352**, 353 (1990) <https://doi.org/10.1086/168542>

Sabti, N., Alvey, J., Escudero, M., Fairbairn, M., Blas, D.: Refined Bounds on MeV-scale Thermal Dark Sectors from BBN and the CMB. *JCAP* **01**, 004 (2020) <https://doi.org/10.1088/1475-7516/2020/01/004> arXiv:1910.01649 [hep-ph]

Slatyer, T.R.: Indirect dark matter signatures in the cosmic dark ages. I. Generalizing the bound on s-wave dark matter annihilation from Planck results. *Phys. Rev. D* **93**(2), 023527 (2016) <https://doi.org/10.1103/PhysRevD.93.023527> arXiv:1506.03811 [hep-ph]

Antel, C., *et al.*: Feebly-interacting particles: FIPs 2022 Workshop Report. *Eur. Phys. J. C* **83**(12), 1122 (2023) <https://doi.org/10.1140/epjc/s10052-023-12168-5> arXiv:2305.01715 [hep-ph]

Krnjaic, G., McDermott, S.D.: Implications of BBN Bounds for Cosmic Ray Upscattered Dark Matter. *Phys. Rev. D* **101**(12), 123022 (2020) <https://doi.org/10.1103/PhysRevD.101.123022> arXiv:1908.00007 [hep-ph]

Boyarsky, A., Drewes, M., Lasserre, T., Mertens, S., Ruchayskiy, O.: Sterile neutrino Dark Matter. *Prog. Part. Nucl. Phys.* **104**, 1–45 (2019) <https://doi.org/10.1016/j.ppnp.2018.07.004> arXiv:1807.07938 [hep-ph]

Siegert, T., Berteaud, J., Calore, F., Serpico, P.D., Weinberger, C.: Diffuse Galactic emission spectrum between 0.5 and 8.0 MeV. *A&A* **660**, 130 (2022) <https://doi.org/10.1051/0004-6361/202142639> arXiv:2202.04574 [astro-ph.HE]

Sieger, T., Boehm, C., Calore, F., Diehl, R., Krause, M.G.H., Serpico, P.D., Vincent, A.C.: An INTEGRAL/SPI view of reticulum II: particle dark matter and primordial black holes limits in the MeV range. *Mon. Not. Roy. Astron. Soc.* **511**(1), 914–924 (2022) <https://doi.org/10.1093/mnras/stac008> arXiv:2109.03791 [astro-ph.HE]

Sieger, T., Diehl, R., Khachatryan, G., Krause, M.G.H., Guglielmetti, F., Greiner, J., Strong, A.W., Zhang, X.: Gamma-ray spectroscopy of Positron Annihilation in the Milky Way. *Astron. Astrophys.* **586**, 84 (2016) <https://doi.org/10.1051/0004-6361/201527510> arXiv:1512.00325 [astro-ph.HE]

Sieger, T., Crocker, R.M., Macias, O., Panther, F.H., Calore, F., Song, D., Horiuchi, S.: Measuring the smearing of the Galactic 511-keV signal: positron propagation or supernova kicks? *Mon. Not. Roy. Astron. Soc.* **509**(1), 11–16 (2021) <https://doi.org/10.1093/mnrasl/slab113> arXiv:2109.03691 [astro-ph.HE]

Prantzos, N., *et al.*: The 511 keV emission from positron annihilation in the Galaxy. *Rev. Mod. Phys.* **83**, 1001–1056 (2011) <https://doi.org/10.1103/RevModPhys.83.1001> arXiv:1009.4620 [astro-ph.HE]

Aghaie, M., Torre Luque, P., Dondarini, A., Gaggero, D., Marino, G., Panci, P.: (H)ALPing the 511 keV line: A thermal DM interpretation of the 511 keV emission (2025) arXiv:2501.10504 [hep-ph]

Vincent, A.C., Martin, P., Cline, J.M.: Interacting dark matter contribution to the Galactic 511 keV gamma ray emission: constraining the morphology with INTEGRAL/SPI observations. *JCAP* **04**, 022 (2012) <https://doi.org/10.1088/1475-7516/2012/04/022> arXiv:1201.0997 [hep-ph]

Liu, H., Slatyer, T.R., Zavala, J.: Contributions to cosmic reionization from dark matter annihilation and decay. *Phys. Rev. D* **94**(6), 063507 (2016) <https://doi.org/10.1103/PhysRevD.94.063507> arXiv:1604.02457 [astro-ph.CO]

Diamanti, R., Lopez-Honorez, L., Mena, O., Palomares-Ruiz, S., Vincent, A.C.: Constraining Dark Matter Late-Time Energy Injection: Decays and P-Wave Annihilations. *JCAP* **02**, 017 (2014) <https://doi.org/10.1088/1475-7516/2014/02/017> arXiv:1308.2578 [astro-ph.CO]

Bartels, R., Gaggero, D., Weniger, C.: Prospects for indirect dark matter searches with MeV photons. *JCAP* **05**, 001 (2017) <https://doi.org/10.1088/1475-7516/2017/05/001> arXiv:1703.02546 [astro-ph.HE]

Carenza, P., Giannotti, M., Isern, J., Mirizzi, A., Straniero, O.: Axion astrophysics. *Phys. Rept.* **1117**, 1–102 (2025) <https://doi.org/10.1016/j.physrep.2025.02.002> arXiv:2411.02492 [hep-ph]

Calore, F., Carenza, P., Giannotti, M., Jäckel, J., Lucente, G., Mirizzi, A.: Supernova bounds on axionlike particles coupled with nucleons and electrons.

Phys. Rev. D **104**(4), 043016 (2021) <https://doi.org/10.1103/PhysRevD.104.043016>  
[arXiv:2107.02186](https://arxiv.org/abs/2107.02186) [hep-ph]

Aramaki, T., et al.: Snowmass2021 Cosmic Frontier: The landscape of cosmic-ray and high-energy photon probes of particle dark matter (2022) [arXiv:2203.06894](https://arxiv.org/abs/2203.06894) [hep-ex]

Caputo, A., Negro, M., Regis, M., Taoso, M.: Dark Matter prospects with COSI: ALPs, PBHs and sub-GeV Dark Matter (2022) [arXiv:2210.09310](https://arxiv.org/abs/2210.09310) [hep-ph]

Coogan, A., Morrison, L., Profumo, S.: Precision gamma-ray constraints for sub-GeV dark matter models. JCAP **08**, 044 (2021) <https://doi.org/10.1088/1475-7516/2021/08/044> [arXiv:2104.06168](https://arxiv.org/abs/2104.06168) [hep-ph]